MODELLING OF STREAMER INITIATION AND PROPAGATION PHENOMENA IN DIELECTRIC LIQUIDS

A thesis submitted to The University of Manchester for the degree of PhD

in the Faculty of Science and Engineering

2021

DONGLIN LIU

Department of Electrical and Electronic Engineering

School of Engineering

Contents

Word Count 47292

List of Figures

List of Tables

Nomenclature

Variables	Meaning
V	Voltage potential
$\vec{E}$	Electric field
$c_{+,-,e}$	Charge density of positive ions, negative ions and electrons
$\mu_{+,-,e}$	Charge mobility of positive ions, negative ions and electrons
$\vec{J}$	Current density
$\overrightarrow{v_l}$	Liquid velocity
p	Thermodynamic pressure
p_{EF}	Electrostrictive force pressure
p_{CF}	Coulomb force pressure
p_{total}	Total pressure
ρ_l	Liquid density
ε_0	Permittivity of vacuum
ε_r	Relative permittivity
V_b	Breakdown voltage
V_a	Acceleration voltage
α_T	First Townsend ionization coefficient
G_I	Impact ionization charge generation rate
G_M	Molecular ionization charge generation rate
n_0	Number density of ionisable molecules
q	Electronic charge
a	Molecular separation
h	Planck's constant
m^*	Effective electron mass
Δ	Ionization potential
$R_{\pm}$	Recombination rate of positive ions and negative ions
R_{+e}	Recombination rate of positive ions and electrons
τ_a	Electron attachment time

Abstract

Dielectric liquids have been widely used in high voltage equipment, such as power transformers, for over a century, and have also generated interest in the application of immersion cooled, power dense equipment in recent years. Electrical breakdown and pre-breakdown phenomena in dielectric liquids, known as streamers, are vital characteristics that need studying. In addition to experimental research, modelling studies can provide supplementary descriptions on streamer dynamics and mechanisms, as well as enable parametric investigations by considering a wide range of factors. Therefore, this study will model streamer initiation and propagation phenomena in dielectric liquids. The finite element method based on a set of governing equations including Poisson equation, charge continuity equations, Navier-stokes equations and thermal diffusion equation have been adopted and implemented using COMSOL Multiphysics.

Electron saturation velocity was proposed to explain the stable propagation velocity of a 2nd mode positive streamer. Instant streamer velocity shows an initial increasing and then decreasing trend until reaching a stabilised value recognised as the typical 2nd mode streamer propagation velocity. Decreasing ESV greatly decreases streamer propagation velocity. An ESV of 7.5 km/s for cyclohexane is proven suitable, based on comparisons of streamer velocity between simulations in the present work and experiments in [1] under a wide range of voltage levels.

The dynamics of cavity formation induced by electrostrictive force was initially studied in cyclohexane. Electrostrictive force tends to stretch the liquid due to dielectric polarisation. Higher voltage rise rates require lower voltage magnitude to form a cavity. However, when the voltage rise rate is smaller than 30 kV/ns, a cavity is hard to form in cyclohexane. Comparisons of the dynamics of cavity formation in different liquids were then conducted, showing that a cavity is harder to form in cyclohexane and rapeseed oil than in deionised water due to the smaller relative permittivity of cyclohexane and rapeseed oil.

The streamer initiation process was investigated over a wide range of voltage rise rates from 0.075 kV/ns to 70 kV/ns. When considering both electrostrictive force and space charge generation, it is hard to form a cavity before the liquid reaches vaporisation threshold during positive streamer initiation. Besides, decreasing the voltage rise rate also reduces the streamer initiation voltage and streamer initiation length, whilst increasing the streamer initiation time.

Modelling low-density channel formation during streamer propagation was attempted by combining charge drift model and smooth phase transition model. When the low-density channel is formed due to liquid vaporisation, a secondary electric field peak is formed on the low-density channel tip, which is followed by a positive space charge density peak. The voltage drop along the streamer channel is reduced compared with the case without considering the low-density channel.

Declaration

I declare that no portion of the work referred to in the thesis has been submitted in support of an application for another degree or qualification of this or any other university or other institute of learning.

Copyright Statement

Acknowledgement

When I finished the technical part of this Ph.D. thesis, I just realized that I have grown up a lot in academic and social knowledge during my four-year Ph.D. life. Looking back to the four years, there is no way in which I could achieve this without the help of so many people.

First and foremost, I thank my supervisor, Dr. Qiang Liu, and co-supervisor, Prof. Zhongdong Wang, for their continuous guidance and support in both technical and life knowledge which made my Ph.D. life very colourful and go very well. I also thank Dr. Qiang Liu and Prof. Zhongdong Wang very much for offering me so excellent modelling workstation and working environment for my research. Sincere appreciations are also given to them for allowing me to work remotely during the toughest time. Their understanding is the warmest action to support my Ph.D. life.

Great thanks are also given to my colleagues in the transformer groups. I thank very much to Dr. Xiang Zhang who gave me a lot of guidance on simulation tools and directions. I thank Dr. Shuhang Shen very much for his great help on my understanding of experimental techniques and his suggestions. I thank Prof. Paul Jarmon for kind suggestions. Special thanks are given to Dr. Xiaozhou Mao, Mr. Bozhi Cheng, Dr. Yiming Huang, Mr. Haichuan Yu, Mr. Sicheng Zhao and Mr. Xiaohan Li. Discussion on techniques and gathering for entertainment with them have made my Ph.D. life very interesting and full of fun.

I also thank the support from the President Doctoral Scholarship in the university which support me financially for three years.

Finally, I thank my grandparents and parents for their support, love, encouragement and care during my Ph.D. life and my whole life. I also thank my Taoism master for care, support and guiding my life. I love you all.

1 Introduction

1.1 Background

1.1.1 Application of Dielectric Liquids in Transformers

Electricity, as one of the most significant forms of energy in modern society, is closely integrated with every aspect of daily life, including work, education, transportation, catering, entertainment and medicine. Reliability in the generation, transmission and distribution of electricity is thus of critical importance, with the power system network playing an important role. Transformers, first used in the high voltage AC power system in the late 19th century, have been widely recognised as one of the key network components [2]. Liquid filled transformers have been the dominating type although gas insulated and dry type transformers do exist. The liquid used in transformers acts as an electrical insulator, cooling medium and information carrier regarding the health status of the transformer [3].

Mineral oil has been used for a century for its key advantages, especially its high insulating properties, low cost and good compatibility with cellulose solid insulation. In recent decades, alternative liquids have been used more in power systems due to their better environmental performance and, for some liquids, their higher fire point [3]. However, the experience in terms of insulation design gained through mineral oil may not be applicable for alternative liquids. For example, in a divergent field, streamers in ester liquids propagate faster and further than in mineral oil at the same voltage level [3]. Hence, a large number of experiments are required to test new liquids based on small-scale to large-scale test platforms, which are indeed time consuming and costly. Therefore, it is necessary to develop simulation models for studying streamer and breakdown phenomena.

1.1.2 Electrical Breakdown in Dielectric Liquids

Electrical breakdown is an important process to study. For any insulation design, electrical breakdown should be prevented to the utmost, which has stimulated research interest on investigating the pre-breakdown process.

The pre-breakdown phenomenon of dielectric liquids, also called streamer, has been investigated by extensive experiments for the aims that include, (a) providing data for the insulation design of high voltage equipment, (b) studying the mechanisms of

streamers and breakdown, and (c) evaluating new alternative liquids [4]. A streamer is conventionally regarded as a stream of charge density variation [4-11] and mass density variation [6, 11-14] in liquid driven by an electric field, which is also accompanied by light and energy dissipation [4, 15, 16]. Generally, a streamer is classified as either a positive (anode-initiated) or negative (cathode-initiated) streamer. Besides, for the sake of better clarification and more detailed discussion, streamers are recognised into four modes according to their average propagation velocity [4, 17]: (a) 1st mode: ~0.1 km/s, (b) 2nd mode: ~2 km/s, (c) 3rd mode: ~10 km/s and (d) 4th mode: ~100 km/s. In most cases, a positive 2nd mode streamer is the most popular object for researchers since it is accepted to be most commonly observed [4, 17] and responsible for breakdowns across a wide range of gap distances and voltage levels [1, 18-21]. Besides, experiments showed that alternatives of mineral oil, such as ester liquids, have a significantly lower positive acceleration voltage than mineral oil [22-25]. Therefore, a positive streamer is of significant interest among researchers.

Experiments on the streamer characteristics of dielectric liquids have been conducted under various conditions, including applied voltage waveform [26-29], electrode geometry [4, 26, 30, 31], liquid type [3, 32, 33], ambient pressure [13, 34, 35] and additives [1, 36, 37]. In terms of voltage waveforms, experiments under lightning impulse voltage waveform have enabled researchers to observe a single streamer at a time and eliminate the effects of previous discharges when compared with AC voltage waveforms. Step voltage [1] is a simpler voltage waveform than lightning impulse voltage waveform and is also used to avoid the quench of streamers during the voltage tail time. In terms of the electrode geometry, a needle-plane geometry has been widely used, due to its high electric field divergence at the needle tip which helps trigger streamers without causing electrical breakdowns. In comparison, it is much easier for a streamer to cross the gap once initiated in plane-plane and plane-needle-plane geometry. Concerning liquid types, most experiments have focused on mineral oils due to their wide application in power transformers. Due to the complexity of the mineral oil, white oil, as a highly refined and hydrogenated mineral oil virtually free from polyaromatics, is also used in research as a benchmark due to its simpler composition [38]. In the meanwhile, cyclohexane (C_6H_{12}) has also gained significant attention due to its purity and similarity to the major components of mineral oil (paraffinic/naphthenic molecules) [39]. Recently, ester liquid, an alternative to mineral

oil, has gained increasing attention among academics and industry due to its higher fire point and better biodegradability in transformers [3, 40, 41].

Some of the most important characteristics of streamers obtained from experiments include low-density area (streamer channel) formation, streamer velocity, streamer morphology, current signal, light emission and shockwave. A streamer consists of a low-density area which is also known as its gaseous nature. The gaseous nature of a streamer has been confirmed by pressure-dependent streamer characteristics, especially its channel dynamics [13, 34]. The current signal followed by positive streamer formation is pulsed, meaning that the propagation of a positive streamer is stepwise [42]. The velocity of the extension of the low-density area tip is generally regarded as the streamer velocity in experiments. It has been found that the streamer velocity keeps relative stable in 2nd mode within a wide voltage magnitude rang from inception voltage V_i until acceleration voltage V_a . For a general 2nd mode positive streamer, the streamer shows a filamentary shape with tens of μm in diameter and luminous light emission [4].

1.1.3 Importance of Streamer Simulation

Streamers are the developing process of electrical breakdown in dielectric liquids. It is generally agreed that both streamers and electrical breakdowns are closely related to the molecular properties of dielectric liquids. Accordingly, with more applications of alternative dielectric liquids being used in power systems, many experiments are needed to test the properties of the liquids and their further application in real electrical devices, such as power transformers. For example, detailed research on streamer characteristics in ester liquids under different voltage waveforms, voltage polarities, field factors and pressboard influences have been conducted [3, 43-46]. Research on streamer characteristics in Gas-to Liquids (GTL) can also be found in [20, 40, 47, 48]. However, conducting the full range of tests under various conditions are both time consuming and costly. Therefore, developing a simulation model is of significant interest and importance for researchers to help guide experimental tests, optimise test plans and save resources.

Besides, unlike the well-known Paschen's law in air, although there are a large number of experimental studies on streamer characteristics in different dielectric liquids, the mechanism of streamers is still unclear. For example, the reason for the stable velocity of a positive 2nd mode streamer has not been fully explained. Besides, how likely the cavity-stimulated streamer initiation could happen in dielectric liquids is also unclear.

Compared with experiments, a simulation could use mathematical equations to describe the physical nature of a streamer from a microscopic view by keeping experimental findings in mind. Besides, one or several variables affected by the nature of liquid could be controlled manually in order to investigate their influence on streamer characteristics. For example, it is found in simulations that instead of ionic ionization, charge injection or impact ionization, molecular ionization dominates positive streamer propagation [7, 49]. Besides, the reason for streamer branching was proposed in [9], which is caused by the inhomogeneity inside dielectric liquids. The number of branching channels could also be predicted. All these simulation studies indicate that simulations could help researchers further understand the dominating mechanisms of streamers under certain conditions from a microscopic view, something experiments cannot do.

Also, due to the benefits of computing science developments, it is becoming increasingly possible for researchers to use modern techniques to simulate streamers. In 1984, researchers could only use lattice points to simulate streamer dynamics, which could only include a few streamer characteristics such as an electric field [50]. Nowadays, more calculation methods can be adopted to solve the controlling equations of a physical phenomenon, including the finite element method (FEM) [7-9, 51, 52], finite difference method (FDM), finite volume method (FVM) [53, 54] and flux-corrected transport (FCT) method [55-58]. Researchers can also use a self-coded platform [54] to simulate streamer dynamics. Besides, the development of commercial software, such as COMSOL Multiphysics [7-9], makes it much easier for researchers without deep coding knowledge to simulate streamer dynamics. Therefore, simulation has become an increasingly popular method to investigate streamer characteristics.

1.2 Research Objectives

The aim of this Ph.D. thesis is to study streamer dynamics in both initiation and propagation processes using FEM based simulations. To achieve this aim, the following research objectives define and guide this research project:

(1) Modelling of 2nd mode positive streamers with focus on the stable propagation velocity

The relatively stable velocity (2 km/s) over a wide range of applied voltage is one of the key characteristics of 2nd mode positive streamers. However, recent experiments [59] indicate that a classic explanation based on streamer branching

and shielding effects may not be or at least may not be the only mechanism. Besides, the previously published charge-drift model [60, 61] showed unreasonable streamer velocity results when compared with experimental results. Therefore, better explanation and model improvement are needed to simulate 2nd mode positive streamers with the aim of correctly reflecting the propagation velocity.

(2) Modelling of the electrostrictive-force-induced cavity formation in dielectric liquids

Apart from traditional "bubble theory" and direct ionization, the cavity formation process during the streamer initiation process has gradually gained significant interest among researchers. A cavity is generally formed under a fast-rising voltage waveform due to elelctrostrictive force and could facilitate streamer initiation. However, few simulation studies have been conducted in cyclohexane. Therefore, it is of interest to investigate the possibility of electrostrictive-force-induced cavity formation during streamer initiation in cyclohexane under different conditions. Besides, the differences in cavity formation among different dielectric liquids are also worth investigating.

(3) Modelling of the streamer initiation process in cyclohexane

The streamer initiation process is the starting of a propagating streamer. The mechanism involved in streamer initiation may not be the same as in streamer propagation. However, most previous streamer simulations did not pay much attention to the streamer initiation stage. Therefore, it is worth investigating electronic and liquid dynamics during streamer initiation in cyclohexane under different conditions. The influence of the voltage rise rate on streamer initiation is also an area of interest worth studying.

(4) Modelling of the low-density channel formation during streamer propagation

It is generally agreed that a 2nd mode positive streamer consists of a low-density channel inside the streamer channel. However, due to the complex physics involved and calculation difficulties, most previous simulations based on the charge-drift model did not consider the low-density area formation process. Therefore, work needs to be conducted on studying the effects of the low-density channel formation on streamer dynamics.

1.3 Major Contributions

The major contributions of this thesis are the following.

(1) The reason for the stable velocity of a 2nd mode positive streamer has been well explained by the constrain of electron saturation velocity (ESV), which is an important modification of the current streamer model and offers a possible explanation for recent experimental findings on streamer velocity. It has been found that decreasing ESV greatly decreases the instant streamer velocity. ESV of 7.5 km/s is optimized according to experimental observation of streamer velocity at 100 kV. The streamer model with ESV of 7.5 km/s is further applied to other different voltage levels. Streamer propagation velocity in simulation increases from 1.59 km/s at 80 kV to 1.91 km/s at 100 kV, which all match closely to the experimtal observations under the same conditions in experiments [1].

(2) Electrostrictive-force-induced cavity formation is simulated in cyclohexane. Decreasing the voltage rise rate decreases the negative pressure inside cyclohexane. The boundary of the voltage rise rate to form a cavity inside cyclohexane is found to be 30 kV/ns under the needle-plane geometry used in this thesis. Below 30 kV/ns, a cavity is hard to form in cyclohexane due to electrostrictive force. Besides, a cavity is more difficult to form inside cyclohexane and rapeseed oil than in deionized water due to the smaller relative permittivity of cyclohexane and rapeseed oil.

(3) The dynamics of streamer initiation is simulated with consideration of both electrostrictive force and Coulomb force. Liquid is pushed outwards away from the needle tip by the combined electrostrictive force and Coulomb force at several m/s. The total pressure in cyclohexane does not reach the threshold for cavity formation over a wide voltage magnitude from 0.075 kV/ns to 70 kV/ns, illustrating that a cavity may not form during the positive streamer initiation stage based on the present model. The effects of voltage rise rates on streamer initiation, which is induced by Joule heating, have been studied. It has been found that decreasing the voltage rise rate increases streamer initiation time but decreases streamer initiation

voltage. The corresponding streamer initiation length also decreases accordingly. The simulation results are in similar trend with experimental observations [62].

1.4 Thesis Outline

This thesis consists of seven main chapters. A brief introduction of each chapter is presented below.

Chapter 1 Introduction

This chapter introduces this Ph.D. thesis, including the background and motivation for the research, the aim and focus, the major contributions and an outline of this thesis.

Chapter 2 Literature Review

This chapter presents a detailed review of published literature on streamer simulations based on both discrete and continuous models. An overview of streamer dynamics in dielectric liquids is initially summarised. Then, the history, simulation methodology and key findings of the discrete model are presented. Next, the history, controlling equations, parameters of dielectric liquids and key findings of the continuous model are presented. Finally, the research gaps are identified.

Chapter 3 Modelling of 2nd Mode Positive Streamers in Cyclohexane by Considering Electron Saturation Velocity

This chapter presents a detailed explanation on the stable velocity of 2nd positive streamers in cyclohexane. The factors affecting streamer velocity are initially discussed, with simulation methodology then described. Next, time-dependent streamer dynamics are described in detail with consideration of electron saturation velocity (ESV). The effects of ESV on streamer properties are then discussed to help select a reasonable ESV value. The streamer propagation velocity in the present simulation is finally compared with experiments under a wide range of voltage magnitudes.

Chapter 4 Modelling of the Electrostrictive-force-induced Cavity Formation in Dielectric Liquids

This chapter presents the simulation of the electrostrictive-force-induced cavity formation process in three dielectric liquids: cyclohexane, rapeseed oil and deionized

water. The mechanism of electrostrictive-force-induced cavity formation are initially described, followed by the simulation methodology. Then, a description of the dynamics of cavity formation in cyclohexane is presented. Next, the effects of voltage rise rates on cavity formation in cyclohexane are investigated. Finally, the dynamics of cavity formation due to electrostrictive force in the three dielectric liquids are compared.

Chapter 5 Modelling of the Streamer Initiation Process in Cyclohexane

This chapter presents the simulation of the streamer initiation process in cyclohexane. The mechanism of streamer initiation is firstly discussed, followed by the simulation methodology. Then, the electronic and liquid dynamics during the streamer initiation process are presented. Next, the possibility of cavity formation during streamer initiation with consideration of both electrostrictive force and Coulomb force is estimated. Finally, the effects of voltage rise rates on streamer initiation length, initiation voltage and initiation time are studied.

Chapter 6 Modelling of the Low-density Channel Formation During Streamer Propagation

This chapter presents the simulation of the streamer propagation process with consideration of the low-density channel formation inside streamer channels. The modifications of controlling equations are initially presented, followed by streamer dynamics with consideration of the low-density channel formation. Finally, a detailed discussion on the limitation of simulation results is presented.

Chapter 7 Conclusions and Future Research

This chapter presents a summary of the main conclusions of this research, before offering suggestions for future research related to simulating streamers.

2 Literature Review

2.1 Introduction

Streamers have been a popular researcher topic during past decades. Apart from experiments, there are also many different groups conducting streamer simulations, which can be catalogued as discrete model and continuous model. The structure of this chapter is as follows. Firstly, an overview of the streamer phenomena in dielectric liquids is introduced. Then, streamer simulation based on the discrete model is introduced, followed by streamer simulation based on the continuous model. Finally, a summary of this chapter is given.

2.2 Overview of Streamer Phenomena in Dielectric Liquids

2.2.1 Streamer Initiation and Propagation

The process of a streamer is generally divided by the initiation and propagation stages. In experiments, the streamer initiation stage is generally defined by the occurrence of the first visible streamer channel, which is closely related to sensitivity of the optical devices. The effects of oil types [19], electric field uniformity [21] and needle tip radii [42] on the streamer inception field and voltage have all been studied. After the streamer channel is first observed, the streamer moves to the propagation stage. During the streamer propagation stage, the average streamer propagation velocity and corresponding streamer mode, streamer morphology, and streamer channel characteristics such as the low-density channel formation are all of significant importance.

2.2.2 Streamer Mode

The streamer mode is one of the most important parameters to describe streamer characteristics and can be catalogued into 1^{st}, 2^{nd}, 3^{rd} and 4^{th} mode according to its average propagation velocity [63]. The voltage or electric field required for the four modes has an increasing trend. Typical values of streamer velocities of 1^{st} to 4^{th} mode are on the order of 0.1, 1, 10 and 100 km/s [5, 63-67]. A 1^{st} mode streamer generally has a low risk of leading to breakdown. A 2^{nd} mode streamer is more commonly observed [4, 17] and is responsible for breakdown in many situations [1, 18]. The voltage when breakdown happens inside dielectric liquid is called breakdown voltage

V_b. The transition from 2nd to 3rd mode is also important since the 3rd mode can quickly lead to breakdown before it can be extinguished. The voltage when the streamer transfers into the 3rd mode is called the acceleration voltage V_a. A 4th mode streamer only occurs under an extremely high electric field. The addition of low ionization potential molecules is found to decrease V_b and increase V_a.

The relationship between average streamer propagation velocity, applied voltage in cyclohexane and the effects of additives of pyrene that has smaller ionization potential in cyclohexane is shown in Figure 2-1 [1]. Line 0 M represents the results of pure cyclohexane, while line 1 M represents the results of the mixture of cyclohexane and pyrene. 1 M means the concentration of pyrene reaches saturation in cyclohexane. From below V_b of ~105 kV to V_a of ~123 kV, average streamer propagation of pure cyclohexane keeps relatively stable from 1.5 km/s to 2 km/s, which is in 2nd mode. After V_a, streamer velocity jumps quickly to over 10 km/s which is in 3rd mode. Adding pyrene into cyclohexane decreases V_b to ~75 kV and increases V_a to ~170 kV.

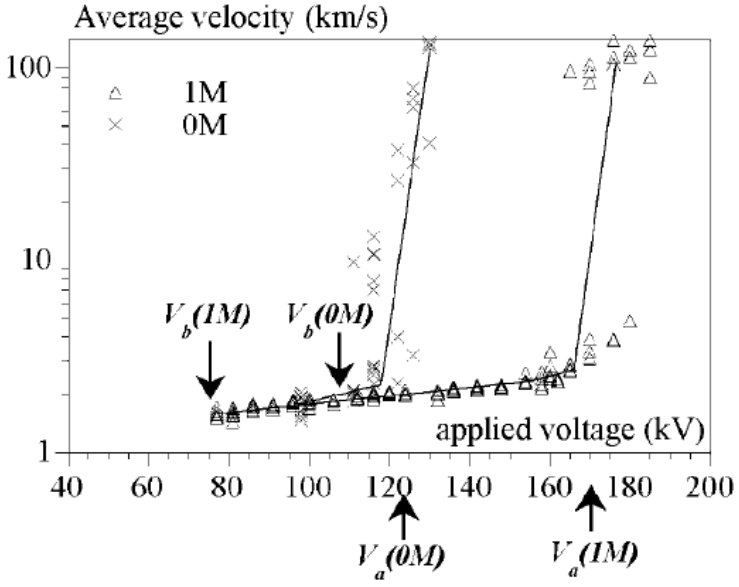

Figure 2-1 Effects of pyrene concentration on streamer average velocity in cyclohexane under different voltage level in a needle-plane geometry at gap distance of 5 cm. 0M means that there is no pyrene while 1M means that pyrene reaches saturation in cyclohexane [1].

2.2.3 Streamer Morphology

The streamer branching phenomenon plays a very important role in streamer dynamics since it can change the direction of streamer branches and may be the reason for the stable velocity of 2nd mode streamers when the applied voltage is larger than V_b due to the shielding effect of multiple streamer channels [9]. Figure 2-2 [4, 63, 68] shows

different typical images of the positive streamer branching phenomenon that changes with the applied voltage and streamer mode. In Figure 2-2 (a), a 1st mode streamer propagates for a very small distance with very weak light emission. In comparison in Figure 2-2 (b), a 2nd mode streamer becomes more luminous with filamentary streamer channels. From Figure 2-2 (c) to (d), it is found that more channels with strong light emissions are generated when streamer mode changes from 2nd to 3rd+2nd mode. When a streamer transfers to 4th mode in Figure 2-2 (e), the streamer channel number reduces considerably but the velocity increases significantly.

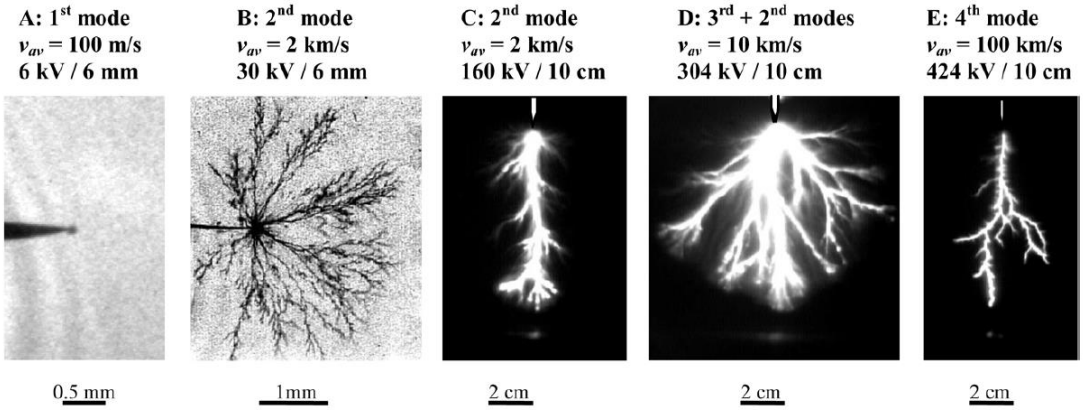

Figure 2-2 Typical images of positive streamers in mineral oil: (a) 1st mode streamer [4], (b) 2nd mode streamer [68], (c) 2nd mode streamer [63], (d) 3rd+2nd mode streamer [63], (e) 4th mode streamer [63].

Apart from applied voltage magnitude, the voltage polarity will also affect streamer branching phenomenon. Typical images of positive and negative streamers in different dielectric liquids are shown in Figure 2-3 (a) [15] and (b) [16], respectively. In Figure 2-3 (a), from the left figure to the right figure, the applied voltages are 116 kV, 131 kV, 130 kV, 125 kV and 144 kV. Figure 2-3 (b), from the left figure to the right figure, the applied voltages are -190 kV, -328 kV, -308 kV, -390 kV and -319 kV. Comparing Figure 2-3 (a) and (b) in the same dielectric liquid, it can be concluded that streamer branching is more filamentary in a positive streamer while it is bushier in a negative streamer.

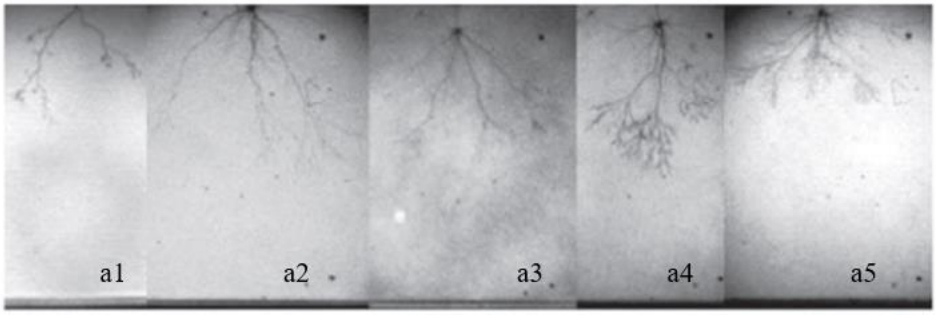

(a)

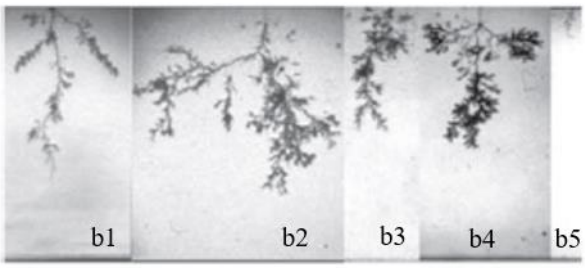

(b)

Figure 2-3 Typical images of positive and negative streamers in different dielectric liquids. (a) positive streamer in a1: cyclohexane, a2:Nytro 10XN, a3:Diala S4 ZX1, a4:Marcol 52 and a5:Primol 352 [15] and (b) negative streamer in b1: cyclohexane, b2:Nytro 10XN, b3:Diala S4 ZX1, b4:Marcol 52 and b5:Primol 352 [16].

2.2.4 Gaseous Nature of a Positive Streamer

It is agreed that a positive streamer consists of a low-density phase inside the streamer channel [13, 34]. Therefore, the characteristics inside a streamer channel should not be considered as a pure liquid phase. The effects of hydrostatic pressure on streamer stopping length are shown in Figure 2-4, which is replotted according to [13]. It is found that increasing hydrostatic pressure from 0.1 MPa to 6.5 MPa will decrease streamer stopping length from ~1.5 mm to ~0.35 mm. However, as Figure 2-5 [13] shows, ambient pressure has little effect on streamer propagation velocity, indicating that the factors affecting streamer velocity must exist in the liquid phase of the streamer channel.

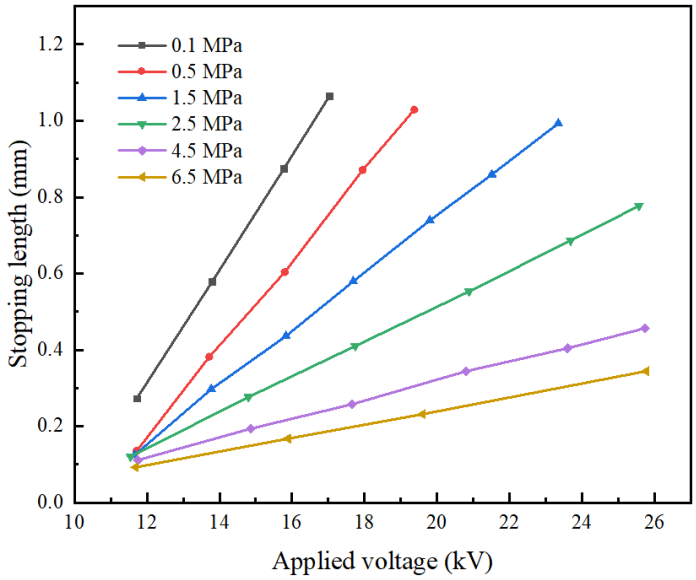

Figure 2-4 Effects of hydrostatic pressure on streamer stopping length, replotted according to [13].

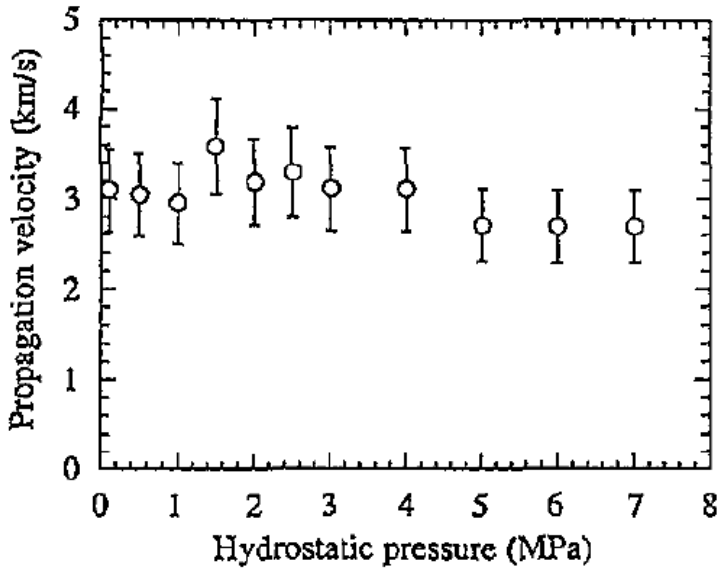

Figure 2-5 Effects of hydrostatic pressure on streamer propagation velocity [13].

2.3 Streamer Modelling Based on the Discrete Model

2.3.1 History

The study of random patterns, such as the fracture of glass and soil, began to become popular since the 1930s [69]. Since then, a few discrete models have been proposed based on the fractal ideas explored by Mandelbrot [70]. Typical models, such as Eden's model [71], "self-avoiding walks" model [72], "percolating clusters" model [73, 74], "random animal" models [72] and "diffusion-limited aggregation" (DLA) model [75]

were proposed. Among these models, Eden's model is the simplest to simulate the growth of a cluster of particles.

In the 1980s, it was proposed that for discharge in solids, repetitive discharges in the existing discharge channel will happen and new channels form in a stepwise manner [76, 77]. Based on this important assumption, the first attempt to simulate a discharge pattern in all kinds of insulation, including gases, liquids and solids, was undertaken in 1982 [69] when Eden's model was modified by a tip priority factor R (the ratio of the straight-tip growth rate to the side-branching rate). Although this model can simulate filamentary-like and bushy-like channels by adjusting different R values, it cannot describe the discharge nature due to the lack of a relationship with the underlying physics of the discharge process. Then, in 1984 [50], the "NPW" model was established by L. Niemeyer, L. Pietronero and H.J. Wiesmann, which assumed that the processes responsible for discharge initiation and propagation, such as charge generation and recombination, were mainly related to the local electric field. The probability of pattern growth position is closely and positively dependent on the local electric field magnitude. This model is of great importance and has been further modified by others.

2.3.2 Simulation Methodology

This section presents a detailed description of the simulation methodology for the discrete model. The typical schematic diagram of the simulation methodology for the discrete model is shown in Figure 2-6. In brief, the first step to simulate the streamer process using the discrete model is to build the simulation base in a set of lattice points or coordinate system, which is followed by building geometry and setting boundary conditions. Here, the simulation base describes whether the simulation is based on the lattice points or coordination system. As one of the most important variables in a discrete model, the local electric field is then calculated. Next, the time instant in the simulation is calculated. If a streamer arises when meeting a series of different criteria, the streamer arising position and direction are then calculated. After that, streamer channel characteristics are calculated based on different assumptions and a new streamer pattern is generated. The values of variables are then updated and the simulation moves into another simulation circle. Streamer dynamics will be updated step by step until the streamer arising condition is not met. Then, the simulation will

stop. A detailed description of the simulation methodology at different simulation steps is shown as follows.

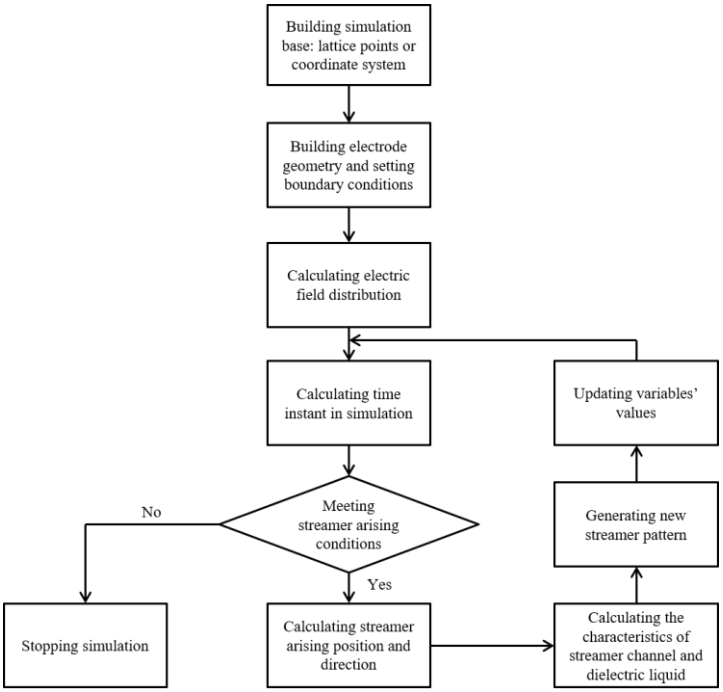

Figure 2-6 A flow chart of the simulation methodology of the discrete model.

2.3.2.1 Simulation base

The first kind of simulation base is called the "lattice point model" which was used in the "NPW" model shown in Figure 2-7 (a) [50], where the black and white points are the so-called lattice points. The black bonds connecting two black points represent streamer channels. Black points connecting to three white points are the streamer tips. All the white points mean the potential positions for the next streamer tip. For all lattice point based discrete models, a collection of lattice points can be set in either 2D or 3D dimensions [78, 79]. Most lattice-point-based models use non-dimensional parameters that have no unit of physical meaning and have not been used in recent years.

If the density of the lattice point is infinitely large, the lattice point model is transferred into a coordinate system model. With the development of computer performance, the coordinate system model has gradually replaced the application of the lattice point model. A streamer channel in a coordinate system model is represented either by lines between two points [80, 81] or a collection of points without bonds connecting each other [82]. A typical streamer pattern in the 3D dimension based on the coordinate system model is shown in Figure 2-7 (b) [82] where the collection of blue dots represents the streamer channel and Figure 2-7 (c) [81] where the black lines are

streamer channels. Compared with the streamer channels shown in a lattice point model, the simulated streamer pattern in a coordinate system model has a higher resolution.

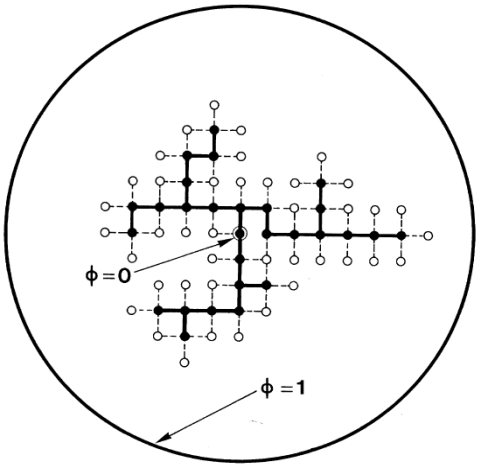

(a)

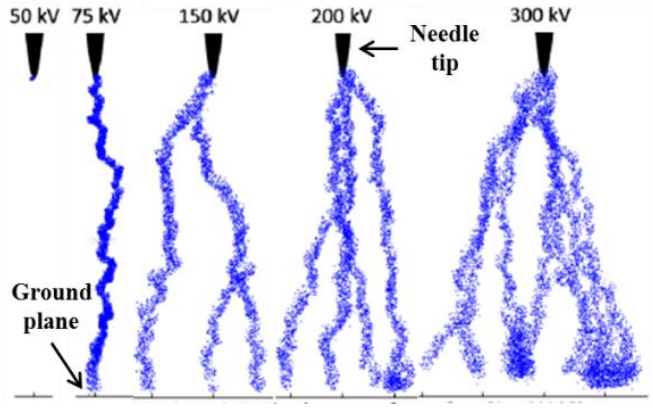

(b)

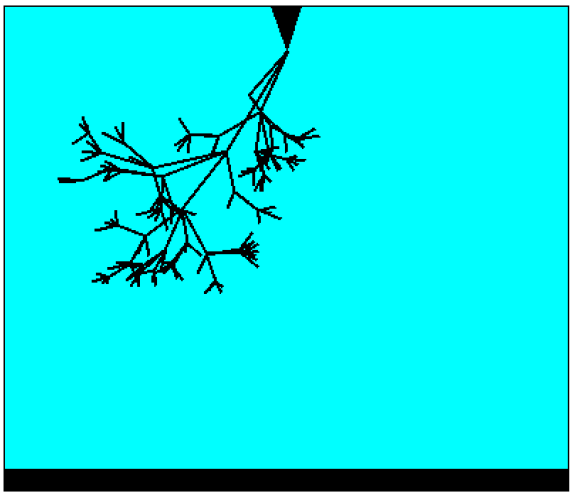

(c)

Figure 2-7 Discharge pattern distribution simulated (a) by lattice point model in 2D dimension [50] and (b) by coordinate system model in 3D dimension [82], and (c) by coordinate system model in 3D dimension [81].

2.3.2.2 Streamer arising condition and position

In general, a new streamer channel will form at the position where the streamer arising condition is met. Besides, it should be noted that the conditions mentioned in this section are used in simulations separately.

The first criteria is called the definite threshold condition and was proposed in [81]. The electric field magnitudes calculated from experimental results on different streamer modes [64, 83] are used as streamer initiation and propagation criteria in simulations. The inception electric field for 2nd, 3rd and 4th mode positive streamers are set as 3.85 MV/cm, 13 MV/cm and >20 MV/cm, respectively [64, 83].

The second kind of criteria is related to Townsend-Meek criterion. Due to the electronic nature of streamers, the charge generation mechanism is also taken into consideration as streamer initiation and propagation conditions, although what kinds of mechanisms dominate the streamer process is still unclear. One of the possible mechanisms is impact ionization (also known as electron avalanche) [84, 85]. In order to define whether the electric field is strong enough for electron avalanche repetition, the Townsend-Meek criterion proposed in [86] is usually used. The Townsend-Meek criterion expressed in Equation 2-1 was adopted in [10, 82, 87, 88]. The important parameters related to the Townsend-Meek criterion are the seed electron density n_e, first Townsend ionization coefficient α_T, the size of the corona region d_a and Meek constant Q_c. Due to the nature of an electron avalanche, impact ionization will not happen without seed electrons. The seed electrons can be created by processes such as photoionization, thermal excitation, field assisted dissociation of negative ions and background radiation [82]. It is easy to understand that more seed electrons will lead to higher impact ionization if the Meek criterion is met. Note that α_T is electric field dependent.

$$\int_0^{d_a} \alpha_T dx = Q_c \qquad \text{Equation 2-1}$$

Where α_T is the electric field dependent first Townsend impact ionization coefficient which means the number of ionizing collisions per electron per unit distance, d_a is the size of the corona region (high field region in the vicinity of needle tip or streamer tip) and Q_c is the Meek constant [10, 84, 85, 88-91].

One typical streamer modelling method using the Town-Meek criterion is shown in Figure 2-8 [10, 82, 87]. The probability of the existence of electrons is simplified by assuming randomly distributed negative charges in the dielectric liquid before

simulation. These negative charges will release electrons and become seed electrons under a high enough electric field. Besides, for simplification of calculations, the movement and division of the streamer head is determined by the following approach. The needle tip or previous steamer channel tip is represented by a hyperbolic solid line ν_0 with a "join circle" plotted as a dash line. In the inserted figure of Figure 2-8, the black dots represent the seed electrons for impact ionization. When electric field is applied, conditions according to Equation 2-1 are calculated among these seed electrons. Electron avalanches with a critical size are the potential positions for the next streamer channel generation. Electron avalanches that happen inside the join circle behind the streamer tip are removed while that inside the join circle in front of the streamer tip are regarded as an extension of previous streamer channel tip ν_0. All the electron avalanches with a critical size happening outside the join circle are regarded as new streamer channels, which means streamer branching happens there.

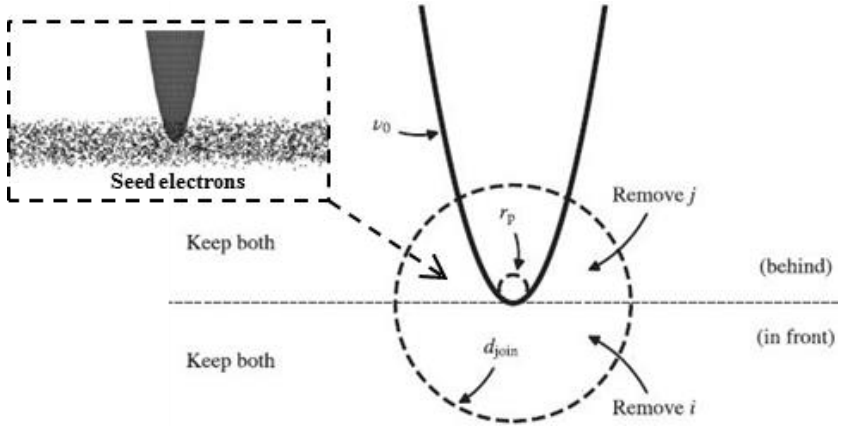

Figure 2-8 Schematic diagram of electron avalanche position dependent streamer channel generation [82, 87].

2.3.2.3 Characteristics of a streamer channel and dielectric liquid

The characteristics of a streamer channel and liquids are generally regarded as resistance and capacitance, respectively, which is also referred to as a "RC model", as shown in Figure 2-9 [10, 81].

In the left figure in Figure 2-9 (a), HT represents the high voltage needle tip, while position 1 represents the ground plane. Position 2 is the start of the streamer tip. Line 2-3, line 3-4 and line 3-5 are streamer channels with no channel radius. Point 4 and 5 are the streamer tips. On the right figure in Figure 2-9 (a), the green numbers 2, 3 and 5 represent resistances that are the streamer channels, while the green numbers 4 and 6 represent the capacitances that are the dielectric liquid between streamer tip and ground plane. The resistance is calculated by Equation 2-2 by assuming streamer channel is

cylinder where l is streamer channel length, σ is streamer channel conductivity and r_0 is streamer channel radius. The capacitance is calculated by Equation 2-3 to Equation 2-6 where L is the axis length from streamer tip to ground plane. This calculation is based on a hyperboloidal approximation and taking into account the solid angle constituted by the streamer head [81].

$$R = l/\sigma\pi r_0^2 \quad \text{Equation 2-2}$$

$$C = 2\pi\varepsilon_0\varepsilon_r\alpha_c\left(1+\frac{m_1}{1-m_2}\right) \quad \text{Equation 2-3}$$

$$\alpha_c = 1-\left(1+\left(\frac{\phi/2d}{1-m_2}\right)^2\right)^{-1/2} \quad \text{Equation 2-4}$$

$$m_1 = \frac{r_0}{d} \quad \text{Equation 2-5}$$

$$m_2 = \frac{L}{d} \quad \text{Equation 2-6}$$

In comparison, the streamer channel is represented by a collection of points, as shown in Figure 2-9 (b). The streamer channel between each streamer tip and needle tip is regarded as a separate resistance, as shown in the right figure in Figure 2-9 (b). The dielectric liquid between streamer tip and ground plane is also regarded as a capacitor. Based on the RC model described above, the voltage potential at the streamer tip can be calculated. Then, the electric field at the streamer tip can be calculated by the Mason equation and its modified equation [10, 81].

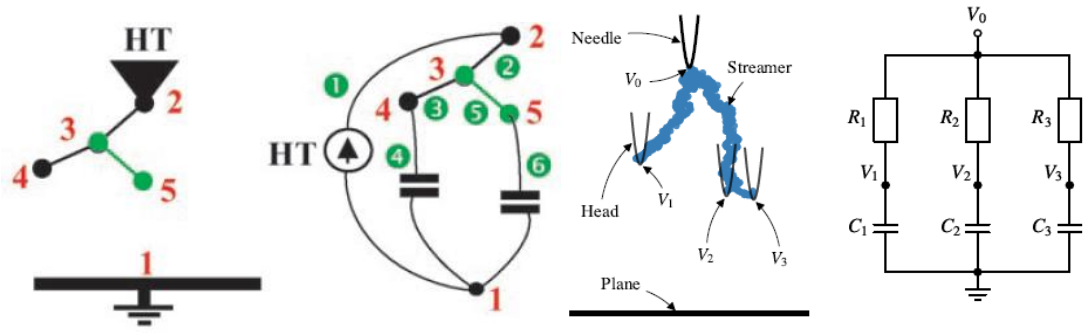

(a) (b)

Figure 2-9 Schematic diagram of RC model in dielectric liquids: (a) streamer channel is represented by a line with no radius [81] and (b) streamer channel is represented by a collection of points [10].

2.3.3 Key Findings

2.3.3.1 Streamer velocity

This section mainly discusses the effects of different parameters on streamer velocity. The variables include meek constant Q_c, time constant and channel conductivity in the RC model, and streamer channel breakdown electric field.

(1) Meek constant Q_c

As a parameter to decide whether an effective electron avalanche will happen, the value of Meek constant Q_c is important to know. Meek constant Q_c is typically 18 in gases [92, 93]. In dielectric liquids, this value is expected to be higher due to the higher dielectric strength of liquids than gases. Effects of Q_c ranging from 5 to 80 on streamer velocity were studied in [37, 87, 94]. Since higher Q_c makes an electron avalanche with a critical size more difficult to happen, more time is required for an electron avalanche to generate enough charges for further ionization in front of the precious streamer tip. Therefore, as shown in Figure 2-10 [87], it is reasonable to find that increasing Q_c leads to lower streamer velocity.

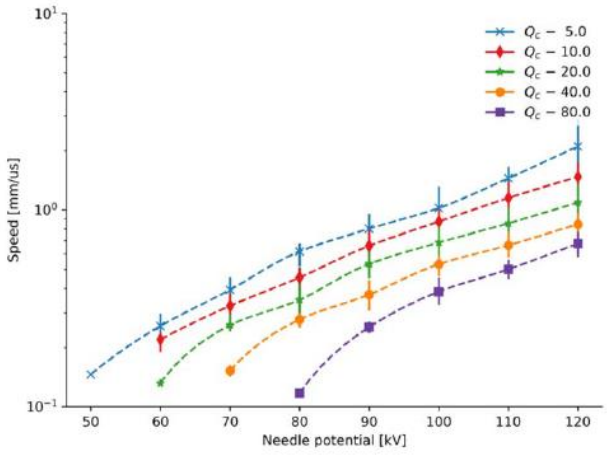

Figure 2-10 The effects of Meek constant Q_c on the average streamer propagation velocity for the middle 50% of the gap [87].

(2) Time constant and channel conductivity in the RC model

Based on the assumption of equivalent RC model of streamer, time constant τ_0 represents how fast the streamer tip can be recharged to the same voltage level as the needle tip. Therefore, smaller time constant τ_0 also represents higher channel conductivity [87]. Figure 2-11 [10] shows that smaller τ_0 leads to higher streamer velocity because the voltage drop inside the streamer channel is lower. The effects of streamer channel conductivity on streamer velocity were simulated in [91] and [95].

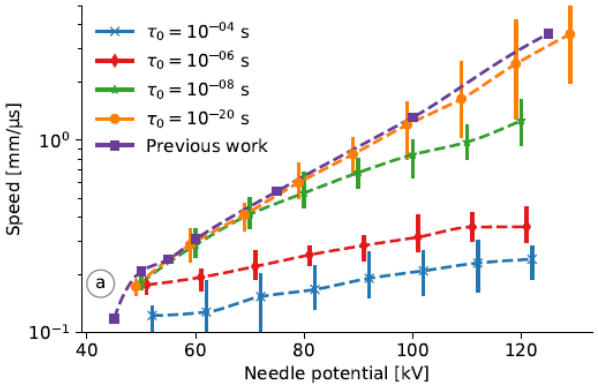

Figure 2-11 Propagation speed calculated for the mid 1.5 mm of 3 mm gap distance in needle-plane geometry under different τ_0 [10]. Data from previous work is derived from Figure 17 in [87].

(3) Streamer channel breakdown electric field

When the electric field peak, generally regarded as the streamer tip in simulation, leaves the needle tip, the voltage potential at the streamer tip will be smaller than that at the needle tip due to the voltage drop inside the streamer channel. In experiments [65], it has been found that the streamer channel shows re-illumination phenomena during streamer propagation. Therefore, it is assumed that when the electric field inside the streamer channel is larger than a threshold, breakdown occurs along the streamer channel, and hence the voltage drop along the streamer channel reduces [10]. The effects of the streamer channel breakdown electric field E_{bd} on streamer velocity at different voltage magnitudes are shown in Figure 2-12 [10]. Obviously, a smaller breakdown field results in higher streamer velocity. $E_{bd} = 0$ kV/mm means the streamer channel is totally conductive, which is an extreme case. Based on experimental studies, the electric field inside the streamer gaseous channel is 2~5 kV/mm for different dielectric liquids [4, 13].

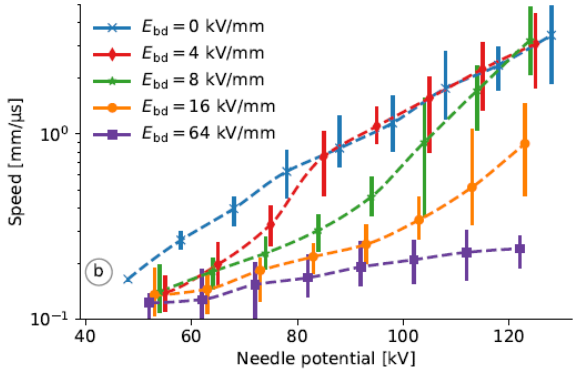

Figure 2-12 Propagation speed calculated for the mid 1.5 mm of 3 mm gap distance in needle-plane geometry under different streamer channel breakdown electric field E_{bd} with time constant $\tau_0 = 10^{-4}$ s [10].

2.3.3.2 Streamer mode transition

It is argued in [96, 97] that photoionization may be the dominant mechanism for fast streamers since a lowered ionization potential of molecules in a strong electric field may lead to photoionization. A detailed theoretical analysis on the possibility of photoionization is undertaken by discussing the molecular energy state and radiation [97]. However, due to simulation difficulty, the effects of photoionization on streamer velocity are simulated by simply adding a constant velocity to the streamer head if the electric field at the streamer tip is over an extremely high threshold, typically 3.04~3.1 GV/m [91, 97]. Figure 2-13 shows a schematic diagram of the electric field magnitude, voltage potential and position of a streamer tip [97]. Position 10 mm and 0 mm represent the needle tip and ground, respectively. The three white dash lines are three equipotential lines where the electric field magnitude equals 1.4 GV/m, 1.9 GV/m and 3.1 GV/m, respectively. The dash lines represent two conditions of voltage drop. When the voltage drop inside the streamer channel is assumed to be 0 kV/mm, the voltage potential at streamer tip keeps 70 kV during streamer propagation from needle tip (10 mm) to the ground (0 mm). When the voltage drop inside streamer channel is assumed to be 4 kV/mm, the voltage potential at streamer tip is 90 kV at the needle tip (10 mm) and reduces to 50 kV at the ground (0 mm). The electric field at streamer tip at different positions is indicated by the electric field scale bar. Taking the grey dash line, which starts from $V_0 = 70$ kV at a position of 10 mm with a voltage drop inside the streamer channel $E_s = 0$ kV/mm, for example. Streamer will initially be a 2nd mode streamer since the electric field at the streamer tip is smaller than 3.1 GV/m. When the grey dash line is below the white dotted line (3.1 GV/m), which means the local electric field at the streamer tip is over the threshold, the streamer is converted into a 3rd mode streamer. Similarly, for the grey line with $E_s = 4$ kV/mm, the streamer starts from 3rd mode and is converted into 2nd mode when propagating around 3 mm, before finally becoming a 3rd mode streamer again when the streamer tip is close to the ground.

In comparison with Figure 2-13, Figure 2-14 shows the effects of voltage potential at the needle tip and streamer channel breakdown electric field on streamer velocity [97]. For the red solid line with applied voltage V_0 of 80 kV and streamer channel breakdown electric field E_{bd} of 4 kV/mm, the streamer remains in 2nd mode until it is very close to the ground where it changes into 3rd mode. When V_0 increases to 95 kV, as is shown by the orange point-dash line, the streamer starts from 3rd mode. When the streamer

position reaches ~8 mm, the streamer begins to switch to 2nd mode until it is very close to the needle tip where the streamer switches back to 3rd mode. Further increasing V_0 in the light blue line leads to longer existence time for the start of the 3rd mode streamer. Besides, the streamer propagation time is decreasing. In comparison with the red line, when E_{bd} decreases to 1 kV/mm (shown in the sky-blue dot-dash line), since the voltage potential at the needle tip is easier to be transferred to the streamer tip, the streamer starts from 2nd mode and switches to a 3rd mode streamer earlier.

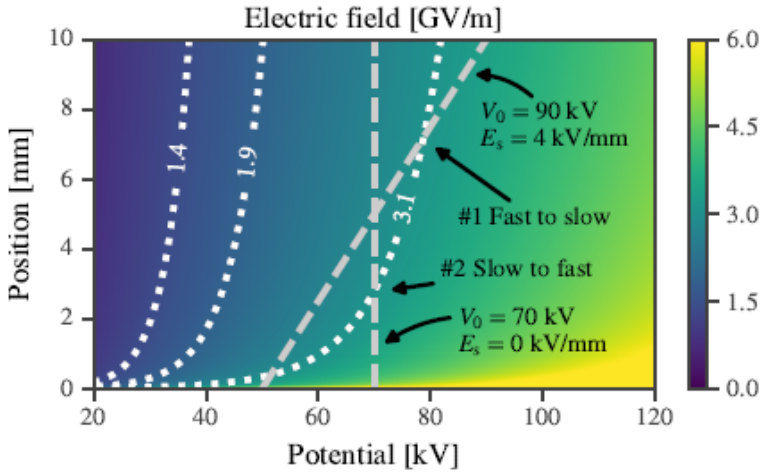

Figure 2-13 Schematic diagram of the electric field magnitude, voltage potential and position of a streamer tip [97]. Position 10 mm and 0 mm represent the needle tip and ground, respectively. The electric field represents the electric field at the streamer tip of an electric hyperboloid with a tip curvature of 6.0 μm for a given position and potential. Doted white lines show the thresholds for ionization potential (IP) reduction by 2 eV (1.4 GV/m) and 3 eV (3.1 GV/m), as well as the exponential parameter E_α =1.9 GV/m of impact ionization. Dashed grey lines represent streamers with a different voltage drop inside the streamer channel.

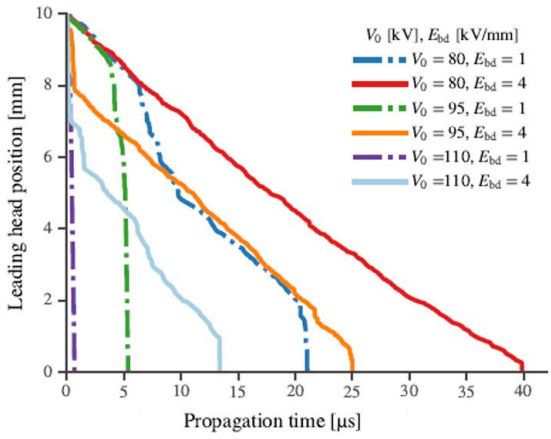

Figure 2-14 Effects of voltage potential at the needle tip and streamer channel breakdown electric field on streamer velocity [97].

2.3.3.3 Streamer stopping length

Streamer stopping length is an important factor to know since not all streamers lead to breakdown in dielectric liquids. The effects of streamer channel conductivity on streamer stopping length are shown in Figure 2-15 [98]. Since higher streamer channel conductivity means lower voltage drop inside the streamer, with the increase of streamer channel conductivity, the streamer stopping length also shows an increasing trend.

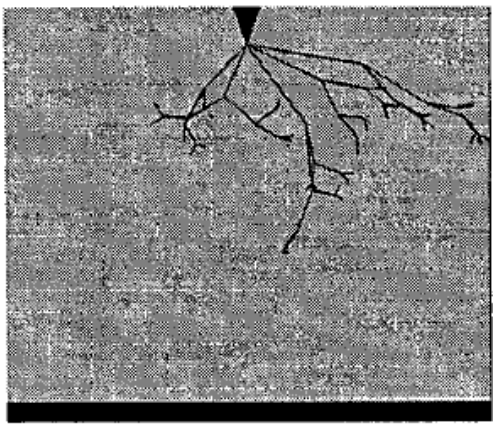

(a)

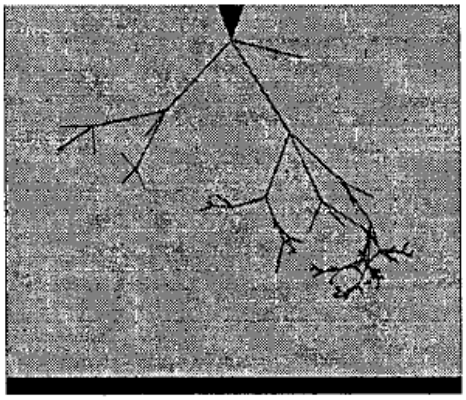

(b)

Figure 2-15 Effects of streamer channel conductivity σ on streamer stopping length: (a) $\sigma = 0.05\ (\Omega m)^{-1}$ and (b) $\sigma = 0.5\ (\Omega m)^{-1}$ [98].

2.3.3.4 Streamer branching phenomenon

In the very early study of streamer simulation, only non-dimensional parameters without units were used in simulations to qualitatively describe streamer dynamics. The possibility of a new streamer channel arising at a certain position is determined by $|\vec{E}|^{\eta}$ where $|\vec{E}|$ is local electric field magnitude and η is a parameter. When η is 1, the growth probability of a new streamer channel is proportional to the local electric field

magnitude. The effects of η on streamer branching extent are shown in Figure 2-16 [99]. Increasing η means that the positions of the higher electric field have a greater possibility of forming a new streamer channel. The simulation geometry in [99] is similar to Figure 2-7 (a), where the central point is zero voltage potential, while the outside circle is high voltage potential. When the streamer tip is closer to the outside circle, the local electric field is higher. Therefore, increasing η from 1 to 2 will reduce the extent of streamer branching.

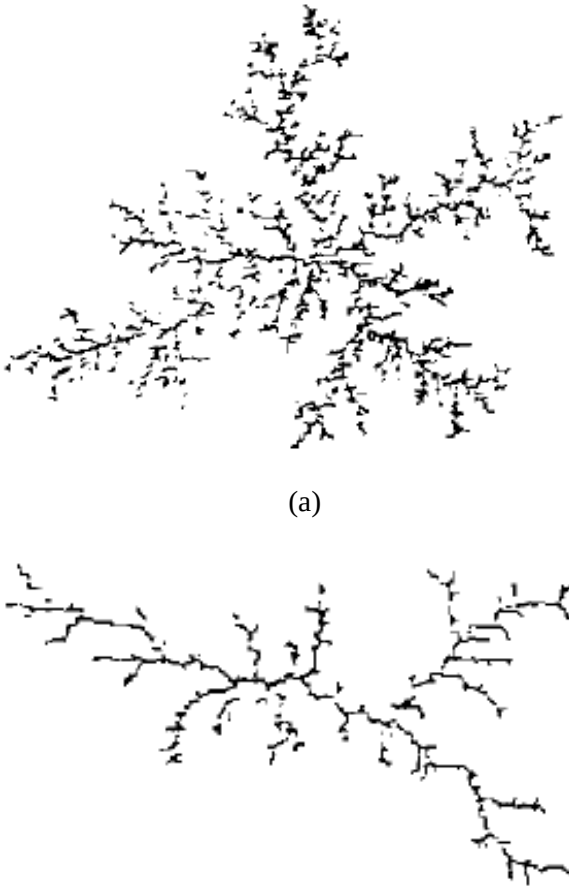

(a)

(b)

Figure 2-16 Effects of parameter η on streamer branching extent [99].

In later research, more dimensional parameters with units of real physical meanings were adopted in simulations. Based on the streamer arising condition mentioned in Figure 2-8, the voltage magnitude effects on streamer branching phenomenon are shown in Figure 2-17 [87]. It was stated in [87] that with an increase in applied voltage magnitude, streamer branching phenomenon was enhanced. However, this trend seems to be limited.

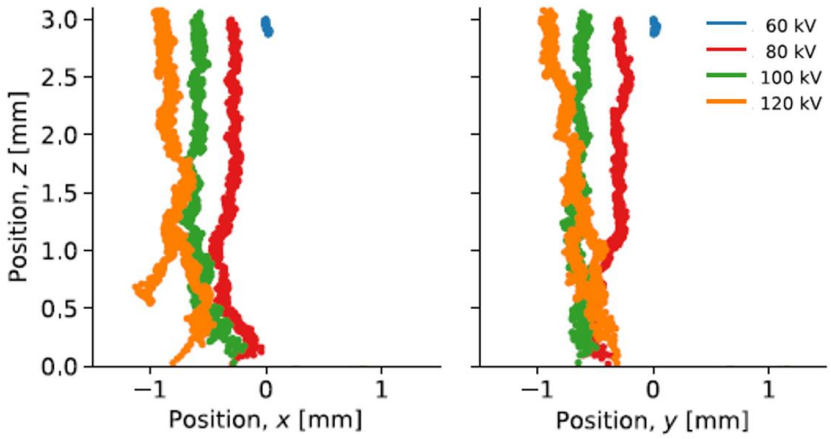

Figure 2-17 Streamer trails, xz- and yz- projection for a range of voltages from 60 kV to 120 kV. Each dot represents the position of a streamer head at some point of the propagation [87].

2.4 Streamer Modelling Based on the Continuous Model

2.4.1 History

The nature of the continuous model comes from the application of mathematical equations, namely controlling equations, to describe streamer physical phenomena. For example, in 1979, a simple 1D model was first used to simulate charge injection and ionic dissociation on the interface of an electrode [100-102]. This model was based on a combination of the simplified form of the Poisson equation and charge continuity equations, and considered charge generation and recombination in 1D with reasonable boundary conditions. Then, modification of a field-enhanced charge generation rate was made to further study the conduction of dielectric liquid [103, 104]. Based on the 1D model, in 1992, an ion-drift time-dependent model, which could be calculated in both 1D and 2D, was proposed to study electric field distribution and current density in bulk oil [105]. Since then, authors from different groups began studying the dynamics of streamers based on the ion-drift model with various modifications.

2.4.2 Simulation Methodology

The simulation methodology of the continuous model is shown in Figure 2-18. As usual, the simulation geometry is built initially. Then, the controlling equations, boundary conditions and constant variable values are input into the calculating platform. The controlling equations may include Poisson equation, charge continuity equations and Navier-stokes equations. Then, the meshing process is set up. Then, calculation of the

equation set is conducted using different methods, such as FEM and FVM. Next, the variables' values are generally initially calculated at time instant t. If the simulation meets the stopping criterion, the simulation is stopped. If not, the variables' values are updated at each calculating node and time is increased by dt. Finally, the time-dependent streamer process is simulated automatically until meeting the stopping criterion.

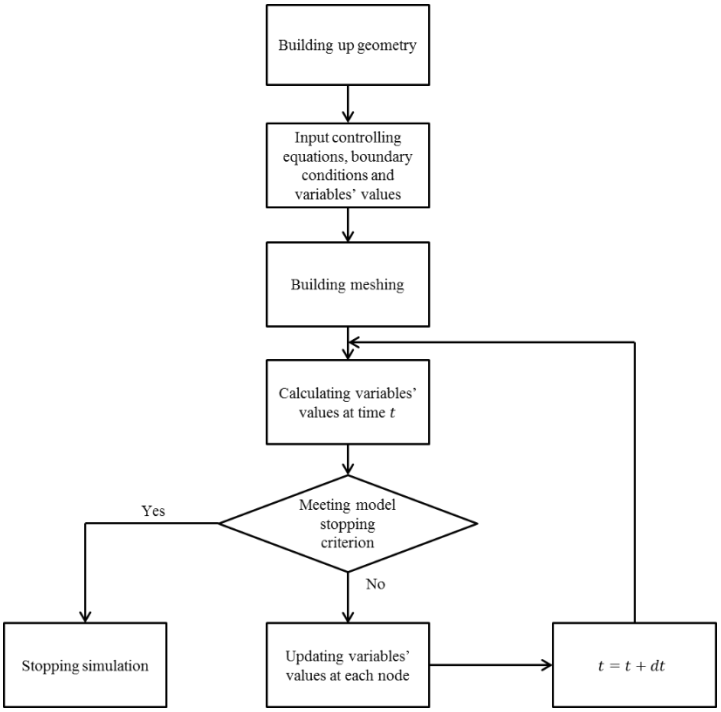

Figure 2-18 A flow chart of the simulation methodology of the continuous model.

2.4.2.1 Controlling Equations and Boundary Conditions

The controlling equations and their boundary conditions play the most important roles in describing streamer dynamics in the continuous model. Typical controlling equations in streamer simulations include:

a) Poisson equation
b) Charge continuity equation
c) Navier-Stoke equations
d) Thermal diffusion equation

(a) Poisson equation

The expression of the Poisson equation is shown in Equation 2-7 [106]. The Poisson equation describes the relationship between space charge density c and electric field distribution $\vec{E}$ ($\vec{E} = -\nabla V$). Here, the space charge density is the sum of all possible charge carriers in dielectric liquids, including the charge densities of positive ions c_+,

negative ions c_- and electrons c_e. When considering the electron injection process on a negative needle tip, only electrons and negative ions are considered [7, 49, 107] due to lack of positive ion generation in the bulk liquid. However, the types of charge groups generated by the ionization process in the bulk liquid do not reach a consensus. It is assumed that c_+, c_- and c_e can all exist in the liquid in [7-9], while only c_+ and c_e can exist due to much longer electron attachment time than the interests of simulation time in [11].

$$\nabla \cdot (-\nabla V) = c/\varepsilon_0 \varepsilon_r \qquad \text{Equation 2-7}$$

Where V is voltage potential, c is space charge density, ε_0 and ε_r are permittivity in vacuum and relative permittivity of dielectric liquids, respectively.

The boundary conditions of the Poisson equation are as follows [7-9]. For needle-plane geometry, the voltage potential on the needle electrode is set to be $V = V(t)$, while on the ground plane the voltage potential is set to be $V = 0$ V. On the boundary of the calculating domain, the condition is set to be $\vec{n} \cdot \vec{E} = 0$, which means no electric field can go outside of the calculated boundary. Here, $\vec{n}$ is the normal vector of the boundaries.

(b) Charge continuity equation

The charge continuity equation expresses how the distribution of free charges are modified by electric field drift and liquid movement [105]. Due to the conservation of charges, the charge continuity equation for space charge density can be expressed as follows:

$$\frac{\partial c}{\partial t} + \nabla \cdot \vec{J} = 0 \qquad \text{Equation 2-8}$$

Where c is space charge density, $\vec{J}$ is the current density and equals $\vec{J} = \sum_{i=\pm e}\left(z_i c_i \mu_i \vec{E} - D_i \nabla c_{\pm e} + c_i \overrightarrow{v_l}\right)$, c_i is charge density, z_i is polarity constant. z_i equals 1 when the charge is positive and equals -1 when the charge is negative. μ_i is the charge mobility for different charges, $D_{\pm e}$ is the diffusion coefficient of charges, $\overrightarrow{v_l}$ is the liquid velocity.

Charge diffusion is related to the charge movement due to charge concentration differences and can be calculated according to Einstein relation [49, 108]. Liquid velocity can be estimated according to the electro-hydro-dynamics (EHD) process [62, 109]. It should be noted that the charge movement induced by charge diffusion and liquid movement is generally much smaller than that caused by electric field drift, which is on a similar order of magnitude to streamer velocity. Therefore, $D_{\pm e}$ and $\overrightarrow{v_l}$

are always neglected in the streamer simulation process when simulating 2nd and 3rd mode streamers but are considered in the conduction process of dielectric liquid [49]. If all three kinds of charges are assumed to exist in dielectric liquids during the streamer process, Equation 2-8 can be separated as Equation 2-9 to Equation 2-11 which consider the existence of all of c_+, c_- and c_e in dielectric liquids without consideration of charge diffusion and liquid velocity. The calculation of electron velocity is shown in Equation 2-12.

$$\frac{\partial c_+}{\partial t} + \nabla \cdot c_+ \mu_+ \vec{E} = source_+ + sink_+ \quad \text{Equation 2-9}$$

$$\frac{\partial c_-}{\partial t} + \nabla \cdot (-c_- \mu_- \vec{E}) = source_- + sink_- \quad \text{Equation 2-10}$$

$$\frac{\partial c_e}{\partial t} + \nabla \cdot (-c_e \mu_e \vec{E}) = source_e + sink_e \quad \text{Equation 2-11}$$

$$v_e = \mu_e \vec{E} \quad \text{Equation 2-12}$$

Where $source_{+,-,e}$ is the charge generation rate of positive ions, negative ions and electrons, $sink_{+,-,e}$ represents the charge recombination rate of positive charges and negative charges, and electron attachment rate.

A detailed description of charge generation rates will be discussed in 2.4.3.3. In general, all kinds of charge generation mechanism are closely and positively related to the local electric field, which indicates that a higher electric field will definitely result in larger charge density and facilitate streamer initiation and propagation. However, according to the assumption in the discrete model [99], the position where the streamer channel arises may be related to both the electric field and the probability. Therefore, it is assumed in [110] that a stochastic term F should be added to the source term as $F \cdot source_{\pm e}$, where F jumps between 0 and 1 according to a probability density function based on power-law expression. The power-law expression in shown in Equation 2-13. Therefore, a higher electric field means a higher probability of charge generation. However, the probability concept is more closely related with streamer branching phenomenon, which is not the main object of most continuous model simulations. Besides, adding a stochastic term may lead to convergence problems in a continuous model. Therefore, this assumption was only used in [110] to study the partial discharge process to the author's best knowledge.

$$P = A\left(\left|\vec{E}\right|/E_b\right)^n \quad \text{Equation 2-13}$$

Where P is the probability, A, E_b, n are constant values. A, E_b, n are chosen to be 1, 10^9 and 4 by [110].

The boundary conditions of charge continuity equations are generally set to be $\vec{n} \cdot \mu_i c_i \vec{E} = 0$ on the boundary of the calculation domain, which means no charge can go outside of the simulation boundary [7-9]. If charge injection is not considered, the boundary condition on the electrodes is set as $\nabla c_{\pm e} = 0$, which means only convective fluxes of charge densities are allowed on the electrodes [7-9]. If charge injection is considered, the boundary condition on the needle electrode is $\vec{J} = c_e \mu_e \left|\vec{E}\right| = \vec{J}_e(t)$, which means the electron density c_e on the needle electrode is set to be $c_e = J_e(t)/\mu_e \left|\vec{E}\right|$, where $J_e(t)$ is the injected current density [7].

(c) Navier-stokes equations

Navier-Stoke equations [111] describe the motion of viscous fluid substances [112-116]. Two conservation equations are included, namely conservation of mass and conservation of momentum, which are shown in Equation 2-14 and Equation 2-15, respectively.

$$\frac{\partial \rho_l}{\partial t} + \nabla \cdot (\overrightarrow{v_l} \rho_l) = 0 \qquad \text{Equation 2-14}$$

$$\rho_l \left(\frac{\partial \overrightarrow{v_l}}{\partial t} + (\overrightarrow{v_l} \cdot \nabla) \overrightarrow{v_l} \right) = \vec{F} - \nabla p \qquad \text{Equation 2-15}$$

Where p is the thermodynamic pressure, $\vec{F}$ is the volumetric force density acted on the liquids, $\overrightarrow{v_l}$ is liquid velocity, ρ_l is liquid density.

The relationship between liquid density ρ_l and thermodynamic pressure of dielectric liquid p is assumed to be either pressure-dependent or pressure-independent under different conditions. For example, when studying the cavity formation process with short voltage rise time, liquid density is assumed to be pressure-dependent [113-115] which is mainly calculated by the equation of state. In comparison, dielectric liquid is regarded as pressure-independent [49, 108, 117] when studying the conduction process under longer voltage rise time when the cavity phenomenon is negligible because liquid has enough time to move to compensate the pressure difference.

The relationship between liquid density and thermodynamic pressure when considering liquid to be compressible can be calculated by the equation of state. Here, we list the equation of state of three typical liquids, cyclohexane, rapeseed oil and deionized water (a typical polar dielectric liquid).

The equation of state of the three liquids have similar forms, as shown in Equation 2-16, for deionized water [113-116], and Equation 2-17 for cyclohexane [118] and rapeseed oil [119]. The related parameter values for deionized water, cyclohexane and rapeseed oil are shown in Table 2-1. When assuming liquid is in a steady state under atmospheric

pressure p_0, if the thermodynamic pressure p of dielectric liquid is over p_0, liquid density ρ_l will also be over ρ_0.

$$p = (p_0 + B)\left(\frac{\rho_l}{\rho_0}\right)^{\gamma} - B \quad \text{Equation 2-16}$$

$$\rho_l = \frac{\rho_0}{1 + C ln\left(\frac{B+p_0}{B+p}\right)} \quad \text{Equation 2-17}$$

Where p_0 is atmospheric pressure, ρ_0 is the liquid density under atmospheric pressure, B, C and γ are constant parameters.

Table 2-1 Summary of the parameters used in the equation of state for deionized water, cyclohexane and rapeseed oil.

Parameter	References		
	Deionized water [113-116]	**Cyclohexane [118]**	**Rapeseed oil [119]**
ρ_0 (kgm^{-3})	1000	774.1	907.3
B (MPa)	307	40.96	380
C	---	0.05382	0.052
γ	7.5	---	---

Generally speaking, the volumetric force $\vec{F}$ acting on a dielectric liquid under a non-uniform electric field can be expressed according to the Helmholtz equation [120-122] as Equation 2-18.

$$\vec{F} = \vec{E}c - \frac{\varepsilon_0}{2}\left|\vec{E}\right|^2 \nabla\varepsilon + \frac{\varepsilon_0}{2}\nabla\left(\left|\vec{E}\right|^2 \frac{\partial\varepsilon_r}{\partial\rho_l}\rho_l\right) \quad \text{Equation 2-18}$$

Where the first term corresponds to the Coulomb force acting on the non-neutral dielectric liquids with space charge density $c = c_+ + c_- + c_e$, the second term is related to the force due to the local inhomogeneous properties of dielectric liquids and the third term represents the electrostrictive force arising from a density-dependent permittivity [123]. The latter two terms are also called ponderomotive forces.

For non-polar dielectric liquid, $\frac{\partial\varepsilon_r}{\partial\rho_l}\rho_l$ can be simplified by the Clausius-Mosotti formula [124] as Equation 2-19.

$$\frac{\partial\varepsilon_r}{\partial\rho_l}\rho_l = \frac{(\varepsilon_r+1)(\varepsilon_r-1)}{3} \quad \text{Equation 2-19}$$

And for polar dielectric liquid, such as deionized water, $\frac{\partial\varepsilon_r}{\partial\rho_l}\rho_l$ can be simplified as Equation 2-20.

$$\frac{\partial\varepsilon_r}{\partial\rho_l}\rho_l = \varepsilon_r\alpha \quad \text{Equation 2-20}$$

Where $\alpha \leq 1.5$ is the empirical factor for most of the studied polar dielectric liquids, including deionized water [113, 125].

It is argued that the Coulomb force [62, 109] may play a key role in streamer initiation in mineral oil while the electrostrictive force [113-116] may be important in streamer initiation in deionized water with fast rise voltage fronts. Due to the electro-mechanical forces acting on local dielectric liquids, a so-called "negative pressure" will be generated in the liquids locally, which gives rise to the possibility of cavity formation. The concept of "negative pressure" is introduced here as in Figure 2-19 [126]. Consider a mass point in the liquid, which is shown as the white circle in Figure 2-19. Without the force $\vec{F}$ on the piston, the total pressure of the mass point equals the sum of thermodynamic pressure p and hydrodynamic pressure $\rho_l g h$, where h is the depth from the liquid surface to the mass point, g is the acceleration of gravity. If the direction of $\vec{F}$ is towards the liquid, the force tends to compress the mass point, with the total pressure of the mass point equalling $p_{total} = p + \rho_l g h + |\vec{F}|/S$, where S is the piston area. However, if the direction of $\vec{F}$ is outwards the liquid as in Figure 2-19, the total pressure of the mass point equals $p_{total} = p + \rho_l g h - |\vec{F}|/S$. The negative pressure $-|\vec{F}|/S$ means that the force tends to stretch the mass point. The total pressure can be negative if $\vec{F}$ is large enough, which means the mass point will be stretched.

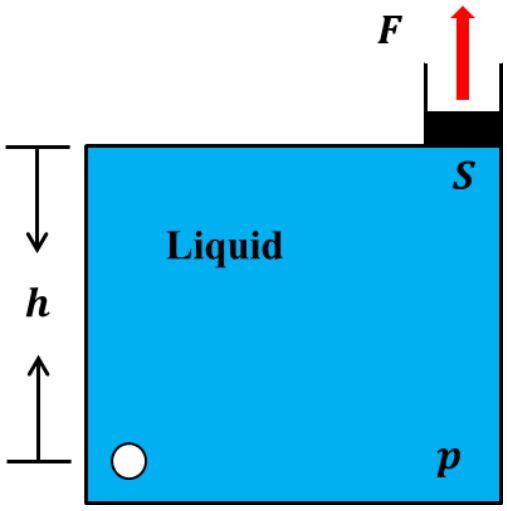

Figure 2-19 Schematic diagram of negative pressure [126].

Concerning liquid during the streamer process, the total pressure related with cavity formation in the liquid is calculated by Equation 2-21, with the volumetric force $\vec{F}$ on the liquid shown in Equation 2-18.

$$-\nabla p + \vec{F} = -\nabla p_{total} \qquad \text{Equation 2-21}$$

The effects of electrostrictive force on the streamer initiation process in deionized water have been studied in both experiments and simulations [113, 115, 127-129]. However,

electrostrictive force may have much less effect on the streamer process in mineral oil due to its much lower permittivity than deionized water. There is lack of published research discussing streamer dynamics and in consideration of cavities under short voltage rise time or DC voltage [11, 61].

The boundary conditions of Navier-stoke equations are given as follows [113]. For all the boundaries on the electrodes and calculating domain, $\vec{n} \cdot \overrightarrow{v_l} = 0$, which means liquid velocity on all the boundaries is zero. Besides, on the boundary of the calculation domain, $p = p_0$, which means the test cell is large enough so that the pressure on the cell boundary equals ambient pressure.

(d) Thermal diffusion equation

Similar to the charge continuity equation, the thermal diffusion equation describes how the temperature distribution is modified by energy dissipation due to Joule heating. The expression of the thermal diffusion equation is shown in Equation 2-22.

$$\frac{\partial T}{\partial t} + \overrightarrow{v_l} \cdot \nabla T = K_T \nabla^2 T + \frac{\emptyset_d}{\rho_l c_v} \quad \text{Equation 2-22}$$

Where T is the liquid temperature distribution, $\vec{v}$ is liquid velocity, K_T is the thermal diffusivity, $\emptyset_d$ is the energy dissipation source term as shown in Equation 2-23, ρ_l is the liquid density, c_v is the liquid specific heat.

$$\emptyset_d = \vec{E} \cdot \vec{J} \quad \text{Equation 2-23}$$

The boundary condition of the thermal diffusion equation for all the boundaries is $\vec{n} \cdot \nabla T = 0$, which means the system is assumed to be perfectly thermally insulated for simplification [8].

2.4.3 Dielectric Liquid Parameters

The values of the constant parameters of dielectric liquids are important when calculating mathematical equations. Among all the dielectric liquids, mineral oil is one of the most commonly used dielectric liquids in oil-filled power transformers due to its excellent insulating properties, long service history and wide availability [130]. Experiments have been conducted by many researchers investigating the electrical properties of mineral oils. However, due to the complexity of mineral oil components, where naphthenic molecules, paraffinic molecules and aromatic molecules account for the majority [131, 132], it is hard to directly test or calculate the parameters in commercial mineral oil. Since the molecular structure of cyclohexane is similar to the naphthenic/paraffinic molecules in mineral oil, cyclohexane is usually taken as an

alternative to represent some characteristics of mineral oil. The parameter values of different dielectric liquids inside the liquid phase during the streamer process are summarised from Section 2.4.3.1 to Section 2.4.3.4.

2.4.3.1 Charge mobility

Charge mobility $\mu_{\pm e}$ describes how quickly the charges can move under the effects of electric field and is important during streamer simulation since it is closely related to the charge velocity in Equation 2-12 and energy dissipation in Equation 2-23, which can affect the streamer velocity and the low-density channel formation, respectively. A summary of the mobilities of positive ions, negative ions and electrons in different dielectric liquids at room temperature are shown in Table 2-2 and Table 2-3. It should be noted that positive ions and negative ions share the same values.

Table 2-2 Mobility of positive and negative ions calculated based on experiments and used in simulations in a liquid phase at room temperature.

Source	Mobility ($m^2V^{-1}s^{-1}$)	Dielectrics	References
Calculations based on experiments	$\sim 1 \times 10^{-9}$	Mineral oil	[105]
	$1 \times 10^{-7} \sim 1 \times 10^{-8}$	Cyclohexane	[100, 109, 133-138]
Simulations	1×10^{-9}	Mineral oil	[8, 9, 49, 54, 105, 110, 139-141]
	1×10^{-8}	Cyclohexane	[11, 142]
	3×10^{-7}	Cyclohexane	[62, 82, 87, 91, 107]

Table 2-3 Mobility of electrons calculated based on experiments and used in simulations in a liquid phase at room temperature.

Source	Mobility ($m^2V^{-1}s^{-1}$)	Dielectrics	References
Calculations based on experiments	$\sim 1.1 \times 10^{-4}$	Cyclopentane	[143]
	$\sim 0.45 \times 10^{-4}$	Cyclohexane	[109, 143-145]
	$\sim 0.025\text{-}0.038 \times 10^{-4}$	n-Decane	[109, 143]
	$\sim 0.038 \sim 400 \times 10^{-4}$	Hydrocarbons	[89, 143, 146-148]
Simulations	1×10^{-4}	Mineral oil	[8, 9, 49, 54, 110, 139-141]
	1×10^{-4}	Cyclohexane	[11, 142]
	0.45×10^{-4}	Cyclohexane	[62, 82, 87, 91, 107]

Apart from the mobility values mentioned above, it should be noted that charge mobility in dielectric liquids also varies with temperature [135, 143-145, 147] and electric field [109, 135, 138, 143, 145, 147]. For example, with the temperature rising from 295 K to 455 K, ion mobility in cyclohexane rises from 1×10^{-8} to 70×10^{-8} $m^2V^{-1}s^{-1}$ [135].

Electron mobility in cyclohexane also rises from 0.45×10^{-4} to 1.7×10^{-4} $m^2V^{-1}s^{-1}$ when the temperature rises from 294 K to 395 K under an electric field of 6.7 kV/cm [144].

Besides, the mobility of electrons is also constrained by the electron saturation velocity (ESV), which is the maximum velocity a charge carrier can gain in the presence of very high electric field [9, 109, 138, 149]. ESV can be explained by the transfer of energy and momentum from electrons to phonons at high velocity and the increase of effective electron mass based on the well-known Shockley theory and the following study [150-153]. A schematic representation of electron drift velocity under different electric field magnitude for three types of dielectric liquids is shown in Figure 2-20 [109]. It is shown that all three kinds of liquid will reach ESV between 10 and 100 km/s. The ESV is argued to happen at electric fields ranging from 1 to 7×10^8 V/m [109, 138, 154] for slow liquids. The electron drift velocity of liquid Argon [143, 154], liquid Xenon and liquid Krypton [143] are shown in Figure 2-21. The ESV of these three types of liquids are all estimated to be between 1-10 km/s.

To the author's best knowledge, no equation has been derived based on experiments to describe ESV in liquids. A rational function from semiconductor models [58, 154] is adopted by [155] to describe the ESV model, as in Equation 2-24.

$$v_e = v_0 \frac{\left|\vec{E}\right|}{(\left|\vec{E}\right| + E_0)} \qquad \text{Equation 2-24}$$

Where v_0 is the ESV and is taken as 41 km/s to keep the velocity of the streamers formed at 4 MV/cm and equal to 40 km/s, which has been observed in experiments [63]. E_0 is taken as 0.1 MV/m.

However, it should be noted that v_0 is unknown in mineral oil, and is only the ESV of electrons rather than streamers under positive polarity. Therefore, it is questionable whether v_0 should be the same as streamer velocity for positive streamers. Besides, it is also doubtful that electron mobility under a low to moderate electric field used in [155] is calculated to be 4.1×10^{-3} $m^2V^{-1}s^{-1}$, which is around 41 times larger than the estimation in [143].

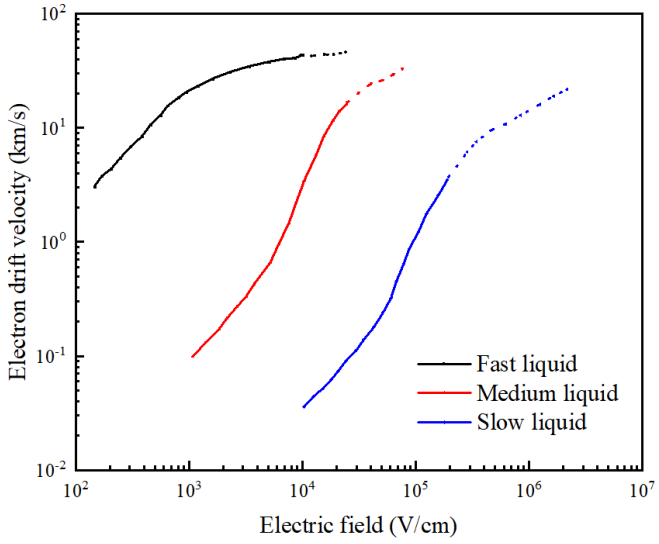

Figure 2-20 Schematic representation of electron drift velocity under different electric fields for three types of dielectric liquids. This figure is reproduced from [109].

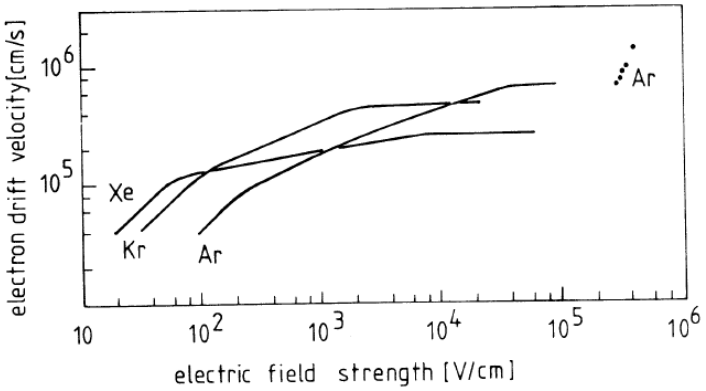

Figure 2-21 Electron drift velocity of liquid Argon, liquid Krypton and liquid Xenon [143].

2.4.3.2 Relative permittivity

The relative permittivity, or dielectric constant, of a material is its (absolute) permittivity expressed as a ratio relative to the vacuum permittivity. The relative permittivity value has a significant impact on the magnitude of the electrostrctive force. The relative permittivity ε_l of transformer oil and cyclohexane in liquid phase is generally taken as 2.2 [7-9, 110, 139] and 2 [11, 135, 142], respectively.

2.4.3.3 Charge generation mechanisms

Due to the electronic nature of streamers, the sources of charge carriers, which are closely related to charge generation mechanisms, play a vital role during streamer initiation and propagation processes. However, there is no consensus on which mechanism dominates the streamer process. In this part, different kinds of charge generation mechanisms from previous literature that have been considered for this current study are introduced and discussed in detail,

(1) Impact ionization

Impact ionization describes the electron avalanche process which indicates that an electron collides with a neutral molecule and generates a new electron and a positive ion. As is illustrated in Section 2.3.2.2, impact ionization, may play a dominant role in streamer initiation and propagation in dielectric liquids [7, 8, 11, 82, 87, 156], which depends on the collision of an electron on a neutral molecule under Coulomb force. The first Townsend ionization coefficient α_T is used to describe the impact ionization rate and has the following expression shown in Equation 2-25.

$$\alpha_T = A_l N_l \exp(-\frac{B_l N_l}{|\vec{E}|}) \quad \text{Equation 2-25}$$

Where A_l and B_l are constant values, N_l is the molecular number density in dielectrics. It should be noted that $A_l N_l$ is in the unit of (m^{-1}) and represents the reciprocal of electron mean free path between collision in dielectric liquids. $B_l N_l$ is the exponential term.

A summary of the values of $A_l N_l$ and $B_l N_l$ in simulations and experiments are shown in Table 2-4.

Table 2-4 Summary of the values of $A_l N_l$ and $B_l N_l$ of impact ionization calculated based on experiments and used in simulations.

Source	$A_l N_l$ (m^{-1})	$B_l N_l$ (Vm^{-1})	Dielectrics	References
Calculations based on experiments	2.0×10^8	3×10^9	Cyclohexane	[157]
	1.1×10^8	1.8×10^9	Gaseous hexane	[158]
	1.3×10^8	1.9×10^9	Gaseous cyclohexane	[158]
	1.2×10^8	1.8×10^9	Gaseous pentane	[158]
Simulations	25	2×10^7	Mineral oil	[7]
	5×10^6	1×10^5	Mineral oil	[49]
	1.0×10^8	2.5×10^9	Cyclohexane	[8]
	1.3×10^8	1.9×10^9	Cyclohexane	[11]
	2.0×10^8	3×10^9	Cyclohexane	[82]
	1.2×10^8	1.9×10^9	Cyclohexane	[91]
	2×10^8	3×10^9	Cyclohexane	[87]
	5×10^6	3×10^7	Deionized water	[58, 159]

The values in [7, 49] are very different from the others because the authors manually selected the values of $A_l N_l$ and $B_l N_l$ to fit experimental results due to a lack of knowledge in transformer oil.

The charge generation rate based on impact ionization can be expressed as Equation 2-26 [8].

$$G_I = \alpha_T |c_e| v_e = \alpha_T |c_e| \mu_e \left|\vec{E}\right| = A_l N_l \exp\left(-\frac{B_l N_l}{|\vec{E}|}\right) |c_e| \mu_e \left|\vec{E}\right| \quad \text{Equation 2-26}$$

Therefore, G_I is closely related with $|c_e|$, μ_e and $\left|\vec{E}\right|$.

It should be noted that although impact ionization is considered as a possible charge generation mechanism, arguments about the conditions under which impact ionization dominates still exist. It is suggested in [8] that impact ionization is the dominating mechanism for 4th mode streamers with a velocity over 100 km/s under an extremely high electric field. In comparison, it is assumed in [11, 94, 142] that impact ionization is responsible for streamer initiation and propagation with different velocities ranging from 2 km/s to 300 km/s. This assumption in the continuous model is similar to the assumption adopted in the discrete model [82, 87, 91].

(2) Molecular ionization

Molecular ionization, known as a direct ionization mechanism based on Zener's theory [160], was proposed in [6] as the dominant mechanism for positive streamer initiation and propagation. It indicates that under a high enough electric field, an electron will be directly extracted from a neutral molecule, thus forming a free electron and a positive ion. The charge generation rate of molecular ionization G_M is calculated as Equation 2-27.

$$G_M = \frac{n_0 q^2 a |\vec{E}|}{h} exp\left(-\frac{\pi^2 m^* a \Delta^2}{q h^2 |\vec{E}|}\right) \quad \text{Equation 2-27}$$

Where n_0 is the number density of ionisable molecules in the dielectric liquids, q is the electronic charge, a is the molecular separation, h is Planck's constant, m^* is the effective electron mass, Δ is the ionization potential of molecules and dependent on the dielectric liquid's components.

According to density function theory (DFT) [96], the IP of hydrocarbons shows a decreasing trend with the increasing electric field magnitude [161], as in Equation 2-28. However, constant IP was also once used in a simulation for simplification [7, 8, 58, 110, 140, 141, 162-164]. Typical values of IP for different dielectric liquids are summarised in Table 2-5. It should be noted that it may not be reasonable to use IP in the gaseous phase to simulate streamers in the liquid phase, as was used in [8, 141].

$$\Delta = \Delta_0 - \gamma\sqrt{\left|\vec{E}\right|} \quad \text{Equation 2-28}$$

Where Δ_0 is the ionization potential under no electric field, γ is the coefficient.

Table 2-5 Ionization potential of different dielectric liquids.

Source	Ionization potential (eV)	Dielectrics	Reference
Calculations based on experiments	$10.22 - 6.78 \times 10^{-5}\sqrt{\lvert\vec{E}\rvert}$	Cyclohexane in gaseous phase	[96, 148, 166, 167]
	~8.41	Cyclohexane in liquid phase	[168, 169]
	~9.86	Cyclohexane in gaseous phase	[169-172]
	~6.20	Pyrene in liquid phase	[169-171, 173]
	~7.43	Pyrene in gaseous phase	[169, 173, 174]
Simulations	$8.5 - 6.9875 \times 10^{-5}\sqrt{\lvert\vec{E}\rvert}$	Mineral oil	[9, 60, 61, 139, 155, 175, 176]
	7.1	Mineral oil	[110, 162]
	6.20	Aromatic	[8, 141]
	7.40	Aromatic	[177]
	9.86	Naphthenic/paraffinic	[8, 141]
	4	Deionized water	[58]

Similar to Δ, n_0 is also dependent on the dielectric liquid's components. The values of n_0 are summarised in Table 2-6. It is also argued that n_0 will increase when the electric field is high because not only do the easily ionisable molecules get ionized but so do the "ordinary" molecules [165]. The values of other parameters in Equation 2-27 are summarised in Table 2-7.

According to the different parameters, a comparison of the molecular ionization charge generation rate based on different Δ and n_0 is presented in Figure 2-22. It is shown that when the electric field magnitude is lower than around 10^9 V/m, aromatic molecules with an IP of 6.2 eV [8, 141] have the highest charge generation rate, meaning that the streamer can initiate at a lower voltage. The charge generation rate of mineral oil with an IP of 7.1 eV [110, 162] in the red line is similar to mineral oil with a field dependent IP [9, 60, 61, 139, 155, 175, 176] in the blue line. The differences between the black line with an IP of 6.2 eV and the other two lines are relatively large when the electric field is increased from 10^8 V/m to 10^9 V/m. With an electric field higher than 10^9 V/m, all the results show similar values.

Table 2-6 Density of ionisable molecules n_0 in different dielectric liquids.

Source	Density of ionisable molecules n_0 (m^{-3})	Dielectrics	Reference
Estimation	10^{21}~10^{22}	Mineral oil	[178]
	10^{23}	Aromatic	[131, 132, 179]
	10^{25}	Naphthenic/paraffinic	[131, 132, 179]
	10^{23}~10^{25}	Mineral oil	[165]
	10^{21}	Mineral oil	[162]
Simulation	10^{23}	Mineral oil	[9, 60, 61, 155, 175, 176]
	10^{23}	Mineral oil	[110]
	10^{23}	Aromatic	[8, 177]
	10^{25}	Naphthenic/paraffinic	[8]
	10^{26}	Naphthenic/paraffinic	[177]

Table 2-7 Summary of other parameters used in Equation 2-27

Variable	Values	Reference
q	1.602×10^{-19} C	[180]
h	6.62608×10^{-34} m^2kgs^{-1}	[180]
a	3.0×10^{-10} m	[7, 8, 58, 110, 139-141, 159]
m^*	$0.1 \times m_e = 9.1 \times 10^{-32}$ kg	[7, 8, 58, 110, 139-141, 148]

Where m_e is the mass of an electron.

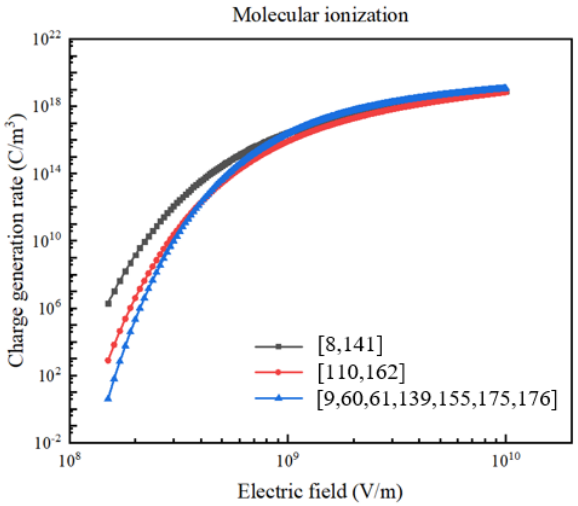

Figure 2-22 Comparison of molecular ionization charge generation rate based on different ionization potentials.

(3) Photoionization

Photoionization implies a transition from bound to a free state for the electrons [181]. It results in the generation of a positive ion and a free electron, both of which are formed from the interaction of a photon with an atom or molecule [181]. The sources of photon radiation may originate from thermal background radiation and molecules relaxing from an excited state [13, 181, 182].

The role of photoionization is generally assumed to facilitate 3rd and 4th mode streamers [5, 8, 33] because photoionization is assumed to happen under a much higher electric field than impact ionization and molecular ionization [91], which may act as a feed-forward mechanism at the streamer tip [5]. In the discrete model, photoionization is assumed to happen at 3.04 GV/m [91]. The physical model of photoionization in air was formulated in [183, 184], and is complicated. Therefore, a simplified method was used to include photoionization into streamer modelling in liquid.

It is assumed that photoionization results in background ionization, which gives initial electrons and positive ions with number density equal to 10^{14} m^{-3} [8]. This value is much smaller than the space charge number density at the streamer tip during streamer propagation, which is typically around 1.5×10^{22} m^{-3} [8]. This method has also been used to simulate photoionization in gas by different authors [185-187].

(4) Ionic dissociation

Similar to molecular ionization, ionic dissociation is also a direct ionization mechanism used to describe how conductivity of a weak electrolyte is dependent upon the level of electric field stress [188]. The charge generation rate due to ionic dissociation under the effects of an electric field is calculated by Equation 2-29 [7, 101, 189, 190]. Under the application of an electric field, ion pairs in weak electrolyte dissociate into free positive ions and negative ions. As non-hydrocarbon-based impurities unavoidably exist in hydrocarbons liquids, different authors have used ionic dissociation to describe electrical conduction in transformer oil [100-102, 104, 105, 137, 189].

$$G_{ID} = qn_cK_D^0F_{ID}\left(\left|\vec{E}\right|\right) = q\left(\frac{\sigma}{q(\mu_+ + \mu_-)}\right)^2 R_{\pm}\, F_{ID}\left(\left|\vec{E}\right|\right) \qquad \text{Equation 2-29}$$

Where n_c is the number density of neutral ion-pairs, K_D^0 is the dissociation constant under no electric field, $F_{ID}\left(\left|\vec{E}\right|\right)$ is the field enhancement factor of the dissociation constant, σ is liquid conductivity, $R_{\pm}$ is the recombination rate of positive ions and negative ions.

(5) Field emission

Based on the quantum-mechanical effect, electrons can be emitted from a metal surface through the potential barrier at the metal/liquid interface [7] under a high electric field with negative polarity [191], typically greater than 5×10^8 V/m [7, 192]. The occurrence of field emission has been physically verified by experiments in dielectric liquids [193, 194], including cyclohexane for a very small radius of curvature ($R < 1$ μm) [134]. However, whether this mechanism could dominate negative streamer initiation and propagation is unclear.

The method used to describe emission current was initially proposed by Fowler and Nordheim in 1928 [195]. Considering the effects of the image force barrier were decreasing, modification was undertaken later [196, 197]. The modified emitted current density J is calculated as Equation 2-30. By using Equation 2-30, the injected current density on the electrode can be calculated. Therefore, the effects of injected electrons on streamer dynamics can be further simulated and discussed.

$$J = \frac{q^3|\vec{E}|^2}{8\pi h\phi t^2(y)} exp\left(-\frac{8\pi\sqrt{2m}\phi^{3/2}}{3hq|\vec{E}|}v(y)\right) \quad \text{Equation 2-30}$$

Where h is plank's constant, q is electron charge, ϕ is the metal's work function in J and is assumed to be 4.5 eV in [7] on a copper electrode, y is an electric field dependent parameter, $t^2(y)$ and $v(y)$ are two electric field dependent functions representing general correction factors [198, 199].

In streamer simulations, the set of values to estimate y, $t^2(y)$ and $v(y)$ by [107, 199, 200] is summarised in Table 2-8.

Table 2-8 Summary of parameters for ionic dissociation.

y	$t^2(y)$	$v(y)$	**Reference**
$1.4299\times10^{-9}\|\vec{E}\|\phi^{-2}$	1	$1-y+\frac{1}{6}ylny$	[107, 199, 200]

Where $|\vec{E}|$ is in (V/m), ϕ is in (eV).

The injected current densities calculated according to the values above are plotted in Figure 2-23 under different electric field magnitudes. The current density increases greatly from 10^{-14} A/m^2 to 0.73 A/m^2 with electric field magnitude increasing from 10^9 V/m to 2×10^9 V/m.

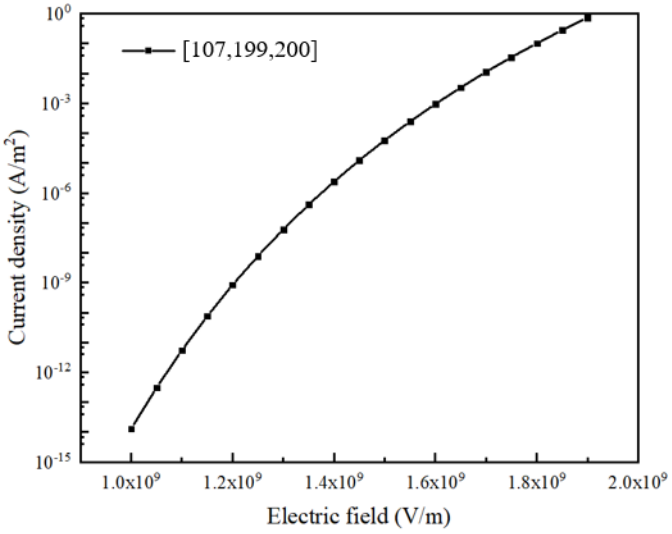

Figure 2-23 Calculation of injected current density by modified Fowler-Nordheim equation.

(6) Comments on the charge generation mechanism

In general, molecular ionization and impact ionization are considered as the dominating mechanisms in the literature [7-9, 49, 82, 87, 91, 107]. Besides, it is generally assumed that photoionization requires a higher electric field to occur and may be responsible for the 4th mode streamer.

2.4.3.4 Charge recombination mechanism

According to [89], one possible method to simulate the recombination process of ion/ion and electron/ion is to treat it as a chemical reaction, which is based on the spatial density distribution of the charges. In dielectric liquids, neutral molecules and free charge carriers, including positive and negative ions and electrons, will interact with each other by three possible methods: ion and ion recombination, electron and ion recombination and attachment of electron to neutral molecules.

(1) Ion and ion recombination

The diffusion-controlled recombination rate of positive and negative ions $R_{\pm\_D}$ in (m^3s^{-1}) can be calculated as Equation 2-31 [7]. The assumption is that if the energy induced by Coulomb force between a positive ion and a negative ion within the distance $r = r_+ + r_-$ equals the thermal energy k_BT, the recombination can be regarded as inevitable. r_+ and r_- are the radius of positive ions and negative ions, respectively. k_B and T are the Boltzmann constant and temperature, respectively.

$$R_{\pm\_D} = \frac{q(\mu_+ + \mu_-)}{\varepsilon_0 \varepsilon_r} \qquad \text{Equation 2-31}$$

Equation 2-31 is also called the Langevin-Deybe relationship [89, 105]. Typical values of $R_{\pm\_D}$ equals 1.64×10^{-17} m^3s^{-1} when $\mu_{\pm}$ equals 1×10^{-9} $m^2V^{-1}s^{-1}$ in mineral oil and 1.64×10^{-16} m^3s^{-1} when $\mu_{\pm}$ equals 1×10^{-9} $m^2V^{-1}s^{-1}$ in cyclohexane.

(2) Electron and ion recombination

The diffusion-controlled recombination rate between a positive ion and electron R_{+e_D} also has a similar relationship with ion and ion recombination. However, the distance, within which the recombination of an electron and a positive ion can be regarded as an inevitable process, is described by Onsager Radius r_s. Thus, the R_{+e_D} is calculated as Equation 2-32 [181, 201-203].

$$R_{+e\_D} = \frac{4\pi q(\mu_+ + \mu_e)}{\varepsilon_0\varepsilon_r} \approx \frac{4\pi q\mu_e}{\varepsilon_0\varepsilon_r} \qquad \text{Equation 2-32}$$

Note that μ_e is generally $10^3 \sim 10^5$ times larger than μ_+.

It should be noted that R_{+e_D} is generally considered as the total ion and electron recombination rate under a low to moderate electric field. Experiments show that the recombination rate of electrons and positive ions R_{+e} in cyclohexane is ~3.2×10^{-13} m^3s^{-1} at room temperature under a low to moderate electric field [204]. According to Equation 2-32, R_{+e_D} in cyclohexane is calculated as 4.6×10^{-13} m^3s^{-1} when μ_e is 0.45×10^{-4} $m^2V^{-1}s^{-1}$, which is similar to ~3.2×10^{-13} m^3s^{-1} [204].

However, it is also argued in [7-9] that R_{+e_D} overestimates R_{+e} under an extremely high electric field ranging from 1×10^8~1×10^9 V/m, since electrons will have energies on the order of several electron-volts [205]. Therefore, electrons at the reaction radius may have excess energy due to the external field.

For compensation of electron recombination with positive ions under a relatively high electric field, two methods are considered. The first compensation method adopted by most authors [7-9, 58, 140, 164] to calculate R_{+e} is using the same recombination rate as $R_{\pm\_D}$. The second compensation method considers a reduction of $R_{\pm\_D}$ by a fraction of η_D and the effects of energy exchange controlled two-body and three-body recombination [11, 203], which may lead to a lower electron-ion recombination rate R_{+e} than R_{+e_D}. η_D was selected to be 0.1 due to theoretical analysis [203] and was used in [11]. R_{+e} under an intensive electric field is estimated to be 1.64×10^{-16} m^3s^{-1} and 1.08×10^{-13} m^3s^{-1} in liquid cyclohexane based on method one and two, respectively, which is a considerable difference. However, due to lack of experimental results under a high electric field, it is hard to validate the exact value of R_{+e}.

(3) Electron attachment

Besides electron and ion recombination, electrons may also be attached to neutral molecules to form negative ions. Electron attachment is modelled via attachment time constant τ_a which describes the life time of energetic electrons in dielectric liquids [7, 8, 58] and is calculated as Equation 2-33.

$$\tau_a = \frac{\lambda_a}{\mu_e|\overrightarrow{E_a}|} \quad \text{Equation 2-33}$$

Where λ_a is the attenuation length of electrons, $|\overrightarrow{E_a}|$ is the average electric field strength on electrons.

By assuming $|\overrightarrow{E_a}| = 5\times10^7$ V/m and $\lambda_a = 1$ mm, τ_a is calculated to be 200 ns [7-9, 58]. However, it is argued that the electric-field-dependence of τ_a should be taken into consideration [49, 107, 206]. A constant zero-field attachment rate cannot reflect the fact that electron attachment dominates under a low electric field while it is less intensive with a high electric field [207]. The electric field dependent electron attachment time τ_{a_E}, according to [49], can be re-written as Equation 2-34. Apparently, an increasing electric field results in a decreasing τ_{a_E}.

$$\tau_{a\_E} = \frac{1}{(m_{att}E + b_{att})\mu_e E} \quad \text{Equation 2-34}$$

Where m_{att} and b_{att} are constants.

The values of constant τ_a used in simulations and calculated from experiments are summarised in Table 2-9. The electric field dependent τ_{a_E} used in [49] is plotted in Figure 2-24. It is found that τ_{a_E} is over 10^4 smaller than that used in other studies shown in Table 2-9 when the electric field is over 10^8 V/m.

Table 2-9 Summary of electron attachment time in calculations based on experiments and in simulations.

Sources	τ_a (ns)	Dielectrics	Reference
Calculations based on experiments	500	Cyclohexane	[134]
	~100	Hydrocarbons	[109, 138]
	200	Nitrogen	[208]
	200	Helium	[209]
Simulations	200	Mineral oil	[7-9]
	200	Deionized water	[58]
	500	Cyclohexane	[107]
	Field-dependent	Cyclohexane	[107]

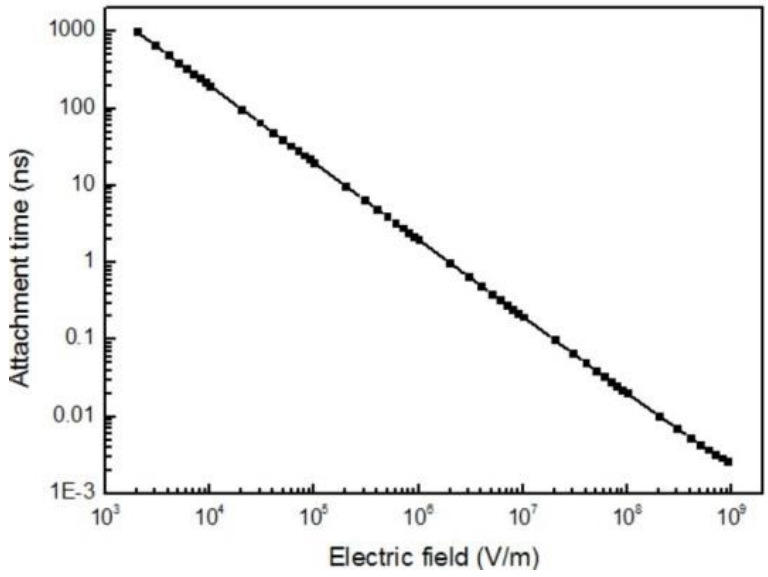

Figure 2-24 Electric field dependent electron attachment time used in simulation [49].

2.4.4 Key findings

Different from the discrete model that mainly shows streamer velocity and streamer pattern shapes, the continuous model can give a lot of detailed microscopic property information, such as electric field distribution, space charge density distribution, temperature distribution and Joule heating energy density distribution. The results are often shown in 1D or 2D plots. A 1D plot is typically from needle tip to the bulk oil along z-axis, which is the symmetry of electrode geometry. A 2D plot generally shows the distribution of parameters on the surface. For a 2D-axisymmetric model in COMSOL Multiphysics, a 2D plot shows the distribution of parameters in r-direction and z-direction at the same time. Detailed simulation results will be introduced in the following sections.

2.4.4.1 Conduction current

Since conduction current is regarded as a pre-process of a streamer, the conduction current induced by different charge generation rates has been simulated and compared with experiments [49, 107, 117, 163, 210]. However, since the values of some parameters lack experimental evidence, such as molecular separation a, the effective electron mass m^* and the density of ionisable molecules n_0 in Equation 2-27, [49] found that the values in most published research did not perfectly fit the experimental Current-Voltage (IV) curve by conduction current tests. Therefore, new sets of parameter values in the charge generation rate equation were selected to fit the IV curve. In Figure 2-25 (a) [49], it is found that when considering molecular ionization alone,

the simulated conduction current can well fit the IV curve under positive polarity but under-estimate the current under negative polarity [49]. When considering both impact ionization and molecular ionization as the charge contributor in Figure 2-25 (b) by finally fitted parameter values, the IV curve of both positive and negative polarities can fit the experimental results well. The best-fitted final parameter set used in [49] is summarised in Table 2-10. This set can also fit the IV curve when changing another electrode geometry [49]. However, this parameter set is not unique and is dependent on the selection of the electron attachment constant and electron mobility [49].

In comparison with molecular ionization and impact ionization, field emissions alone estimate a much lower IV curve in mineral oil when compared to experiments [49], indicating that field emissions have less effect on streamer dynamics in bulk oil.

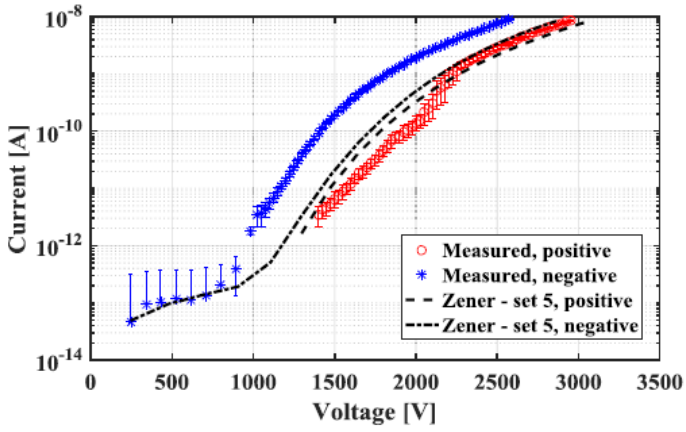

(a)

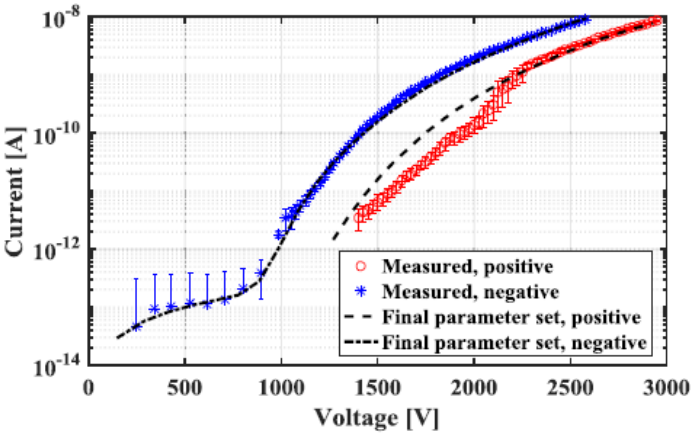

(b)

Figure 2-25 Current-Voltage curve comparison under both positive and negative polarities between experiments and simulation results by (a) only considering molecular ionization by parameter set 5 and (b) considering both molecular ionization and impact ionization using the best-fitted final parameter set [49].

Table 2-10 Summary of the best-fitted final parameter set for impact ionization and molecular ionization [49].

Charge generation rate	Parameter	Values
Molecular ionization	A_M	1.74×10^5 S/m^2
$G_M = A_M\|\vec{E}\|exp(-\|\vec{E}\|/B_M)$	B_M	7×10^9 V/m
Impact ionization	$A_I N$	5×10^6 m^{-1}
$G_I = A_I N\|\rho_e\|\mu_e\|\vec{E}\|exp(-\|\vec{E}\|/B_I N)$	$B_I N$	1×10^5 V/m

2.4.4.2 Streamer mode

Since a streamer behaves as an ionizing wave starting from the needle tip into the oil bulk, electric field peak velocity is generally regarded as streamer velocity in simulations. A typical electric field distribution of a 2nd mode streamer is shown in Figure 2-26 [8]. In Figure 2-26 (a), the electric field is able to leave the needle tip into the oil bulk under the superposition of an initial Laplace field and electric field induced by space charges when considering molecular ionization alone under positive polarity. The space charge density, which is the sum of c_+, c_- and c_e, in Figure 2-26 (b) is positive. The total positive space charge at a streamer tip with the same polarity as the needle tip modifies the $|\vec{E}|$ distribution in the oil such that it will decrease $|\vec{E}|$ behind the streamer tip while increase $|\vec{E}|$ ahead of the ionized volume. The increased $|\vec{E}|$ at the streamer tip leads to further ionization ahead of the streamer tip and keeps ionization occurring in the bulk oil. The corresponding 2D plot of the electric field is shown in Figure 2-27 [8]. It shows that the cylindrical streamer is enveloped by a field enhancement at the streamer boundary where the streamer tip has the most intensive electric field. The electric field peak propagates at a velocity of around 3.0 km/s with a magnitude of 3.5×10^8 V/m. The radius of the streamer channel defined by the outline of the electric field shell at the streamer tip is around 5-10 μm [8].

Similar results have been achieved in electric field distribution studies on 2nd mode streamers due to molecular ionization under negative polarity [61] and impact ionization under positive polarity [11]. In comparison, however, field emissions and ionic dissociation alone can only affect the electric field distribution in the vicinity of the needle tip even under an extremely high electric field [7], which is unable to contribute to streamer dynamics in bulk oil to a large extent.

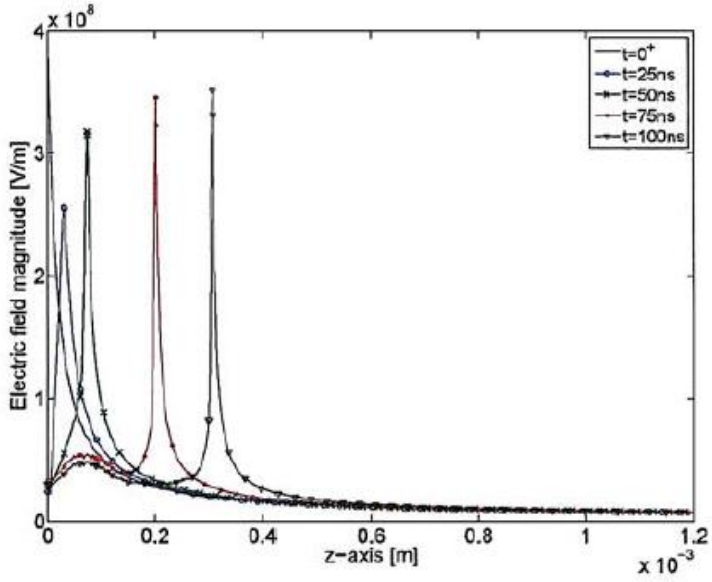

(a)

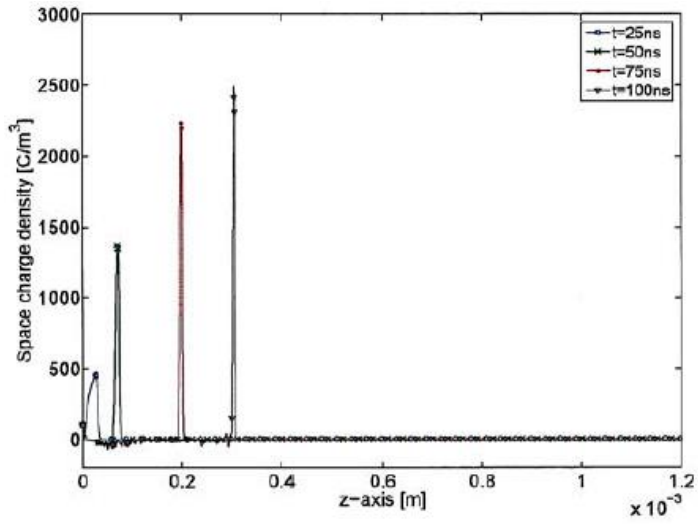

(b)

Figure 2-26 The distribution of the electric field and space charge density generated by molecular ionization in a 1D plot. (a) Electric field, (b) Space charge density. Note that voltage excitation is +130 kV step voltage in needle sphere geometry with a tip radius of 40 μm and a gap distance of 25 mm, respectively. $t = 0^+$ represents the Laplace field distribution under 130 kV [8].

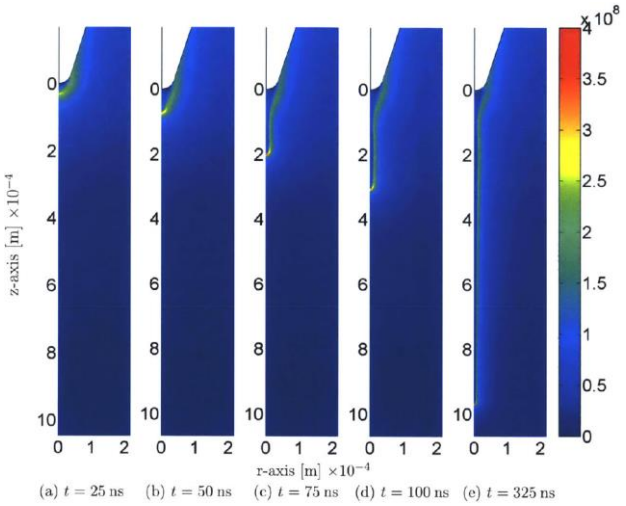

Figure 2-27 The distribution of the electric field of a 2nd mode streamer in a 2D plot at (a) 25 ns, (b) 50 ns, (c) 75 ns, (d), 100 ns, (e) 325 ns [8]. Z-axis means the axis of symmetry from needle tip towards ground. R-axis means in the radial direction.

Concerning streamer mode transition from 2nd mode to 3rd mode, it is proposed in [163, 165] that the streamer modes of 2nd and 3rd modes are dependent on the ionization of aromatic molecules and naphthenic/paraffinic molecules, respectively. The simulation results for 2nd mode streamers in mineral oil are shown in Figure 2-26 and Figure 2-27, with consideration that only aromatic molecules exist in the liquid. In comparison, the 3rd mode streamer shown in Figure 2-28 [8], which only considered naphthenic/paraffinic molecules, propagates at an average velocity of around 9.5 km/s with a magnitude of 7.0×10^8 V/m. The streamer radius of the 3rd mode streamer in the simulation is 1 µm, which is much smaller than the 2nd mode streamer [8].

The simulation results from Figure 2-26 to Figure 2-28 seem to explain the reason for the 2nd and 3rd mode streamer occurrences. However, it seems unreasonable in a simulation to use the values of different components separately to represent the streamer dynamics of a mixture such as mineral oil. To be clearer, mineral oil was assumed to be pure aromatic molecules when simulating 2nd mode streamers, while it consisted of pure paraffinic/naphthenic molecules when studying 3rd mode streamers in [8, 163]. Simulation results of the effects of combining aromatic and naphthenic/paraffinic molecules are shown in Figure 2-29 [8]. Compared with Figure 2-28 (a), the electric field magnitude in Figure 2-29 (a) shows a decreasing trend with time and has a smaller electric field magnitude of ~2 MV/cm at the streamer tip on the axis of symmetry. Besides, the volume of the streamer channel in Figure 2-29 (b) is also larger than that in Figure 2-28 (a). The direction of the electric field seems to propagate into r-direction.

[8] argues that this shows a shielding effect of molecules with low IP and number density. However, the simulation results may also indicate that 3rd mode streamers cannot be generated under reasonable voltage levels. Besides, simulation studies based on this assumption indicate that 2nd mode streamers cannot be initiated from liquids with pure paraffinic/naphthenic molecules due to high IP, such as cyclohexane [8], which is contradictory to the effect of 2nd mode streamers observed in cyclohexane [1].

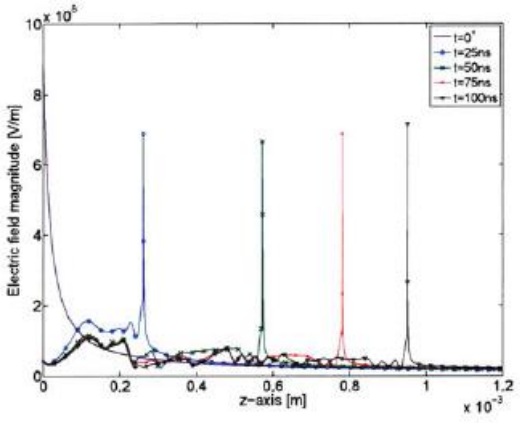

(a)

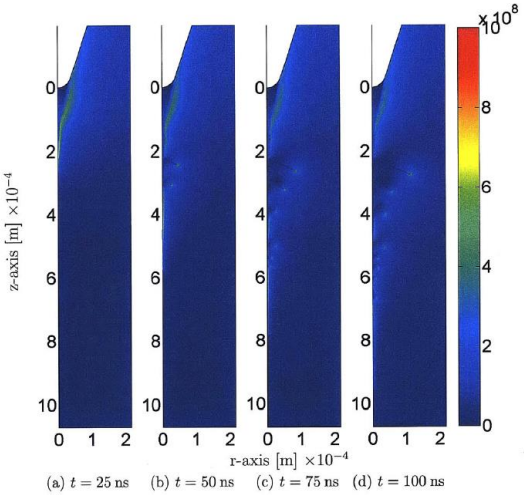

(b)

Figure 2-28 The electric field distribution of a 3rd mode streamer when considering naphthenic/paraffinic molecules (a) in a 1D plot and (b) in a 2D plot. Note that voltage excitation is +300 kV step voltage in needle sphere geometry with a tip radius of 40 µm and a gap distance of 25 mm, respectively. $t = 0^+$ represents the Laplace field distribution under 300 kV [8].

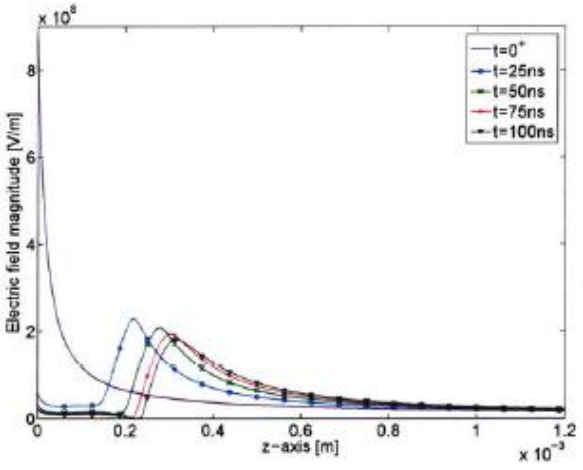

(a)

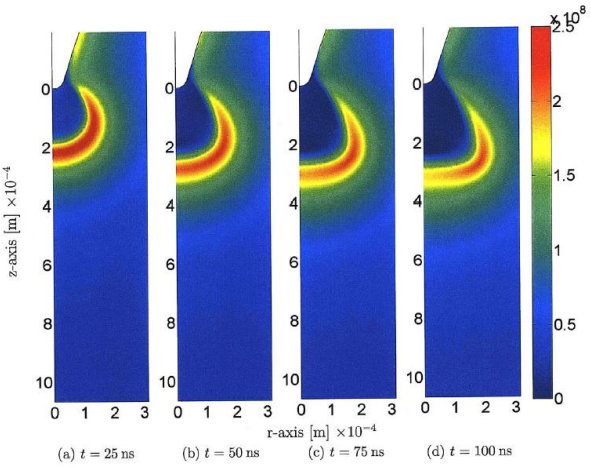

(b)

Figure 2-29 The electric field distribution during the streamer process when considering aromatic and naphthenic/paraffinic molecules (a) in a 1D plot, and (b) in a 2D plot. Note that voltage excitation is +300 kV step voltage in needle sphere geometry with a tip radius of 40 µm and a gap distance of 25 mm, respectively. $t = 0^+$ represents the Laplace field distribution under 300 kV [8].

In addition, there are some problems with streamer velocity when considering reduced IP with an electric field. A re-calculation of instant streamer velocity based on [60, 61] is shown in Figure 2-30 under voltages between V_b and V_a. It is found that although the average streamer velocities are in the range of 2nd mode streamers, the instant streamer velocities show an increasing trend with time and streamer length. This phenomenon indicates that the streamer may not be in the 2nd mode with further propagation. Concerning the remaining four solid lines in Figure 2-30, the average streamer velocities are much higher than the 2nd mode when the streamer covers the whole gap distance under V_b. Therefore, a new mechanism constraining the velocity of 2nd mode streamers should be considered in simulations.

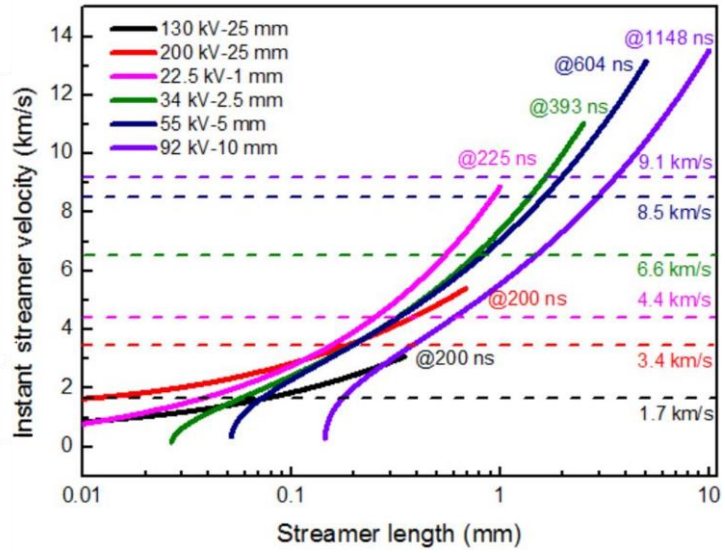

Figure 2-30 Instant streamer velocity at different streamer lengths under different conditions at different times calculated according to [60, 61]. The solid line labels are named "applied voltage-gap distance". Solid lines represent the instant streamer velocities. The dash lines are the average velocities of each condition.

For the 4th mode streamer, it is assumed in [8] that both photoionization and impact ionization are the dominant mechanisms. Photoionization offers the essential initial electrons for impact ionization. In Figure 2-31 (a) [8], the simulation results show that the electric field propagates into the bulk oil at around 100 km/s, with a peak magnitude over 10^9 V/m. A much higher space charge density, as shown in Figure 2-31 (b), was also observed when compared with 2nd and 3rd mode streamers in simulations, indicating intensive ionization inside the streamer channel. Besides, the streamer channel radius shown in Figure 2-32 [8] is also much wider (30-40 μm) than the 2nd and 3rd mode streamers.

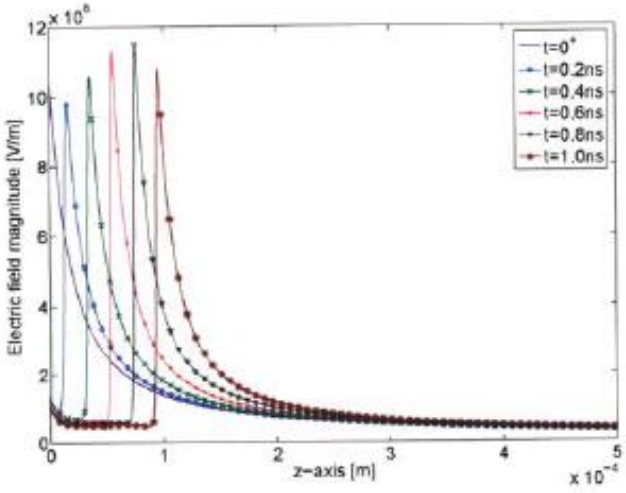

(a)

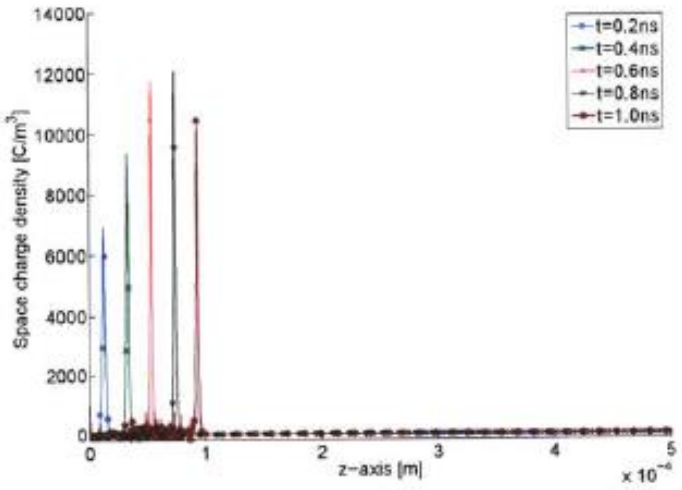

(b)

Figure 2-31 The distribution of (a) an electric field and (b) space charge density during the streamer process in a 1D plot. Note that voltage excitation is +350 kV step voltage in needle sphere geometry with a tip radius of 40 µm and a gap distance of 25 mm, respectively. $t = 0^+$ ***represents the Laplace field distribution under 350 kV [8].***

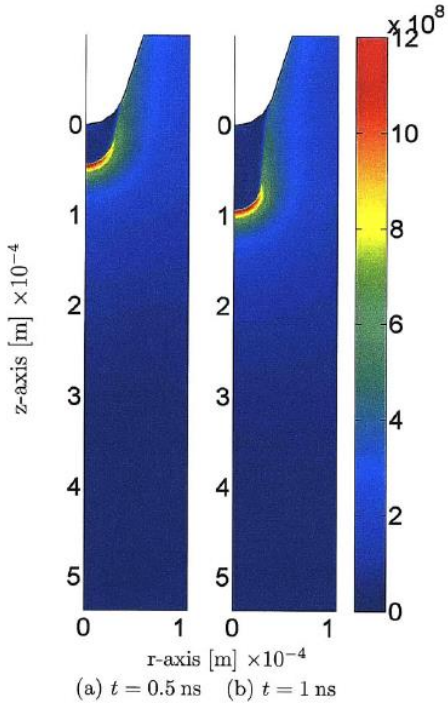

Figure 2-32 The electric field distribution of a 4th mode streamer in a 2D plot at (a) 0.5 ns and (b) 1 ns [8].

2.4.4.3 Streamer morphology

In general, a streamer consists of multiple channels. Streamer morphology simulations have been conducted using two directions. The first is studying the effects of different

parameters on a single streamer channel and the second is studying the formation of multiple streamer channels.

(1) Single streamer channel

For a single streamer channel in a selected dielectric liquid, the voltage excitation and electrode geometry have significant impacts on streamer shape. Voltage peak amplitude and rise time effects on positive streamer tip shape are shown in Figure 2-33 [61]. The positive streamer tip is 0.5 mm away from the needle tip. The filled contours represent the distribution of space charge density, ranging from $0.5|c_e|_{max}$ (yellow) to $|c_e|_{max}$ (black). The electric field is shown as black solid lines from $0.5\left|\vec{E}\right|_{max}$ to $\left|\vec{E}\right|_{max}$. The values on the black solid lines mean the fraction of $\left|\vec{E}\right|_{max}$. It is shown that increasing voltage magnitude and decreasing voltage rise time both increase the streamer channel tip shape. This phenomenon was explained by [61] as the highly mobile electrons being prevented by a faster rising and larger electric field from diffusing into the bulk oil. Therefore, capturing more electrons over a larger volume forms a bulkier initial ionized volume, leading to a greater streamer column diameter.

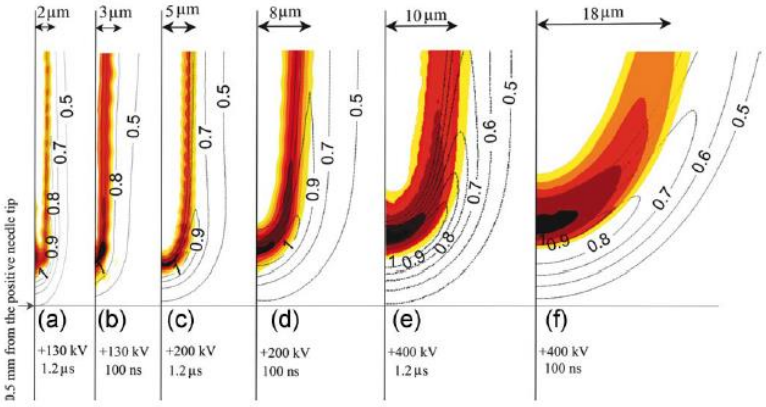

Figure 2-33 The electric field and space charge density distributions for different voltage magnitudes and rise times in a needle-sphere geometry with a tip radius of 40 μm and a gap distance of 25 mm, respectively. (a) +130 kV with a 1.2 μs rise time, $\left|\vec{E}\right|_{max} = 3.1 \times 10^8\ V/m$, $|c_e|_{max} = 4250\ C/m^3$, ***(b) +130 kV with 100 ns rise time,*** $\left|\vec{E}\right|_{max} = 2.9 \times 10^8\ V/m$, $|c_e|_{max} = 3940\ C/m^3$, ***(c) +200 kV with 1.2 μs rise time,*** $\left|\vec{E}\right|_{max} = 2.9 \times 10^8\ V/m$, $|c_e|_{max} = 3120\ C/m^3$, ***(b) +130 kV with 100 ns rise time,*** $\left|\vec{E}\right|_{max} = 2.8 \times 10^8\ V/m$, $|c_e|_{max} = 2430\ C/m^3$, ***(e) +400 kV with 1.2 μs rise time,*** $\left|\vec{E}\right|_{max} = 2.6 \times 10^8\ V/m$, $|c_e|_{max} = 1540\ C/m^3$, ***(f) +400 kV with 100 ns rise time,*** $\left|\vec{E}\right|_{max} = 2.4 \times 10^8\ V/m$, $|c_e|_{max} = 930\ C/m^3$ ***[61].***

The standard electrode geometry for an impulse breakdown voltage test defined in IEC 60897 [211] is a needle-sphere geometry with a needle tip radius of 40-70 μm and a gap distance of 25 mm, respectively. In this case, a positive needle tip facilitates streamer initiation. However, a needle electrode is not necessary to assist streamer propagation when both of the electrodes are needles, when compared to a needle-sphere geometry. For electrode geometry with a gap distance of 25 mm and needle tip radius of 40 μm, the breakdown voltage in a needle-sphere geometry simulation is calculated to be 92 kV. In comparison, the breakdown voltage of needle-needle geometry is calculated to be 112 kV [60]. Since the electric field magnitude at both sides of the electrodes is higher in a needle-needle geometry than in a needle-sphere geometry, the electric field magnitude in the middle of the oil gap in a needle-needle geometry is lower than that in a needle-sphere geometry [60], decreasing the possibility of breakdown in a needle-needle geometry and resulting in a higher breakdown voltage. Besides, as shown in Figure 2-34 [60], a higher electric field in the middle of the oil gap also results in larger streamer channel tip curvature in a needle-sphere geometry than in needle-needle geometry under the same voltage level.

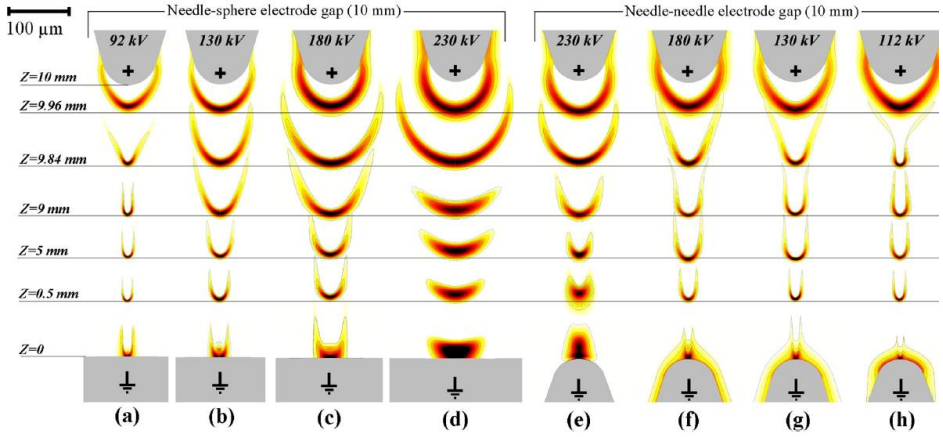

Figure 2-34 Streamer breakdown dynamics at different positions in the needle-sphere and needle-needle geometry with a tip radius of 40 μm and a gap distance of 10 mm, and voltage rise time of 100 ns [60].

(2) Multiple streamer channels

Concerning the reason for the formation of streamer channels, it is argued that finite perturbation in the dielectric liquids is required for the initiation of streamer branching [212-214]. Finite perturbation is generally regarded as inhomogeneity and can be catalogued from both macroscopic and microscopic views.

From a macroscopic view, inhomogeneity may come from bubbles and solid particles such as dirt, water droplets or other large particles [9, 40, 58, 213-218].

From a microscopic view, the initial condition in dielectric liquids before streamer initiation, such as previous discharge under AC voltage [214], and intrinsic noise are the main contributors of streamer branching. The intrinsic noise includes (1) local different ionization density due to radiation sources, such as cosmic rays and other sources of ionizing radiation [9, 214], (2) variations of dielectric densities or molecule alignment [9, 219] and (3) stochastic motion of molecules [220].

In streamer branching simulations in dielectric liquids or high-pressure gases, the effects of inhomogeneity are simulated using different charge generation rates and/or dielectric constant inside the inhomogeneity compared with surrounding media [58, 155, 213]. Accordingly, perturbation of charge density near the inhomogeneity can finally either direct streamer branch propagation [58, 213] or stochastically cause streamer branching by breaking the symmetry of the streamer channel [155]. However, the charge generation rates considered inside inhomogeneity are based on different mechanisms due to different surrounding media and assumptions. Detailed information is presented in Table 2-11. It should be noted that since the inhomogeneity positions are stochastically selected and put inside the media, the continuous model thus has stochastic properties when studying streamer branching.

Table 2-11 Information on streamer branching simulations in different dielectric media

Inhomogeneity type	Surrounding media	Charge generation mechanism inside inhomogeneity	Reference
Micro bubbles with 40 μm radius	Humid-air	Photoionization	[213]
Micro bubbles with 0.5 μm radius	Deionized water	Impact ionization	[58]
Micro weak areas with 5 μm radius with additional charge generation rate	Mineral oil	Molecular ionization with additional background ionization	[155]

The effects of voltage magnitude on streamer branching in mineral oil are studied in [9, 155] in a needle-sphere geometry with a needle tip radius of 40 μm and gap distance of 25 mm in a 3D model. The number density of micro weak areas is assumed to be $10^{11}\ \mathrm{m}^{-3}$ in the oil bulk. For simplification, 12 micro weak areas, also called inhomogeneity, with radius of 5 μm are placed randomly in the vicinity of the needle tip [9]. The charge generation rates inside the inhomogeneity are added using constant values ranging from 0 to $10^{10}\ \mathrm{Cm}^{-3}\mathrm{s}^{-1}$, which is around one order of magnitude

smaller than the charge generation rate of a positive streamer tip [9]. The variation of streamer branching channels on the increasing voltage magnitudes and rise time are shown in Figure 2-35 [155]. It is found that when the applied voltage is low, as in Figure 2-35 (a), no branching occurs but the symmetry of the streamer branch is broken due to charges caused by inhomogeneity. Comparing Figure 2-35 (b), (d), (i), (f) and (m), when the applied voltage increases from 6 V_i to 18.3 V_i under a voltage rise time of 100 ns, the streamer branching numbers also increase accordingly. Besides, when comparing Figure 2-35 (b) and (c), (d) and (e) and (j) and (k), it is found that when the applied voltage is similar, decreasing voltage rise rates will also increase streamer branching numbers.

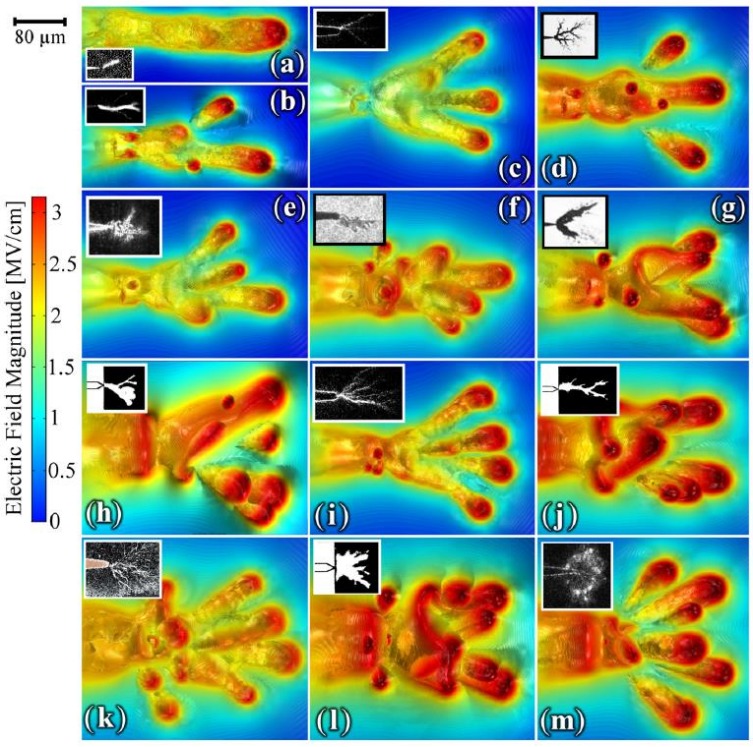

Figure 2-35 Iso-surface plot of electric field distribution compared with corresponding experimental image in the inset image. The simulation conditions for voltage magnitude and rise time are (a) 2.85 V_i, 1 ns. (b) 6 V_i, 100 ns. (c) 7.66 V_i, 10 ns. (d) 8.66 V_i, 100 ns. (e) 9 V_i, 10 ns. (f) 10.66 V_i, 100 ns. (g) 11.33 V_i, 10 ns. (h) 12.6 V_i, 10 ns. (i) 10 V_i, 100 ns. (j) 15.2 V_i, 10 ns. (k) 15.83 V_i, 1 ns. (l) 16.1 V_i, 10 ns. (m) 18.3 V_i, 100 ns. V_i equals 30 kV in these simulation cases. Experimental conditions are not identical to the simulation conditions but are reasonably similar [155].

In order to investigate the deterministic reason for streamer branching and the possible branching number, a streamer head model with certain important characteristics was proposed in [9, 155], as shown in Figure 2-36 [9, 155]. The core-shape streamer head

is represented by space charge density ranging from $0.5|c_{max}|$ (brightest colour) to $|c_{\max}|$ (darkest colour) with r_a, r_b and d defined as in Figure 2-36 [9, 155]. The relationship between streamer shape (r_a, r_b and d) and the number of streamer branches is shown in Figure 2-37 [9, 155]. These values are the average values based on 10 different inhomogeneity positions. From Figure 2-37, the separation lines between single column, two/three-column and multi-column streamers roughly show the critical streamer head ratio. Larger r_a/d, which means larger r_a or smaller d, generally indicates more streamer branches since shells with thinner thickness and larger diameter are easily broken by new heads [9, 155]. Therefore, the streamer head curvature ratio r_a/d approximately determines the occurrence of branching and the number of just born branches [9]. However, this ratio depends closely on the inhomogeneity density and charge generation rate inside the inhomogeneity. No further discussion on the exact ratio values is presented.

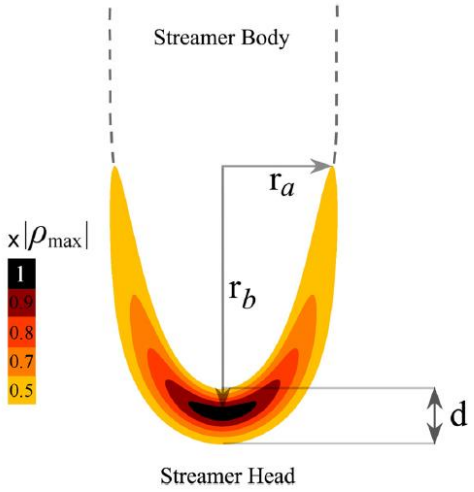

Figure 2-36 Streamer head model based on the distribution of space charge density. r_a is defined as the radius of the space charge core from central to the boundary of $0.5|c_{max}|$. r_b is defined as the length from $|c_{max}|$ to the boundary of $0.5|c_{max}|$ in axial direction. d is defined as the thickness of the streamer tip between the boundaries of $0.5|c_{max}|$ [9, 155].

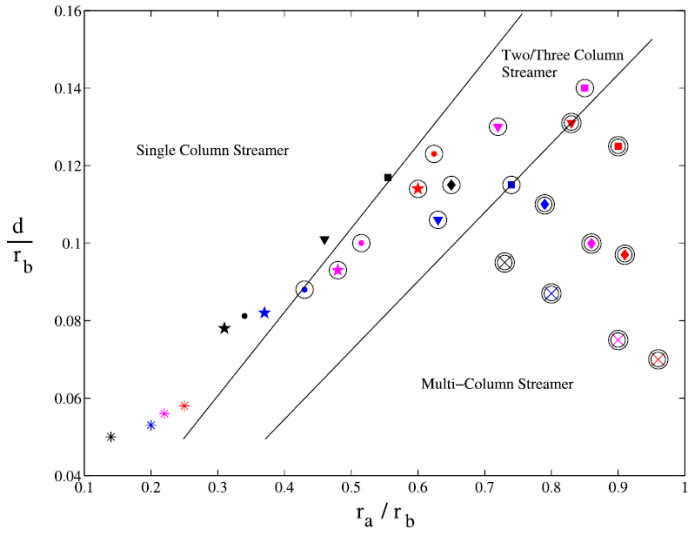

Figure 2-37 The distribution of streamer branches number based on the streamer head model in Figure 2-36. The colours represent different voltage rise times: black (1 μs), blue (100 ns), purple (10 ns) and red (1 ns). The marker shapes mean different applied voltage peaks: * (130 kV), ⋆ (200 kV), ● (250 kV), ▾ (300 kV), ■ (350 kV), ♦ (400 kV) and × (500 kV). No circle, one circle and two circles on the marker shapes represent single column, two/three column and multi-column streamers, respectively [9, 155].

However, it should be noted that the effects of voltage magnitude on streamer channel branching number in simulations [9, 155] is not always similar to those in experiments [40, 221], especially when the applied voltage is over the acceleration voltage. With the increase of applied voltage in experiments, the streamer mode generally varies from 1st mode to 4th mode, with branch number and area first increasing from 1st to 2nd mode, then decreasing at the beginning of the 3rd mode streamer and finally increasing again from 3rd to 4th mode. However, in simulations, the branching number shows a directly increasing trend with applied voltage, as shown in Figure 2-35.

The reason for streamer branching has been discussed in detail in [9, 155], which is based on local inhomogeneities. Besides, due to the differences between positive and negative streamers, the polarity effect on streamer branching is also interesting to study. The effects of voltage polarity on streamer branching are shown in Figure 2-38 [58], which was simulated based on three microbubbles with a radius equal to 0.5 μm in deionized water. Three bubbles are placed randomly in the deionized water for both positive and negative polarities. The first bubble on the left side is used to initiate the streamer by using field emission. For the positive streamer in Figure 2-38 (a), the positive ion density is higher in the micro bubbles than other positions due to the higher impact ionization charge generation rate inside the bubbles than the molecular

ionization charge generation rate in deionized water. When the initial streamer channel reaches another two bubbles, two new filamentary streamer branches are triggered due to the re-distribution and re-adjustment of the electric field by the two bubbles. For the negative streamer in Figure 2-38 (b), a single broad distribution of negative ions occurs with a much wider and bushier streamer channel than the positive one. No internal branching into two or three streamers is evident, which may be due to the fast mobility of electrons that results in a single, overall smeared distribution [58].

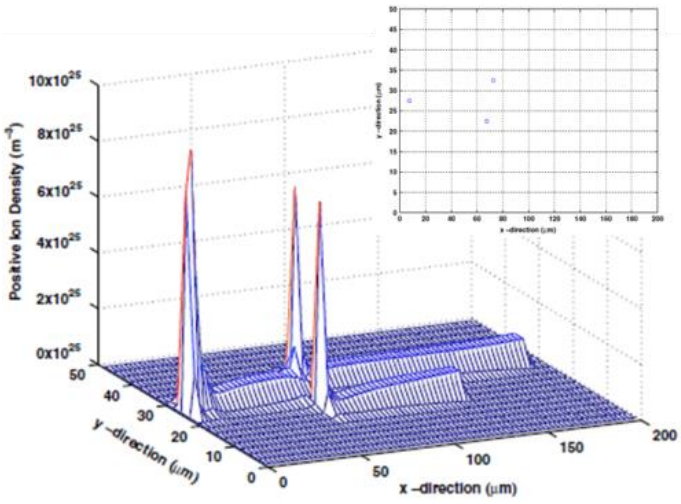

(a)

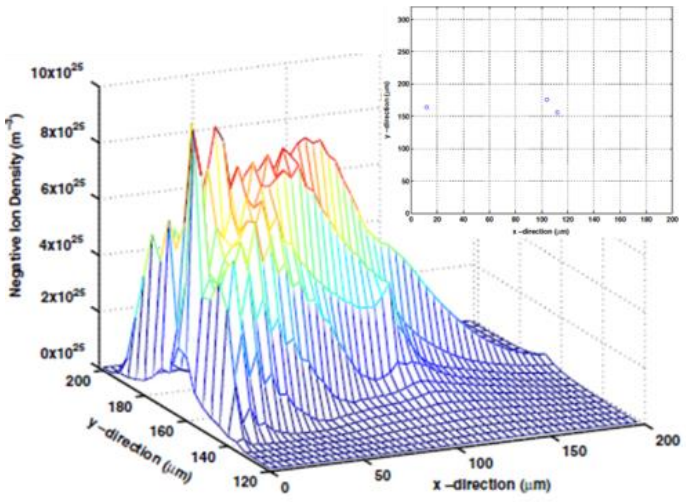

(b)

Figure 2-38 Effects of voltage polarity on streamer branching characteristics in a needle-plane geometry with a gap distance of 200 μm. $x = 0$ represent the position of the needle tip while $x = 200$ μm means the ground potential. (a) Distribution of positive ion density at 63.26 ns. (b) Distribution of negative ion density at 192.00 ns. The initial microbubble positions are shown as blue circles at the right top corner of (a) and (b). Note that the blue circles represent bubbles and are not drawn to scale [58].

2.4.4.4 Cavity formation

Although the streamer process under a fast voltage rise time (several nanoseconds) [9] or DC voltage [10, 11] has been simulated in mineral oil, no cavity formation process has been considered, which may be an over-simplification when compared with experimental phenomena. Due to lack of knowledge on cavity formation in mineral oil and cyclohexane, only the simulation results for the cavity formation process in deionized water discharge are introduced here.

The simulation of deionized water discharge under impulse voltage has been simulated in [113-116]. The applied voltage waveform in experiments is shown in Figure 2-39 [114], which includes a relatively linear rise time, a flat period and a relatively linear tail time. The voltage waveform used in the simulation is more ideal.

The pressure distribution of electrostrictive force pressure p_{EF}, thermodynamic pressure p and total pressure p_{total} along the axis of symmetry from the needle tip to oil bulk at $t = t_0 = 3$ ns (t_0 is the voltage rise time) is shown in Figure 2-40 (a) [115]. The distribution of liquid velocity $\overrightarrow{v_l}$ is shown in Figure 2-41 (a) [115]. Under the effect of electrostrictive force, liquid is pushed towards the needle tip. As a result, the thermodynamic pressure (line 2) in the vicinity of the needle tip is larger than atmospheric pressure, meaning that the liquid density is higher than ρ_{l_0}. The total pressure, shown in line 3, is negative. When the negative total pressure reaches a preset threshold, a cavity is able to form. In Figure 2-40 (b), due to a longer voltage rise time $t = t_0 = 100$ ns, the liquid has sufficient time to move towards the needle tip with higher velocity, as shown in Figure 2-41 (b), which increases the thermodynamic pressure locally. Therefore, the magnitude of total pressure in Figure 2-40 (b) is not as high as that in Figure 2-40 (a).

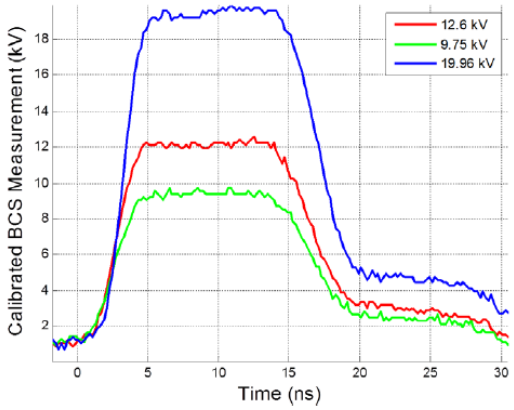

Figure 2-39 Voltage waveform of pulsed voltage used in the experimental study of the cavity process [114].

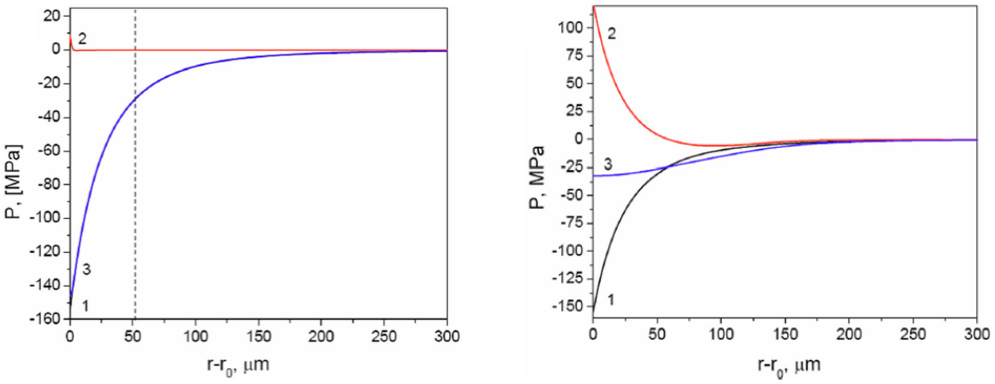

(a) (b)

Figure 2-40 The pressure dependence on the distance from the needle tip into the oil bulk at (a) $t = t_0 = 3$ ns and (b) $t = t_0 = 100$ ns, where t_0 is the voltage rise time. Line 1: electrostrictive force pressure, Line 2: thermodynamic pressure, and Line 3: total pressure [115].

The total pressure distribution p_{total} at different time moments along the axis of symmetry under different voltage rise times is shown in Figure 2-42 [113]. It is shown that during the voltage rise period, the total pressure gradually decreases because of the increase in electric field magnitude at the needle tip. Concerning Figure 2-42 (a) and (b) when $t_0 = 1$ ns and 5 ns, p_{total} is well below -30 MPa, the threshold set for cavity formation in deionized water. Areas with pressure lower than -30 MPa means the cavity formation areas where a rupture of continuity of fluids occurs due to the tensile force caused by electrostrictive force. Cavities mainly form in the vicinity of the needle tip during the voltage rise period. In comparison, in Figure 2-42 (c) with slower t_0, p_{total} is always above -30 MPa. This means that if the voltage rise time t_0 is slow enough, the flow of liquid has time to reduce the total pressure to such an extent that cavity rupture cannot form in the liquid during voltage rise time.

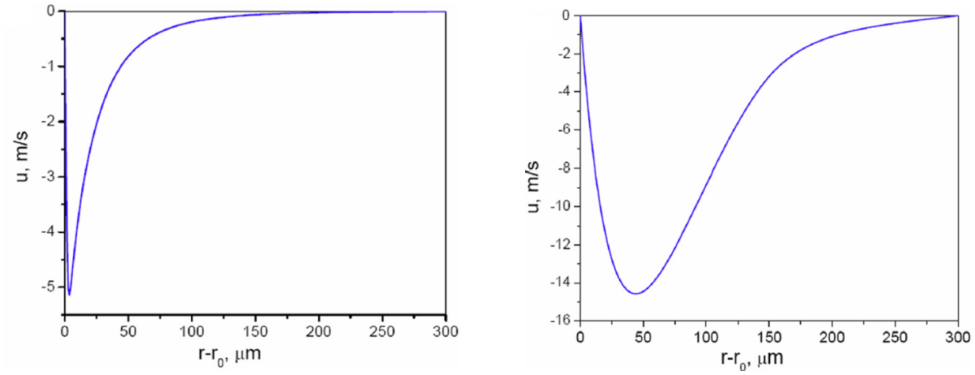

(a) (b)

Figure 2-41 The liquid velocity on the distance from the needle tip into the oil bulk at (a) $t = t_0 = 3$ ns and (b) $t = t_0 = 100$ ns, where t_0 is the voltage rise time [115].

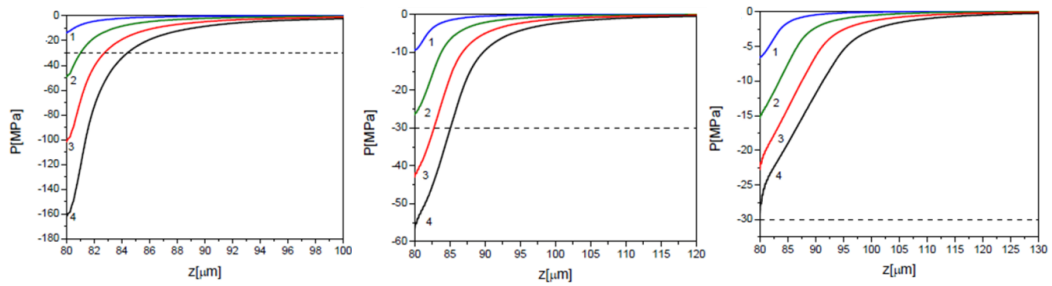

(a) (b) (c)

Figure 2-42 Longitudinal distribution of total pressure p_{total}. Voltage rise time (a) $t_0 = 1$ ns, (b) $t_0 = 5$ ns, (c) $t_0 = 10$ ns. Line 1 to line 4 represents the time moment at $t/t_0 = 0.25, 0.5, 0.75$, and 1, respectively [113].

Concerning the liquid thermodynamic pressure during the tail time, the distribution of thermodynamic pressure along the axis of symmetry at different times is shown in Figure 2-43 [113]. Before $t = 0$ ns, the voltage has already been applied to the deionized water for a while so that the liquid has reached a stable condition where the thermodynamic pressure equals the electrostrictive force pressure. At $t = 0$ ns in Figure 2-43, the applied voltage is removed. Due to lack of an electric field, the electrostrictive force pressure is also removed so that the liquid is only under a thermodynamic pressure force. Due to the stress before $t = 0$ ns, the liquid is pushed towards the needle tip, leading to a higher liquid density than ρ_0 and larger positive pressure than 0.1 MPa. After the voltage is removed, higher pressure in the vicinity of the needle tip pushes the liquid outwards, forming a pressure wave propagating from the needle tip into the liquid bulk, as shown from 0.5 ns to 5 ns in Figure 2-43. The magnitude of thermodynamic pressure decreases since the initial higher liquid density is compensated by the movement of the liquid.

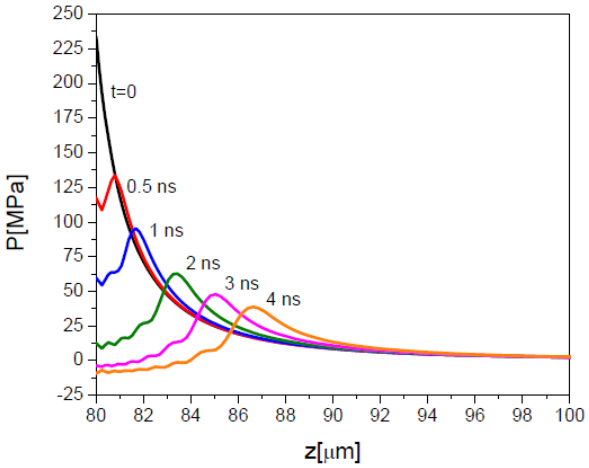

Figure 2-43 Distribution of thermodynamic pressure along the axis of symmetry at different times after voltage interruption [113].

2.4.4.5 Low-density channel formation

According to [13, 34], the streamer channel will begin to switch from liquid phase to low-density phase when the temperature reaches the vaporisation threshold. Therefore, the variables mentioned above in the liquid phase will change during the transition between phases.

The phase diagram for cyclohexane shows that at atmospheric pressure (~0.1 MPa), cyclohexane will turn into the low-density phase when the temperature is over approximately 353 K, while at 4 MPa (critical pressure), the temperature for vaporisation is around 554 K [109, 138, 222, 223]. For mineral oil, it is estimated that it will begin to vaporise if the local oil temperature is over 498 K [7]. However, additional energy is also required for the latent heat from the liquid phase to low-density phase [7].

The threshold for phase transition from liquid phase to low-density phase in simulations is generally based on the local dissipation energy density W for simplification, as calculated in Equation 2-35.

$$W = \int_0^t \emptyset_d dt \qquad \text{Equation 2-35}$$

The simplified form of the thermal diffusion equation is shown in Equation 2-36, which uses the energy density threshold W_0 for liquid vaporisation shown in Table 2-12. The latent heat of cyclohexane is found to be 2.59×10^8 $\mathrm{Jm^{-3}}$ [224-226].

$$\rho_l c_v \Delta T = \mathrm{W} = \int \emptyset_d \, dt \qquad \text{Equation 2-36}$$

Table 2-12 Summary of threshold W_0 for dielectric liquid vaporisation.

Source	W_0 ($\mathrm{Jm^{-3}}$)	ΔT (K)	Dielectrics	Reference
Calculations based on experiments	4×10^8	200+latent heat	Mineral oil	[7, 162]
	5.3×10^7	~55	Cyclohexane	[109, 138, 223, 227]
	8×10^7	55	Cyclohexane	[224-226]
Simulations	6×10^7	45	Mineral oil	[7, 162]
	1×10^8	75	Cyclohexane	[11]

It is generally assumed that if W is over the threshold W_0, the values of variables such as charge mobility, permittivity, charge generation rate and recombination rate will be switched from the liquid phase to the low-density phase. The variation in parameter values is generally calculated according to the variation in molecular number density in the phase, as shown in Table 2-13 [11]. It should be noted that in the low-density phase, all authors agree that impact ionization dominates the streamer process [7, 11, 162].

Table 2-13 Charge mobility and relative permittivity values in the low-density phase [11].

Variables	Relationship between parameter values and phase molecular number density
Ion/Electron mobility	$\mu_{\pm e\_g} = \frac{N_l}{N_k}\mu_{\pm e\_l}$
Relative permittivity	$\varepsilon_{r\_g} = 1 + (\varepsilon_{r\_l} - 1)\frac{N_k}{N_l}$
Impact ionization coefficient	$A_g N_k \phi(N_k)\exp(-\frac{B_g N_k \phi(N_k)}{\lvert\vec{E}\rvert})$

Where $\mu_{\pm e\_g}$, $\mu_{\pm e\_l}$, ε_{r_g}, ε_{r_l} are the mobility of positive ions, negative ions and electrons and permittivity of low-density phase and liquid phase, respectively, N_l is the molecular number density of liquids (typically 5.6×10^{27} m^{-3} for cyclohexane [11]), N_k is the molecular number density in the low-density phase and ranges from N_l to N_g, N_g is the molecular number density of the corresponding gas which is related to ambient pressure p (typically 2.5×10^{25} m^{-3} [11] at atmospheric pressure). For simplification, the mobility of charge carriers is also assumed to be 100 times larger in the low-density phase than the liquid phase under atmospheric pressure [7]. $A_g N_k \phi(N_k)$ and $B_g N_k \phi(N_k)$ are the impact ionization coefficients in gas at different N_k, whilst $\phi(N_k)$ is an interpolation formula as in Equation 2-37.

$$\phi(N_k) = \xi[1 + (N_k/N_{int})^3]/[\xi + (N_k/N_{int})^3] \quad \text{Equation 2-37}$$

Where ξ is a coefficient related with N_g and N_l and is assumed to be 0.27 [11] for cyclohexane, N_{int} is an interpolation number between N_g and N_l and is taken as 10^{27} m^{-3} [11].

Although the charge generation mechanism is considered to be impact ionization in the low-density phase, the charge recombination mechanism is different in simulations conducted by different groups [7, 11]. The charge recombination mechanism is considered be zero in [7] due to consideration of the very low relative concentrations of free species in the low-density region [58]. In comparison, the effects of two-body and three-body recombination with varying molecular number density N_k [228, 229] are considered in [11]. Table 2-14 summarises the charge recombination rates variation from the liquid phase to the low-density phase in [7, 11, 162]. All results show a smaller R_{+e} in the low-density phase than in the liquid phase due to the higher charge kinetic energy. However, the values used by different authors still are significantly different and similar to those used in the liquid phase.

Table 2-14 Summary of the recombination rates in liquid and the low-density phase used by different groups.

Reference	[7, 162]		[11]
Dielectrics	Mineral oil		Cyclohexane
Phase	Liquid	Low-density	Liquid to low-density
$\boldsymbol{R_{+e\_D}}$ **(m^{3}s^{-1})**	1.64×10^{-17}	0	$1.08 \times 10^{-13} \sim 1.08 \times 10^{-11}$
$\boldsymbol{R_2 + R_3 N_k}$ **(m^{3}s^{-1})**	---	---	$2.24 \times 10^{-11} \sim 1.00 \times 10^{-13}$
$\boldsymbol{R_{+e}}$ **(m^{3}s^{-1})**	1.64×10^{-17}	0	$1.07 \times 10^{-13} \sim 0.99 \times 10^{-13}$

In order to achieve varying parameter values between the liquid phase and low-density phase mentioned above, two methods have been used.

The first method is a direct transition based on Heaviside function switching from 0 to 1 [7, 162]. The phase state directly changes between the liquid and low-density phase when energy density reaches the threshold and no intermediate state exists. This means the interface between two phases is represented by a surface of zero thickness. Therefore, physical quantities, such as mobility and permittivity, are discontinuous across the interface.

The second method represents a smooth transition phase based on the gradual decrease in molecular number density from N_l to N_g when the streamer channel expands due to Joule heating [11]. The ambient pressure-dependent N_g is calculated as in Equation 2-38.

$$N_g = \frac{p}{p_0} N_{g\_0} \qquad \text{Equation 2-38}$$

Where p_0 is the atmospheric pressure and equals 0.1 MPa, N_{g_0} is the number density of gas molecules under atmospheric pressure.

Considering the "phase field model" concept initially proposed in [230] to generally study the physics on the interface between two or three liquids, the second method that can well describe the smooth transition phase is more appropriate than the direction transition.

In order to study the streamer dynamics under consideration of the low-density channel formation by a simpler model, a so-called 1.5D model was proposed in [11, 231-234] with some pre-set variables that constrained streamer shapes according to experiments. For example, in [11], the streamer channel radius was set as 2 μm and the radially expanding velocity of the low-density channel was assumed to be 300 m/s according to experiments [34] when energy density reached the liquid vaporisation threshold. The streamer channel tip was also assumed as a hyperbolic shape [11], which was similar

to the discrete model when calculating the local electric field at the needle tip [10, 87]. The electric field dynamics under consideration of the low-density channel formation is shown in Figure 2-44 (a) [11]. The variable variation is calculated based on the smooth transition phase.

It is found that the average electric field inside the low-density phase is $5\sim6\times10^6$ V/m, which is much smaller than that without consideration of the low-density channel as shown in Figure 2-44 (b), and is closer to the value calculated by the applied voltage over streamer stopping length from experimental results [13]. This lower voltage drop inside the streamer channel allows the streamer to propagate at a relatively constant speed ~2 km/s when compared with Figure 2-44 (b) in which the streamer only propagates at an average velocity of ~0.6 km/s from 3 ns to 11 ns and will stop quickly. A clear transition phase can also be found and is shown in Figure 2-44 (a).

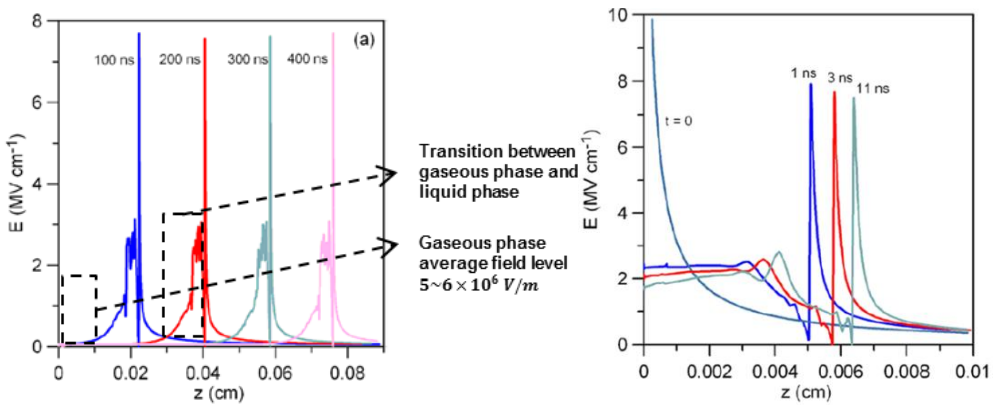

(a) (b)

Figure 2-44 The distribution of electric field (a) with and (b) without gaseous phase consideration under positive 30 kV DC voltage with a needle tip radius of 2 µm and a gap distance of 3 mm and in a needle-plane geometry [11].

The effects of ambient pressure on streamer length are also studied in [11], and shown in Figure 2-45 [11]. Similar to experiments [13], increasing ambient pressure will decrease streamer stopping length. When the ambient pressure is as high as 22 MPa, no low-density channel is formed in the simulation. However, the vaporisation threshold in the simulation remains constant under different ambient pressure in [11], which contradicts the findings in [109, 138, 222].

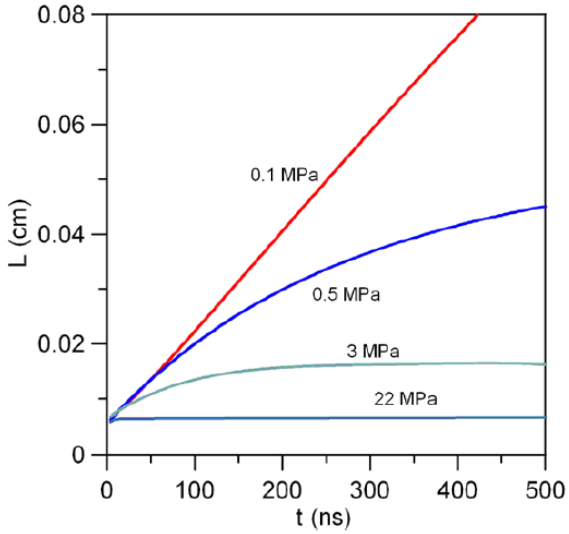

Figure 2-45 Effects of ambient pressure on streamer stopping length [11].

It should be noted that although the above-mentioned results on the low-density channel formation show similar results to experiments, the gaseous nature of streamers was only considered in [7, 11, 162]. The reason for this gap in the gaseous nature of streamer in other studies may be the complex physics involved and poor convergence between calculating partial differential equations that suddenly change and limited calculating resources. Besides, the effect of low-density phase expansion on liquid movement, thus causing shockwave during streamer propagation, is another difficult phenomenon to simulate.

[11] simplified the model by changing it into 1.5D with a relatively fixed streamer channel diameter that can lower the required calculating resources and speed up calculation. Channel expansion is also simplified by assuming constant channel radial expansion velocity. However, the limitation is that streamer dynamics will be then strictly constrained by the pre-set parameters and may not fully reflect its dynamics during streamer initiation and propagation under different conditions such as different voltage magnitudes and rise times. For example, since it was found that shorter voltage rise time may lead to a visibly larger diameter in gaseous media in experiments [205, 235] and in dielectric liquids in simulations [61], it is hard to estimate the ultimate gaseous channel diameter and its time variation under different voltage rise times.

2.5 Summary

This chapter has provided a detailed review and summary of streamer simulation literature.

Firstly, the streamer simulation models used during previous years can be catalogued as the discrete model and the continuous model. According to the physics involved, the continuous model is based on mechanisms from both microscopic and macroscopic views, including space charge densities and electric field distribution, charge generation and recombination mechanism. These mechanisms can also be studied in space and time, which affect streamer patterns. In comparison, the discrete model is mainly based on electric field distribution from a macroscopic view, which will affect the probability at the tip of the streamer channel where the streamer channel arises. Although charge generation has been considered and added in later discrete model modifications [87], it is mainly taken as a condition for streamer initiation and propagation, and is simplified during calculation. The benefit of the discrete model is that it is easier to show the stochastic properties of streamer dynamics (branching) with certain assumptions. However, it is hard for the discrete model to provide as detailed a picture of streamer properties from a microscopic view as the continuous model does.

Concerning the drawbacks of the continuous model, in most cases, it can only show a single-column streamer channel due to a lack of stochastic factors which increase the difficulty in solving highly non-linear controlling equations. In terms of computational resources, compared to the discrete model, although the continuous model generally requires more computing resources, it can also reflect more detailed physical phenomena in simulation results. Therefore, the continuous model is chosen for use in this current research project.

Secondly, although researchers have tried to explain the reason for the formation of 2^{nd}, 3^{rd} and 4^{th} mode streamers [8], the reproduced results from [8] in Figure 2-30 show that the instant streamer velocity is not in the 2^{nd} mode. This indicates that current mathematical model cannot correctly reflect the propagation characteristics of 2^{nd} mode streamer. Therefore, a new mechanism needs to be considered to explain the stable velocity of 2^{nd} mode streamers.

Thirdly, due to a lack of previous research, the cavity formation process in cyclohexane needs to be considered during the streamer initiation process. Besides, electronic and liquid dynamics during the streamer initiation process should also be studied.

Finally, due to the difficulty of solving highly non-linear partial differential equations, low-density channel of streamer is rarely simulated in most studies based on charge-drift model. However, due to the gaseous nature of streamer channel, the streamer propagation process with consideration of the low-density channel formation is also worthy of simulating in order to include more physics in the continuous model and better understand streamer dynamics.

3 Modelling of 2nd Mode Positive Streamers in Cyclohexane by Considering Electron Saturation Velocity

3.1 Introduction

Streamer velocity is the determining parameter used to describe different modes of streamer propagation. For most studied 2nd mode streamers, the relatively stable velocity over a wide range of voltage magnitude is recognised as one of the key characteristics. It is generally agreed that the mechanism dominating streamer velocity must remain in the liquid phase rather than in the low-density phase of the streamer [4]. Previously, the shielding effects of streamer branches and the voltage drop inside the streamer channel are assumed to be the main reasons for the 2nd mode streamer's stable velocity [63, 67]. However, a recent study [59] suggested that increasing pressure during streamer propagation, which decreased streamer branching extent, had little effect on the streamer acceleration voltage V_a. This result indicates that the branching extent increases from a macroscopic perspective may not be the underlying mechanism for the stable velocity of a 2nd mode streamer. Therefore, a new mechanism may be needed to explain this phenomenon.

Currently, the streamer simulation models in the literature [8, 11, 58, 60, 61, 236] consider the movement of different kinds of charge carriers that are driven by the electric field, which is based on the ion-drift model [105]. In simulations, streamer velocity is calculated to be the velocity of the moving electric field peak. The effects of voltage excitation and electrode geometry on the characteristics of 2nd mode streamers in mineral oil were simulated by assuming that molecular ionization dominated the streamer process [60, 61]. However, Figure 2-30, which is derived according to [60, 61], shows that under a voltage level of 130 kV ($< V_a$) and gap distance of 25 mm, although the average streamer velocity is in the range of a 2nd mode streamer, instant streamer velocities show an increasing trend, indicating that the streamer may go beyond the 2nd mode after further propagation. Concerning the five remaining cases in Figure 2-30 [60, 61], even the average streamer velocities are higher than that for the 2nd mode Therefore, improvement of the charge-drift model is necessary to solve this problem.

In this study, electron saturation velocity (ESV) is included to explain and simulate the stable velocity of the 2nd mode positive streamer. The effect of ESV was considered in [236]. However, the mobility of electrons under a low electric field was 41 times larger than the electron mobility mentioned in [11, 142], which led to an unreasonably abrupt velocity increase during streamer propagation [236].

In this chapter, a streamer in cyclohexane is simulated using the charge-drift model and the same needle-plane geometry specified in the experiment by [1]. A detailed explanation on the factors affecting positive streamer velocity is initially presented in Section 3.2. Secondly, the simulation methodology is introduced in Section 3.3. Next, streamer propagation dynamics in the simulation, such as electric field distribution and streamer head radius, are explained in detail in Section 3.4. Then, a sensitivity study on the effects of different ESVs on streamer properties, such as propagation velocity and channel radius, is carried out in Section 3.5. Next, streamer velocities under a wide range of voltage magnitudes are modelled and compared to the experimental results in [1] in Section 3.6, followed by a detailed discussion on using ESV to explain the stable velocity of 2nd mode positive streamer in Section 3.7. Finally, a conclusion of this chapter is presented in Section 3.8.

3.2 Factors Affecting Positive Streamer Propagation Velocity

A positive streamer is accepted to be composed of a low-density phase and liquid phase according to [13, 34] but the factors affecting streamer velocity are believed to mainly occur in the liquid phase [4]. A schematic diagram of streamer propagation is presented in Figure 3-1. The positive needle tip is shown on the left side. A streamer is composed of a low-density phase (light blue area) and liquid phase (sky blue area), with the dark blue area representing the dielectric liquid at the streamer tip where the local electric field is the highest and where ionization occurs.

During streamer propagation, molecular ionization happens at the streamer tip, generating both positive ions and electrons. Under positive polarity, electrons are pulled towards the positive needle at a much faster velocity than positive ions that are being pushed in the opposite direction due to their charge mobility and polarity differences. Some electrons are also attached to the neutral molecules to form negative ions during the movement. The separation of positive and negative charges for a positive streamer leaves a positive space charge cluster at the streamer tip, which further enhances the electric field and pushes the electric field peak to move forward. Therefore, the electric

field peak movement in a simulation represents the propagation of the streamer tip. The movement of charges, mainly highly mobile electrons, can generate Joule heating, which contributes to the local liquid temperature rise caused by heat accumulation. Therefore, the streamer channel close to the ionizing tip is still the liquid phase, with the other parts gradually transforming to the low-density phase after heat accumulation. Here, the term "low-density phase" is adopted since during its expansion, the pressure inside low-density channel is reducing, which means the molecular number density is decreasing.

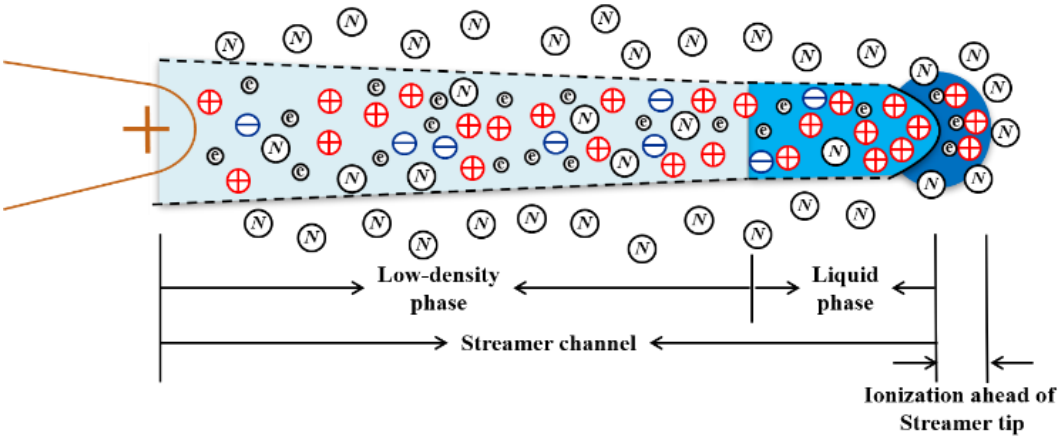

Figure 3-1 Schematic diagram of a streamer during propagation.

From the description above, it can be concluded that streamer velocity is determined by how fast the electric field at the streamer tip moves forward. From a microscopic perspective, the movement velocity of the electric field peak during streamer propagation is mainly dominated by the positive space charge peak behind it. When the positive space charge peak forms more quickly, the electric field peak can be enhanced faster and correspondingly move farther, meaning that the streamer velocity is faster. Considering the formation process of the positive space charge peak, two parameters should be taken into consideration, namely electron velocity $v_e = \mu_e E$ and electron attachment time τ_a.

Electrons with smaller v_e cannot leave the ionizing zone fast enough to form the positive space charge peak. Besides, smaller τ_a represents an easier attachment to neutral molecules to form negative ions. The velocity of generated negative ions is slower than electrons, which further slows down the formation of the positive space charge peak. Therefore, both smaller v_e and τ_a can constrain positive streamer velocity. Due to 2nd mode streamers existing over a wide range of applied voltage magnitudes,

the highly electric-field-dependent nature of electron velocity is assumed to be the key reason for the 2nd mode positive streamer's stable velocity.

Under a low to moderate electric field, μ_e is calculated to be $\mu_{e\_0} = 1 \times 10^{-4}$ $\mathrm{m^2V^{-1}s^{-1}}$ [146, 147] and electron velocity v_e equals $\mu_{e\_0}E$, where E is the local electric field and μ_{e_0} is electron mobility under a zero electric field. The previous charge-drift model [8, 11, 58] assumed constant electron mobility under an electric field ranging from zero to several MV/cm, as shown in the black line (labelled 'No ESV') in Figure 3-2. However, electron velocity may reach saturation velocity under an extremely high electric field possibly due to the transfer of energy and momentum from electrons to phonons, and the increase of effective electron mass based on the well-known Shockley theory and its follow up studies [150-153].

ESV has been confirmed in different dielectric liquids by [109, 237] and is estimated to be on the order of 10 km/s, which occurs when the electric field is over 1 MV/cm in liquid argon [154]. Although electron velocity, without considering ESV, may reach 30-40 km/s at 3~4 MV/cm in previous simulations [8, 58, 60, 61], it is worth examining whether this is too high for electron velocity in cyclohexane.

Within a wide range of electric field magnitudes, the widely adopted empirical equation describing electron velocity in semiconductors is shown in Equation 3-1 [238]. For simplification, β is set as 1 in this study. Therefore, ESV equals $\mu_{e\_0}E_0$ at extremely high electric field magnitude. The simplified expression form of ESV in Equation 3-1 is the same as that adopted in [236] and shown in Equation 3-2, when $v_1/E_1 = \mu_{e\_0}$. A comparison between ESV calculated by Equation 3-1 and Equation 3-2 [236] is shown in Figure 3-2. It is found that v_e increases linearly when the electric field is a low to moderate electric field and then gradually reaches ESV, which is a similar trend as mentioned in [237]. However, the values of v_1 and E_1 are selected separately in [236], making electron mobility under a low to moderate electric field 41 times larger than the electron mobility mentioned in [11, 142]. Therefore, Equation 3-1 is more representative and hence adopted in this study.

$$v_e = \mu_{e\_0} \frac{E}{\left(1+(E/E_0)^{\beta}\right)^{1/\beta}} \qquad \text{Equation 3-1}$$

$$v_e = v_1 \frac{E}{E_1+E} \qquad \text{Equation 3-2}$$

Where E_0, β, v_1 and E_1 are fitting parameters. $v_1 = 41$ km/s and $E_1 = 0.1$ MV/cm are used in [236].

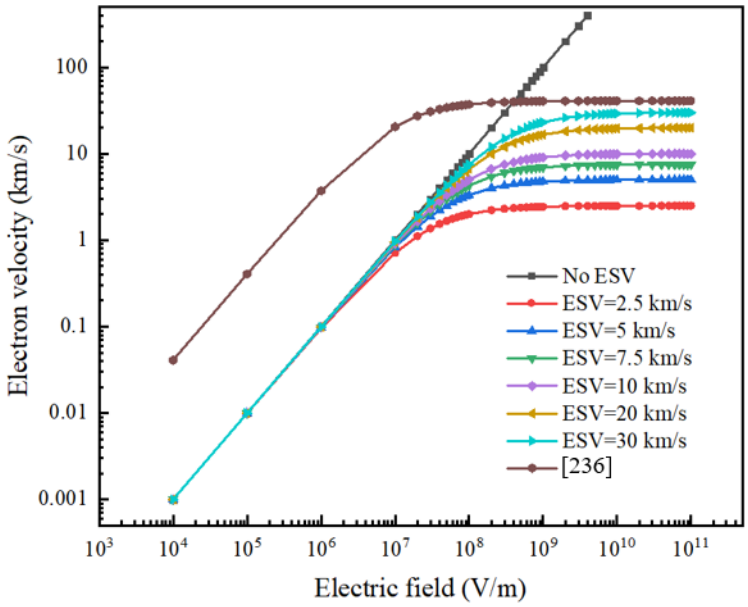

Figure 3-2 Electric-field-dependent electron velocity using simplified equation (6), with the results compared to [236]. Note that ESV ranging from 2.5 km/s to 30 km/s is based on the simplified form of Equation 3-1. ESV is assumed to be 41 km/s in [236].

3.3 Simulation Methodology

According to the literature review in Chapter 2, there are two main methods simulating streamer dynamics that have been developed in the field, namely the discrete model and the continuous models, respectively. The continuous model has been selected for this study since it can reflect more physics processes and hence, better describe streamer dynamics.

3.3.1 Controlling Equations

3.3.1.1 Poisson equation

The Poisson equation [106], as is shown in Equation 3-3, describes the relationship between space charge density and electric field distribution.

$$-\nabla \cdot \left(\varepsilon_0 \varepsilon_r \vec{E}\right) = c_+ + c_- + c_e \qquad \text{Equation 3-3}$$

Where $\vec{E} = -\nabla V$ is the local electric field, V is the local voltage potential, $c_{+,-,e}$ are the charge densities of positive ions, negative ions and electrons, and ε_0 and ε_r are the vacuum permittivity and relative permittivity of dielectric liquids.

3.3.1.2 Charge continuity equation

The charge continuity equations [105] for positive ions, electrons and negative ions express how the distribution of free charges are modified by the drift of the electric field, liquid movement and charge generation and recombination. Since the velocity of liquid movement is much smaller than free charge velocity during the streamer process, the liquid movement effects on charge distribution are neglected in this study. The charge continuity equations simulated in this study are summarised from Equation 3-4 to Equation 3-6.

$$\frac{\partial c_+}{\partial t} + \nabla \cdot c_+ \mu_+ \vec{E} = G_+\left(\left|\vec{E}\right|\right) + \frac{c_+ c_e R_{+e}}{e} + \frac{c_+ c_- R_{\pm}}{e} \qquad \text{Equation 3-4}$$

$$\frac{\partial c_e}{\partial t} + \nabla \cdot -c_e \mu_e(E) \vec{E} = G_e\left(\left|\vec{E}\right|\right) - \frac{c_+ c_e R_{+e}}{e} - \frac{c_e}{\tau_a} \qquad \text{Equation 3-5}$$

$$\frac{\partial c_-}{\partial t} + \nabla \cdot -c_- \mu_- \vec{E} = G_-\left(\left|\vec{E}\right|\right) - \frac{c_+ c_- R_{\pm}}{e} + \frac{c_e}{\tau_a} \qquad \text{Equation 3-6}$$

Where $\mu_{+,-,e}$ are the mobilities for positive ions, negative ions and electrons, $\mu_e(E)$ means electron mobility is highly electric field dependent, $G_+\left(\left|\vec{E}\right|\right)$, $G_e\left(\left|\vec{E}\right|\right)$ and $G_-\left(\left|\vec{E}\right|\right)$ are the charge generation rates for positive ions, electrons and negative ions, respectively.

In this study, molecular ionization is assumed to be the dominating charge generation mechanism for positive streamers in cyclohexane. The calculation of $G_+\left(\left|\vec{E}\right|\right)$ and $G_e\left(\left|\vec{E}\right|\right)$ is shown in Equation 3-7, with $G_-\left(\left|\vec{E}\right|\right)$ equalling zero. However, negative ions can be generated by the attachment of electrons to the neutral molecules.

$$\mathrm{G}_+\left(\left|\vec{E}\right|\right) = -\mathrm{G}_e\left(\left|\vec{E}\right|\right) = \frac{q^2 n_0 a \left|\vec{E}\right|}{h} exp\left(-\frac{\pi^2 m^* a}{q h^2}\left(\frac{\Delta_0}{\sqrt{\left|\vec{E}\right|}} - \gamma\right)^2\right) \qquad \text{Equation 3-7}$$

The meanings and values of the parameters used in Equation 3-3 through Equation 3-7 are shown in Table 3-1. It should be noted that the electric field dependent electron mobility values will be discussed under model modification in the following sections.

Table 3-1 Meanings and values of parameters from Equation 3-3 to Equation 3-7.

Parameter	Meaning	Value	Reference
ε_0	Permittivity of vacuum	8.854×10^{-12} F/m	
ε_r	Relative permittivity of cyclohexane	2	[11, 135, 142]
μ_+, μ_-	Charge mobility of ions	1×10^{-8} $\mathrm{m^2 V^{-1} s^{-1}}$	[11, 142]

μ_e	Charge mobility of electrons	1×10^{-4} $m^2V^{-1}s^{-1}$ (under low electric field)	[11, 142]
R_{+e}	Recombination rate of positive ions and electrons	1.64×10^{-16} m^3s^{-1}	Calculated based on [7, 11, 142]
$R_{\pm}$	Recombination rate of positive and negative ions	1.64×10^{-16} m^3s^{-1}	Calculated based on [7, 11, 142]
τ_a	Electron attachment time	200 ns	[61, 155]
n_0	Density of ionisable molecules	10^{23} m^{-3}	[61, 155]
a	Molecular separation	3.0×10^{-10} m	[61, 155]
h	Planck's constant	6.62608×10^{-34} m^2kgs^{-1}	[180]
q	Electronic charge	1.602×10^{-19} C	[180]
m^*	Effective electron mass	9.1×10^{-32} kg	[61, 155]
Δ_0	Ionization potential of cyclohexane under no electric field	8.5 eV	[9, 168]
γ	Coefficient of electric field dependent ionization potential of cyclohexane	6.9875×10^{-5} $eV \cdot (V/m)^{-1/2}$	[9]

3.3.2 Electrode Geometry, Voltage Excitation and Boundary Conditions

A needle-plane geometry with a needle tip radius of 40 µm and a gap distance of 50 mm has been selected as the simulation geometry, which is the same as those used in experiments [1]. The needle-plane geometry built in COMSOL Multiphysics version 5.4 in a 2D planar view is shown in Figure 3-3. The geometry in COMSOL Multiphysics interface can be built by adding different shapes of geometry, such as rectangular, arc and circle. It should be noted that the boundaries B1, B2 and B3 are the boundaries of calculating domain rather than the testing cell in experiments since a small separation distance will greatly distort the electric field in the vicinity of the needle tip. The plane diameter and separation distance have been tuned large enough to eliminate their effects on the needle tip electric field. The needle tip geometry is built according to Ogura needle shape which is widely used in experiments [239-241]. The details of the effects of needle tip shape on needle tip electric field were discussed in [242].

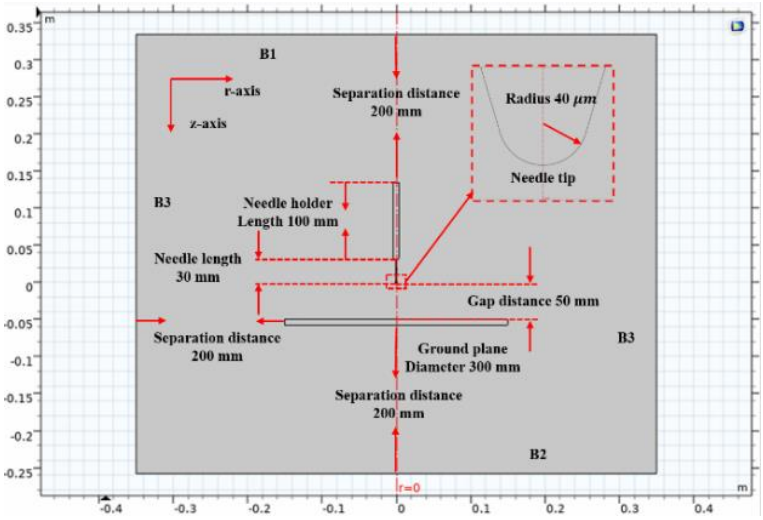

Figure 3-3 Schematic diagram of a needle-plane geometry plotted in COMSOL Multiphysics.

For the voltage application, the boundary condition on the needle electrode is set to a positive high voltage $V = V_0(t)$, while on the ground plane it is set to $V = 0$ V. The applied voltage waveform is step voltage with a fixed voltage rise time. The voltage rise time is selected as 400 ns, as shown in Figure 3-4, which is the same as the voltage rise time used in experiments [1].

For the charge density, the boundary condition on the needle and plane electrode is set as zero diffusion flux, which is $\vec{n} \cdot \nabla c_{\pm e} = 0$, where $\vec{n}$ is the normal vector on the electrodes. On B1, B2 and B3, the boundary condition is set as zero charge flux, which is $\nabla \cdot c_{\pm e} \mu_{\pm e} \vec{E} = 0$.

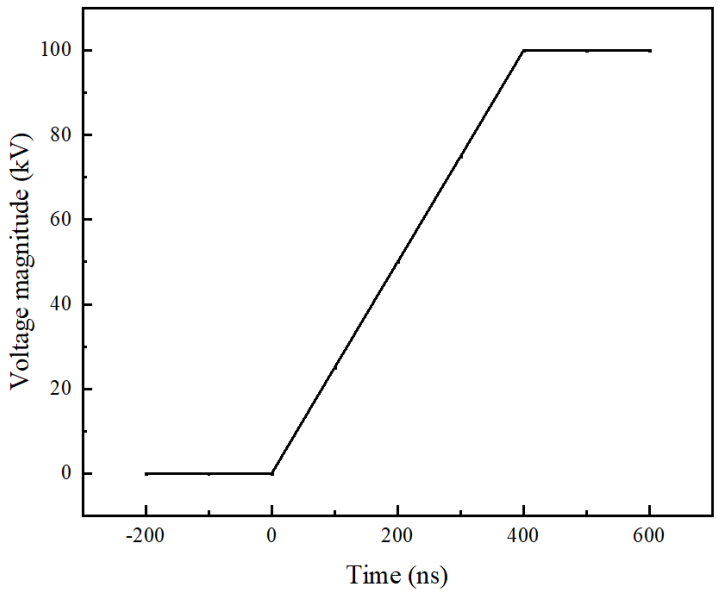

Figure 3-4 Voltage waveform of step voltage at a voltage magnitude of 100 kV and rise time of 400 ns.

3.3.3 Simulation Refinement

3.3.3.1 Refinement methodology

For finite element method, meshing refinement study is a very important process to conduct to increase the accuracy of the calculation and reliability of the conclusion. For the geometry selected with a needle tip radius of 40 μm and a gap distance of 50 mm, the meshing strategy close to the needle tip is of great importance and a challenge, due to the much smaller needle tip, when compared with the large electrode scale. Besides, since a streamer is a dynamic process, the maximum time step size and relative tolerance in COMSOL Multiphysics are another two vital settings to refine for a time-dependent study. A detailed introduction to these settings is presented in Table 3-2 [243].

Table 3-2 Factors affecting simulation accuracy [243].

Factor	Explanation
Meshing size and area	• In order to solve partial differential equations, discretization should be used to divide the simulation domain into small units of simple shapes, which is called "mesh". "Free triangular" size is generally selected since it can mesh all kinds of geometries. • Meshing size is an important factor affecting calculation accuracy. Apparently smaller meshing size leads to more reliable results but may significantly increase calculating time and the required RAM. • Generally, dense meshing size is only needed in an area where intensive variations in variable values occur or in areas where the physical scale of the geometry is small. Typically, in streamer simulations, the area is in the vicinity of the needle tip. A large area with dense meshing will result in high accuracy and also lead to long calculating time and more RAM being needed.
Maximum time step size	• The maximum time step size is the one taken by COMSOL to calculate time-dependent partial differential equations over pre-set time interval. • The real time step size may not always be the maximum pre-set time step size. If the calculated results for each time step do not meet the pre-set relative tolerance, the real time step size taken by COMSOL will be automatically reduced, as shown in Figure 3-5. • A smaller maximum time step size will be more accurate but require a longer calculating time.
Relative tolerance	• For a time-dependent study, relative tolerance is a parameter used to describe the maximum difference between two calculating time instances.

If the time interval is infinitesimal, the relative difference will also be infinitesimal

- Different COMSOL versions set different relative tolerance values by default. The relative tolerance default value is 0.01 before COMSOL v5.3 and is 0.005 after v5.4.
- It is suggested in the COMSOL reference manual that changing the relative tolerance is generally unnecessary unless the simulation does not behave as expected.

Figure 3-5 shows the convergence/time step size plot generated by COMSOL Multiphysics. The initial time step size at time step 0 is set as 10^{-5} ns which is small enough in order to avoid a sudden jump in the variable values during simulation calculation. The maximum time step size and relative tolerance are set as 1 ns and 0.001, respectively. With time increasing, the calculating time step size automatically decreases to fit relative tolerance after the time step is over 160.

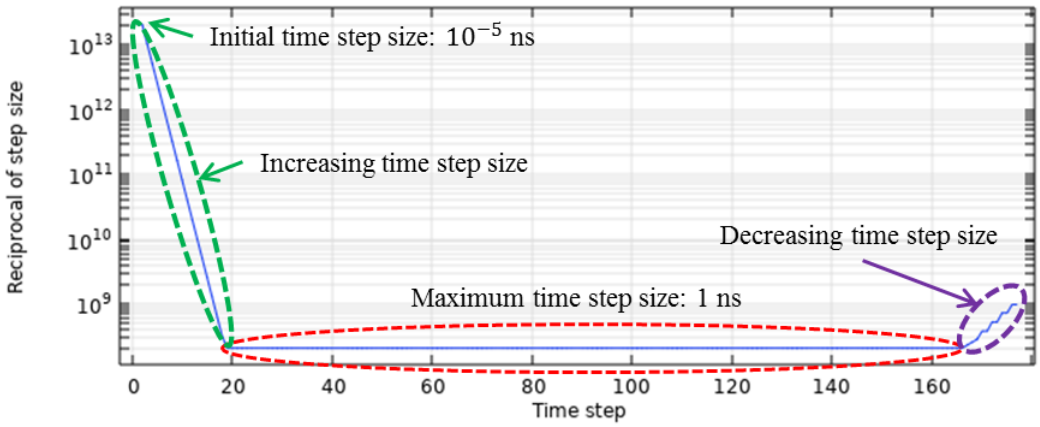

Figure 3-5 Convergence/time step size plot generated by COMSOL Multiphysics. The values in the figure are non-dimension values.

Briefly speaking, smaller meshing size, larger dense meshing area, smaller maximum time step and smaller relative tolerance will all result in a more accurate calculated result. However, these strategies will gradually lead to unaffordable calculating time and computing resources. Besides, an even looser strategy of meshing and dynamic setting was adopted in simulations [7-9] to obtain results in a reasonable time period. Therefore, it may not be necessary in this study to get the most accurate refinement results but it is necessary to select a relatively reasonable setting when compared with in the literature. The schematic diagram of the refinement study as defined in this study is shown in Figure 3-6. It is necessary to conduct a meshing refinement study to maintain the accuracy of every position before the time-dependent refinement study, thus ensuring the accuracy of every instant.

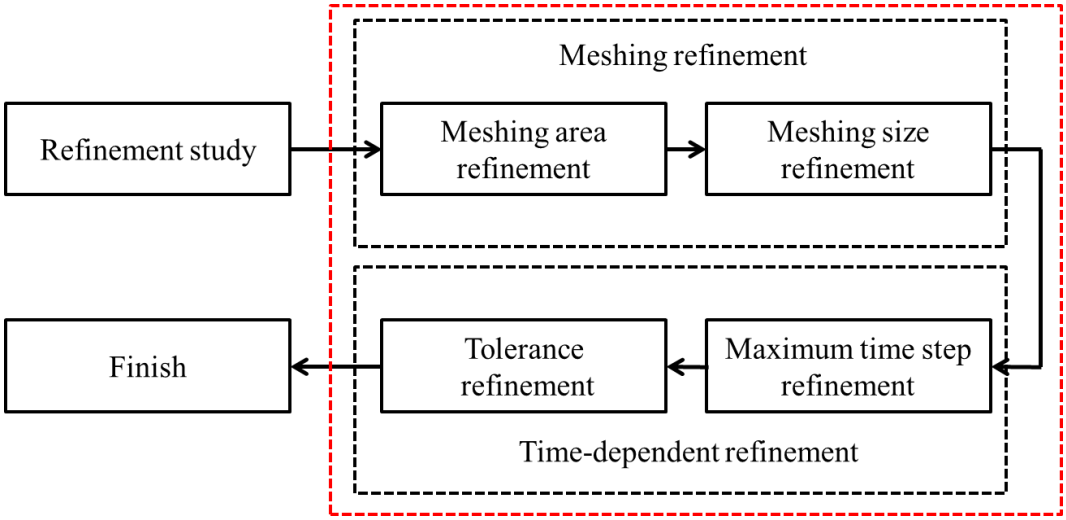

Figure 3-6 Schematic diagram of the refinement study for a time-dependent study.

3.3.3.2 Refinement study results

This chapter describes the simulation results of the effects of electron saturation velocity (ESV) on streamer characteristics that mainly include electric field dynamics. Therefore, the dynamics of the electric field position and magnitude at the streamer tip are both of significant interests to be focused on as refinement variables.

The meshing areas close to the needle tip are shown in Figure 3-7 (a). The meshing elements are selected as a free triangular shape. A zoomed-in plot of the meshing elements is shown in Figure 3-7 (b) with maximum meshing size of 0.5 μm along the axis of symmetry and needle tip boundary and 0.65 μm in the area nearby. Note that the ESV setting in the refinement study is 10 km/s. The voltage application is a step voltage with a voltage magnitude of 110 kV and rise time of 400 ns. A summary of all the refinement study cases for this chapter are shown in Table 3-3. The detailed results of the refinement study are shown as follows.

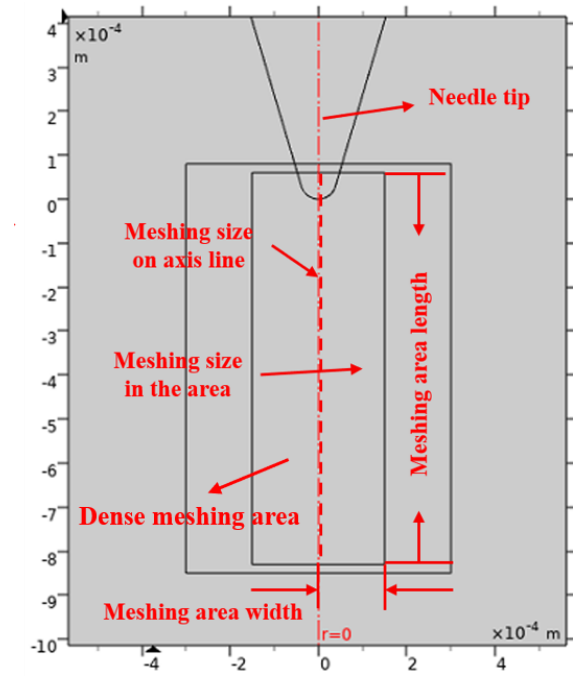

(a)

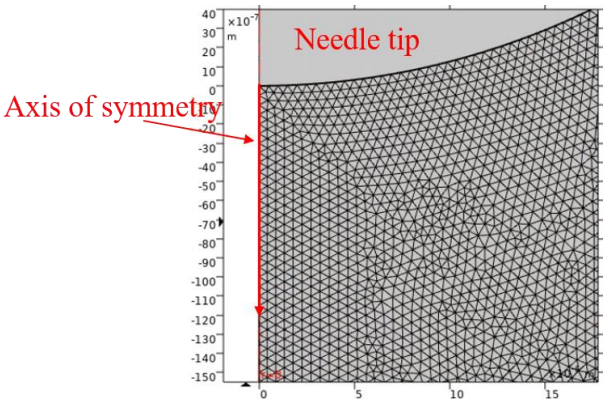

(b)

Figure 3-7 Meshing set-up used in Chapter 3 (a) boundaries of different meshing areas (b) zoomed-in plot of the meshing elements. Note that the meshing size in the central rectangular is discussed in Table 3-3. The meshing sizes in other areas are relatively coarse.

Table 3-3 A summary of refinement study in Chapter 3.

R3-Case	Length	Width	Line meshing size	Area meshing size	Maximum time step size	Relative tolerance	RAM required	Simulation time
1	0.73 mm	150 μm	0.5 μm	0.65 μm	0.1 ns	0.0008	75 G	3d2h
2	0.83 mm	150 μm	0.5 μm	0.65 μm	0.1 ns	0.0008	75 G	3d23h
3	1.03 mm	150 μm	0.5 μm	0.65 μm	0.1 ns	0.0008	75 G	4d3h
4	0.73 mm	175 μm	0.5 μm	0.65 μm	0.1 ns	0.0008	67 G	3d17h
5	0.73 mm	200 μm	0.5 μm	0.65 μm	0.1 ns	0.0008	69 G	4d4h
6	0.73 mm	150 μm	0.45 μm	0.6 μm	0.1 ns	0.0008	70 G	3d16h
7	0.73 mm	150 μm	0.5 μm	0.65 μm	0.08 ns	0.0008	61 G	3d13h
8	0.73 mm	150 μm	0.5 μm	0.65 μm	0.06 ns	0.0008	52 G	4d14h
9	0.73 mm	150 μm	0.5 μm	0.65 μm	0.04 ns	0.0008	66 G	6d15h
10	0.73 mm	150 μm	0.5 μm	0.65 μm	0.06 ns	0.0006	34 G	2d7h

The simulation time, for example 3d2h, is short for 3 days and 2 hours. The relative tolerance default value set in COMSOL Multiphysics v5.4 is 0.005.

(1) Results of the meshing refinement study

The first step in the meshing refinement study is refining the meshing area length. A comparison of the refinement study cases, which are from R3-Case 1 to R3-Case 3, is shown in Figure 3-8. The meshing area length of 1.03 mm is set as the comparative base. Variations in the electric field peak position and magnitude begin to show differences among different meshing settings from ~275 ns. The electric field distribution along the axis of symmetry from the needle tip into cyclohexane is shown in Figure 3-9. The electric field leaves the needle tip at 180 ns and reaches its maximum magnitude at 275 ns. Since R3-Case 3 is not the finally refined case, the electric field after 275 ns in R3-Case 3 then decreases and finally increases again. Note that for the finally refined cases in this chapter, the electric field will then decrease and finally reach a relatively stable value. Since the electric field at 275 ns reaches its maximum value, the variation of the variable in R3-Case 3 at 275 ns is also the most intensive. Therefore, the variation of the variable among the different cases also begins to vary intensively.

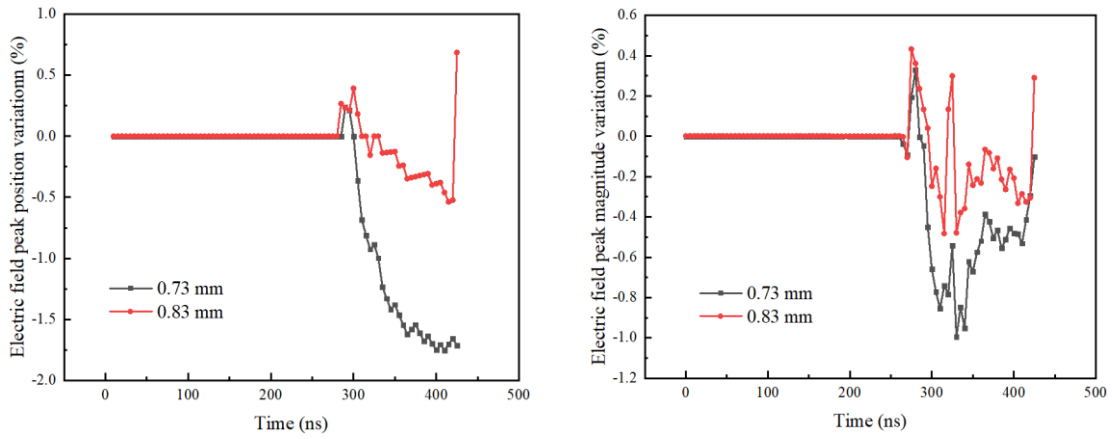

(a) (b)

Figure 3-8 Results of the refinement study for the meshing area length on electric field dynamics at the streamer tip of Chapter 3. (a) Electric field peak position and (b) electric field peak magnitude.

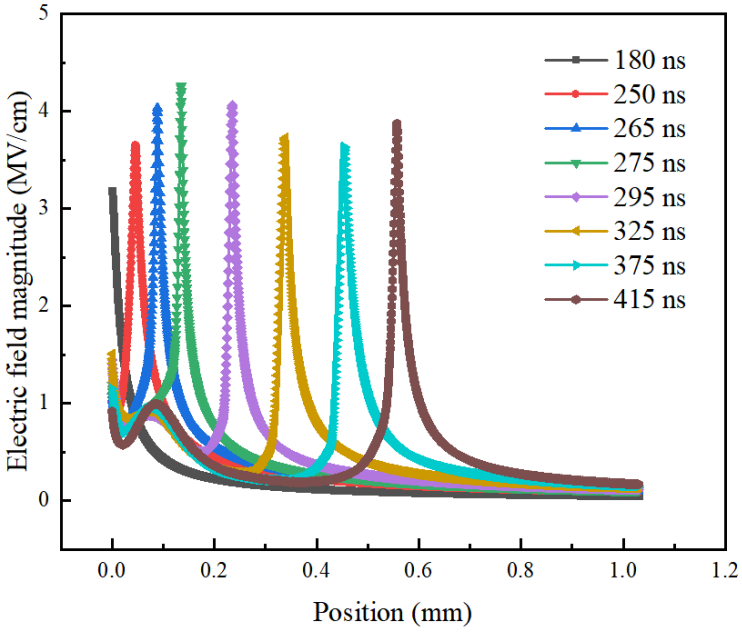

Figure 3-9 Electric field distribution along the axis of symmetry in case R3-Case 3.

In the studied time interval, the variations in the electric field peak position and magnitude for R3-Case 1 and R3-Case 2 are all smaller than 2%. Therefore, a meshing area length of 0.73 mm is selected for further refinement.

The second meshing refinement study step is to refine the meshing area width. A comparison of the refinement study cases, which are R3-Case 1, R3-Case 4 and R3-Case 5, is shown in Figure 3-10. When setting the meshing area width of 200 µm as the comparative base, variations in the electric field peak position and magnitude for R3-Case 1 and R3-Case 4 are all smaller than 3.5%. Therefore, a meshing area width of 150 µm is selected for further refinement.

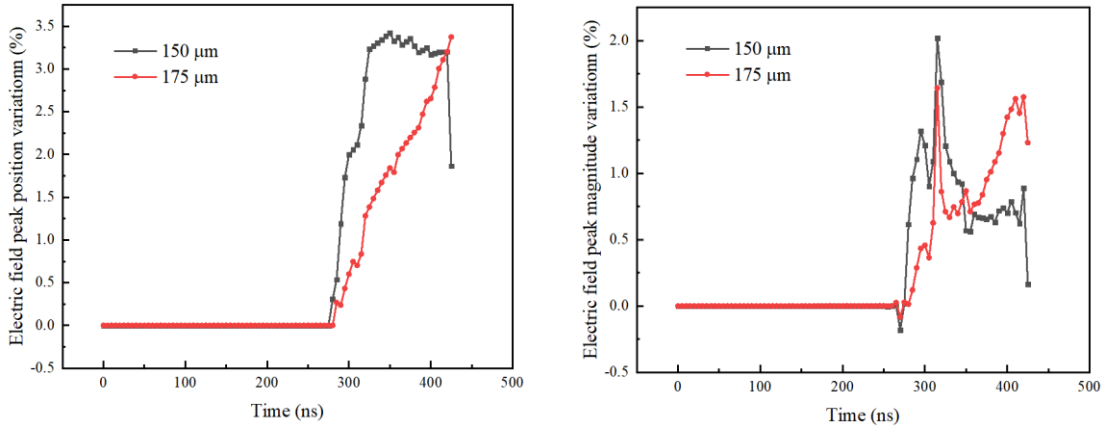

(a) (b)

Figure 3-10 Results of the refinement study for the meshing area width on electric field dynamics at the streamer tip of Chapter 3. (a) Electric field peak position and (b) electric field peak magnitude.

The third meshing refinement study step is to refine the maximum meshing size on the axis of symmetry and in the dense meshing area. A comparison of the refinement study cases, which are R3-Case 1 and R3-Case 6, is shown in Figure 3-11. When setting the meshing size on the axis of symmetry of 0.45 μm and the meshing size in the dense meshing area of 0.6 μm as the comparative base, variations in the electric field peak position and magnitude for R3-Case 1 are all smaller than 2.5%. Therefore, a meshing size on the axis of symmetry of 0.5 μm and a meshing size in the dense meshing area of 0.65 μm are selected for further refinement.

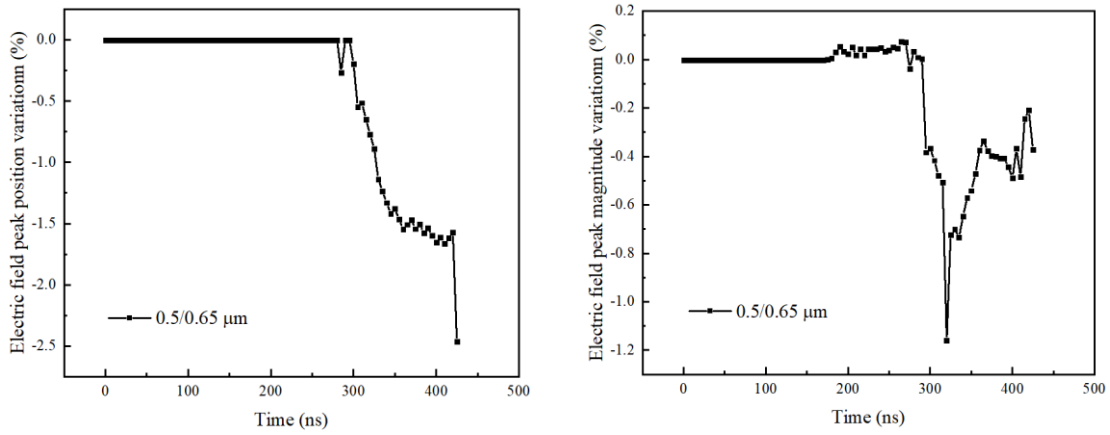

(a) (b)

Figure 3-11 Results of the refinement study for the meshing size on the axis of symmetry and dense meshing area on electric field dynamics at the streamer tip of Chapter 3. (a) Electric field peak position and (b) electric field peak magnitude.

(2) Results of time-dependent refinement study

The first time-dependent refinement study step is to refine the maximum time step size. A comparison of the refinement study cases, which are R3-Case 1, and R3-Case 7 to R3-Case 9, is shown in Figure 3-12. When setting the maximum time step size of 0.04 ns as the comparative base, variations in the electric field peak position and magnitude for R3-Case 8 are all smaller than 2%. Therefore, a maximum time step size of 0.06 ns is selected for further refinement.

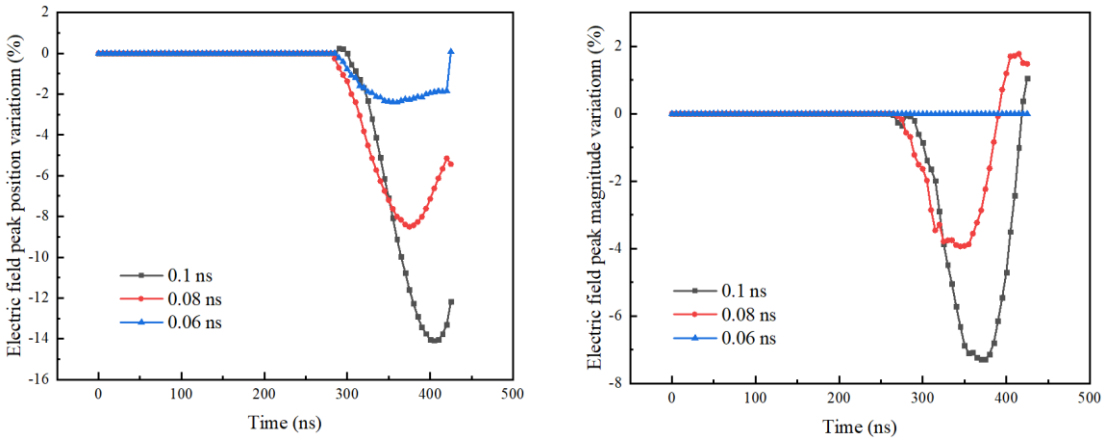

(a) (b)

Figure 3-12 Results of the refinement study for the maximum time step size on electric field dynamics at the streamer tip of Chapter 3. (a) Electric field peak position and (b) electric field peak magnitude.

The second time-dependent refinement study step is to refine the relative tolerance. A comparison of the refinement study cases, which are R3-Case 8 and R3-Case 10, is shown in Figure 3-13. When setting the relative tolerance of 0.0006 as the comparative base, variations in the electric field peak position and magnitude for R3-Case 8 are all smaller than 2%. Therefore, a relative tolerance of 0.0008 is selected for further refinement.

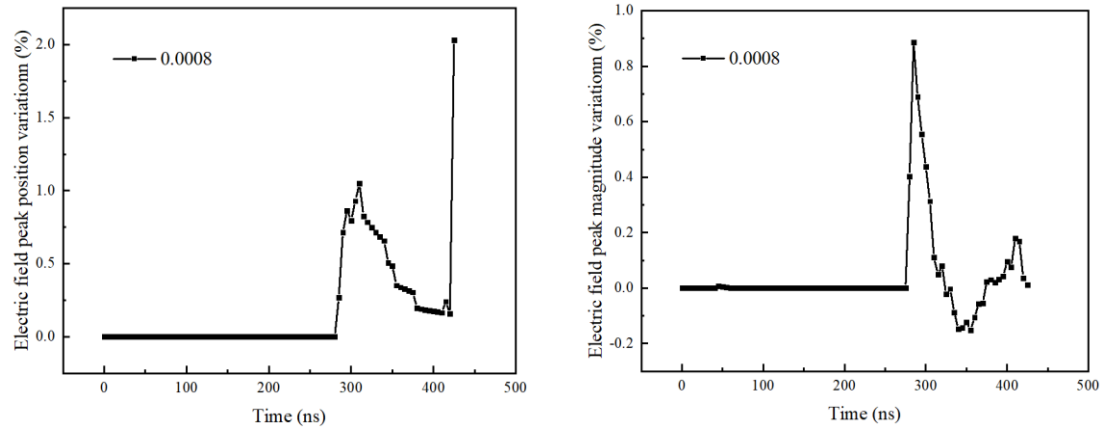

(a) (b)

Figure 3-13 Results of the refinement study for the relative tolerance on electric field dynamics at the streamer tip of Chapter 3. (a) Electric field peak position and (b) electric field peak magnitude.

Based on the refinement study above, the simulation condition of R3-Case 8 is selected as the refinement case and used for further study.

3.4 Description of Streamer Dynamics during Streamer Propagation

Since the velocity of the movement of the electric field peak is generally regarded as streamer velocity in a simulation, the electric field distribution at a different time with a voltage magnitude of 100 kV when ESV is set at 7.5 km/s is shown in Figure 3-14. The reason for using an ESV of 7.5 km/s will be explained from Section 3.5 to Section 3.6.

In Figure 3-14 (a), initially with a voltage increase during rise time from 0 to 180 ns, the electric field magnitude along the axis of symmetry from the needle tip into cyclohexane gradually rises, which is similar to the Laplace field. The electric field peak leaves the needle tip and propagates into cyclohexane at 180 ns with a magnitude of 3.07 MV/cm due to the effects of the accumulated space charges generated by molecular ionization. The electric field peak magnitude shows an initial increasing and then decreasing trend until it reaches a stable magnitude which equals ~3.7 MV/cm during propagation. Since this study only considers one single streamer branch due to the limitation of the 2D-axisymmetric model, the streamer shape looks like a tube during propagation as shown in Figure 3-14 (b), which can be regarded as an extension of the positive needle tip into cyclohexane. According to the calculation method used in [7, 11], the average voltage drop of the flat electric field area inside the streamer channel is ~1.76×10^7 V/m.

Due to lack of discussion on how to define the streamer radius in previous simulations, a sensitivity discussion on streamer radius during streamer propagation is shown in Figure 3-15. The streamer radius is defined as the maximum radius of the boundary of the pre-defined electric field tube at the streamer head. The boundary of the pre-defined electric field tube is from 30% to 70% of the maximum electric field at streamer tip E_{max}, as shown in the 2D distribution of the electric field in Figure 3-15. It is found that during streamer propagation, the streamer radius keeps relatively stable at different streamer lengths, while the percentile of the pre-defined electric field tube at the streamer head greatly affects the streamer radius. For a streamer length of 0.6 mm, the streamer radius decreases from 68.0 μm to 33.7 μm with the pre-defined percentile increasing from 30% to 70%. In the following chapters, the streamer radius is reported as the boundary of the electric field tube at 50% E_{max} at the streamer head when the streamer length equals 0.6 mm.

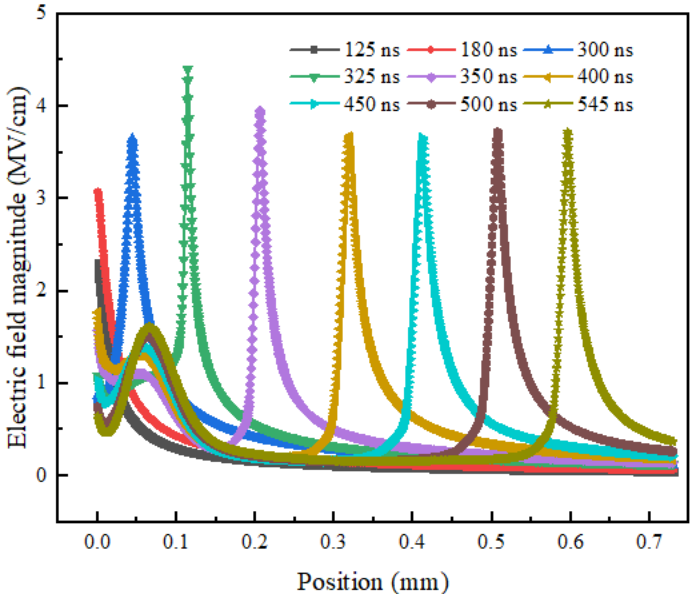

(a)

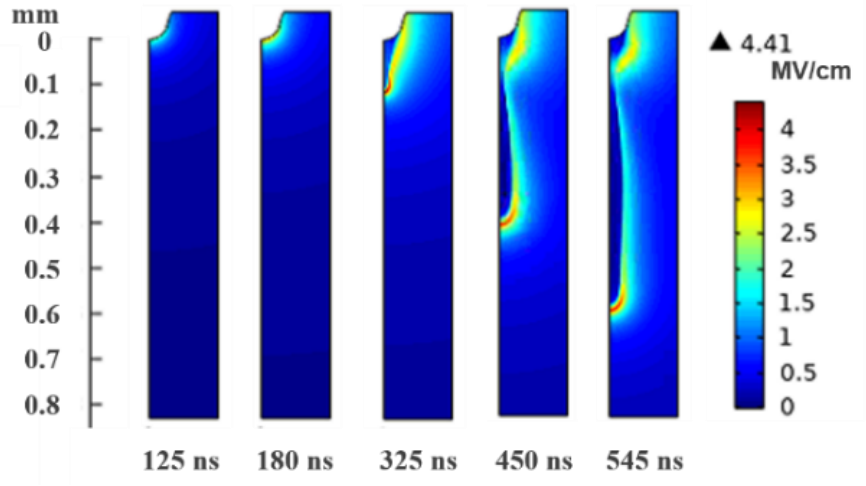

(b)

Figure 3-14 Distribution of the electric field during streamer propagation in (a) 1D plot along the axis of symmetry and (b) 2D plot with voltage magnitude of 100 kV. ESV=7.5 km/s.

Instant streamer velocity at different streamer lengths and the corresponding peak electric field magnitude and space charge density at the streamer tip are shown in Figure 3-16. The space charge density equals the sum of the charge density of positive ions, negative ions and electrons. It shows that the instant streamer velocity initially increases to ~4 km/s and then decreases to a relatively stable value of ~1.91 km/s. This initial increasing and then decreasing trend to a stable stage phenomenon of streamer velocity has also been observed in experiments based on high resolution shockwave observation [244]. The stable stage of streamer velocity is termed 'propagation velocity' in this study.

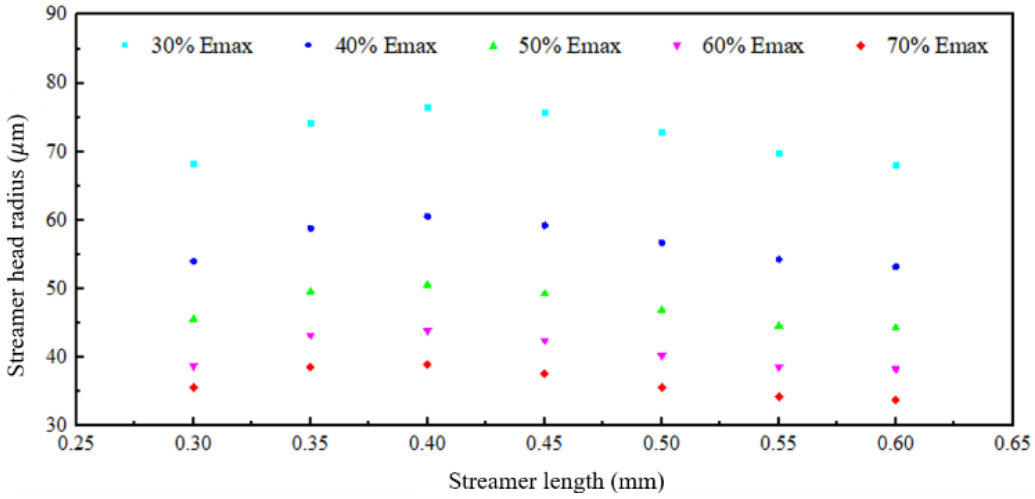

(a)

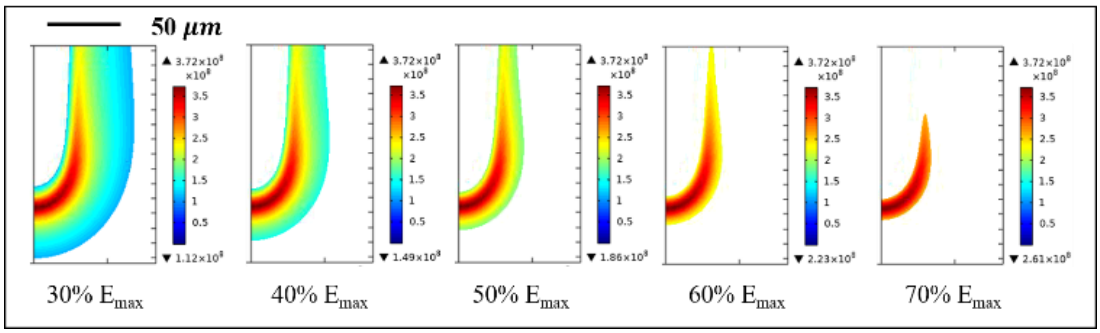

(b)

Figure 3-15 (a) Streamer head radius at different streamer lengths under different measurement standards. (b) 2D distribution of a predefined electric field tube at the streamer head with a streamer length at 0.6 mm and standard from 30% to 70% E_{max}. Voltage magnitude equals 100 kV and ESV equals 7.5 km/s.

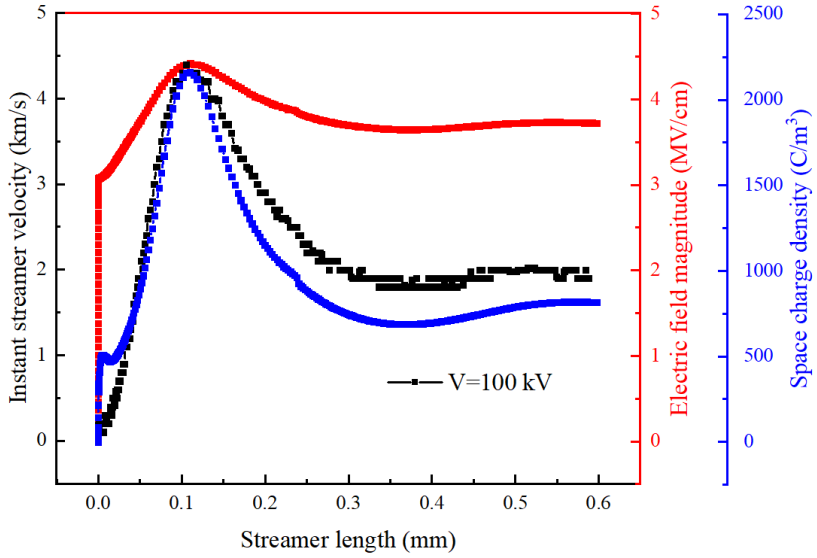

Figure 3-16 Instant streamer velocity and corresponding electric field magnitude and space charge density at the streamer tip at different streamer lengths when ESV equals 7.5 km/s with a voltage magnitude of 100 kV.

It is important to observe that the streamer velocity variation correlates with the local electric field magnitude variation at the streamer tip, which supports the argument in Section 3.2 that positive streamer velocity is partially dependent on electric field dependent v_e. The electric field peak magnitude variation could be explained by the distance between the local electric field peak position and space charge density peak position at streamer tip $d_{E\rho}$. The corresponding time-dependent relationship between the electric field peak magnitude and $d_{E\rho}$ during streamer propagation is shown in Figure 3-17. The electric field and space charge distributions along the axis of symmetry from the needle tip into cyclohexane from 200 ns to 270 ns are shown in Figure 3-18. It is found that the electric field peak is always some distance ahead of the space charge density peak. As shown in Figure 3-16 and Figure 3-17, the electric field peak leaves the needle tip after 180 ns at 3.07 MV/cm while the space charge density peaks stay at the needle tip so that the distance between them, $d_{E\rho}$, increases. With time increasing, the electric field peak moves further into the cyclohexane while the space charge density peak remains at the needle tip. From 0 ns to 250 ns, only the space charge density volume increases, as shown in Figure 3-18, which leads to a consistent increase in the distance $d_{E\rho}$. The electric field distribution in cyclohexane is also mainly determined by the Laplace field induced by applied voltage, rather than space charge induced electric field as shown in Figure 3-19.

At 250 ns, the position of the space charge density peak switches from the needle tip to the position just behind the electric field peak, leading to a sudden decrease in distance $d_{E\rho}$, with the space charge induced electric field from this point beginning to dominate the total electric field in cyclohexane. Afterwards, the variation of distance $d_{E\rho}$ has an opposite relationship with that of the electric field peak magnitude. The distance $d_{E\rho}$ initially decreases to its smallest value ~1.5 μm at 325 ns when the electric field magnitude reaches its highest value ~4.4 $\mathrm{MV/cm}$. Then the distance $d_{E\rho}$ gradually increases to a stable value of ~3.5 μm when the electric field magnitude decreases to ~3.7 $\mathrm{MV/cm}$.

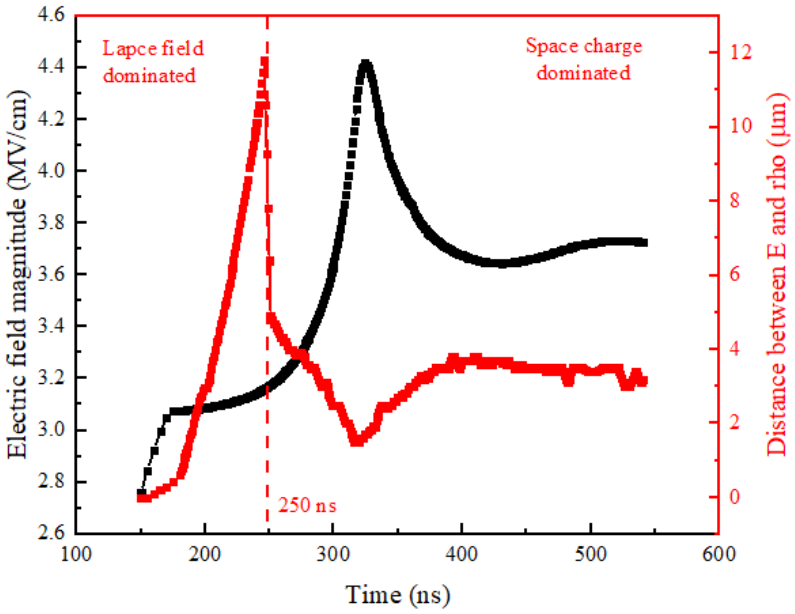

Figure 3-17 Time-dependent distribution of electric field peak magnitude and the distance $d_{E\rho}$ between electric field peak and space charge density peak during streamer propagation with a voltage magnitude of 100 kV. ESV is 7.5 km/s.

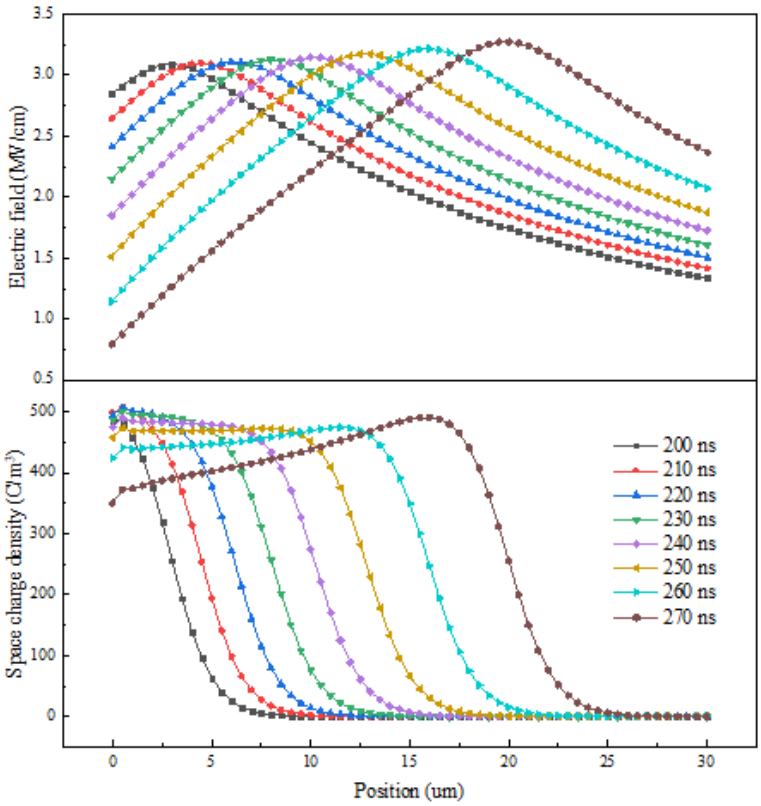

Figure 3-18 Distribution of electric field and space charge density along the axis of symmetry from 200 ns to 270 ns.

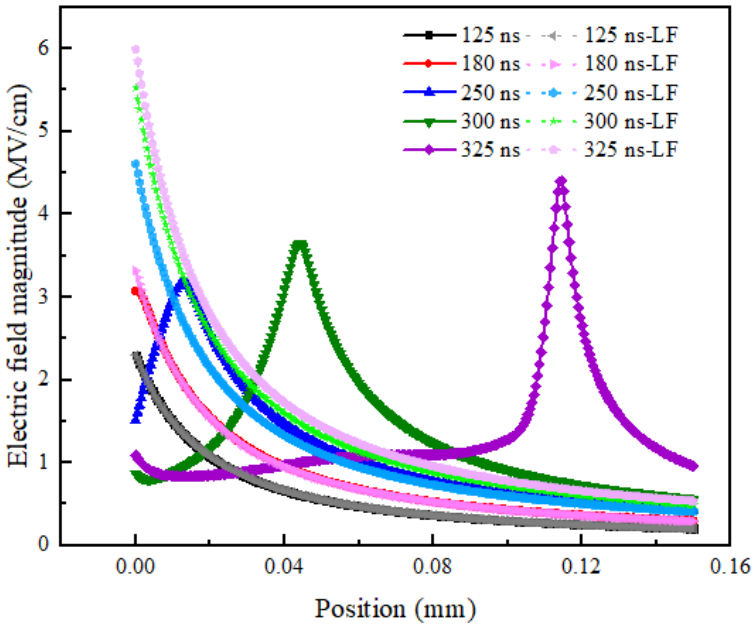

Figure 3-19 Comparison between the electric field distribution in cyclohexane during the streamer process and the corresponding Laplace field generated by applied voltage in cyclohexane along the axis of symmetry from 125 ns to 325 ns. "−LF" means Laplace field.

3.5 Effects of Electron Saturation Velocity on Streamer Dynamics

The effects of ESV on the electric field peak magnitude during propagation is shown in Figure 3-20. It is found that the streamer peak electric field magnitudes when electric field peak leaves needle tip are all ~3.07 MV/cm under different ESVs. The corresponding charge generation rate is calculated to be 16.6 $C/ns \cdot m^3$ according to Equation 3-7. For the studied ESV range, all the electric field magnitude distributions show an initially increasing and then decreasing trend. With the decrease of ESV value from 30 km/s to 2.5 km/s, the maximum electric field peak magnitude decreases from 5.07 MV/cm to 3.73 MV/cm. Besides, decreasing ESV reduces the electric field peak magnitudes during streamer propagation from 4.35 MV/cm to 3.25 MV/cm. According to Equation 3-1 and Figure 3-2, the corresponding electron velocity decreases from 17.8 km/s to 2.32 km/s.

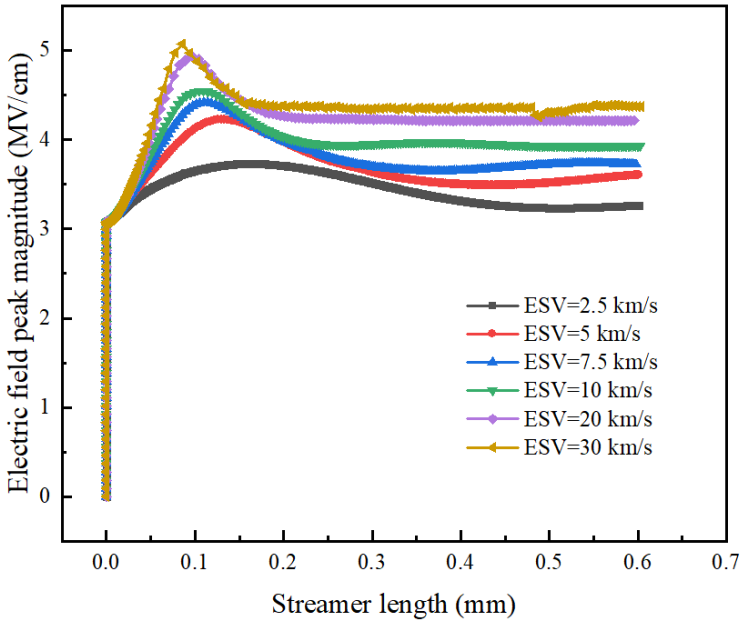

Figure 3-20 Effects of electron saturation velocity on electric field peak magnitude at the streamer peak with voltage magnitude of 100 kV.

The effect of ESV on instant streamer velocity is shown in Figure 3-21. The corresponding streamer propagation velocity and voltage drop inside streamer channel are shown in Figure 3-22. When ESV reduces from 30 km/s to 2.5 km/s, streamer propagation velocity also decreases from ~4.15 km/s to ~0.50 km/s correspondingly, which decreases 87.95%. Besides, the voltage drop inside streamer channel decreases from 34.80 kV/mm to 10.63 kV/mm.

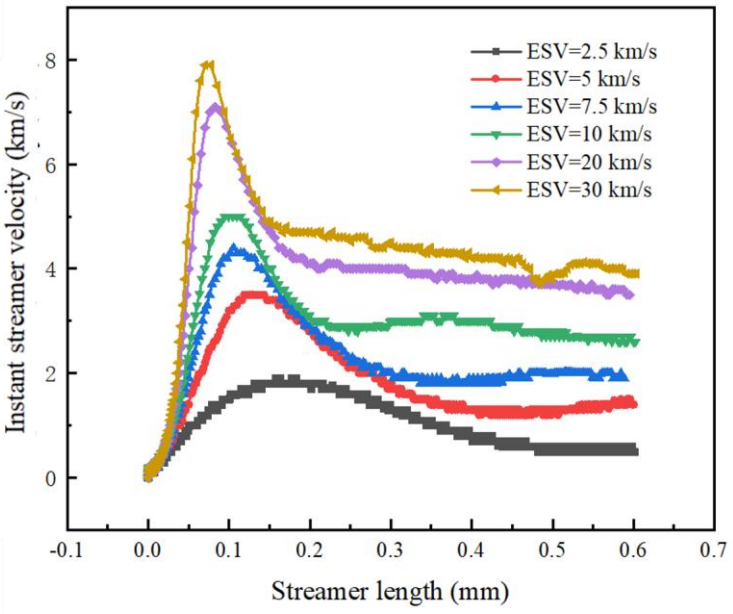

Figure 3-21 Effects of electron saturation velocity on instant streamer velocity with voltage magnitude of 100 kV.

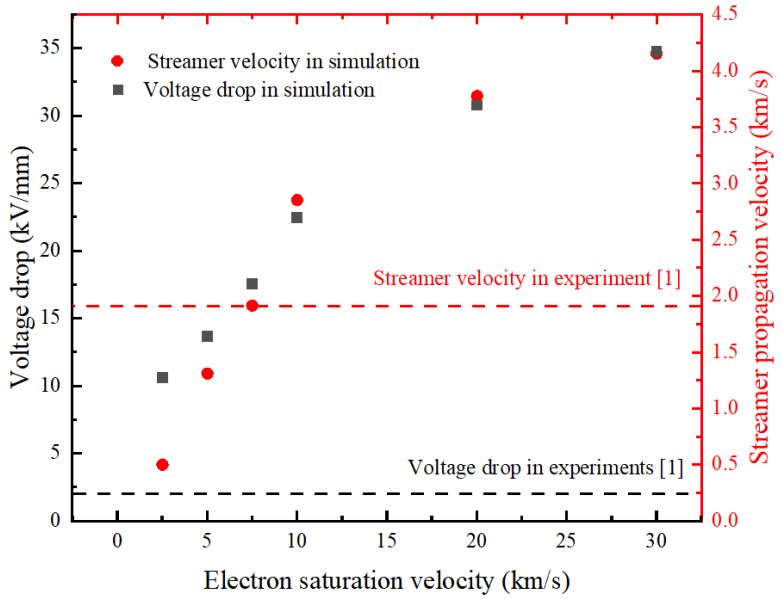

Figure 3-22 Effects of electron saturation velocity on streamer propagation velocity and voltage drop with voltage magnitude of 100 kV.

In this chapter, matching streamer propagation velocity with experiments [1] is considered to be more important than matching voltage drop because the voltage drop might be related with the low-density channel formation inside streamer body which is not simulated in this chapter. Streamer radius also increases from 18 μm to 73.6 μm with the decrease of ESV as shown in Figure 3-23. Streamer radius of 44 μm in simulation is also close to the experimental observations of 2nd mode streamer channel radius of ~50 μm in [1, 34]. Therefore, ESV equal to 7.5 km/s is selected as the best optimized value to fit experimental results with voltage magnitude at 100 kV.

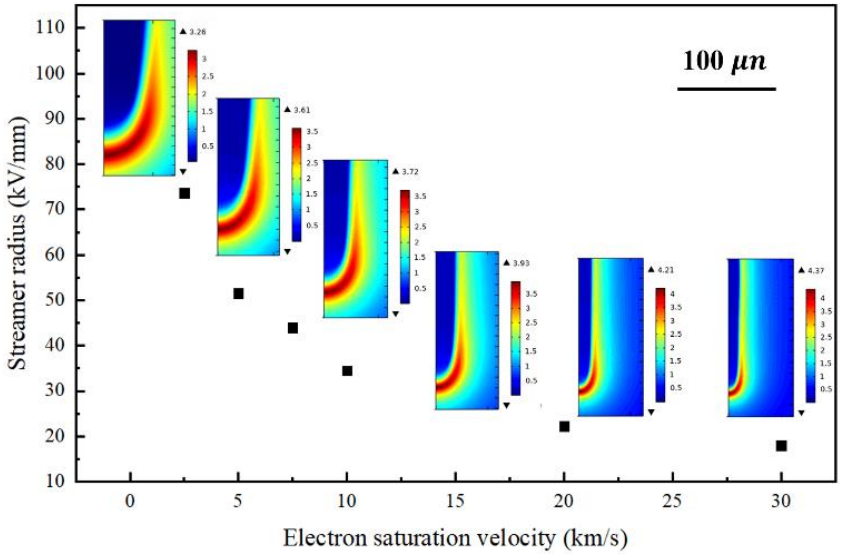

Figure 3-23 Effects of electron saturation velocity on streamer radius during streamer propagation with voltage magnitude of 100 kV. Streamer radius is defined as the boundary of 50% E_{max} at the streamer head at 0.6 mm.

3.6 Effects of Applied Voltage on Streamer Dynamics with Consideration of Electron Saturation Velocity

The optimized ESV value of 7.5 km/s based on experiment at voltage of 100 kV is further applied to other voltage levels ranging from 80 kV to 95 kV to confirm the optimized model. The effects of voltage magnitudes on instant streamer velocity and the distance between electric field peak and space charge density peak have been first shown in Figure 3-24. As expected, increasing applied voltage magnitudes increases streamer propagation velocity slightly from ~1.59 km/s to ~1.91 km/s. The instant streamer velocities all show an initially increasing and then decreasing trend until they reach relatively stable values.

Besides, the maximum distances between electric field peak and space charge density peak $d_{E\rho\_max}$ for voltage magnitude rising from 80 kV to 100 kV all happen very close to the needle tip where space charge density peaks jump from needle tip to further into the oil which is similar with Figure 3-17. $d_{E\rho\_max}$ at this position ranges from 12 μm to 13 μm. The maximum $d_{E\rho\_max}$ happens at voltage magnitude of 80 kV.

The positions of the minimum distance between electric field peak and space charge density peak $d_{E\rho\_min}$ at streamer tip for voltage magnitude rising from 80 kV to 100 kV are always at the same positions where instant streamer velocities reach the peak values. The positions of $d_{E\rho\_min}$ are similar among all the selected voltage magnitudes, which are close to 0.1 mm. $d_{E\rho\_min}$ is found to be from 1.5 μm to 2 μm. The minimum value of $d_{E\rho\_min}$ is 1.5 μm at voltage magnitude of 100 kV. Then, the distance between electric field peak and space charge density peak $d_{E\rho\_stable}$ gradually increases to from 3 μm to 3.5 μm and keeps relatively stable.

The effect of applied voltage magnitudes on streamer propagation velocity is shown in Figure 3-25 which is also compared with experimental results [1]. With the magnitude of applied voltage increasing from 80 kV to 100 kV, streamer propagation velocity in simulation shows a good agreement with experimental results of cyclohexane in [1]. The deviation between simulations and experimental results is smaller than 3%.

Besides, as shown in Figure 3-26 (a) and (b), streamer radius also shows an increasing trend from 37.5 μm to 44.0 μm when the applied voltage increases. The voltage drop inside streamer channel also increases from 12.72 kV/mm to 17.65 kV/mm when increasing voltage magnitudes from 80 kV to 100 kV as is shown in Figure 3-27.

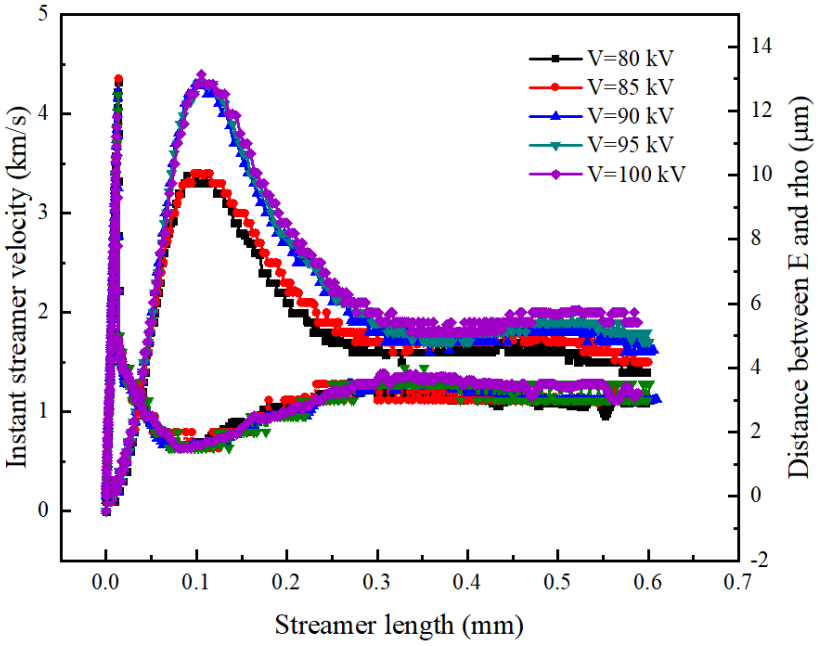

Figure 3-24 Effects of the external voltage on instant streamer velocity and the distance between electric field peak and space charge density peak. ESV is 7.5 km/s.

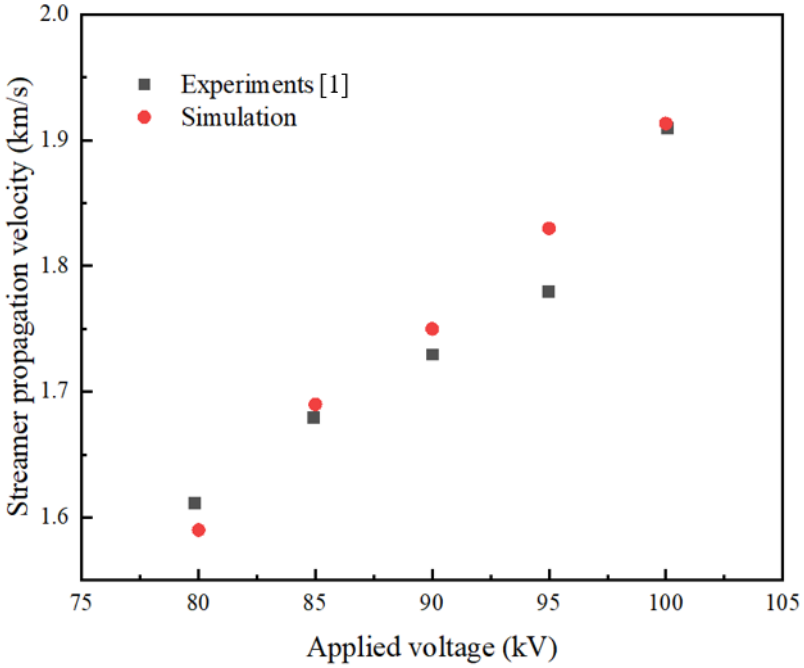

Figure 3-25 Comparison of streamer propagation velocity in simulations and experiments under different voltage magnitudes. Black dots are from [1].

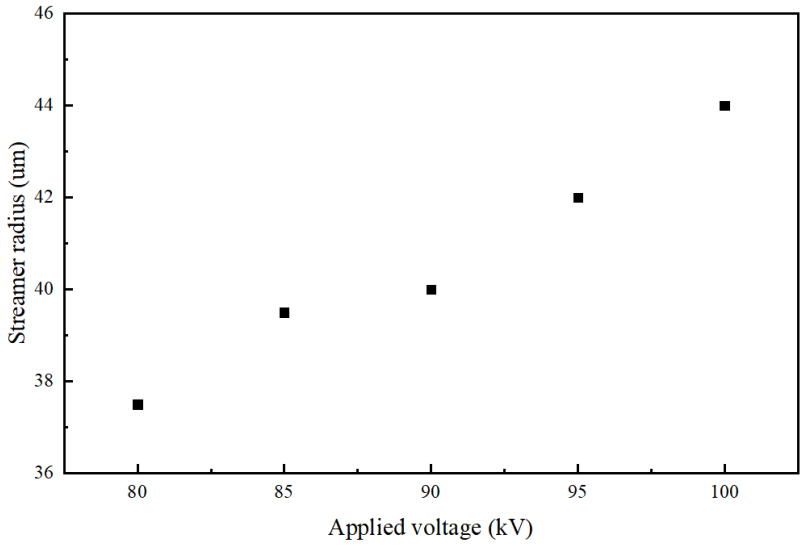

(a)

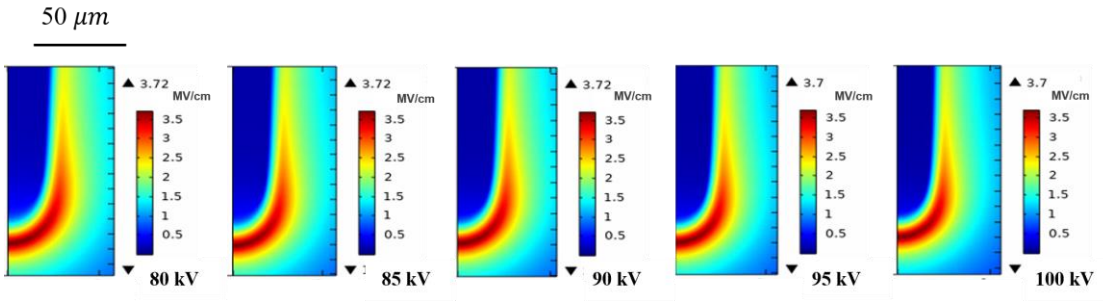

(b)

Figure 3-26* (a) *Effects of voltage magnitudes on streamer radius during streamer propagation. ESV is 7.5 km/s. (b) Streamer tip shape at different voltage levels. Streamer radius is defined as the boundary of 50% E_{max} at the streamer head at 0.6 mm.

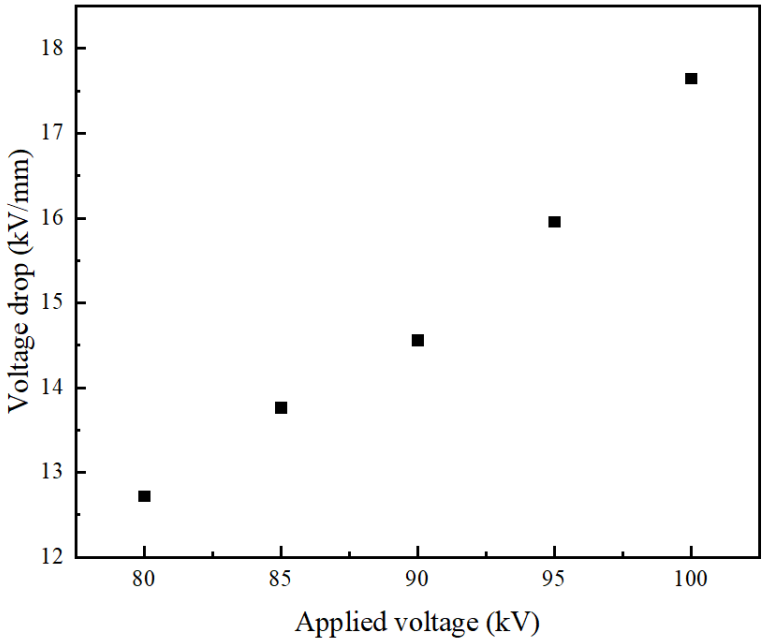

Figure 3-27 Effects of voltage magnitudes on the voltage drop inside the streamer channel. ESV is 7.5 km/s.

3.7 Discussion

The aim of this chapter is to explain the reason for the stable velocity of 2nd mode positive streamers by using ESV. It has been confirmed that ESV can successfully constrain streamer velocity to a reasonable level when compared with experimental results [1]. Therefore, it is necessary to further explain whether ESV could happen in cyclohexane during streamer propagation.

Due to a lack of experiments confirming ESV in cyclohexane to the author's best knowledge, only theoretical analysis is presented in this section. According to the argument in [145], at a sufficiently high electric field, when electrons gain more energy than $k_B T$ between collisions with molecules, electron mobility goes down, where k_B is the Boltzmann constant and T is local temperature. As described above, a streamer consists of a low-density phase and liquid phase, with the mechanism dominating streamer velocity should be occurring in the liquid phase [4, 13, 34]. Assuming the maximum temperature at the streamer tip under atmospheric pressure in cyclohexane is the same as the liquid boiling temperature 353 K [109], $k_B T$ equals 0.030 eV. Under a local electric field of 3.7 MV/cm at the streamer tip according to Figure 3-16, an electron could gain $W_e = eEa = 0.111$ eV before collision with neutral molecules, which is high enough to justify the existence of ESV.

Besides, due to the complexity of the nature of streamers and the challenge of computational resources, some phenomena have been simplified and are further discussed in the following.

The first simplification is that the model in this chapter does not consider the physics inside the low-density phase of the streamer channel. As is presented in Figure 3-1, the low-density phase inside the streamer channel will be formed due to the temperature rise induced by Joule heating. Inside the low-density phase of the streamer, the parameter values, such as charge mobility, charge generation and recombination rate, and the relative permittivity of dielectric material, will all change accordingly [11], and are not the same as the parameters in the liquid phase. The main difficulties associated with simulating streamers with the low-density channel are the complexity of the physics involved and the hard convergence when solving the highly non-linear partial differential equations. Modelling of the low-density phase will be presented in Chapter 6.

Besides, when considering the factors affecting streamer velocity by the low-density phase of streamer, the most important effect from a macroscopic perspective is to lower the voltage drop inside the streamer channel. The voltage drop inside the streamer channel is calculated to be $\sim 2 \times 10^6$ V/m in cyclohexane in the experiments in [1], while it is $\sim 1.76 \times 10^7$ V/m in the flat area of electric field in the simulation in this chapter when ESV is assumed to be 7.5 km/s under a voltage magnitude of 100 kV. The higher voltage drop decreased the voltage potential at the streamer tip and then slightly slowed down the streamer velocity. Therefore, the true ESV might be a bit smaller than estimated in this chapter.

Secondly, this chapter does not simulate the effects of electron attachment time τ_a on streamer velocity. τ_a is closely related to the components and purity of the dielectric liquids. τ_a has been found to be ~500 ns in cyclohexane [134] and ~100 ns in hydrocarbons [109, 138] in experiments, while it is argued to be much smaller and also electric field dependent in simulation [49]. The value $\tau_a = 200$ ns is somewhat a compromise for different values in the literature. The further effects of τ_a in liquid are unable to be simulated in this chapter because a too small τ_a will significantly increase the voltage drop when excluding the low-density phase inside the streamer channel.

Thirdly, this chapter only simulates the propagation of a single streamer branch instead of streamer with multiple branches due to the limitation of the 2D-axisymmetric model and demanding computational resources of the 3D model. Although streamer branching may have some shielding effects on the velocity of streamer branches to some extent, the recent results in [59], as discussed in Section 3.1, indicated that the shielding effects of streamer branching are not the dominant reason constraining streamer velocity. Therefore, it is acceptable to only simulate a single streamer channel.

Based on the descriptions above, although there are limitations when simulating a low-density channel inside a streamer channel and the multiple streamer branches, this chapter has presented a valuable modelling of the stable propagation velocity of a 2nd mode positive streamer, which is dominated by electron velocity in the liquid phase of the streamer.

3.8 Summary

This chapter has presented the effects of electron saturation velocity on streamer dynamics by modelling in order to explain the reason for the stable velocity of 2nd mode

positive streamers. The variation of instant streamer velocity is found to be positively related to the electric field magnitude at the streamer tip. The magnitude of the electric field at the streamer tip initially increases and then decreases to a relatively stable value, which is explained by the peak distance between the electric field and space charge density during streamer propagation. The mechanism of the stable propagation velocity of a 2nd mode positive streamer in cyclohexane is thought to be the constrain of ESV. The simulation found that reducing ESV from 30 km/s to 2.5 km/s decreased streamer propagation velocity from 4.15 km/s to 0.50 km/s. Besides, the streamer channel radius also increased from 18 μm to 73.6 μm. ESV of 7.5 km/s was optimised according to experimental observation of streamer velocity at 100 kV. The streamer model with ESV of 7.5 km/s was further applied to other different voltage levels. Streamer propagation velocity in the simulation increased from 1.59 km/s at 80 kV to 1.91 km/s at 100 kV, which all closely matched the experimental observations under the same conditions in experiments [1].

4 Modelling of the Electrostrictive-force-induced Cavity Formation in Dielectric Liquids

4.1 Introduction

A streamer is composed of an initiation stage and propagation stage. However, the streamer initiation stage is not well defined in most simulations. In some cases simulating streamer dynamics, DC voltage was directly applied on the needle in the simulation without clearly defining the voltage rise time [10, 11, 81, 87, 97]. The mechanism involved during the streamer initiation stage may not be necessarily the same as during the streamer propagation stage. In recent years, a cavity, which can be formed under fast voltage rise rates, has gradually gained more interest among researchers [62, 112-116, 128, 245]. Accordingly, it will be interesting to investigate whether a cavity can be formed in dielectric liquids under fast voltage rise rates during streamer initiation.

In this chapter, the cavity formation mechanism induced by electrostrictive force during streamer initiation is initially introduced in Section 4.2 with the simulation methodology introduced in Section 4.3. Then, a description of the dynamics of cavity formation in cyclohexane and the effects of voltage rise rates on cavity formation in cyclohexane are studied in Section 4.4. Next, the differences in cavity formation among cyclohexane, rapeseed oil and deionised water are compared in Section 4.5. Finally, a summary of this chapter is presented in Section 4.6.

4.2 Description of Electrostrictive-force-induced Cavity Formation in Dielectric Liquids

When speaking of cavity formation in dielectric liquids, electrostrictive force is commonly regarded as the key factor. The expression of electrostrictive force is shown in the third components on the right side of Equation 2-18. Since electrostrictive force is related to dielectric polarisation, a schematic diagram of a molecule with and without electric field is shown in Figure 4-1. Without electric field, a molecule, consisting of a positive ion and a negative ion, is electrically neutral. Since the external electric field could slightly shift the positive and negative electric charge in opposite directions within the dielectric liquids, the opposing force will stretch the liquid. Therefore, the electrostrictive force tends to always stretch the liquid.

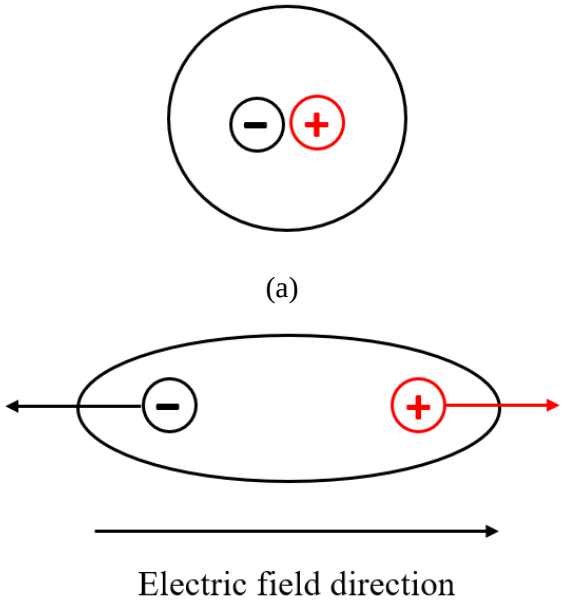

Figure 4-1 Schematic diagram of a molecule (a) without and (b) with electric field.

In experimental and modelling studies on cavities, the most commonly investigated liquid is deionised water [62, 112-116, 128, 245]. It is argued that a negative pressure [246] of around −10 MPa to −30 MPa is enough for cavity formation in deionised water [62, 113]. Experiments also confirm that cavity can form under electrostrictive force in deionised water. A schematic diagram explaining the effects of cavity on streamer initiation is presented in Figure 4-2 [129]. The cavity, a kind of nanopore, is thought to be almost a vacuum, thus having a much longer electron mean free path than in dielectric liquid. Therefore, electrons are able to be accelerated to such an extent inside the nanopores that an electron avalanche is also able to occur outside the nanopores. Under the electric field drift inside a nanopore, which is larger than in the liquid due to differences in permittivity, an electron can gain energy higher than 10 eV in the vicinity of the needle tip during the movement inside a nanopore even when the radius of the nanopore is assumed to be 2 nm [115]. This high electron energy is sufficient to enable ionization by electron avalanche in dielectric liquids. The impact ionization will further generate more charges inside the dielectric liquids and, therefore, accelerate the streamer initiation process. It should be also mentioned that in such studies, only electrostrictive force is considered, with no space charge assumed to be involved in the simulation.

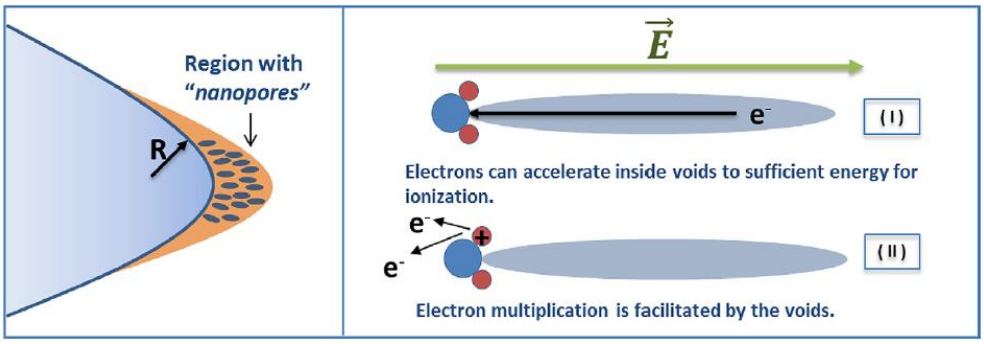

Figure 4-2 A schematic diagram explaining the effects of a cavity on streamer initiation [129].

4.3 Simulation Methodology

4.3.1 Controlling Equations

In this Chapter, the controlling equations involved are Poisson equation [106] as shown in Equation 3-3 and Navier-stokes [111] equations as shown in Equation 2-14 and Equation 2-15. In Equation 3-3, the space charge density is assumed to be zero. In Equation 2-15 in general, volumetric force $\vec{F}$ is determined using the Helmholtz equation [120-122] shown in Equation 4-1.

$$\vec{F} = \sum c_{\pm e} \cdot \vec{E} - \frac{\varepsilon_0}{2}\left|\vec{E}\right|^2 \nabla\varepsilon_r + \frac{\varepsilon_0}{2}\nabla\left(\left|\vec{E}\right|^2 \frac{\partial\varepsilon_r}{\partial\rho_l}\rho_l\right) \qquad \text{Equation 4-1}$$

The first term on the right-hand side of Equation 4-1 is Coulomb force. The second term represents the force acting on an inhomogeneous dielectric liquid and the third term is the electrostrictive forces in a non-uniform electric field associated with the tensions within the dielectric liquids [113]. The second term is always ignored when assuming the extremely small variation of permittivity in space. For non-polar dielectric liquid such as cyclohexane and polar dielectric liquid such as deionized water, $\frac{\partial\varepsilon}{\partial\rho_l}\rho_l$ can be simplified using the Clausius-Mosotti formula [124] as in Equation 2-19 and Equation 2-20. Therefore, $\vec{F}$ can be expressed as Equation 4-2 for non-polar dielectric liquids and Equation 4-3 for polar dielectric liquids, which is related to the Coulomb force and electrostrictive force.

$$\vec{F} = \sum c_{\pm e} \cdot \vec{E} + \frac{\varepsilon_0(\varepsilon_r-1)(\varepsilon_r+1)}{6}\nabla\left(\left|\vec{E}\right|^2\right) \qquad \text{Equation 4-2}$$

$$\vec{F} = \sum c_{\pm e} \cdot \vec{E} + \frac{\alpha\varepsilon_r}{2}\nabla\left(\left|\vec{E}\right|^2\right) \qquad \text{Equation 4-3}$$

Where $\vec{E}$ is local electric field and $\alpha \leq 1.5$ the empirical factor for most of the studied polar dielectric liquids, including deionized water [113, 125]. $\alpha = 1.5$ is used in this study.

Combining Equation 2-15 and Equation 4-1, when considering electrostrictive force and Coulomb force, the total pressure in dielectric liquid p_{total} can be expressed by Equation 4-4. The second and third components on the right-hand side of Equation 4-4 are termed as Coulomb force pressure p_{CF} and electrostrictive force pressure p_{EF} in this study.

$$p_{total} = p + \int_{\vec{l}} \vec{E} \sum c_{\pm e} \cdot d\vec{l} - \frac{\varepsilon_0}{2} \frac{\partial \varepsilon_r}{\partial \rho_l} \rho_l \left|\vec{E}\right|^2 \quad \text{Equation 4-4}$$

The relationship between the thermodynamic pressure and liquid density of cyclohexane [118] and rapeseed oil [119] can be described by the equation of state, as shown in Equation 2-16. In comparison, the equation of state of deionized water can be described as in Equation 2-17 [113, 114]. This will allow us to describe the state of liquid under the effects of Coulomb force and electrostrictive force.

4.3.2 Electrode Geometry, Voltage Excitation and Boundary Conditions

The needle-plane geometry is the same as in Chapter 3 and is shown in Figure 3-3. The boundary conditions of Poisson equation of Equation 3-3 is the same as in Chapter 3. The boundary conditions of Navier-stokes equations of Equation 2-14 and Equation 2-15 as follows.

For the liquid velocity, all the boundaries are set as zero normal flux, which is $\vec{n} \cdot \overrightarrow{v_l} = 0$.

For the pressure, on boundary B1, B2 and B3 in Figure 3-3, p is set as $p = p_0$, where p_0 is ambient atmospheric pressure.

The applied voltage waveforms are ramping voltage waveforms with different voltage rise rates. A typical voltage waveform of a ramping voltage with a voltage rise rate of 50 kV/ns is as shown in Figure 4-3.

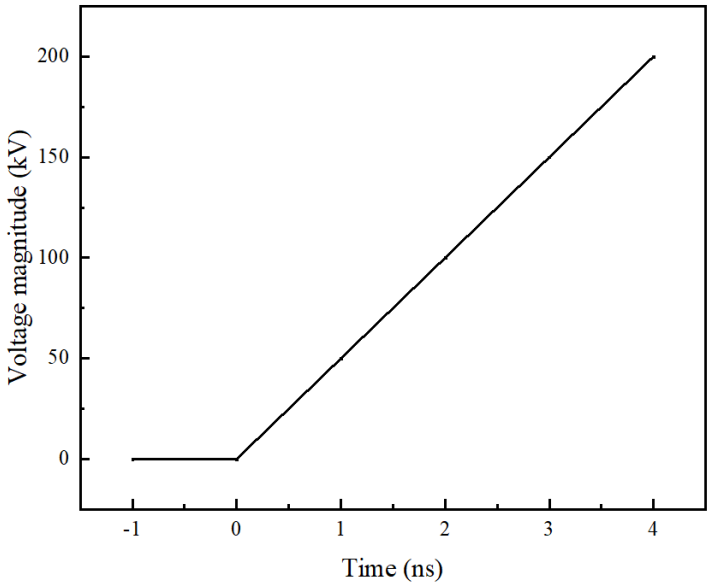

Figure 4-3 Typical voltage waveform of ramping voltage with a voltage rise rate of 50 kV/ns.

4.3.3 Simulation Refinement

In this section, the detailed refinement study results are not shown. Only the dense meshing area and the refined setting are shown here.

The dense meshing area is shown in Figure 4-4 (a). Due to the rapid variation in the electric field and corresponding electrostrictive force, a mapped mesh strategy is adopted to achieve a much denser meshing size close to the needle tip. A zoomed-in plot of the meshing elements close to the needle tip is shown in Figure 4-4 (b). The element number on line 1, Arc 2 and Line 3 is 450, 600 and 900, respectively. The meshing element is similar to a rectangular shape with a minimum length and width of 0.2 μm and 0.1 μm, respectively, close to the needle tip. The maximum time step size and relative tolerance are refined to 0.06 ns and 0.0008.

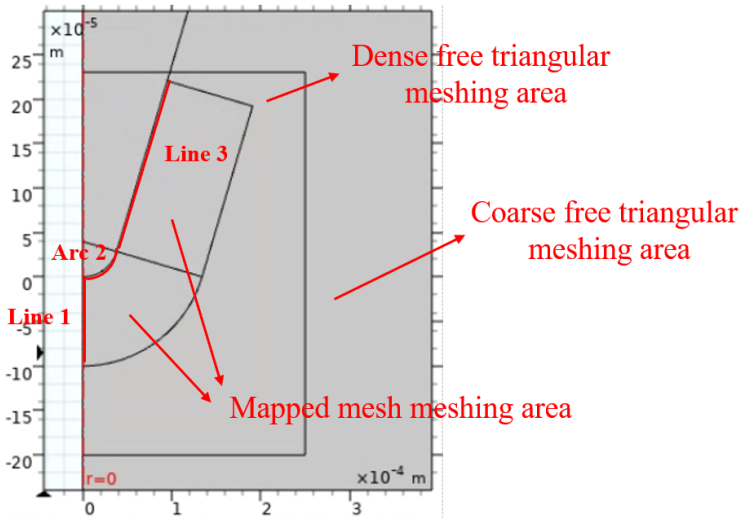

(a)

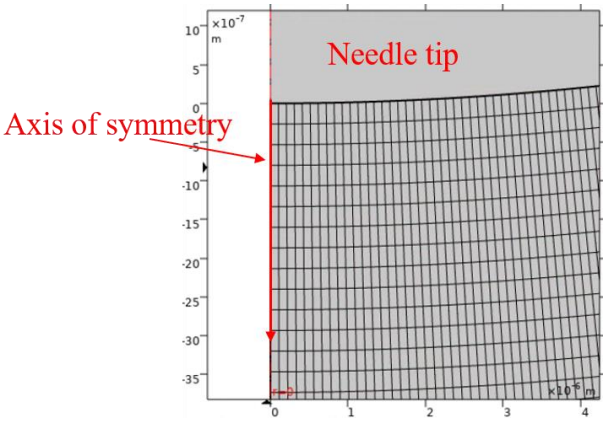

(b)

Figure 4-4 Meshing set-up used in Chapter 4 (a) boundaries of different meshing areas (b) zoomed-in plot of the meshing elements.

4.4 Cavity Formation in Cyclohexane

4.4.1 Dynamics of Electronic and Liquid Properties under Fixed Voltage Rise Rates

The distribution of time-dependent electric field magnitude along the axis of symmetry from the needle tip into cyclohexane with a voltage rise rate of 50 kV/ns is presented in Figure 4-5. Since no space charge density is considered in this chapter, the distribution of the electric field is in the shape of a Laplace field. From 2 ns to 8 ns, the maximum electric field magnitude happens at the needle tip from 7.37 MV/cm to 29.49 MV/cm.

The distribution of time-dependent electrostrictive force along the axis of symmetry from the needle tip into cyclohexane with a voltage rise rate of 50 kV/ns is shown in

Figure 4-6. The magnitude of electrostrictive force is defined to be positive when the direction of the electrostrictive force is upside towards the needle tip. According to Equation 4-3, the magnitude of electrostrictive force is positively related to the magnitude of the electric field magnitude. Therefore, with time ranging from 2 ns to 8 ns, the magnitude of the electrostrictive force also increases from 2.38×10^{11} N/m^3 to 3.81×10^{12} N/m^3.

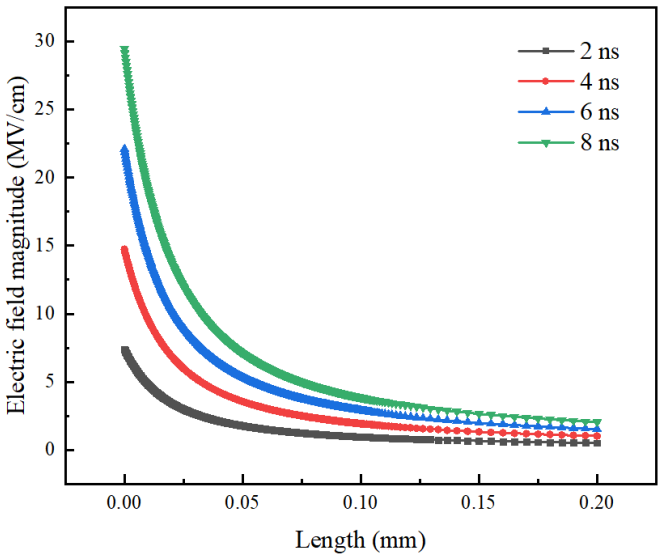

Figure 4-5 Distribution of electric field magnitude along the axis of symmetry from the needle tip into cyclohexane with a voltage rise rate of 50 kV/ns. Position 0 mm means the needle tip.

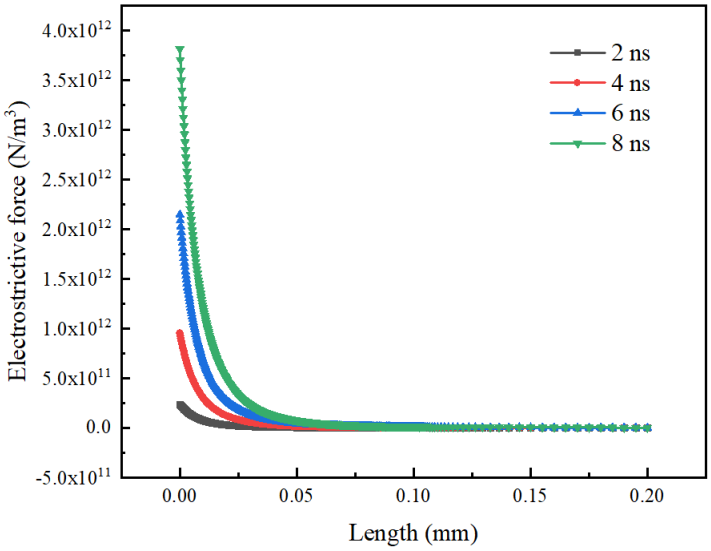

Figure 4-6 Distribution of electrostrictive force along the axis of symmetry from the needle tip into cyclohexane with a voltage rise ate of 50 kV/ns. Position 0 mm means the needle tip.

The corresponding direction of electrostrictive force in a 2D plot is shown in Figure 4-7. The directions of the red arrows represent the electrostrictive force direction. The lengths of the red arrows represent the magnitude of electrostrictive force in a logarithmic scale. According to the expression of electrostrictive force, as shown in Equation 4-3, the direction of the electrostrictive force is always towards where the electric field magnitude increases. Therefore, the direction of electrostrictive force is always towards the needle tip in the needle-plane geometry.

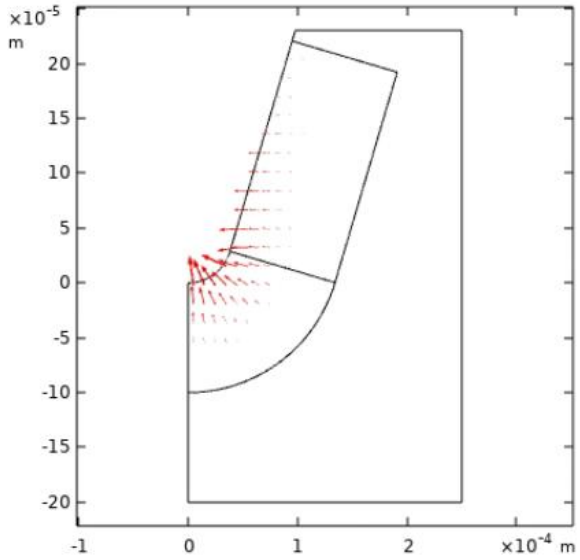

Figure 4-7 2D plot of the direction of electrostrictive force at 8 ns with a voltage rise rate of 50 kV/ns. Position 0 mm means the needle tip.

The distribution of time-dependent electrostrictive force pressure along the axis of symmetry from the needle tip into cyclohexane with a voltage rise rate of 50 kV/ns is shown in Figure 4-8. The minimum value of electrostrictive force pressure happens at the needle tip. With time increasing from 2 ns to 8 ns, the minimum value of the electrostrictive force pressure p_{EF} decreases from -2.5 MPa to -38 MPa.

Under the drive of electrostrictive force, the local cyclohexane near the needle tip is pushing towards the needle tip at a velocity of several m/s, as shown in Figure 4-9. The liquid velocity increases with the increase in electrostrictive force.

Under the drive of electrostrictive force and the movement of liquid, local liquid density also varies accordingly. The liquid density variation is calculated by Equation 4-5. In Figure 4-10, liquid density close to the needle tip is larger than ρ_{l_0}, while liquid density a bit further from the needle tip is smaller than ρ_{l_0}. The liquid density variation varies from -0.17% to 2.7%. The corresponding liquid thermodynamic pressure is shown in Figure 4-11. Due to the equation of state used to describe the relationship between

liquid density and its thermodynamic pressure, liquid thermodynamic pressure shows a similar trend to liquid density. Thermodynamic pressure is larger than atmospheric pressure when liquid density is higher than ρ_{l_0} close to the needle tip.

$$\rho_{\%} = (\rho_l - \rho_{l\_0})/\rho_{l\_0} \times 100\% \qquad \text{Equation 4-5}$$

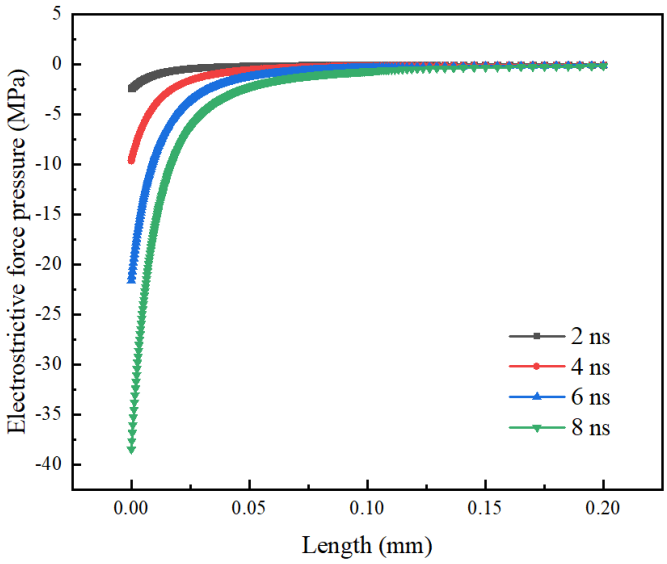

Figure 4-8 Distribution of electrostrictive force pressure along the axis of symmetry from the needle tip into cyclohexane with a voltage rise rate of 50 kV/ns. Position 0 mm means the needle tip.

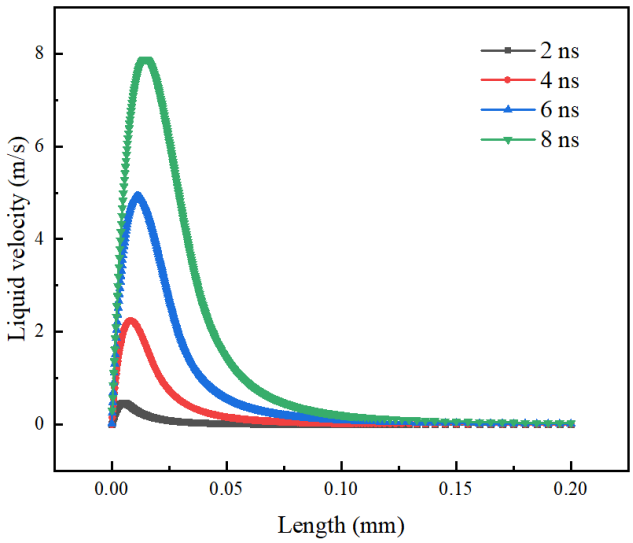

Figure 4-9 Distribution of liquid velocity along the axis of symmetry from the needle tip into cyclohexane with a voltage rise rate of 50 kV/ns. Position 0 mm means the needle tip.

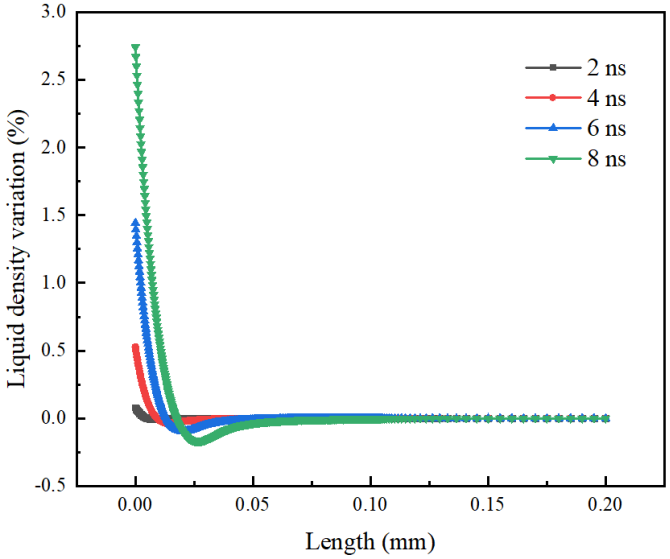

Figure 4-10 Distribution of liquid density variation along the axis of symmetry from the needle tip into cyclohexane with a voltage rise rate of 50 kV/ns. Position 0 mm means the needle tip.

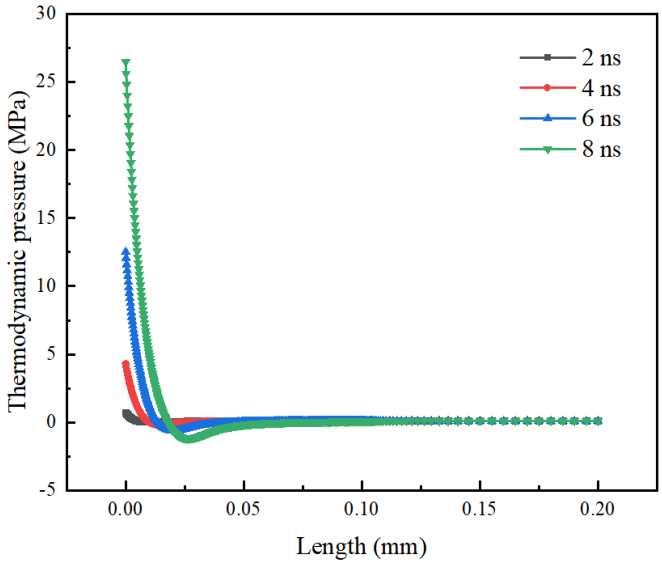

Figure 4-11 Distribution of thermodynamic pressure along the axis of symmetry from the needle tip into cyclohexane with a voltage rise rate of 50 kV/ns. Position 0 mm means the needle tip.

A summary of three kinds of pressure at 4 ns, which are the components of total pressure, is presented in Figure 4-12. As described above, the thermodynamic pressure p close to the needle tip is positive and much larger than atmospheric pressure $p_0 = 0.1$ MPa because liquid density ρ_l is larger than ρ_{l_0} under the drive of electrostrictive force. The electrostrictive force pressure p_{EF} is negative. The absolute value of p_{EF} is larger than p because the inertia of liquid prevents the quick variation of p under the drive of

electrostrictive force. Therefore, the total pressure p_{total} in the vicinity of the needle tip is negative.

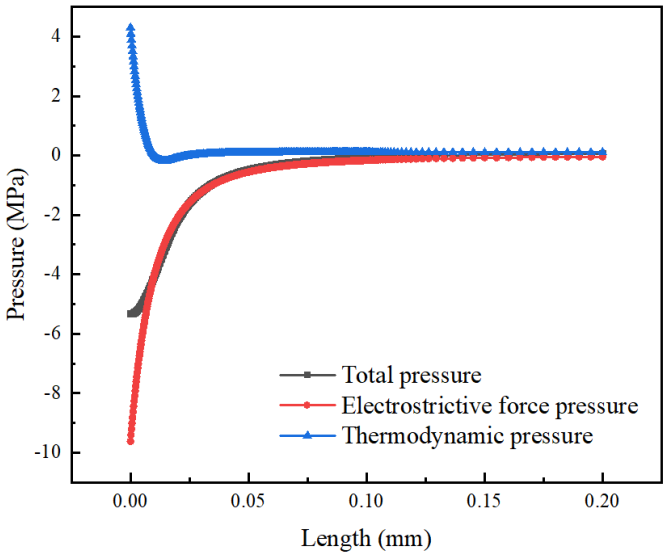

Figure 4-12 Distribution of total pressure, electrostrictive force pressure and thermodynamic pressure along the axis of symmetry from the needle tip into cyclohexane at 4 ns with a voltage rise rate of 50 kV/ns. Position 0 mm means the needle tip.

As mentioned in [113], when the total pressure of dielectric liquid is below a negative threshold, a cavity is likely to form. The theoretical calculation of the critical negative threshold for cavity formation p_c is expressed by Equation 4-6 according to nucleation theory [247]. p_c of deionised water is calculated to be from -184 MPa to -150 MPa based on Equation 4-6. However, in experiments, p_c in deionised water has been tested to range between -50 MPa and -6 MPa, which is an enormous overestimation [113, 248]. The reason for this over-estimation may be that p_c is sensitive to the degree of the purity of the liquid and the presence of dissolved gas and dust particles [113].

$$p_c = p_{sat} - \sqrt{\left(\frac{16\pi\sigma^3}{3kTln(NB/J_{NR})}\right)} \qquad \text{Equation 4-6}$$

Where p_{sat} is the vapour pressure of liquid, σ is the surface tension coefficient, k is the Boltzmann constant, N is the density of molecules and is 10^{27}~10^{28} m^{-3} for cyclohexane, B is the kinetic coefficient and is 10^{11}~10^{15} s [113, 249], J_{NR} is the nucleation rate equal to the density of vapour bubbles of a critical size appearing per one second and generally ranges from 10^{18}~10^{22}, and T is temperature.

In simulation [113], p_c in deionised water was assumed to be $p_{c\_water} = -30$ MPa. According to Equation 4-6, since p_c should be mainly dependent on the surface tension coefficient σ of liquid than on other parameters, and due to a lack of experimental

results on p_c for other liquids; in this current study, we simply assume that the differences in p_c of different dielectric liquids to be also dependent on σ. Comparing the surface tension coefficient of cyclohexane, which is 0.024 $\mathrm{N/m^3}$ [250], with deionised water, which is 0.072 $\mathrm{N/m^3}$ [251], the threshold for cavity formation in cyclohexane is estimated to be $p_{c\_cyclohexane} = -6$ MPa. Therefore, in this study, when the total pressure of cyclohexane is smaller than -6 MPa, a cavity is assumed to form. The total pressure along the axis of symmetry from 2 ns to 8 ns is shown in Figure 4-13. It should be noted that the minimum value of p_{total} is always at the needle tip, which is decreasing from -1.68 MPa to -12.02 MPa, with time decreasing from 2 ns to 8 ns. A 2D plot of the area where total pressure is smaller than the threshold for cavity formation is shown in Figure 4-14. It is indicated that the cavity formation area is very close to the needle tip. The distance from the needle tip is not far from 50 μm.

The time dependent variation of p_{EF}, p and p_{total} at the needle tip with a voltage rise rate of 50 kV/ns is shown in Figure 4-15. At the needle tip, p keeps increasing, which means liquid density is always larger than ρ_{l_0} at the needle tip, while p_{EF} keeps decreasing alongside increasing time. p_{total} gradually decreases to around -13.5 MPa and then becomes relatively stable.

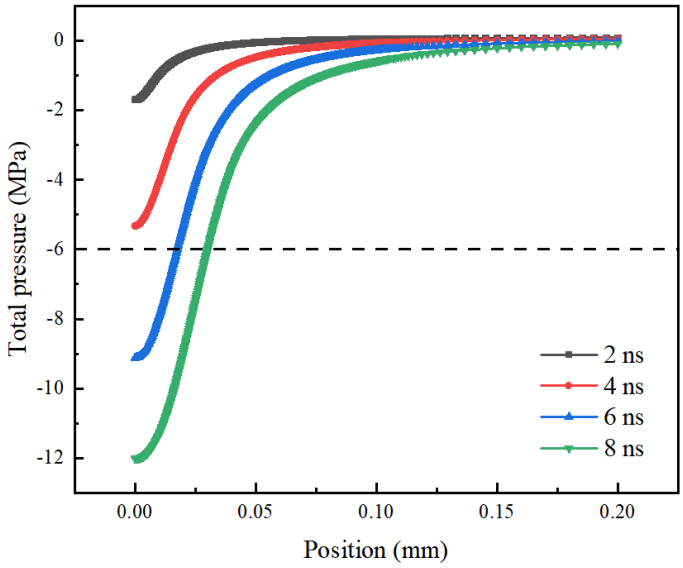

Figure 4-13 Time-dependent distribution of total pressure along the axis of symmetry from the needle tip into cyclohexane at different time moments with a voltage rise rate of 50 kV/ns. Position 0 mm means the needle tip.

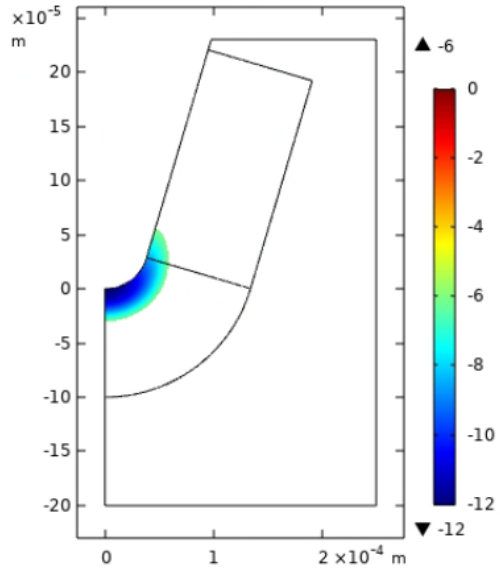

Figure 4-14 2D plot of the area where total pressure is smaller than the threshold for cavity formation at 8 ns with a voltage rise rate of 50 kV/ns.

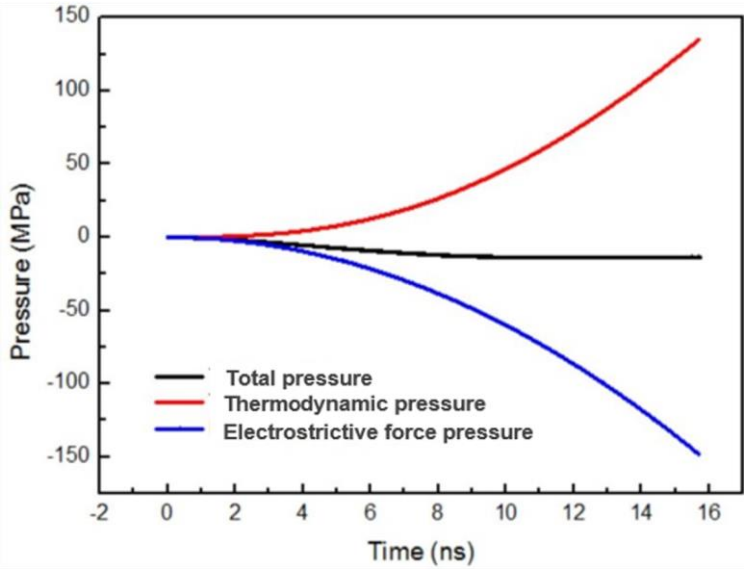

Figure 4-15 Time-dependent distribution of total pressure, electrostrictive force pressure and thermodynamic pressure at the needle tip at different time moments in cyclohexane with a voltage rise rate of 50 kV/ns.

4.4.2 Effects of Voltage Rise Rates on Cavity Formation in Cyclohexane

It is known that a faster voltage rise rate gives liquid a shorter time to come into motion due to inertia, which helps trigger cavity formation [113]. Since it is presented in Figure 4-15 that p_{total} may reach a stable value with an increase of applied voltage when the voltage rise rate equals 50 kV/ns, it will be interesting to study the effects of the voltage rise rate on the possibility of cavity formation.

As shown in Figure 4-16, the total pressure reaches the threshold for cavity formation faster under higher voltage rise rates. For voltage rise rates from 30 kV/ns to 70 kV/ns, the total pressures all reach a minimum value and then slightly increase or remain relatively stable. When the voltage rise rate is 30 kV/ns, the minimum p_{total} at the needle tip only reaches around -6 MPa. This means that when the voltage rise rate is smaller than 30 kV/ns, the minimum p_{total} may not reach the threshold for cavity formation due to electrostrictive force alone, even though the applied voltage magnitude keeps increasing.

By extracting the intersection points of the data lines with the black line of threshold for cavity formation in Figure 4-16, the required voltage magnitudes and time for cavity formation under different voltage rise rates are shown in Figure 4-17. It is found that the voltage magnitudes when p_{total} just reaches $p_{c\_cyclohexane}$ and the corresponding time both decrease with the increase in the voltage rise rate.

The time-dependent distribution of electrostrictive force and corresponding electrostrictive force pressure at the needle tip under different voltage rise rates ranging from 30 kV/ns to 90 kV/ns are shown in Figure 4-18 (a) and (b), respectively. Based on the time when a cavity has just formed in Figure 4-17, it is found that the electrostrictive force when a cavity has just formed decreases from 2.80×10^{12} N/m^3 to 8.52×10^{11} N/m^3 when the voltage rise rates increase from 30 kV/ns to 90 kV/ns. The corresponding electrostrictive force pressure also decreases from -7.80 MPa to -28.14 MPa.

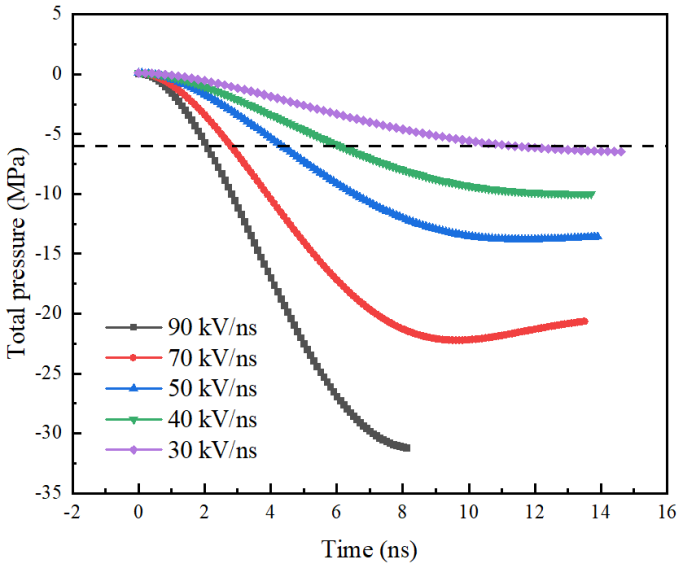

Figure 4-16 Effects of voltage rise rates on the total pressure variation at the needle tip in cyclohexane.

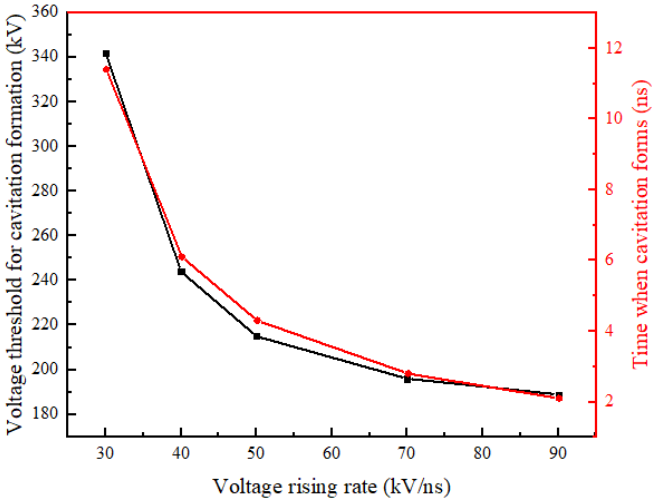

Figure 4-17 Applied voltage magnitude and the corresponding time when a cavity is just formed at different voltage rise rates in cyclohexane.

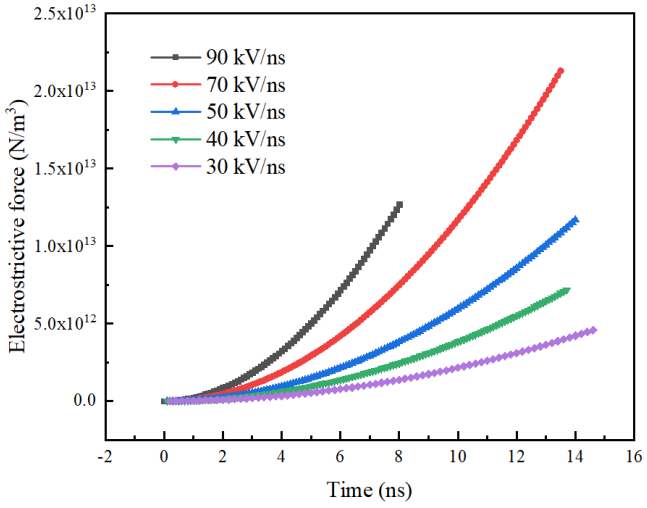

(a)

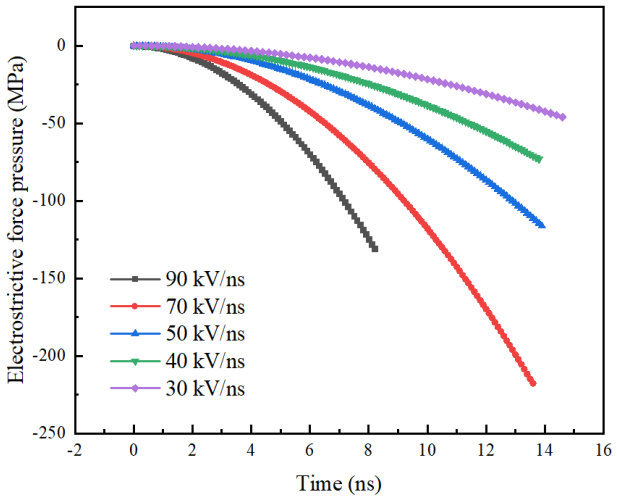

(b)

Figure 4-18 Time-dependent distribution of (a) electrostrictive force and (b) corresponding electrostrictive force pressure at the needle tip under different voltage rise rates.

In addition, when a cavity has just formed under different voltage rise rates, the maximum liquid velocity also decreases from 4.9 m/s to 1.7 m/s when the voltage rise rate increases from 30 kV/ns to 90 kV/ns, as shown in Figure 4-19. Besides, less liquid volume is pushed towards the needle tip under higher voltage rise rates.

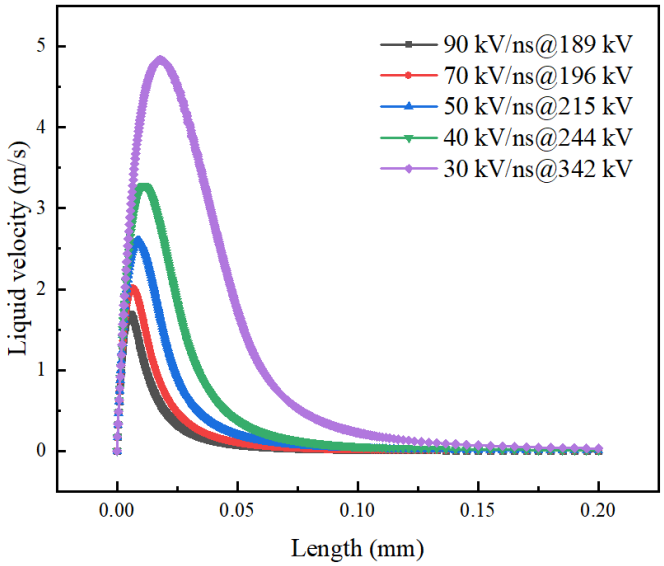

Figure 4-19 Comparison of liquid velocity along the axis of symmetry in cyclohexane under different voltage rise rates when the voltage magnitude reaches the threshold for cavity formation. Position 0 mm means the needle tip.

4.5 Comparison of Cavity Formation in Different Dielectric Liquids

Besides cyclohexane, rapeseed oil and deionised water are another two important dielectric liquids. Non-polar dielectric liquids such as mineral oil have been preferred in power transformers ever since the late 19th century. In recent years, new alternatives, namely ester liquids, have gradually been used due to their better biodegradability, higher flash/fire points and superior moisture tolerance than mineral oil [130, 252, 253]. In comparison, deionised water, as a kind of polar liquid, is suitable in pulsed applications and works well for short-term high-energy density storage due to high conductivity and relative permittivity, respectively [254]. Besides, deionised water is widely used when studying cavities by researchers [113, 115, 116, 245]. Therefore, it will be interesting to compare cavity formation dynamics among these dielectric liquids. Based on an estimation of the total pressure threshold of cavity formation in Section 4.4.1, $p_{c\_rapeseed\ oil}$ is estimated to be -9.31 MPa according to the surface tension of rapeseed oil, equalling 0.033 $\mathrm{N/m^3}$ [255].

4.5.1 Under a Voltage Rise Rate of 50 kV/ns

The distributions of electrostrictive force in the three dielectric liquids along the axis of symmetry at 2.5 ns with a voltage rise rate of 50 kV/ns are shown in Figure 4-20. The directions of the electrostrictive force of the three dielectric liquids are all towards the needle tip. It is found that the electrostrictive force in cyclohexane is around 2.5 times smaller than that in rapeseed oil due to their relative permittivity difference. However, due to the much larger relative permittivity of deionised water, the electrostrictive force in deionised water is more than 40 times larger than in cyclohexane and rapeseed oil. The maximum electrostrictive force at 2.5 ns for cyclohexane, rapeseed oil and deionised water is $3.72 \times 10^{11}\,\mathrm{N/m^3}$, $1.07 \times 10^{12}\,\mathrm{N/m^3}$ and $4.52 \times 10^{13}\,\mathrm{N/m^3}$, respectively, which all always happen at the needle tip.

The distributions of absolute values of electrostrictive force pressure of the three liquids along the axis of symmetry at 2.5 ns with a voltage rise rate of 50 kV/ns are shown in Figure 4-21. Note that all of the electrostrictive force pressures are a negative value but only the magnitudes are compared here. Due to the relative permittivity of deionised water being around 40 times larger than cyclohexane and rapeseed oil and the different simplified forms of $(\partial\varepsilon_r/\partial\rho_l)\cdot\rho_l$ based on the Clausius-Mosotti formula, the electrostrictive force pressure in deionised water is around 125 times and 50 times larger than that in cyclohexane and rapeseed oil, respectively. The absolute value of electrostrictive force pressure in rapeseed oil is around 2.5 times larger than that in cyclohexane.

Under the effects of different electrostrictive forces, a comparison of liquid density variation among cyclohexane, deionised water and rapeseed oil is shown in Figure 4-22. Since the electrostrictive force in deionised water is much larger than that in cyclohexane and rapeseed oil, the liquid density variation in deionised water at the needle tip is also at least 50 times larger than that in cyclohexane and rapeseed oil at 2.5 ns. Besides, the liquid density variations in cyclohexane and rapeseed oil at the needle tip at 2.5 ns are only 0.15% and 0.89%, respectively.

Since the lowest pressure always happens at the needle tip, it is reasonable to regard the voltage under which the total pressure in dielectric liquids p_{total} at the needle tip just reaches p_c as the voltage threshold for cavity formation. The time-dependent total pressure at the needle tip in the three dielectric liquids under a voltage rise rate of 50 kV/ns is shown in Figure 4-23. With the increase of time, the total pressure of deionised

water decreases extremely fast due to the large electrostrictive force. Therefore, the total pressure quickly reaches the threshold for cavity formation. In comparison, the total pressure of cyclohexane and rapeseed oil gradually drops but can also lead to cavity formation. Based on the estimated threshold of cavity formation among the three dielectric liquids, the voltage magnitude thresholds to form a cavity in cyclohexane, rapeseed oil and deionised water are around 215 kV, 330 kV and 35 kV, respectively. The required voltage to form a cavity in rapeseed oil is larger than that in cyclohexane.

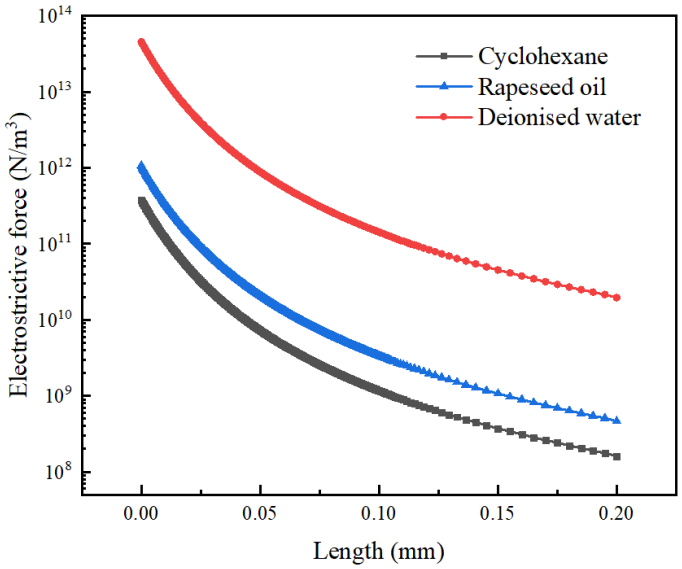

Figure 4-20 Comparison of the distribution of electrostrictive force along the axis of symmetry among cyclohexane, rapeseed oil and deionised water at 2.5 ns with a voltage rise rate of 50 kV/ns. Position 0 mm means the needle tip.

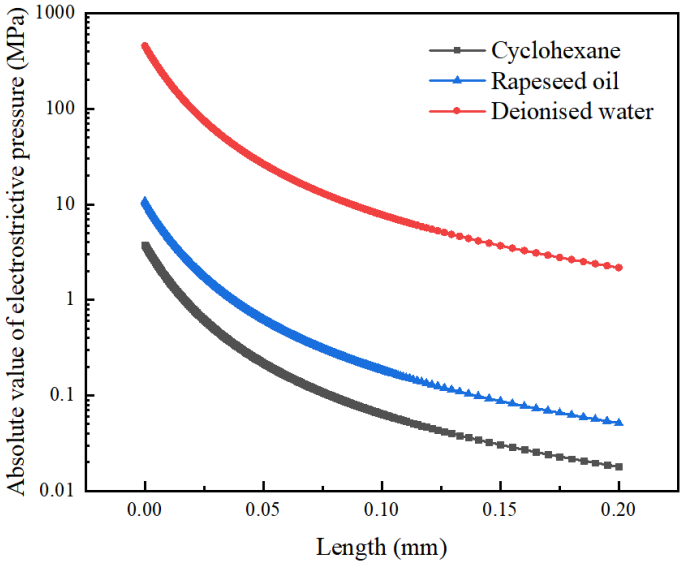

Figure 4-21 Comparison of the distribution of electrostrictive force pressure along the axis of symmetry among cyclohexane, rapeseed oil and deionised water at 2.5 ns with a voltage rise rate of 50 kV/ns. Position 0 mm means the needle tip.

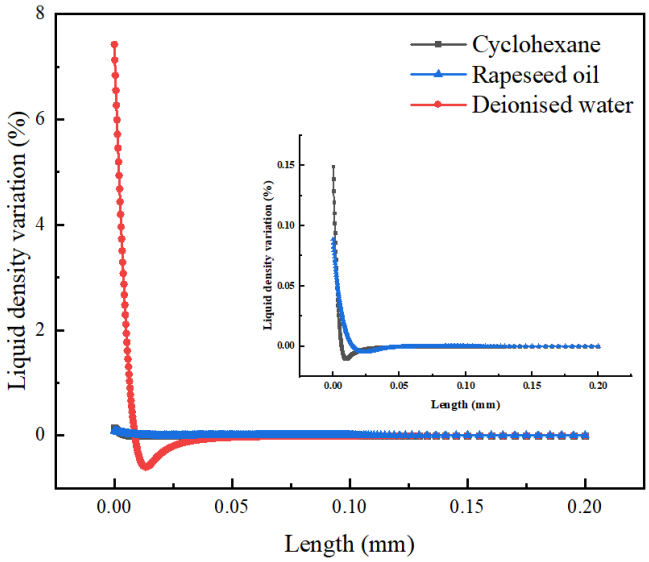

Figure 4-22 Comparison of the distribution of liquid density variation along the axis of symmetry among cyclohexane, rapeseed oil and deionised water at 2.5 ns with a voltage rise rate of 50 kV/ns. Position 0 mm means the needle tip.

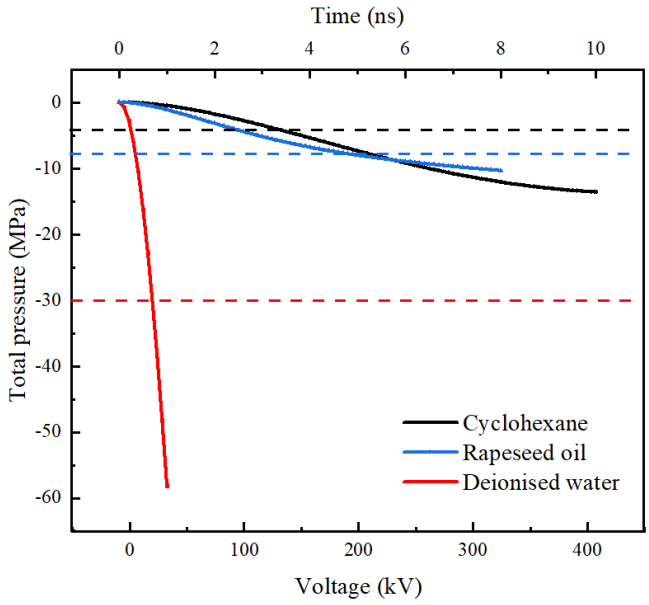

Figure 4-23 Time-dependent total pressure variation at the needle tip among cyclohexane, rapeseed oil and deionised water with a voltage rise rate of 50 kV/ns.

4.5.2 Under a Voltage Rise Rate of 90 kV/ns

Besides the comparison of the dynamics of cavity formation among the three dielectric liquids under a voltage rise rate of 50 kV/ns, differences in the cavity formation dynamics among the three dielectric liquids are also investigated under a voltage rise rate of 90 kV/ns.

The absolute value of the electrostrictive force pressure among the three dielectric liquids along the axis of symmetry at 1.5 ns is shown in Figure 4-24. Similar to the trend in Figure 4-21, the maximum value of the absolute value of electrostrictive force also occurs at the needle tip. The absolute value of electrostrictive force pressure is the highest in deionised water but lowest in cyclohexane. The absolute value of electrostrictive force pressure in rapeseed oil is around 3 times larger than that in cyclohexane.

The time-dependent total pressure at the needle tip in the three dielectric liquids under a voltage rise rate of 90 kV/ns is presented in Figure 4-25. The intersection points of the three solid lines with three dash lines are the cavity formation thresholds of the three dielectric liquids with a voltage rise rate of 90 kV/ns. Compared with Figure 4-23, when increasing the voltage rise rate from 50 kV/ns to 90 kV/ns, the cavity formation thresholds in cyclohexane, rapeseed oil and deionised water all decrease to 189 kV, 171 kV and 33.6 kV, respectively. It is also found that the differences in the thresholds for cavity formation of cyclohexane and rapeseed oil decrease with the increase of the voltage rise rate. At a voltage rise rate of 90 kV/ns, cyclohexane and rapeseed oil require relatively similar voltage magnitudes to form a cavity. Besides, the required voltage for cavity formation in deionised water is always larger than that in cyclohexane and rapeseed oil.

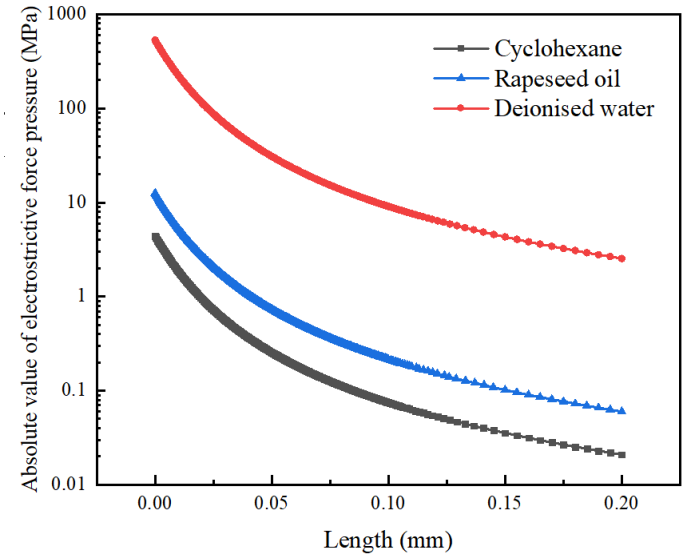

Figure 4-24 Comparison of the distribution of the absolute value of electrostrictive force pressure along the axis of symmetry among cyclohexane, rapeseed oil and deionised water at 1.5 ns with a voltage rise rate of 90 kV/ns. Position 0 mm means the needle tip.

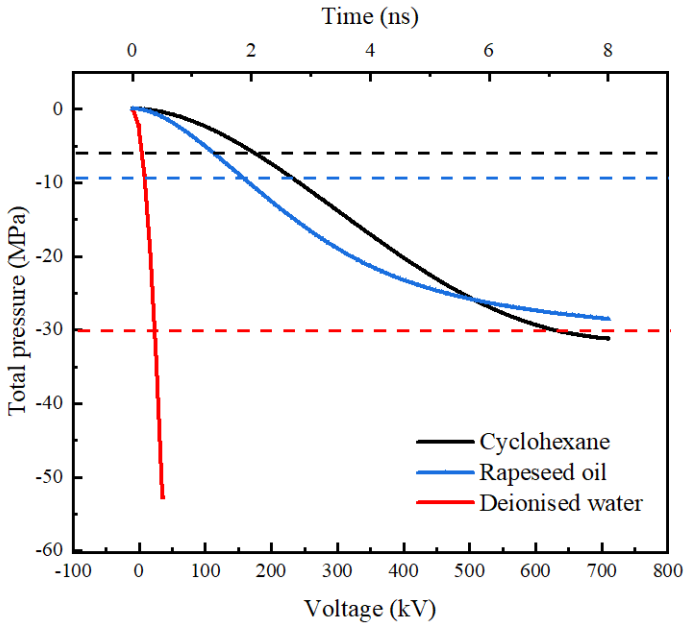

Figure 4-25 Time-dependent total pressure variation at the needle tip among cyclohexane, rapeseed oil and deionised water with a voltage rise rate of 90 kV/ns.

4.6 Summary

When considering cavity formation, electrostrictive force is the first thing to consider. Accordingly, this chapter conducted a detailed simulation of electrostrictive-force-induced cavity formation during streamer initiation, but without considering charge generation. The pressure thresholds of cavity formation in cyclohexane and rapeseed oil were estimated to be −6 MPa and −9.31 MPa, respectively, which were smaller than for deionised water due to their smaller surface tensions. The direction of electrostrictive force was always towards the needle tip. Besides, electrostrictive force always tended to stretch the liquid, making the electrostrictive force pressure negative. Under electrostrictive force, cyclohexane was pushed towards the needle tip at several m/s. In all the studied cyclohexane cases, the total pressure was always negative and reached its minimum value at the needle tip. Besides, a decrease in voltage rise rate increased the magnitude of the voltage required for cavity formation. When the voltage rise rate was smaller than 30 kV/ns, a cavity might be unable to form in cyclohexane due to electrostrictive force alone.

Compared with deionised water, the absolute values of electrostrictive force in cyclohexane and rapeseed oil were much smaller due to the relatively smaller relative permittivity of cyclohexane and rapeseed oil. Therefore, it was much more difficult to form a cavity in cyclohexane and rapeseed oil than in deionised water. Besides, under

a higher voltage rise rate, the differences in the threshold for cavity formation in cyclohexane and rapeseed oil were smaller.

According to the voltage magnitudes summarised in Figure 4-17, the corresponding electric field magnitude was summarised in Figure 4-26. It should be noted that the electric field magnitudes are already high enough for molecular ionization in cyclohexane under the selected electrode geometry, meaning that charge generation and the Coulomb force will also have effects on streamer and liquid dynamics. Therefore, besides electrostrictive force, the Coulomb force, shown as the first term on the right of Equation 4-1, should also be considered in order to provide more detailed descriptions about the streamer initiation stage.

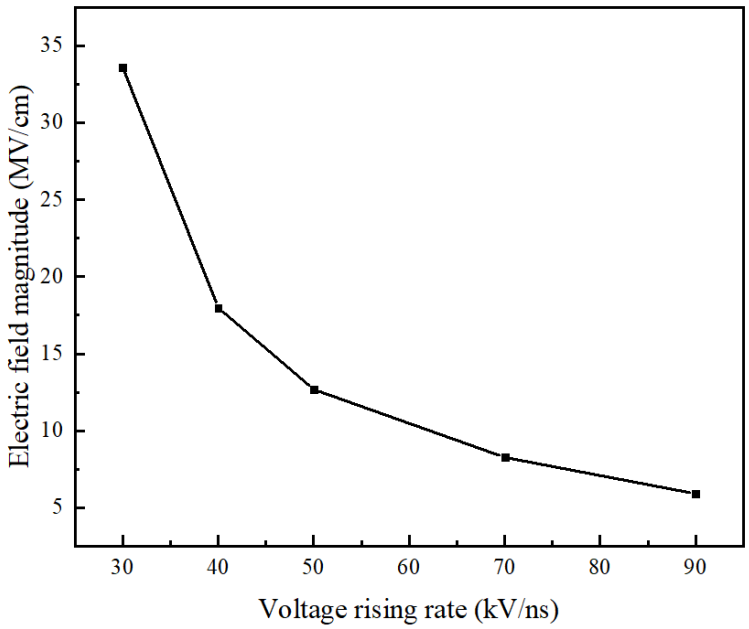

Figure 4-26 Electric field magnitude at the needle tip when a cavity just forms under voltage rise rates ranging from 30 kV/ns to 90 kV/ns.

5 Modelling of the Streamer Initiation Process in Cyclohexane

5.1 Introduction

Streamer initiation is the starting process of streamer phenomenon and of importance for insulation design. When speaking of simulating the streamer initiation process, charge dynamics are always simulated, while the cavity formation process is less considered. In general, electrostrictive force is usually considered to be responsible for cavity formation during streamer initiation (see the results in Chapter 4). However, space charge density, which can induce Coulomb force under an electric field, should also be considered based on the discussion in Section 4.6. Therefore, in this chapter, the positive streamer initiation process is simulated with the consideration of both electrostrictive force and Coulomb force. The mechanism involved during streamer initiation are initially discussed in Section 5.2, with the simulation methodology in Section 5.3. The electrical and liquid dynamics during streamer initiation process are described in detail in Section 5.4. The possibility of cavity formation under different voltage rise rates is discussed in Section 5.5, with the effect of voltage rise rates on the streamer initiation process then studied in Section 5.6. Finally, a summary of this chapter is presented in Section 5.7.

5.2 Description on the Mechanisms Involved in Streamer Initiation

Based on the experimental observation of streamer initiation, i.e. a visible streamer channel formed by a low-density area in a positive streamer [13, 34], the streamer initiation process in this study is defined as the period from the application of external voltage to the moment when local Joule heating energy density reaches the liquid vaporisation threshold.

A framework describing the streamer initiation mechanisms is proposed, as shown in Figure 5-1. Under slow-rising voltage waveform, direct ionization, which is considered as molecular ionization in this thesis, is induced by an increase in the local electric field. Under the electric field drift, free charges generated by molecular ionization lead to Joule heating and vaporise local dielectric liquids. The variation of liquid density caused by vaporisation can then be obverved by optical imagining in experiments, which is often treated as the moment of streamer initiation. When the voltage rise rate

is fast, according to Equation 4-2, the intensive variation of the local electric field can generate electrostrictive force. Besides, the generated charges caused by molecular ionization in the dielectric liquids can also lead to the generation of Coulomb force. The volumetric force acting on the dielectric liquids will push or stretch local liquid and force the liquid to move. When the total pressure p_{total} calculated by Equation 4-4 reaches a pre-defined negative threshold [126], a cavity is thought to be formed.

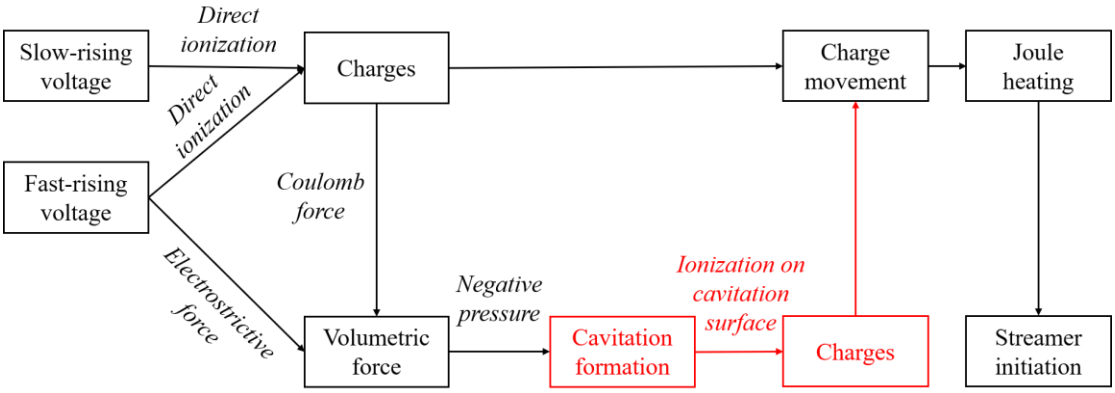

Figure 5-1 Mechanism during the streamer initiation process when considering charge generation and cavity formation.

Although the possibility of cavity formation based on the total pressure induced by Coulomb force and electrostrictive force can be simulated by the controlling equations introduced in Chapter 2, cavity formation (like shape and size), acceleration of electrons inside the cavity and the following impact ionization on the surface of the cavity are hard to simulate in one go due to the lack of references on the parameters related to the process. Therefore, the red blocks shown in Figure 5-1, once a cavity has been formed, are not simulated in this thesis.

5.3 Simulation Methodology

5.3.1 Controlling Equations

In this Chapter, the controlling equations are Poisson equation [106] as shown in Equation 3-3, charge continuity equations [105] are shown in Equation 3-4 to Equation 3-6 and Navier-stokes equations [111] as shown in Equation 2-14 and Equation 2-15. The description of energy density distribution in liquid due to Joule heating is expressed by the thermal diffusion equation as shown in Equation 5-1. The required energy density for raising the temperature of liquid from room temperature to boiling temperature can be calculated using Equation 5-2.

$$W = \int \vec{E} \cdot \sum_{\pm e} z_i \mu_i c_i \vec{E} \; dt \qquad \text{Equation 5-1}$$

$$W_R = \int_{T_0}^{T_b} c_l \rho_l dT$$ Equation 5-2

Where W is Joule heating energy density in liquid, T_0 is room temperature (298 K), T_b is boiling temperature (353 K under atmospheric pressure for cyclohexane) [224, 225], c_l is temperature dependent specific heat, z_i is a polarity factor and equals 1 for positive ion and equals -1 for negative ion and electron. For cyclohexane, $W_R = \int_{T_0}^{T_b} c_l \rho_l dT$ is the energy density required for a temperature rise from ambient temperature to boiling temperature and is calculated to be 8×10^7 J/m^3 [224-226].

5.3.2 Electrode Geometry, Voltage Excitation and Boundary Conditions

The needle-plane geometry is the same as in Chapter 3 and is shown in Figure 3-3. The boundary condition of Poisson equation is the same as in Chapter 3. The boundary conditions of charge continuity equations are the same as in Chapter 3. The boundary conditions of Navier-stokes equations are the same as in Chapter 4. The applied voltage waveforms are ramping voltage waveforms with fixed voltage rise rates which are similar with in Chapter 4.

5.3.3 Simulation Refinement

In this section, the detailed refinement study results are not shown. Only the dense meshing area and the refined setting are shown.

The dense meshing area is shown in Figure 5-2. The meshing elements in the meshing area are in a free triangular shape. After the refinement study, the meshing area width and mesh area length are refined to 200 μm and 0.35 mm, respectively. The meshing size on the line and arc mesh is 0.1 μm. The meshing size on the axis of symmetry inside the dense meshing area is 0.45 μm. The meshing size in the small meshing area and in the dense meshing area is 0.65 μm. The maximum time step size and relative tolerance are refined to 0.045 ns and 0.0007, respectively.

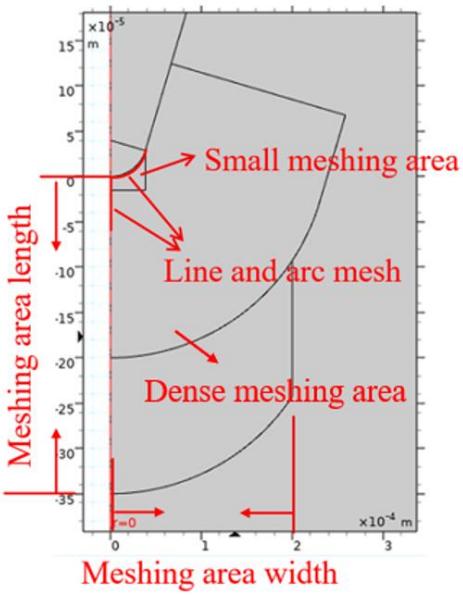

(a)

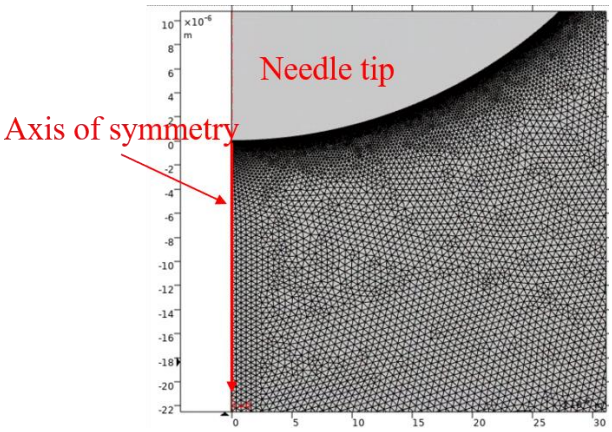

(b)

Figure 5-2 Meshing set-up used in Chapter 5. (a) boundaries of different meshing areas (b) zoomed-in plot of the meshing elements.

5.4 Streamer Dynamics during the Initiation Process

In experimental research [1], a 2nd mode streamer occurred under the step voltage with a magnitude below 100 kV and a voltage rise time of 400 ns. During the time interval before 400 ns, the voltage waveform with a rise rate of 0.25 kV/ns is the same as that with a voltage magnitude of 100 kV and rise time of 400 ns. Besides, it should be noted that the simulation results in Chapter 3 were also compared with the experimental results in [1]. Therefore, for the sake of consistency and convenience, a voltage rise rate of 0.25 kV/ns is adopted initially in this section to describe streamer dynamics during the streamer initiation process.

5.4.1 Electronic Dynamics

The electric field distribution along the axis of symmetry from 125 ns to 325 ns is shown in Figure 5-3. The electric field distribution from 125 ns to 325 ns in Figure 5-3 is the same as that in Figure 3-14 (a). The electric field peak leaves the needle tip and propagates into cyclohexane at 180 ns at 3.07 MV/ns. Then, the electric field peak magnitude keeps increasing to 325 ns at 4.27 MV/ns. This is also the maximum electric field magnitude before Joule heating energy density reaches the liquid vaporisation threshold.

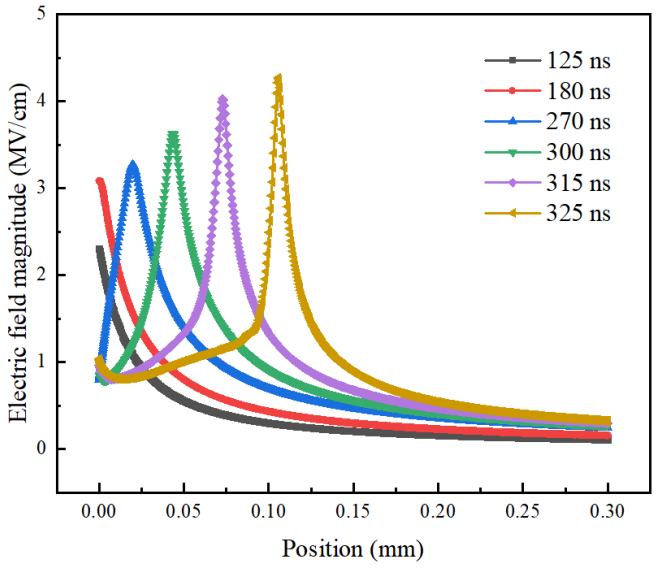

Figure 5-3 Electric field distribution along the axis of symmetry with a voltage rise rate of 0.25 kV/ns.

The corresponding space charge density distribution along the axis of symmetry is shown in Figure 5-4. The space charge density distribution trend is similar to the electric field distribution, both of which propagate into the liquid and show an increasing trend over time from 125 ns to 325 ns. The space charge density at the streamer tip is positive due to the separation of positive ions and electrons generated by molecular ionization. However, the space charge density inside the streamer channel close to the needle tip is negative, as shown by the purple line at 315 ns and the yellow line at 325 ns in Figure 5-4 (b). This is due to the motion of electrons towards the positive needle tip. It should be noted that when compared to the positive space charge density at the streamer tip, the negative space charge density inside the streamer channel close to the needle tip is much smaller.

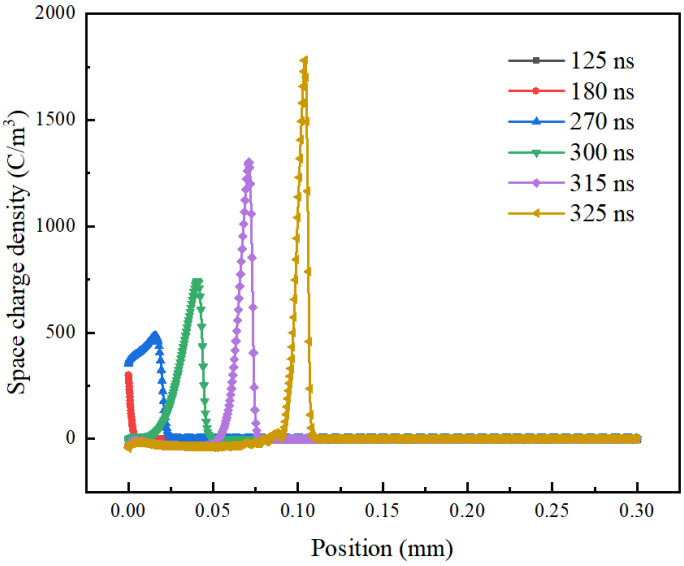

(a)

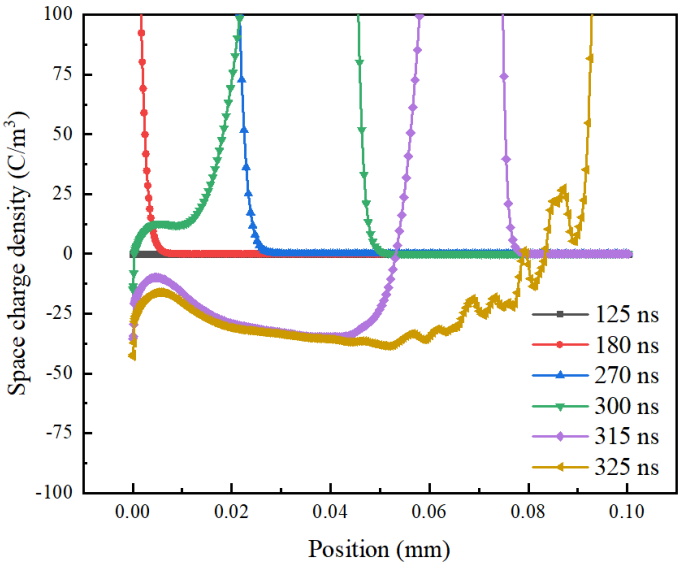

(b)

Figure 5-4 Space charge density distribution along the axis of symmetry with a voltage rise rate of 0.25 kV/ns. Note that (b) is a zoom-in plot of (a) from needle tip to the 0.1 mm position.

5.4.2 Liquid Dynamics

Apart from the electronic dynamics, liquid dynamics during streamer initiation is also of significant importance. Based on Figure 5-3 and Figure 5-4, according to the thermal diffusion equation, the Joule heating energy density distribution along the axis of symmetry can be calculated and is shown in Figure 5-5. Since the Joule heating energy density W is the integration of $\vec{E} \cdot \vec{J}$ over time interval, both electric field magnitude and space charge density magnitude have an effect on W. At the needle tip, both the

electric field and space charge density are smaller than those in the middle of the streamer channel. Therefore, the maximum Joule heating energy density is also inside the streamer channel instead of at the needle tip. The energy density just reaches 8×10^7 J/m^3 when the time instant is 325 ns, which means that a low-density channel should begin to form. Therefore, the time before 325 ns is defined as the streamer initiation stage under a voltage rise rate of 0.25 kV/ns.

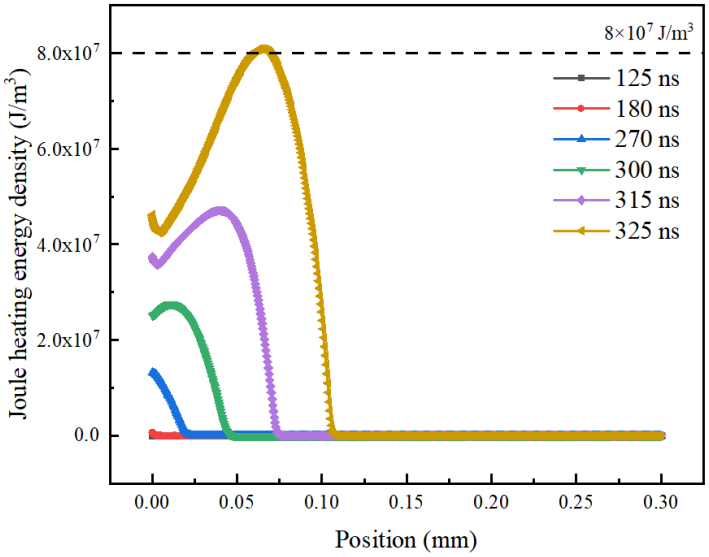

Figure 5-5 Joule heating energy density distribution along the axis of symmetry with a voltage rise rate of 0.25 kV/ns.

Based on the electric field distribution, the time-dependent distributions of electrostrictive force along the axis of symmetry are shown in Figure 5-6 (a). By the mathematical definition during FEM calculation, if the magnitude of electrostrictive force is positive, the direction of electrostrictive force is from the needle tip towards the ground plane, and vice versa. According to the second expression on the right side of Equation 4-2, the direction of electrostrictive force is towards the increase in the electric field magnitude. Therefore, according to the electric field distribution shown in Figure 5-3, the direction of electrostrictive force is towards the electric field peak at the streamer tip. The directions of electrostrictive force are opposite on both sides of the electric field peak. A 2D plot of the direction of electrostrictive force at 325 ns is shown in Figure 5-6 (b). The direction of the red arrows represents the direction of electrostrictive force, while the length of the red arrows represents the magnitude of electrostrictive force in a logarithmic scale. The electric field distribution in a 2D plot at 325 ns is also plotted. The streamer channel is defined by the electric field shell where the local electric field magnitude is the maximum. With reference to the electric field

shell, it is found that the directions of electrostrictive force are all towards the electric field shell on both sides. Besides, with time increasing, the magnitudes of electrostrictive force in both directions near the streamer tip also increase. The maximum magnitude is 1.3×10^{11} N/m^3 at 325 ns.

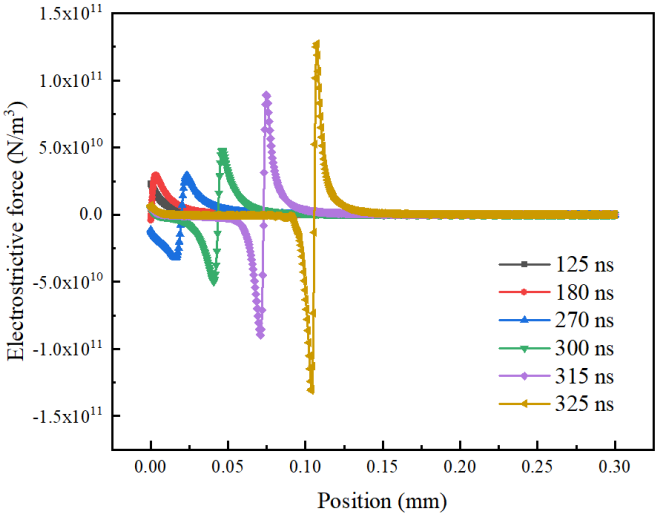

(a)

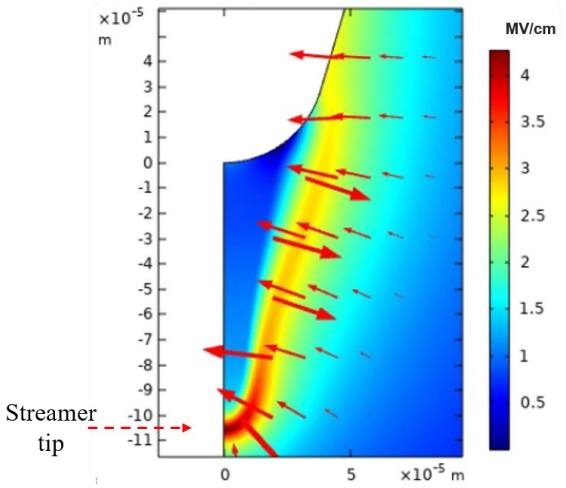

(b)

Figure 5-6 Distribution of electrostrictive force with a voltage rise rate of 0.25 kV/ns (a) along the axis of symmetry, and (b) in a 2D plot at 325 ns with the corresponding electric field distribution in a 2D plot.

Based on electric field distribution and space charge density distribution, the distribution of Coulomb force along the axis of symmetry is shown in Figure 5-7 (a). Since the electric field direction is towards the ground plane and the space charge density at the streamer tip is positive, the magnitude of Coulomb force is negative at streamer tip, meaning that the direction of Coulomb force is towards the ground plane. The magnitude of Coulomb force also increases with time and reaches a maximum of

7.0×10^{11} N/m^3 at 325 ns. In addition, due to the negative space charge density inside the streamer channel close to the needle tip, the Coulomb force direction here is positive and towards the needle tip, as shown in the small zoomed-in figure in Figure 5-7 (a). However, the magnitude of Coulomb force close to the needle tip inside the streamer channel is smaller than 5×10^9 N/m^3 due to the small electric field magnitude and space charge density. The 2D plot of the direction of Coulomb force at 325 ns is shown in Figure 5-7 (b), which clearly shows the direction of Coulomb force. However, the direction of Coulomb force at the needle tip is not shown due to its much smaller magnitude. Since the position of the streamer tip is ~0.1 mm, the space charge density some distance away from the streamer tip is zero, meaning that the corresponding Coulomb force is also zero.

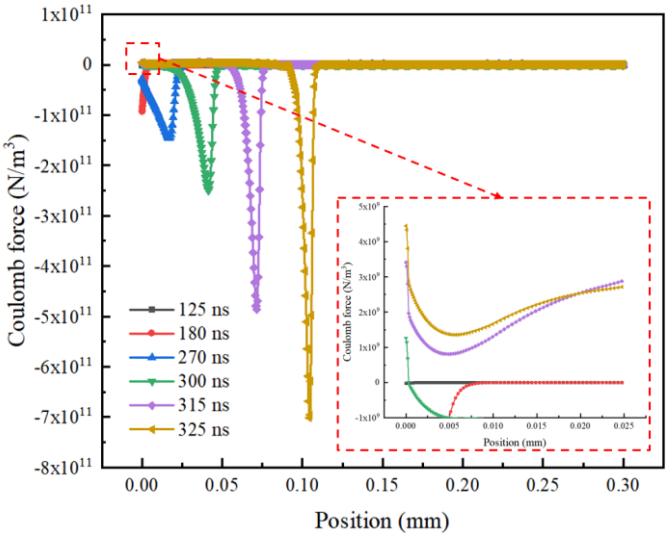

(a)

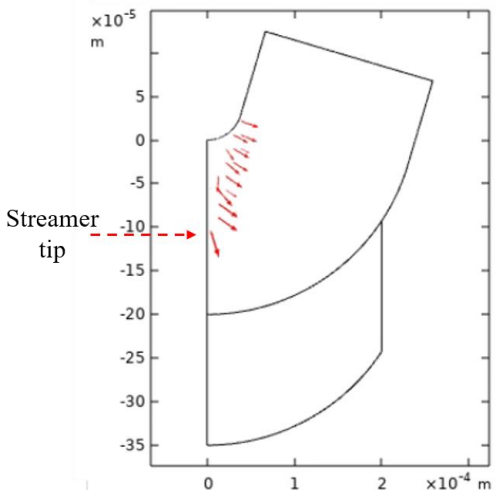

(b)

Figure 5-7 Distribution of Coulomb force with a voltage rise rate of 0.25 kV/ns (a) along the axis of symmetry, and (b) in a 2D plot at 325 ns.

Combining the electrostrictive force and Coulomb force together, the total volumetric force inside cyclohexane along the axis of symmetry is shown in Figure 5-8. The negative peak magnitude of total volumetric force is 7-10 times larger than the positive peak magnitude during streamer propagation. Comparing the magnitude of Coulomb force, electrostrictive force and total force, Coulomb force can be regarded as the dominating force during streamer initiation. Therefore, when the electric field peak leaves the needle tip and propagates into cyclohexane, the total volumetric force pushes the liquid outwards the needle tip. The liquid velocity induced by the total volumetric force is shown in Figure 5-9. The maximum liquid velocity is ~6 m/s with its direction moving towards the ground plane. Besides, the volume of moving liquid is increasing with the movement of the streamer tip, meaning that more liquids are pushed by the total volumetric force.

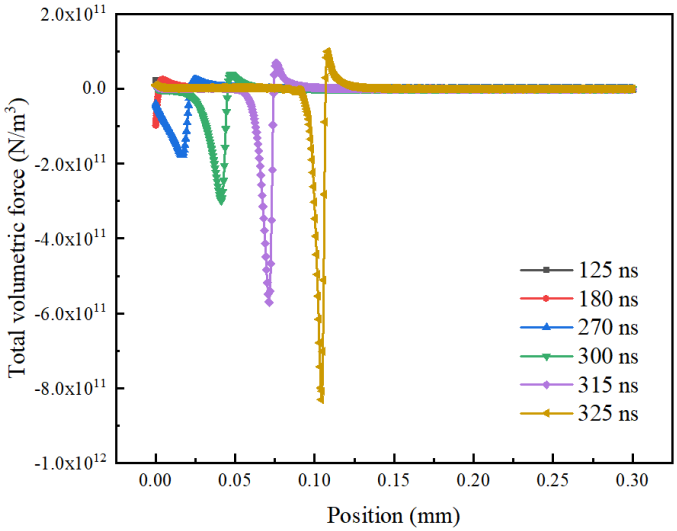

Figure 5-8 Distribution of total volumetric force along the axis of symmetry with a voltage rise rate of 0.25 kV/ns.

Due to the total volumetric force, liquid density will also change accordingly. Liquid density variation extent $\rho_{\%}$ along the axis of symmetry is shown in Figure 5-10. Liquid density variation is calculated according to Equation 4-5. At the streamer tip, since the total volumetric force is pushing the liquid towards the ground plane, liquid moves towards the ground plane so that the liquid density is larger than the initial liquid density ρ_{l_0}, with the liquid density smaller than ρ_{l_0} inside the streamer channel. The variation in liquid density at the streamer tip increases to the maximum at 0.4% at 325 ns, while the liquid density variation inside the streamer channel is always around -0.15%. Besides, the volume of liquid with a density smaller than ρ_{l_0} increases with time.

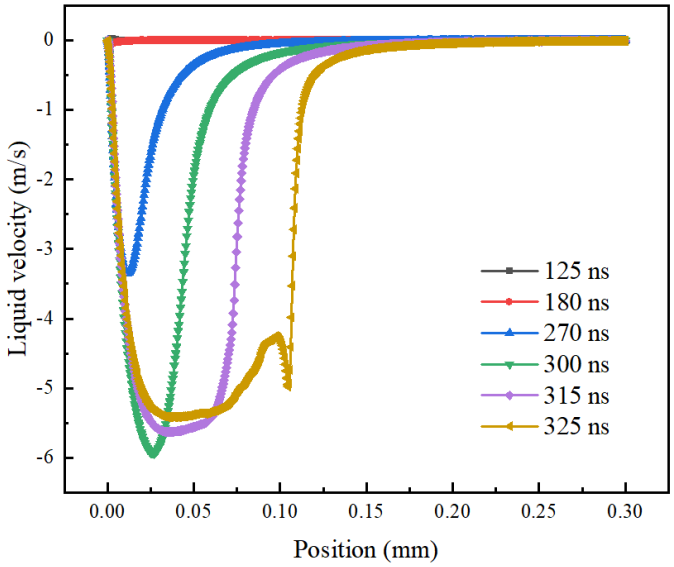

Figure 5-9 Distribution of liquid velocity along the axis of symmetry with a voltage rise rate of 0.25 kV/ns.

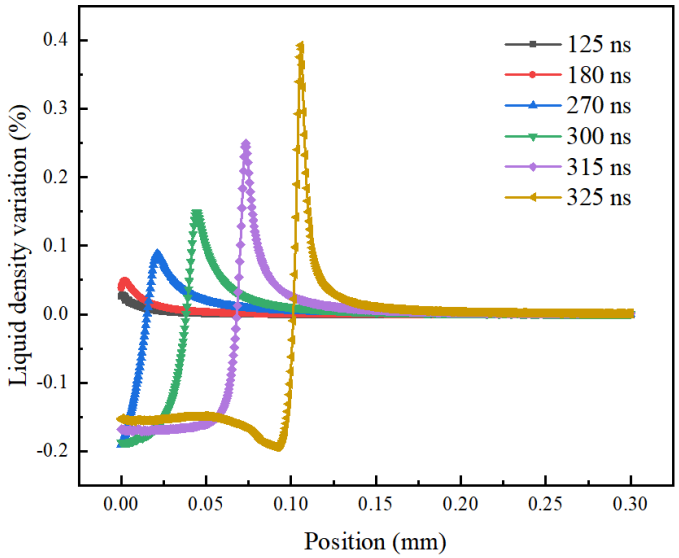

Figure 5-10 Distribution of liquid density variation along the axis of symmetry with a voltage rise rate of 0.25 kV/ns.

Based on the equation of state of cyclohexane, the distribution of thermodynamic pressure p of cyclohexane is shown in Figure 5-11, which has a similar shape to that in Figure 5-10. The thermodynamic pressure of cyclohexane is 0.1 MPa under atmospheric pressure. At the streamer tip, thermodynamic pressure increases with time and is ~3.2 MPa at 325 ns. The thermodynamic pressure remains around -1 MPa inside the streamer channel because the liquid density variation inside the streamer channel is only about -0.15%.

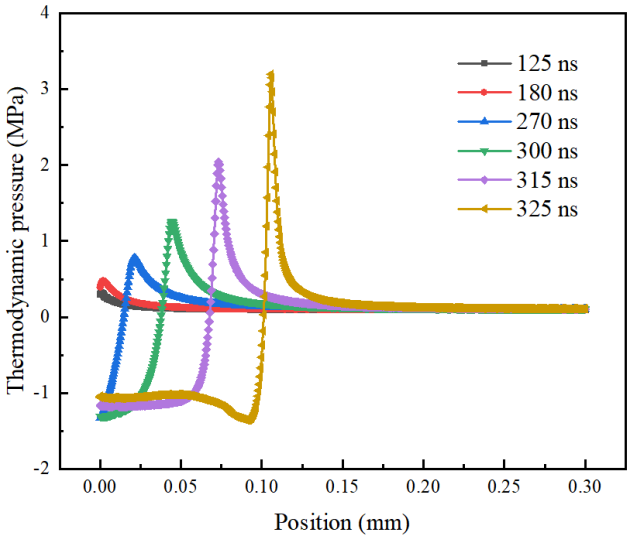

Figure 5-11 Distribution of thermodynamic pressure along the axis of symmetry with a voltage rise rate of 0.25 kV/ns.

In addition to the effects on the movement of liquid and the variation in liquid density, the volumetric force may also lead to cavity formation when the total pressure is below a pre-defined threshold, as shown in Chapter 4. The calculations of electrostrictive force pressure and Coulomb force pressure are shown in Equation 4-4. The time-dependent distribution of electrostrictive force pressure along the axis of symmetry is shown in Figure 5-12. The shape of electrostrictive force pressure is similar to that of electric field distribution. The value of electrostrictive force pressure is always negative, meaning that the electrostrictive force is always stretching the liquid. The minimum value of electrostrictive force pressure is −0.8 MPa. Compared with the threshold of the negative pressure of cavity formation of −6 MPa in cyclohexane, the magnitude of electrostrictive force pressure is too small.

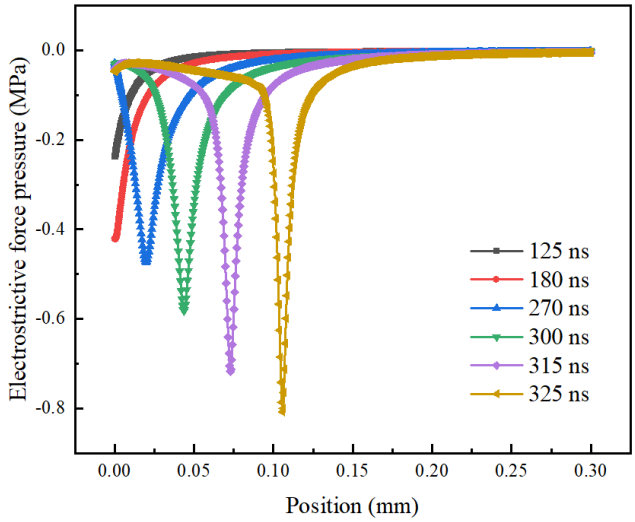

Figure 5-12 Distribution of electrostrictive force pressure along the axis of symmetry with a voltage rise rate of 0.25 kV/ns.

The distribution of Coulomb force pressure along the axis of symmetry is shown in Figure 5-13. Different from the nature of electrostrictive force that always stretches the liquid and generates negative pressure, Coulomb force pressure under positive polarity is always positive with a voltage rise rate of 0.25 kV/ns. The magnitude of Coulomb force pressure increases with time. The magnitude of Coulomb force pressure peak is ~4 MPa at 325 ns, which is 5 times larger than that of electrostrictive force pressure. The position of the peak of Coulomb force pressure is slightly behind the space charge density peak.

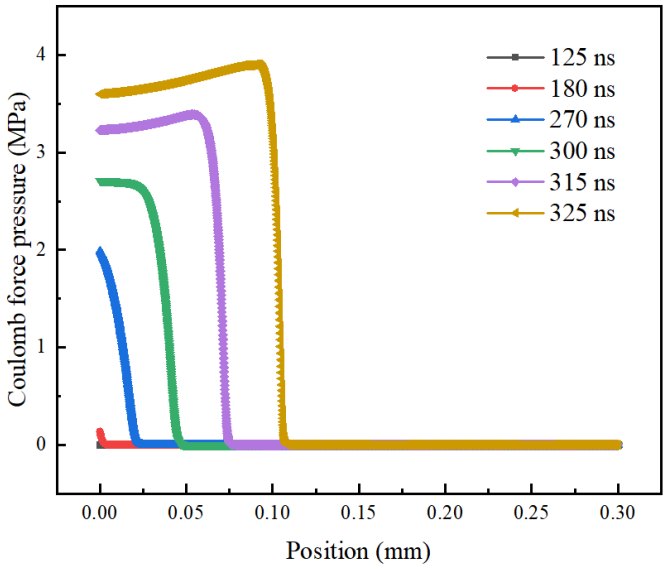

Figure 5-13 Distribution of Coulomb force pressure along the axis of symmetry with a voltage rise rate of 0.25 kV/ns.

The distribution of total pressure p_{total}, which is the sum of electrostrictive force pressure, Coulomb force pressure and thermodynamic pressure, is shown in Figure 5-14. The total pressure of a positive streamer in cyclohexane is always positive in the present simulation. The maximum total pressure is 3.0 MPa at 325 ns. Since a negative threshold is required for cavity formation, it is noted that it is hard to form a cavity during the streamer initiation process under this voltage rise rate of 0.25 kV/ns.

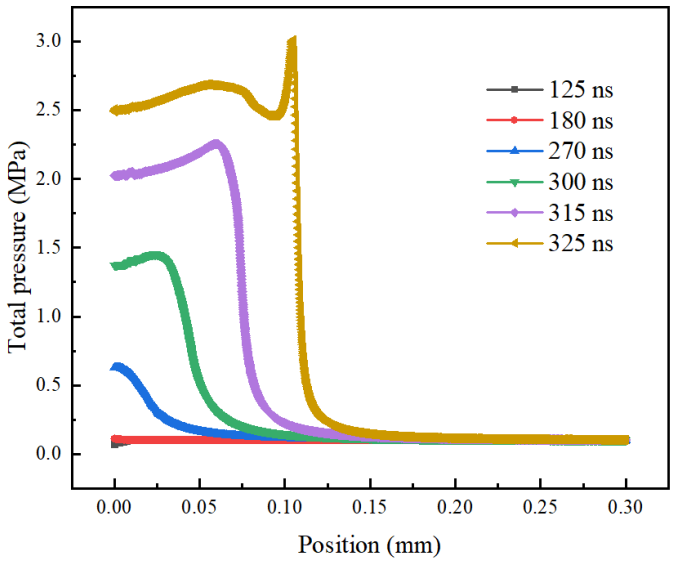

Figure 5-14 Distribution of total pressure along the axis of symmetry with a voltage rise rate of 0.25 kV/ns

5.5 Possibility of Cavity Formation during Streamer Initiation

In Section 5.4, streamer dynamics with a voltage rise rate of 0.25 kV/ns have been studied. However, it is also found that it is hard to form a cavity under a low voltage rise rate. In Chapter 4, simulation results showed that a cavity is likely to form under electrostrictive force alone in cyclohexane under an extremely high voltage rise rate higher than 30 kV/ns. Therefore, in this section, higher voltage rise rates of 70 kV/ns and 30 kV/ns are applied to study the possibility of cavity formation during positive streamer initiation in cyclohexane.

Based on calculation, under a relatively fast voltage rise rate, the Joule heating energy density distribution reaches the threshold for liquid vaporisation at 2.3 ns at a voltage rise rate of 70 kV/ns and 5 ns at a voltage rise rate of 30 kV/ns. Since the maximum variation of different kinds of force and pressure usually occurs at time t_W when Joule heating energy density reaches the threshold for liquid vaporisation, the distributions of different pressure are compared at t_W in the following study.

The distributions of the thermodynamic pressure along the axis of symmetry at t_W with voltage rise rates of 70 kV/ns and 30 kV/ns are shown in Figure 5-15. The thermodynamic pressure is positive at the streamer tip and negative inside the streamer channel. Compared with the thermodynamic pressure under a voltage rise rate of 0.25 kV/ns in Figure 5-11, higher voltage rise rates of 70 kV/ns and 30 kV/ns show a smaller positive thermodynamic pressure at the streamer tip and smaller negative

thermodynamic pressure inside the streamer channel. The magnitude of thermodynamic pressure is related to the variation of liquid density. Since the time for liquid to react with the volumetric force is too short under voltage rise rates of 70 kV/ns and 30 kV/ns in comparison with a small voltage rise rate of 0.25 kV/ns, liquid has less time to react with the volumetric force. Therefore, the magnitudes of thermodynamic pressure are smaller under extremely higher voltage rise rates.

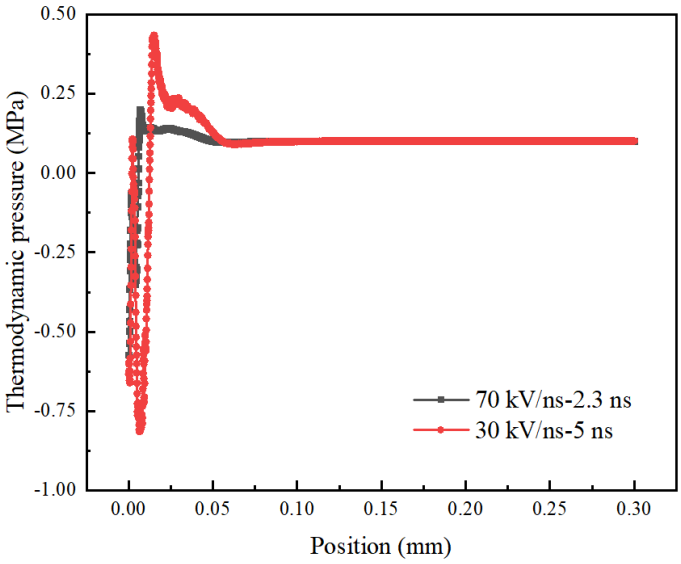

Figure 5-15 Effects of voltage rise rates on the distribution of thermodynamic pressure along the axis of symmetry at the time when Joule heating energy density reaches the threshold for liquid vaporisation with voltage rise rates of 70 kV/ns and 30 kV/ns.

The distributions of electrostrictive force pressure along the axis of symmetry under voltage rise rates of 70 kV/ns and 30 kV/ns at t_W are presented in Figure 5-16. The minimum electrostrictive force pressure under a voltage rise rate of 30 kV/ns is ~ -0.84 MPa. Increasing the voltage rise rate from 30 kV/ns to 70 kV/ns decreases the minimum value of electrostrictive force pressure to ~ -0.95 MPa. Besides, compared to the electrostrictive force pressure shown in Figure 5-12 with a voltage rise rate of 0.25 kV/ns, the electrostrictive force pressure with voltage rise rates of 70 kV/ns and 30 kV/ns shows two minimum peaks. However, it has to be noted that this phenomenon is not fully understood yet. Besides, the minimum values of the electrostrictive force pressure are both smaller than that with a voltage rise rate of 0.25 kV/ns.

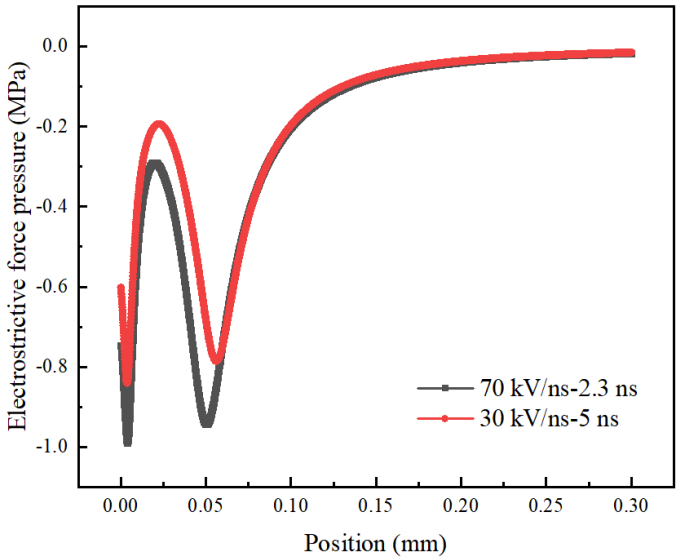

Figure 5-16 Effects of voltage rise rates on the distribution of electrostrictive force pressure along the axis of symmetry at the time when Joule heating energy density reaches the threshold for liquid vaporisation with voltage rise rates of 70 kV/ns and 30 kV/ns.

The distributions of Coulomb force pressure along the axis of symmetry with voltage rise rates of 70 kV/ns and 30 kV/ns at t_W are shown in Figure 5-17. Different from the electrostrictive force value which is always negative, Coulomb force pressure is calculated to be always positive. The maximum values of Coulomb force pressure inside the streamer channel occur at the needle tip and are 4.6 MPa and 3.8 MPa with voltage rise rates of 70 kV/ns and 30 kV/ns, respectively.

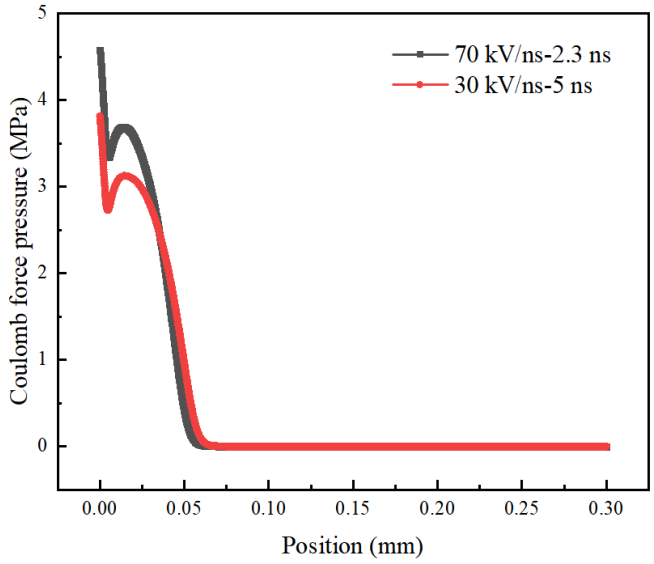

Figure 5-17 Effects of voltage rise rates on the distribution of Coulomb force pressure along the axis of symmetry at the time when Joule heating energy density reaches the threshold for liquid vaporisation with voltage rise rates of 70 kV/ns and 30 kV/ns.

The total pressure distribution along the axis of symmetry under different voltage rise rates at t_W is shown in Figure 5-18. Under voltage rise rates of 30 kV and 70 kV/ns, the total pressure is positive close to the needle tip and negative near the streamer tip. Increasing the voltage rise rate from 30 kV/ns to 70 kV/ns decreases the total pressure to a small extent. In comparison, it should be mentioned that the total pressure with a voltage rise rate of 0.25 kV/ns is always positive. However, the total pressure under voltage rise rates of 30 kV/ns and 70 kV/ns still does not reach the threshold for cavity formation of -6 MPa in cyclohexane before t_W. Therefore, it is indicated that a cavity may not form during the initiation stage in the present modelling.

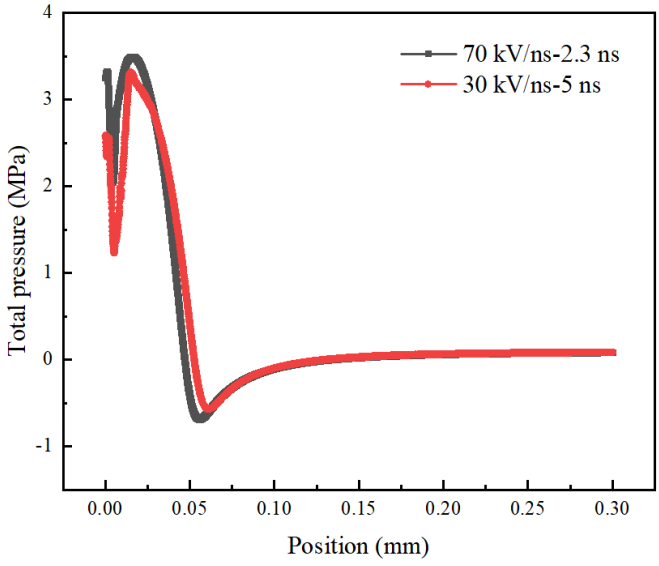

Figure 5-18 Effects of voltage rise rates on the distribution of total pressure along the axis of symmetry at the time when Joule heating energy density reaches the threshold for liquid vaporisation with voltage rise rates of 70 kV/ns and 30 kV/ns.

5.6 Effects of Voltage Rise Rates on Streamer Initiation

As direct cavity formation is less likely to occur in a positive streamer in cyclohexane, Joule heating induced streamer initiation is assumed to be the key mechanism for initiating a positive streamer in this study.

For general voltage excitation, such as a standard lightning impulse, a voltage rise rate of 0.25 kV/ns means that the peak voltage magnitude is 300 kV at the voltage rise time of 1200 ns. 300 kV is high enough for a breakdown occurrence in the needle-plane geometry with a tip radius of 40 μm and gap distance of 50 mm. Therefore, relatively small voltage rise rates ranging from 0.25 kV/ns to 0.075 kV/ns are excited on the needle geometry to study their effects on streamer initiation. It should be noted that a

voltage of 0.075 kV/ns represents the peak voltage magnitude of 90 kV at the voltage rise time of 1200 ns.

The effect of voltage rise rates on streamer initiation time is shown in Figure 5-19. With voltage rise rate decreases from 0.25 kV/ns to 0.075 kV/ns, the streamer initiation time increases from 325 ns to 912 ns. However, the corresponding streamer initiation voltage (see Figure 5-20), decreases from 81.25 kV to 61.4 kV, which conforms to the experimental observations on the relationship between voltage rise rate and streamer initiation voltage [62].

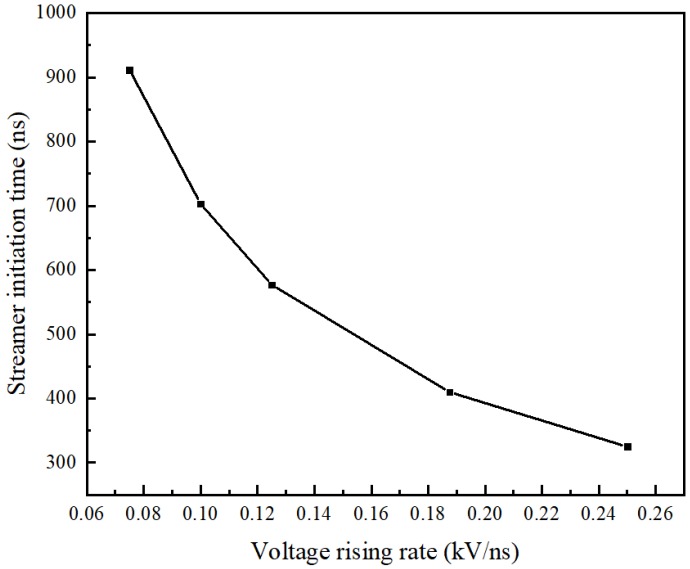

Figure 5-19 Effects of voltage rise rates on streamer initiation time.

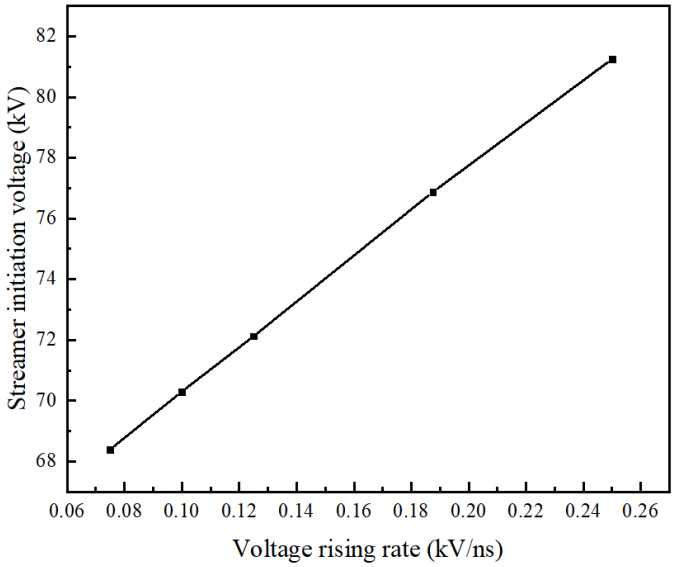

Figure 5-20 Effects of voltage rise rates on streamer initiation voltage.

The effects of voltage rise rates on the relationship between streamer initiation length and time are shown in Figure 5-21. With voltage rise rates decreasing from 0.25 kV/ns

to 0.075 kV/ns, the time for the electric field peak leaves the needle tip increases from 180 ns to 563 ns. Besides, the streamer initiation length, which is defined by the position of the electric field peak, decreases from 0.1057 mm to 0.0611 mm as shown in the black dash line in Figure 5-21.

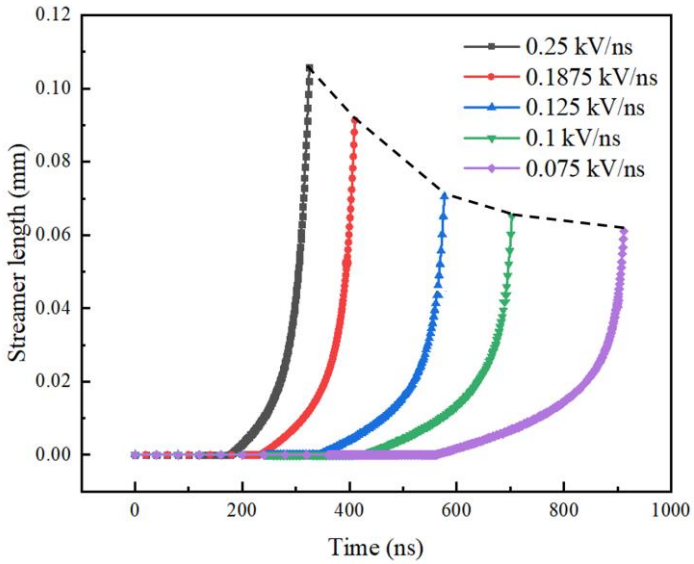

Figure 5-21 Effects of voltage rise rates on time-dependent streamer initiation length.

5.7 Summary

This chapter has presented a detailed description of the dynamics of streamer initiation by considering both electrostrictive force and Coulomb force. During streamer initiation with a voltage rise rate of 0.25 kV/ns, the electrostrictive force pressure was negative and the Coulomb force pressure positive. The minimum electrostrictive force pressure existed at the streamer tip with a minimum value of ~−0.8 MPa. The maximum Coulomb force pressure also occurred close to the streamer tip with a maximum value of ~4 MPa. The total pressure inside the streamer channel during streamer initiation was always positive, indicating that a cavity may not form during the streamer initiation stage with a voltage rise rate of 0.25 kV/ns.

For higher voltage rise rates of 70 kV/ns and 30 kV/ns, the electrostrictive force pressure was still negative and the Coulomb force pressure positive. Increasing the voltage rise rate from 30 kV/ns to 70 kV/ns slightly decreased the minimum electrostrictive force pressure from −0.84 MPa to −0.95 MPa. The Maximum Coulomb force pressure however increased from 3.8 MPa to 4.6 MPa. The total pressure close to the needle tip was positive and the total pressure close to the streamer tip was negative. Overall, the total pressure still did not reach the threshold for cavity

formation inside the streamer channel, indicating that a cavity may not form during the positive streamer initiation stage based on the present study.

For relatively slow voltage rise rates decreasing from 0.25 kV/ns to 0.075 kV/ns, Joule heating induced streamer initiation was assumed to be the key mechanism for initiating a positive streamer. The streamer initiation voltage decreased from 81.25 kV to 61.4 kV, while the streamer initiation time increased from 325 ns to 912 ns. The corresponding streamer initiation length also decreased from 0.1057 mm to 0.0611 mm. The effects of voltage rise rates on streamer dynamics in the simulation were similar to the trend observed in experimental studies [62], which confirms that decreasing voltage rise rate reduces streamer initiation length and streamer initiation voltage but increases streamer initiation time.

6 Modelling of the Low-density Channel Formation during Streamer Propagation

6.1 Introduction

Chapter 5 discussed and simulated the electrical and liquid dynamics during streamer initiation. Another important aspect of the streamer process is the dynamics during the propagation stage. As is introduced in Chapter 2, although many researchers have been simulating streamer propagation using the continuous model or discrete model, the low-density channel formation inside streamer channel is still one of the most difficult issues to study. In Chapter 3, the voltage drop inside the streamer channel was relatively high when compared with other experiments [1], which may be due to a lack of consideration of the low-density channel formation. In this chapter, the streamer propagation dynamics that with consideration of the low-density channel formation are simulated. The simulation methodology is initially introduced in Section 6.2, with simulation results on the dynamics of streamer propagation when considering the low-density channel formation presented in Section 6.3, followed by a detailed discussion of the results in Section 6.4. and finally, a summary of this chapter in Section 6.5.

6.2 Simulation Methodology

6.2.1 Controlling Equations

The basic controlling equations used to describe the streamer propagation dynamics with consideration of the low-density channel formation are the Poisson equation [106], charge continuity equations [105] and the thermal diffusion equation. However, since the variables in the low-density phase are not always the same as those in the liquid phase, the above equations have been modified and presented from Equation 6-1 to Equation 6-5.

It is assumed that the relative permittivity and charge mobility will change when the Joule heating energy density W reaches the threshold of 8×10^7 J/m^3 for liquid vaporisation in cyclohexane. Assuming the molecular number density in the liquid phase and low-density phase at atmospheric pressure are 5×10^{27} m^{-3} and 2.5×10^{25} m^{-3}, respectively [11], the variation of charge mobility from liquid cyclohexane to gaseous cyclohexane is $\mu_{\pm e\_g} = 200\ \mu_{\pm e\_l}$ according to Table 2-13 [11]. The variation of relative permittivity from liquid cyclohexane to gaseous cyclohexane is $\varepsilon_{r\_l} = 2\varepsilon_{r\_g}$.

Meanwhile, inside the low-density channel during its formation from the liquid phase to low-density phase, the charge generation rate and recombination rate also gradually changes. Inside the low-density phase, the charge generation mechanism is assumed to be impact ionization, with charge recombination not considered [7]. Concerning the streamer channel expansion in a radial direction, the streamer channel in the liquid phase will then expand at a relatively stable velocity on the order of 100 m/s [11]. Considering a streamer low-density channel radius of 50 μm in experiments, the channel expansion time $t_{expansion}$, in other words, phase transition time interval, may range from 100 ns to 500 ns. Therefore, the relative permittivity variation and charge mobility variation extent $\mu_{\pm e}/\mu_{\pm e\_l}$, which are based on Joule heating energy density and time, can be schematically shown as in Figure 6-1 (a) and (b). A step function $k(t,W)$, which ranges from 0 (total liquid channel) to 1 (total gaseous channel), is built to represent the variation of ionization and the recombination process, as shown in Figure 6-2. The parameters begin to change at time t_0 when $W = 8\times10^7$ J/m^3 and finish the change after 100 ns. It should be noted that the variation shown in Figure 6-1 and Figure 6-2 are all assumed to be linearly related with time for simplification.

$$-\nabla\cdot\left(\varepsilon_0\varepsilon_r(t,W)\vec{E}\right)=c_+ + c_e + c_- \quad \text{Equation 6-1}$$

$$\frac{\partial c_+}{\partial t}+\nabla\cdot c_+\mu_+(t,W)\vec{E}=\left(G_+\left(\left|\vec{E}\right|\right)+\frac{c_+c_eR_{+e}}{e}+\frac{c_+c_-R_\pm}{e}\right)\left(1-k(t,W)\right)+G_I\left(\left|\vec{E}\right|\right)k(t,W) \quad \text{Equation 6-2}$$

$$\frac{\partial c_e}{\partial t}+\nabla\cdot\left(-c_e\mu_e(E,t,W)\vec{E}\right)=\left(G_e\left(\left|\vec{E}\right|\right)-\frac{c_+c_eR_{+e}}{e}-\frac{c_e}{\tau_a}\right)\left(1-k(t,W)\right)-G_I\left(\left|\vec{E}\right|\right)k(t,W) \quad \text{Equation 6-3}$$

$$\frac{\partial c_-}{\partial t}+\nabla\cdot\left(-c_-\mu_-(t,W)\vec{E}\right)=\left(G_-\left(\left|\vec{E}\right|\right)-\frac{c_+c_-R_\pm}{e}+\frac{c_e}{\tau_a}\right)\left(1-k(t,W)\right) \quad \text{Equation 6-4}$$

$$W=\int\vec{E}\cdot\sum\left(c_+\mu_+(t,W)-c_e\mu_e(E,t,W)-c_-\mu_-(t,W)\right)\vec{E}\,dt \quad \text{Equation 6-5}$$

Where $\varepsilon_r(t,W)$, $\mu_+(t,W)$ and $\mu_-(t,W)$ means that the relative permittivity and charge mobility of positive ions, and negative ions are dependent on both Joule heating energy density W and time. $\mu_e(E,t,W)$ means that charge mobility of electrons is dependent on Joule heating energy density W, time and local electric field.

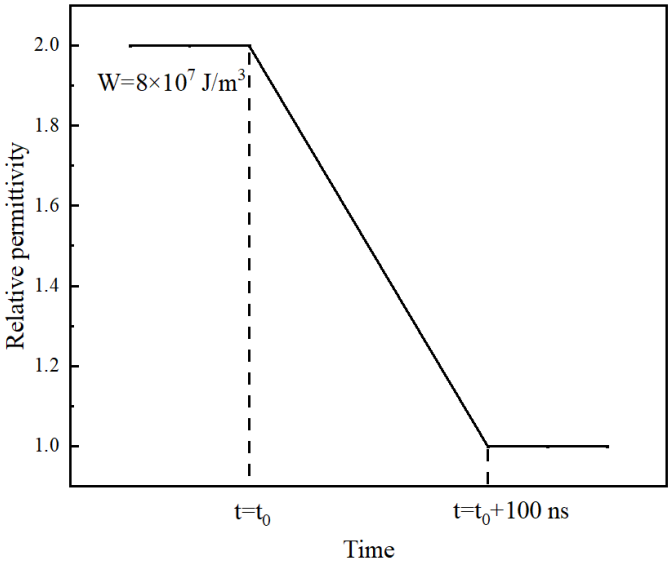

(a)

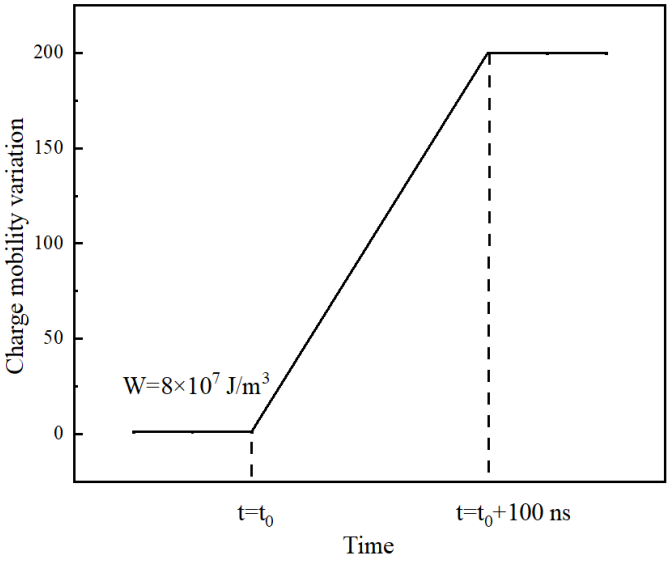

(b)

Figure 6-1 Schematic diagram of the variation of (a) relative permittivity and (b) charge mobility variation $\mu_{\pm e}/\mu_{\pm e\_l}$ during the low-density channel formation.

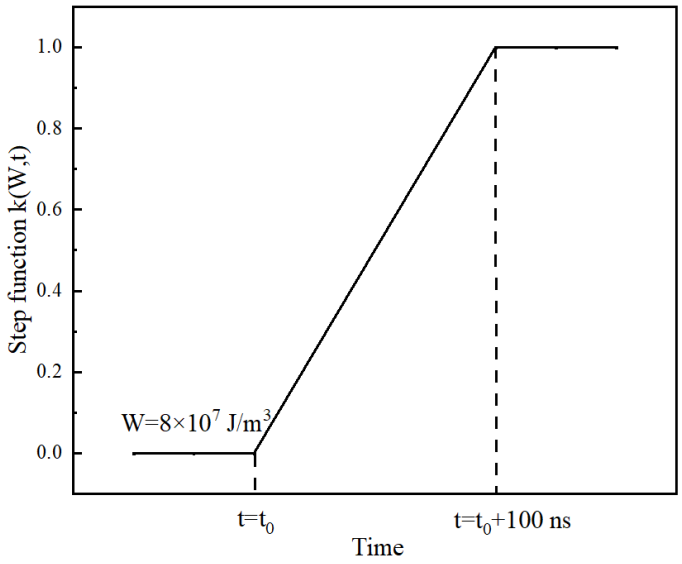

Figure 6-2 Step function of $k(t, W)$ to describe streamer channel transition from liquid phase to the low-density channel.

6.2.2 Electrode Geometry, Voltage Excitation and Boundary Conditions

The needle-plane geometry is the same as in Chapter 3 and is shown in Figure 3-3. The boundary conditions of Poisson equation of Equation 3-3 and charge continuity equations are the same as in Chapter 3. The applied voltage waveform is step voltage with a fixed voltage rise rate which is the same as in Chapter 3.

6.2.3 Simulation Refinement

In this section, the detailed refinement study results are not shown. Only the dense meshing area and the refined setting are shown here.

The dense meshing area used in Chapter 6 is shown in Figure 6-3. In order to achieve simulation convergence, the width of the dense meshing area is set at 600 μm. Besides, in order to save computational resources, the maximum meshing size on the axis of symmetry line 1 and on Arc 2 and Line 3 of the needle tip is set at 1 μm. In the dense meshing area, the maximum meshing size is set at 2 μm.

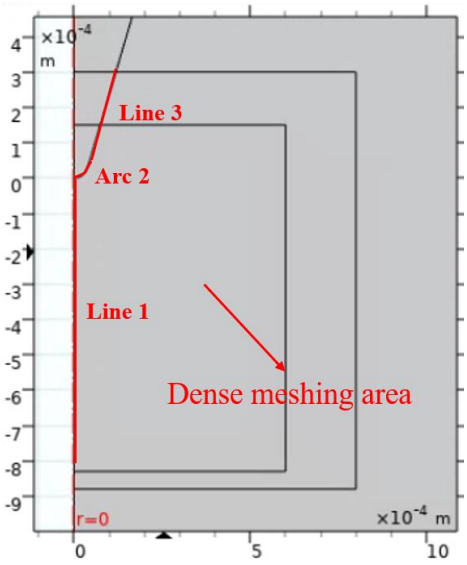

(a)

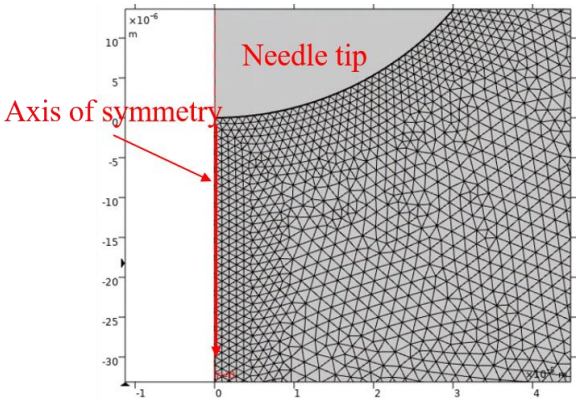

(b)

Figure 6-3 Dense meshing area used in Chapter 6.

6.3 Streamer Dynamics with Consideration of the Low-density Channel Formation

Under atmospheric pressure p_0, the parameter variations are shown in Figure 6-1 and Figure 6-2. However, due to the limited availability of computational resources for the present study, when solving the controlling equations from Equation 6-1 to Equation 6-5 in COMSOL Multiphysics based on the parameter variations in Figure 6-1 and Figure 6-2, the modelled results showed strong instability. This means that the simulation either can only run with extremely small time step size (over 1000 times smaller than the pre-set maximum time step size) or is not convergent. In order to solve the instability problem, the following strategy was adopted.

Since the strong instability in the simulation may be caused by the large variation in charge mobility, relative permittivity and charge generation, a small variation of these

parameters was adopted. Therefore, $\mu_{\pm e\_g} = 3\,\mu_{\pm e\_l}$ was chosen as the variation of charge mobility in the low-density phase. Accordingly, the variation of relative permittivity and step function were all assumed to vary by the same extent. Based on the above-mentioned settings, the instability problem was avoided.

The time-dependent electric field distribution along the axis of symmetry from the needle tip into cyclohexane is shown in Figure 6-4. The electric field leaves the needle tip at 220 ns at 3.0 MV/cm. The electric field peak magnitude then shows an initially increasing and then decreasing trend until reaching a stable magnitude at ~3.6 MV/cm.

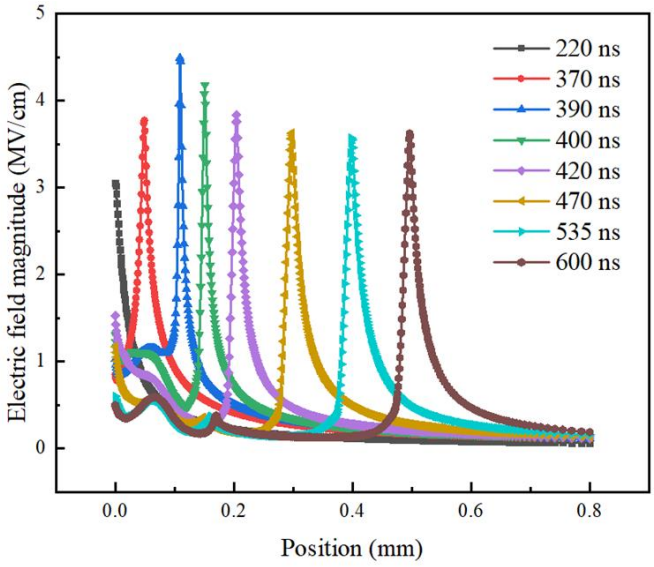

Figure 6-4 Electric field distribution along the axis of symmetry from the needle tip into cyclohexane with consideration of the low-density channel formation.

Similar to the electric field peak magnitude variation trend, the space charge density peak also shows an initially increasing and then decreasing trend until reaching a relatively stable value of $\sim 700\ \mathrm{C/m^3}$. Besides, a small negative space charge density peak appears close to the needle tip, while a small positive space charge density peak appeared at ~0.1 mm, both of which show a decreasing trend over time in their magnitudes. As is illustrated in Chapter 3, the positive space charge density peak at the streamer tip is formed due to the separation of positive ions and negative charges, including the electrons and negative ions. With the electric field peak moving towards the ground plane, newly generated negative charges move towards the positive needle and then compensate for the positive space charge density peak previously generated. Therefore, the positive space charge density peak also moves towards the ground plane, leaving a relatively low space charge density inside the streamer channel. From 220 ns to 390 ns, since the electric field magnitude is increasing, the positive space charge

density peak is also increasing. The newly generated negative charges over-compensate for the previous positive space charges. Therefore, a small negative space charge density peak forms near the needle tip. At 390 ns, both the electric field and space charge density reach their peak values at ~0.1 mm. Since after 390 ns and up to ~470 ns, the electric field peak magnitude decreases, the newly generated space charge density peak is also smaller than that at 390 ns. Therefore, the movement of newly generated negative charges cannot fully compensate the previous positive space charges. Therefore, a small positive space charge density remains but gradually reduces to zero.

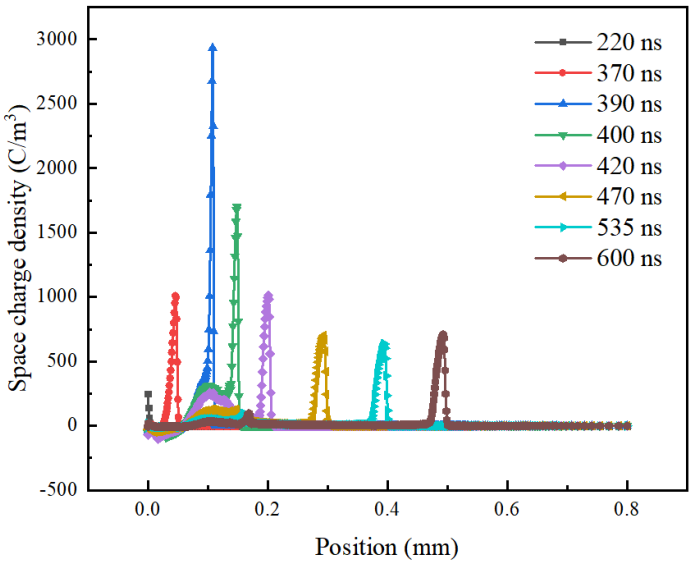

(a)

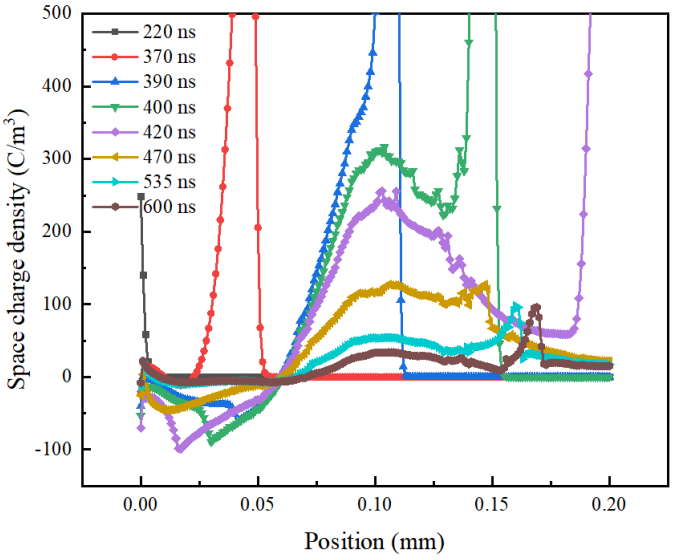

(b)

Figure 6-5 Space charge density distribution along the axis of symmetry from the needle tip into cyclohexane with consideration of the low-density channel formation. Note that (b) is a zoom-in plot of (a) from the needle tip to the 0.2 mm position.

Besides the distribution of electric field peak magnitude and space charge density at the streamer tip, the time-dependent variation of electric field magnitude and space charge density at the needle tip is shown in Figure 6-6. Four stages can be divided according to the variation of the electric field magnitude. Stage 1 is from 0 ns to 220 ns. The electric field magnitude at the needle tip keeps increasing due to the increase in external voltage. Space charge density gradually increases due to the molecular ionization. Stage 2 is from 220 ns to 346 ns. Since the electric field peak leaves the needle tip at 220 ns, the electric field magnitude gradually decreases at the needle tip. The space charge density is positive and initially increases before leaving the needle tip at 260 ns. After space charge density peak leaves the needle tip, the space charge density at the needle tip is also decreasing. Stage 3 is from 346 ns to 419 ns. The external voltage keeps increasing from 346 ns to 400 ns before becoming constant after 400 ns. The positive space charge density decreases from 168.9 C/m^3 to 0 C/m^3 from 346 ns to 362 ns. Therefore, the negative effect of the positive space charge density on the increase in the electric field magnitude gradually decreases. Besides, from 362 ns to 419 ns, the space charge density becomes negative due to the movement of electrons towards needle tip. The space charge density decreases from 0 C/m^3 to -69.6 C/m^3. Since the negative space charge density can increase the electric field at the needle tip, decreasing space charge density contributes to the increase in the electric field at the needle tip. Therefore, the electric field begins to increase during stage 3. Stage 4 is from 419 ns to the end of the simulation. The space charge density gradually increases from -69.6 C/m^3 to -7.7 C/m^3 since the electrons are driven to the positive electrode. The smaller negative space charge density leads to a lower electric field magnitude increase. Therefore, the electric field magnitude at the needle tip decreases again.

Based on Equation 6-5, the Joule heating energy density distribution along the axis of symmetry from the needle tip into cyclohexane is shown in Figure 6-7. Since both the electric field and space charge density reach the maximum at position of ~0.1 mm, the position of maximum Joule heating energy density also happens here. In Figure 6-7, from the position 0.8 mm (in cyclohexane) towards 0 mm (the needle tip), the positions where the Joule heating energy density begins to increase to over zero are regarded as the Joule heating energy density tip. From the Joule heating energy density tip towards the needle tip, the Joule heating energy density initially shows a relatively flat stage of $2\sim3\times10^8$ J/m^3 and then increases quickly over the liquid vaporisation threshold.

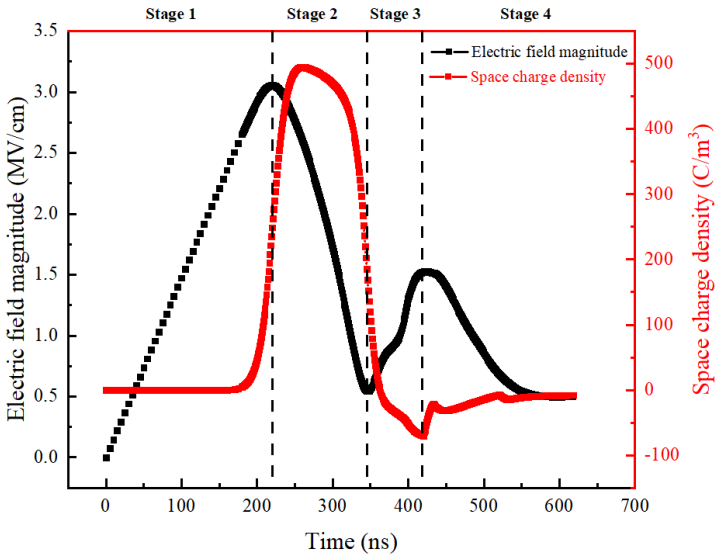

Figure 6-6 Time-dependent electric field magnitude and space charge density variation at the needle tip with consideration of the low-density channel formation.

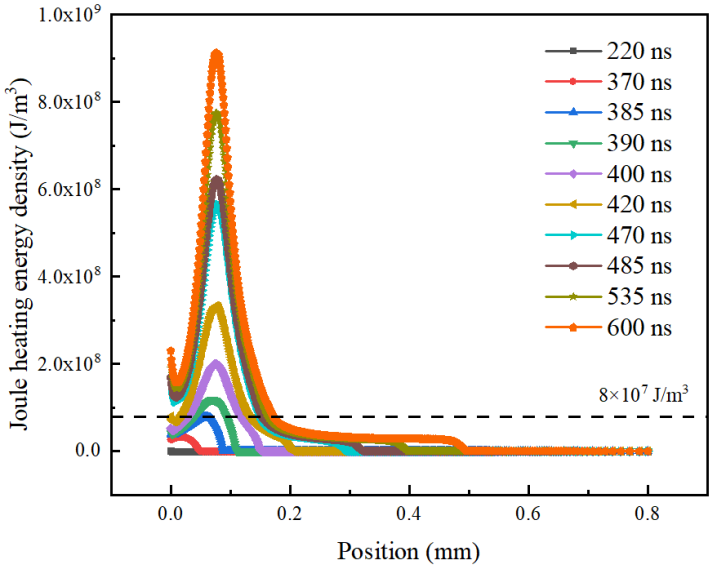

Figure 6-7 Joule heating energy density distribution along the axis of symmetry with the consideration of the low-density channel formation.

Based on the Joule heating energy density distribution, the variation extent of charge mobility is shown in Figure 6-8. The charge mobility variation begins at 385 ns when the Joule heating energy density just reaches the vaporisation threshold. The charge mobility at more parts along the axis of symmetry inside the streamer channel begins to vary afterwards. At 485 ns, the first point inside the low-density channel just reaches the pre-defined low-density channel values because the parameter variation time reaches the pre-set time for the radial expansion of the streamer channel $t_{expansion}$. Therefore, at this point, $\mu_{\pm e\_g} = 3\mu_{\pm e\_l}$. After 485 ns, the charge mobility in more parts

along the axis of symmetry (inside the streamer channel) reaches the pre-set variation extent (three times larger) and finally all finishes variation so that the charge mobility inside the low-density channel is three times larger than that in the liquid phase.

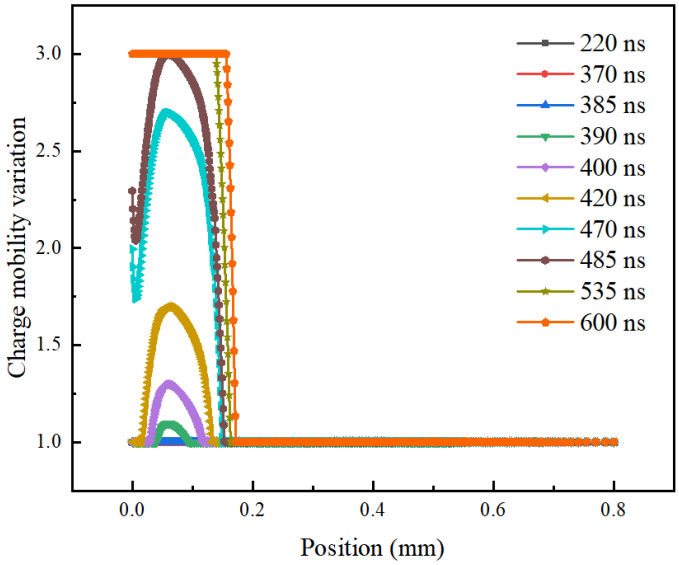

Figure 6-8 Time-dependent charge mobility variation along the axis of symmetry with consideration of the low-density channel formation.

With the aim of ascertaining the impact of the low-density channel on the voltage drop along the streamer, a comparison of the electric field distribution along the axis of symmetry between cases with and without the low-density channel when the streamer reaches 0.5 mm is shown in Figure 6-9. The length of the low-density channel at 600 ns is 0.17 mm, as shown by the red line. Comparing the electric field inside the streamer channel from the needle tip to this point, it is clearly shown that the maximum electric field in the case without the low-density channel is 1.2 MV/cm, while it is ~0.6 MV/cm in the case with the low-density channel. The average electric field, which is also the voltage drop in this area, decreases from 0.68 MV/cm in the case without the low-density channel to 0.36 MV/cm in the case with the low-density channel. This illustrates the existence of the low-density channel that reduces the voltage drop along the streamer. However, it should be noted that when compared to the voltage drop inside the low-density channel calculated by experimental results [1], the voltage drop in the simulation is still higher.

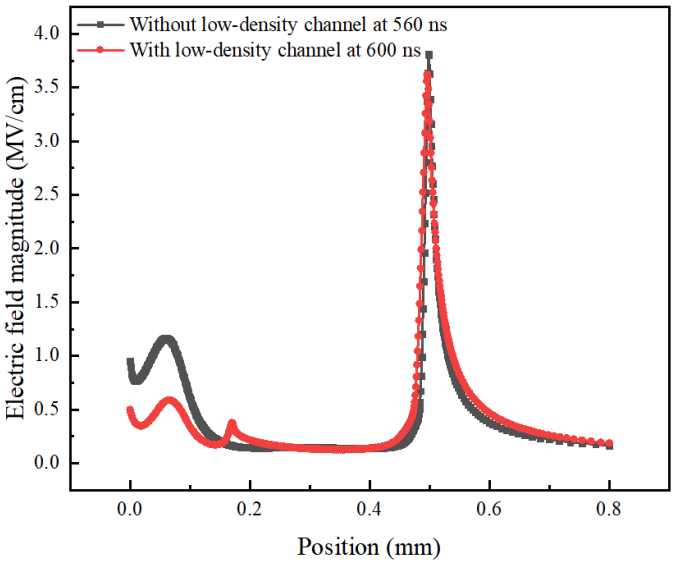

Figure 6-9 Comparison of the electric field distribution between cases with and without the low-density channel along the axis of symmetry when the streamer tip reaches 0.5 mm.

6.4 Discussion

Section 6.3 confirms that the existence of the low-density channel can decrease the voltage drop inside the streamer channel by around half when only a small variation in the parameters from liquid state to gas state is considered. Therefore, the consideration of the low-density channel is of significant importance during streamer propagation since it can significantly affect the voltage drop inside the streamer channel. However, there are two phenomena worthy of further discussion.

The first point concerns the voltage drop inside the low-density channel. The present voltage drop close to the needle tip in the case with consideration of the low-density channel is smaller than that without consideration of the low-density channel. However, it is still higher than the voltage drop calculated according to experiments in [1], as mentioned in Chapter 3.

The second point is related to propagation of the low-density channel tip. Combining Figure 6-4, Figure 6-5 and Figure 6-7, the electric field, space charge density and Joule heating energy density distribution along the axis of symmetry at 600 ns with consideration of the low-density channel formation is shown in Figure 6-10. At 600 ns, Joule heating energy density reaches the threshold for vaporisation at a position of 0.171 mm, meaning that the low-density channel along the axis of symmetry exists from the needle tip to the 0.171 mm position. A secondary electric field peak happens inside the streamer channel at 0.170 mm. Besides, a secondary space charge density peak also

happens inside the low-density channel at 0.169 mm. Inside the low-density channel, charge mobility increases when compared that in the liquid phase. Therefore, electrons and negative ions are more mobile at propagating to the needle tip, while positive ions propagate towards the ground plane faster. Therefore, the separation of charges is faster, leading to the secondary positive space charge density peak being formed, which contributes to the formation of the secondary electric peak ahead of the secondary space charge density peak.

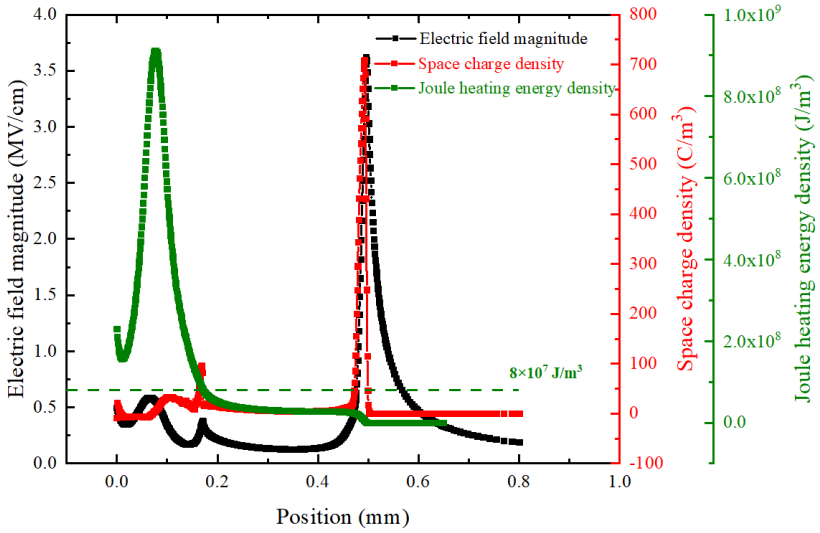

Figure 6-10 Distribution of the electric field, space charge density and Joule heating energy density along the axis of symmetry at 600 ns with consideration of the low-density channel formation.

In the experiments, the observed streamer channel based on different optical methods is likely due to the formation of the low-density channel. Therefore, the velocity of the low-density channel tip is also of significant importance and could be represented by the velocity of the secondary electric field peak. The instant streamer velocities of the first and secondary electric field peaks are shown in Figure 6-11. Both the first and secondary electric field peak velocities reach a relatively stable stage after propagating for some time. However, the velocity of the secondary electric field peak in the stable state is only ~0.1 km/s, which is much smaller than the first electric field tip of ~1.5 km/s.

The main reason for the relatively high voltage drop inside streamer channel and relatively small velocity of the secondary electric field peak may be due to the small variation of charge mobility, relative permittivity and charge generation considered in the present simulation. When the charge mobility variation is larger, positive ions, negative ions and electrons are more mobile, leading to the voltage drop inside the low-

density channel being smaller. Besides, a larger charge generation rate inside the low-density channel will generate more charges, further increasing the secondary electric field peak magnitude. In the meantime, the velocity of the secondary electric field peak position is also increased. Therefore, in future research, a higher extent of parameter variations should be considered if the simulation instability problem is solved and computational resource abundant.

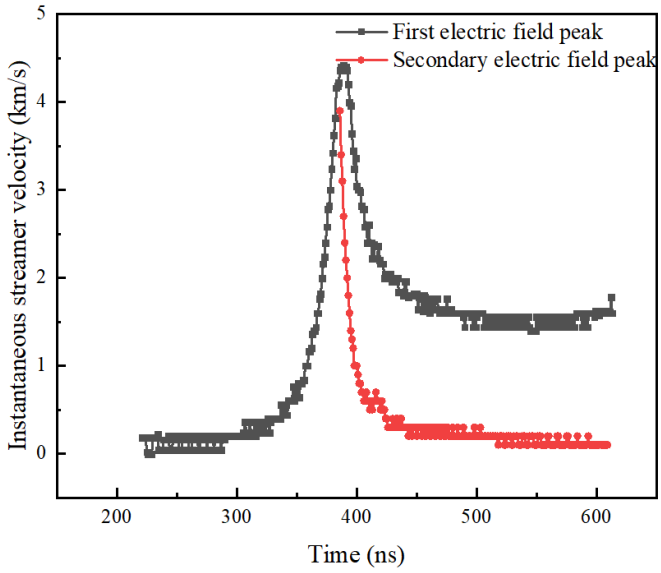

Figure 6-11 Time-dependent instant velocity of the first and secondary electric field peak with consideration of the low-density channel formation.

6.5 Summary

In this Chapter, streamer dynamics with consideration of the low-density channel formation have been simulated. The charge mobility, relative permittivity of dielectrics and charge generation were all assumed to vary from the liquid phase to the low-density phase. The phase transition time from the liquid phase to the low-density phase was assumed to be 100 ns. The voltage drops along the streamer in the cases with and without the low-density channel formation were compared. Based on the variation of charge mobility, relative permittivity and charge generation, it has been found that the voltage drop inside the streamer channel close to the needle tip decreased from 0.68 MV/cm in the case without considering the low-density channel formation to 0.36 MV/cm in the case with consideration of the low-density channel formation. Therefore, it was confirmed that the formation of the low-density channel played a significant role in controlling the streamer channel voltage drop during streamer propagation. However, due to the limited computational resources available to the present study, only small

variations in charge mobility, relatively permittivity and charge generation rate were adopted in this chapter in order to achieve simulation convergence. Accordingly, future research should focus on more significant parameter variations.

7 Conclusions and Future Research

7.1 Conclusions

7.1.1 General

This Ph.D. study has focused on modelling streamer initiation and propagation phenomena in dielectric liquids. A set of equations, including Poisson equation, charge continuity equations, Navier-stokes equations and thermal diffusion equations, have been adopted to describe the physical processes of streamer initiation and propagation. Based on modelling using the finite element method in COMSOL Multiphysics v5.4, the research objectives have been achieved, producing some useful conclusions and findings.

The research topics investigated in this study cover the following:

(1) Modelling of 2nd mode positive streamers in cyclohexane by considering electron saturation velocity
   - ✓ Effects of electron saturation velocity on streamer dynamics
   - ✓ Comparison of streamer dynamics with experiments under different voltage levels

(2) Modelling of the electrostrictive-force-induced cavity formation in dielectric liquids
   - ✓ Cavity formation dynamics induced by electrostrictive force in cyclohexane
   - ✓ Effects of voltage rise rates on cavity formation dynamics in cyclohexane
   - ✓ Comparison of cavity formation dynamics among cyclohexane, rapeseed oil and deionized water

(3) Modelling of the streamer initiation process in cyclohexane
   - ✓ Mechanisms involved during the positive streamer initiation process
   - ✓ Possibility of cavity formation during streamer initiation
   - ✓ Effects of voltage rise rates on Joule heating induced streamer initiation

(4) Modelling of the low-density channel formation during streamer propagation
   - ✓ Streamer dynamics with consideration of the low-density channel formation
   - ✓ Comparison of voltage drops along the streamer with and without the low-density channel formation

7.1.2 Summary of the Key Results and Main Findings

In order to study the underlying mechanism to ascertain a stable velocity for 2nd mode positive streamers, needle-plane geometry with a needle tip radius of 40 μm and a gap distance of 50 mm was adopted in the simulation, which was chosen for its similarity to an experiment conducted in [1]. Streamer velocity was regarded as the velocity of the moving electric field peak in this study. **The electric field peak left the needle tip and propagated into cyclohexane at ~3 MV/cm.** The electric field peak magnitude showed an initially increasing and then decreasing trend until a relatively stable value was ascertained. A positive space charge density followed the electric field tip with some μm behind. The distance between the electric field tip and space charge density peak showed an opposite relationship to the variation of electric field peak magnitude. **During the streamer process, the instant streamer velocity also showed an initial increasing and then decreasing trend until a relatively stable velocity was ascertained, which is recognised as the streamer propagation velocity.** Without considering electron saturation velocity, the streamer propagation velocity was larger than the typical velocity of a 2nd mode streamer. **Decreasing electron saturation velocity to 7.5 km/s in cyclohexane can reduce the streamer propagation velocity to a reasonable value. When applying an electron saturation velocity of 7.5 km/s to other voltage levels, the streamer propagation velocities in cyclohexane increased with a voltage magnitude increase, replicating consistency with experimental results [1] under the same conditions.** Besides, the streamer tip radius, which is defined by the electric field outline from 50% E_{max} to E_{max}, also showed an increasing trend with the applied voltage and was also similar to previous experimental observations [1].

The dynamics of electrostrictive-force-induced cavity formation in cyclohexane were then investigated. Electrostrictive force was induced by variation in electric field magnitudes. **The direction of electrostrictive force was in the same direction as the increase in electric field magnitude.** Without consideration of space charge generation, the electric field distribution was in the form of the Laplace field. Therefore, the direction of electrostrictive force was always moving towards the needle tip. The liquid was also pushed towards the needle tip. **Besides, it has been found that electrostrictive force always tended to stretch the liquid due to dielectric polarization, so the electrostrictive force pressure was always negative.** A slower

voltage rise rate led to smaller negative pressure in cyclohexane. **When the voltage rise rate was smaller than 30 kV/ns, it was hard to form a cavity in cyclohexane by the electrostrictive force alone**. The required voltage for cavity formation in cyclohexane, rapeseed oil and deionised water under fixed voltage rise rates were then compared. **It was more difficult to form a cavity in both cyclohexane and rapeseed oil than it was in deionized water due to much smaller relative permittivity in cyclohexane and rapeseed oil.**

Streamer dynamics during streamer initiation were also investigated. In addition to electrostrictive force, Coulomb force which was induced by the space charge and electric field, was also considered. Coulomb force was more dominating than electrostrictive force. It was found that the total force of electrostrictive force and Coulomb force pushed the liquid outwards the needle tip at several m/s. The liquid density increased at the streamer tip while it was reduced inside the streamer channel. **Over a wide range of voltage rise rates from 0.075 kV/ns to 70 kV/ns, the total pressure in cyclohexane did not reach the threshold for cavity formation before Joule heating energy density reached the threshold for liquid vaporisation. This indicated that cavity may not form during positive streamer initiation in the present study**. Defining the period until Joule heating energy density reaches the threshold for liquid vaporisation as the streamer initiation process, it was found that **decreasing voltage rise rates increased the streamer initiation time. However, the corresponding streamer initiation voltage decreased. Besides, streamer initiation length also decreased with the decrease in voltage rise rate**.

Streamer propagation was finally modelled by consideration of the low-density channel formation. Charge mobility increased from the liquid phase to the low-density channel, while the relative permittivity reduced from the liquid phase to the low-density channel. The charge generation mechanism was assumed to be impact ionization in the low-density channel, rather than the molecular ionization in the liquid phase. **Compared with the streamer dynamics without considering the low-density channel formation, the average electric field within the low-density channel decreased by half. This indicated that the low-density channel helped decrease the voltage drop inside the streamer channel.** However, due to computational resource limitations, larger parameter variations for charge mobility, relative permittivity and charge generation would lead to simulation instability and were thus unachievable in this study.

7.2 Future Research

This thesis presented some useful conclusions concerning the mechanisms controlling 2nd mode positive streamer velocity, streamer initiation mechanisms and streamer propagation dynamics with consideration of the low-density channel formation. Additionally, the following interesting topics were also raised and ideal for exploration in future research.

Investigating the streamer velocity:

i. The stable velocity of a 2nd mode positive streamer is explained using electron saturation velocity in this study. However, due to the difficulty of simulating streamer branching in a 3D model, the simulation only focused on a single streamer channel in a 2D-axisymmetic model. The experiments speculate that streamer branching may also play an important role in controlling streamer velocity. Therefore, it would be interesting to study streamer velocity in 3D dimensions.

ii. When the applied voltage magnitude is over a threshold, namely acceleration voltage, the streamer mode suddenly jumps from 2nd mode to 3rd mode, with the streamer velocity also increasing from 1-2 km/s to ~10 km/s. However, the current model can only simulate the dynamics of a 2nd mode streamer. Therefore, a new mechanism may be involved in leading to a 3rd mode streamer, something worthy of further investigation.

iii. The experiments also found that adding molecules with lower ionization potentials can greatly reduce the breakdown voltage and increase the acceleration voltage. Therefore, it would also be interesting to study the mechanism that changed the breakdown voltage and acceleration voltage in the simulation.

Investigating the cavity formation during streamer initiation:

i. Cavity formation is speculated as being hard to form during positive streamer initiation. However, whether a cavity can form during negative streamer initiation is unclear and worthy of future research.

ii. If a cavity can form under certain circumstances, the dynamics of cavity formation, shape variation of a cavity under both electrostrictive force and Coulomb

force, electron acceleration inside a cavity and the impact of ionization occurring on the surface of a cavity are all interesting areas for future investigation.

iii. After cavity formation, the effects of the charge dynamics inside and on the surface of a cavity on streamer initiation are worthy of investigation. The effects of voltage rise rate and magnitude on the streamer initiation process in cyclohexane and comparisons with different dielectric liquids need deeper research.

Investigating the low-density channel formation:

i. The low-density channel formation has been simulated in this study. However, due to the convergence problem met in COMSOL Multiphysics, the variation extent of charge mobility, relative permittivity and charge generation is not changed fully from the liquid phase to the low-density phase. Further simulation should focus more on the FEM in order to achieve better convergence.

ii. The formation of a shockwave is speculated to be closely related to the formation and elongation of the low-density channels during streamer propagation. Since a shockwave can also reflect some mechanisms during the streamer process, further research should focus attention on the relationship between the low-density channel formation, elongation and shockwave dynamics.

Investigating the liquid types:

i. The main dielectric liquid in this study was cyclohexane because its structure is similar to the main components in cyclohexane: paraffinic/naphthenic molecules. Besides, the parameter values in cyclohexane are easier to obtain. However, oils such as mineral oils and ester liquids are more commonly used in reality. Therefore, future research could focus on simulations using the parameters obtained from mineral and ester liquids in order to offer more guidance in experiments and applications.

References

[1] O. Lesaint and M. Jung, "On the relationship between streamer branching and propagation in liquids: influence of pyrene in cyclohexane," *Journal of Physics D: Applied Physics,* vol. 33, no. 11, p. 1360, 2000.

[2] S. Chakravorti, D. Dey, and B. Chatterjee, "Recent trends in the condition monitoring of transformers," *Power Systems Springer-Verlag: London, UK,* 2013.

[3] Q. Liu, "Electrical performance of ester liquids under impulse voltage for application in power transformers," Ph.D. Thesis, Electrical and Electronic Engineering, University of Manchester, UK, 2011.

[4] O. Lesaint, "Prebreakdown phenomena in liquids: propagation 'modes' and basic physical properties," *Journal of Physics D: Applied Physics,* vol. 49, no. 14, p. 144001, 2016.

[5] L. Lundgaard, D. Linhjell, G. Berg, and S. Sigmond, "Propagation of positive and negative streamers in oil with and without pressboard interfaces," *IEEE Transactions on Dielectrics and Electrical Insulation,* vol. 5, no. 3, pp. 388-395, 1998.

[6] J. C. Devins, S. J. Rzad, and R. J. Schwabe, "Breakdown and prebreakdown phenomena in liquids," *Journal of Applied Physics,* vol. 52, no. 7, pp. 4531-4545, 1981.

[7] F. O'Sullivan, "A model for the initiation and propagation of electrical streamers in transformer oil and transformer oil based nanofluids," Ph.D. Thesis, Massachusetts Institute of Technology, Cambridge, MA, USA, 2007.

[8] J. G. Hwang, "Elucidating the mechanisms behind pre-breakdown phenomena in transformer oil systems," Ph.D. Thesis, Massachusetts Institute of Technology, Cambridge, MA, USA, 2010.

[9] J. Jadidian, "Charge transport and breakdown physics in liquid/solid insulation systems," Ph.D. Thesis, Massachusetts Institute of Technology Cambridge, MA, USA, 2013.

[10] I. Madshaven, O. L. Hestad, M. Unge, O. Hjortstam, and P. O. Åstrand, "Conductivity and capacitance of streamers in avalanche model for streamer

propagation in dielectric liquids," *Plasma Research Express*, vol. 1, no. 3, p. 035014, 2019.

[11] G. V. Naidis, "Modelling of streamer propagation in hydrocarbon liquids in point-plane gaps," *Journal of Physics D Applied Physics*, vol. 48, no. 19, 2015.

[12] A. Beroual *et al.*, "Propagation and structure of streamers in liquid dielectrics," *IEEE Electrical Insulation Magazine*, vol. 14, no. 2, pp. 6-17, 1998.

[13] O. Lesaint and P. Gournay, "On the gaseous nature of positive filamentary streamers in hydrocarbon liquids. I: Influence of the hydrostatic pressure on the propagation," *Journal of Physics D: Applied Physics*, vol. 27, no. 10, p. 2111, 1994.

[14] O. Lesaint and P. Gournay, "Initiation and propagation thresholds of positive prebreakdown phenomena in hydrocarbon liquids," *IEEE Transactions on Dielectrics and Electrical Insulation*, vol. 1, no. 4, pp. 702-708, 1994.

[15] D. Linhjell, L. Lundgaard, M. Unge, and O. Hjortstam, "Prebreakdown phenomena in hydrocarbon liquids in a point-plane gap under step voltage. Part 1: behaviour at positive polarity," *Journal of Physics Communications*, vol. 4, no. 4, p. 045012, 2020.

[16] L. Lundgaard, D. Linhjell, Ø. L. Hestad, M. Unge, and O. Hjortstam, "Pre-breakdown phenomena in hydrocarbon liquids in a point-plane gap under step voltage. Part 2: behaviour under negative polarity and comparison with positive polarity," *Journal of Physics Communications*, vol. 4, no. 4, p. 045011, 2020.

[17] R. Hebner, "The Liquid State and Its Electrical Properties (NATO ASI Series vol B 193)," ed: New York: Plenum, 1988.

[18] O. Lesaint, A. Saker, P. Gournay, R. Tobazeon, J. Aubin, and M. Mailhot, "Streamer propagation and breakdown under ac voltage in very large oil gaps," *IEEE transactions on dielectrics and electrical insulation*, vol. 5, no. 3, pp. 351-359, 1998.

[19] Q. Liu and Z. D. Wang, "Streamer characteristic and breakdown in synthetic and natural ester transformer liquids under standard lightning impulse voltage," *IEEE Transactions on Dielectrics and Electrical Insulation*, vol. 18, no. 1, pp. 285-294, 2011.

[20] W. Lu, Q. Liu, and Z. D. Wang, "Pre-breakdown and breakdown mechanisms of an inhibited gas to liquid hydrocarbon transformer oil under negative

lightning impulse voltage," *IEEE Transactions on Dielectrics and Electrical Insulation,* vol. 24, no. 5, pp. 2809-2818, 2017.

[21] S. Shen, Q. Liu, and Z. Wang, "Effect of electric field uniformity on positive streamer and breakdown characteristics of transformer liquids," *IEEE Transactions on Dielectrics and Electrical Insulation,* vol. 26, no. 6, pp. 1814-1822, 2019.

[22] C. Tran Duy, O. Lesaint, M. Nguyen Ngoc, and A. Denat, "Streamer initiation and breakdown in vegetable-based biodegradable oils," in *International Symposium on High Voltage Engineering*, Cape-Town, 2009: SAIEE, Innes House, Johannesburg, pp. C-47.

[23] R. Liu, C. Törnkvist, V. Chandramouli, O. Girlanda, and L. A. A. Pettersson, "Fast Streamer Propagation in Transformer Oil and Ester Liquids," in *Nordic Insulation Symposium (NORD-IS)*, Gothenburg, Sweden, 2009.

[24] R. Liu, C. Törnkvist, V. Chandramouli, O. Girlanda, and L. A. A. Pettersson, "Ester Fluids as Alternative for Mineral Oil The Difference in Streamer Velocity and LI Breakdown Voltage," in *Conference on Electrical Insulation and Dielectric Phenomena*, Virginia Beach, VA, USA, pp. 543-548, 2009.

[25] C. T. Duy, O. Lesaint, A. Denat, and N. Bonifaci, "Streamer propagation and breakdown in natural ester at high voltage," *IEEE Transactions on Dielectrics and Electrical Insulation,* vol. 16, no. 6, pp. 1582-1594, 2009.

[26] G. Massala and O. Lesaint, "A comparison of negative and positive streamers in mineral oil at large gaps," *Journal of Physics D Applied Physics*, vol. 34, no. 10, pp. 1525-1532, 2001.

[27] A. C. T. Briggs, A. Beroual, and F. Buret, "Prebreakdown current pulses in DC stressed tetraester," in *Conference Record of the 1992 IEEE International Symposium on Electrical Insulation*, 1992, pp. 423-426.

[28] H. I. Marsden and P. B. McGrath, "An optical study of prebreakdown events in AC-stressed n-hexane," *IEEE Transactions on Electrical Insulation,* vol. 26, no. 2, pp. 266-270, 1991.

[29] I. Ohshima, S. Motegi, M. Honda, T. Yanari, and Y. Ebisawa, "HVDC Breakdown of Transformer Oil and the Effect of Space Charge on It," *IEEE Power Engineering Review,* vol. PER-3, no. 7, pp. 44-45, 1983.

[30] O. Lesaint, "Streamers in liquids: Relation with practical high voltage insulation and testing of liquids," in *IEEE International Conference on Dielectric Liquids*, Chasseneuil, France, pp. 1-6, 2008.

[31] O. Lesaint and T. V. Top, "Streamer initiation in mineral oil. Part I: electrode surface effect under impulse voltage," *IEEE Transactions on Dielectrics and Electrical Insulation,* vol. 9, no. 1, pp. 84-91, 2002.

[32] N. V. Dung, H. K. Hoidalen, D. Linhjell, L. E. Lundgaard, and M. Unge, "Influence of Impurities and Additives on Negative Streamers in Paraffinic Model Oil,", *IEEE Transactions on Dielectrics and Electrical Insulation,* vol. 20, no. 3, pp. 876-886, 2013.

[33] S. Ingebrigtsen, L. E. Lundgaard, and P. O. Astrand, "Effects of additives on prebreakdown phenomena in liquid cyclohexane: II. Streamer propagation," *Journal of Physics D: Applied Physics,* vol. 40, no. 18, pp. 5624-5634, 2007.

[34] P. Gournay and O. Lesaint, "On the gaseous nature of positive filamentary streamers in hydrocarbon liquids. II: Propagation, growth and collapse of gaseous filaments in pentane," *Journal of Physics D: Applied Physics,* vol. 27, no. 10, p. 2117, 1994.

[35] D. Linhjell, L. E. Lundgaard, M. Unge, and O. Hjortstam, "Pressure-dependent propagation of streamers under step voltage in a long point-plane gap in transformer oil," *IEEE Transactions on Dielectrics and Electrical Insulation,* vol. 27, no. 5, pp. 1595-1603, 2020.

[36] S. Ingebrigtsen, L. E. Lundgaard, and P. O. Åstrand, "Effects of additives on prebreakdown phenomena in liquid cyclohexane: i. streamer initiation," *Journal of Physics D: Applied Physics,* vol. 40, no. 17, pp. 5161-5169, 2007.

[37] S. Ingebrigtsen, H. S. Smalo, P. O. Astrand, and L. E. Lundgaard, "Effects of electron-attaching and electron-releasing additives on streamers in liquid cyclohexane," *IEEE Transactions on Dielectrics and Electrical Insulation,* vol. 16, no. 6, pp. 1524-1535, 2009.

[38] N. V. Dung, H. K. Høidalen, D. Linhjell, L. E. Lundgaard, and M. Unge, "Effects of reduced pressure and additives on streamers in white oil in long point-plane gap," *Journal of Physics D: Applied Physics,* vol. 46, no. 25, p. 255501, 2013.

[39] M. Eklund, "Mineral insulating oils; functional requirements, specifications and production," in *Conference of IEEE International Symposium on Electrical Insulation*, Toronto, ON, Canada, p. 68-72. 11-14, 2006.

[40] W. Lu, "Pre-breakdown and Breakdown Phenomena of Alternative Transformer Liquids under Lightning Impulse Voltages," Ph.D. thesis, The University of Manchester (United Kingdom), 2016.

[41] J. Mendes, A. Reis, E. Nogawa, C. Ferra, A. Martins, and A. Passos, "Oiled and ready to go," *Advanced application of ABB BIOTEMP vegetable oil in a HV power transformer. ABB Review,* pp. 53-57, 2007.

[42] P. Gournay and O. Lesaint, "A Study of the Inception of Positive Streamers in Cyclohexane and Pentane," *Journal of Physics D: Applied Physics,* vol. 26, no. 11, pp. 1966-1974, 1993.

[43] J. Xiang, "Pre-breakdown and Breakdown Study of Transformer Oil under DC and Impulse Voltages," Ph.D. thesis, School of Electrical and Electronic Engineering, the Universit of Manchester, 2017.

[44] S. Shen, "Study of Prebreakdown and Breakdown Mechanisms of Transformer Liquids under Lightning Impulse by Using Schlieren Optical Method," Ph.D. thesis, School of Electrical and Electronic Engineering, the University of Manchester, 2020.

[45] K. J. Rapp, J. Corkran, C. P. Mcshane, and T. A. Prevost, "Lightning Impulse Testing of Natural Ester Fluid Gaps and Insulation Interfaces," *IEEE Transactions on Dielectrics and Electrical Insulation,* vol. 16, no. 6, pp. 1595-1603, 2009.

[46] S. Arazoe, D. Saruhashi, Y. Sato, S. Yanabu, G. Ueta, and S. Okabe, "Electrical characteristics of natural and synthetic insulating fluids," *IEEE Transactions on Dielectrics and Electrical Insulation,* vol. 18, no. 2, pp. 506-512, 2011.

[47] W. Lu, Q. Liu, Z. D. Wang, and P. W. R. Smith, "Lightning impulse breakdown performance of an inhibited Gas-To-Liquid (GTL) hydrocarbon transformer oil," in *2014 IEEE 18th International Conference on Dielectric Liquids*, Bled, Slovenia, pp. 1-4, 2014.

[48] Z. Liu *et al.*, "Partial discharge behaviour of transformer liquids and the influence of moisture content," in *IEEE International Conference on Dielectric Liquids,* Bled, Slovenia, pp. 1-4, 2014.

[49] M. Aljure, M. Becerra, and M. E. Karlsson, "On the injection and generation of charge carriers in mineral oil under high electric fields," *Journal of Physics Communications,* vol. 3, no. 3, p. 035019, 2019.

[50] L. Niemeyer, L. Pietronero, and H. J. Wiesmann, "Fractal Dimension of Dielectric Breakdown," *Physical Review Letters,* vol. 52, no. 12, pp. 1033-1036, 1984.

[51] N. N. Bunni and P. B. McGrath, "Streamer simulation in a dielectric liquid," in *Conference on Electrical Insulation and Dielectric Phenomena*, Virginia Beach, VA, USA, pp. 588-591, 1995.

[52] N. N. Bunni and P. B. McGrath, "Computer analysis and observation of streamer growth at a dielectric interface," *IEEE Transactions on Dielectrics and Electrical Insulation,* vol. 3, no. 1, pp. 136-143, 1996.

[53] R. A. Arakoni, *Simulation of flowing plasma discharges with applications to lasers, fuel cells, and microthrusters* (no. 11). Citeseer, 2007.

[54] J. Fors, "Modeling and OpenFOAM simulation of streamers in transformer oil," Independent thesis Advanced level (degree of Master (Two Years)) Student thesis, 2012.

[55] J. P. Boris and D. L. Book, "Flux-corrected transport. I. SHASTA, a fluid transport algorithm that works," *Journal of Computational Physics,* vol. 11, no. 1, pp. 38-69, 1973.

[56] D. L. Book, J. P. Boris, and K. Hain, "Flux-corrected transport II: Generalizations of the method," *Journal of Computational Physics,* vol. 18, no. 3, pp. 248-283, 1975.

[57] J. P. Boris and D. L. Book, "Flux-corrected transport. III. Minimal-error FCT algorithms," *Journal of Computational Physics,* vol. 20, no. 4, pp. 397-431, 1976.

[58] J. Qian, R. P. Joshi, E. Schamiloglu, J. Gaudet, J. R. Woodworth, and J. Lehr, "Analysis of polarity effects in the electrical breakdown of liquids," *Journal of Physics D Applied Physics,* vol. 39, no. 2, pp. 359-369, 2006.

[59] D. Linhjell, L. E. Lundgaard, and M. Unge, "Pressure Dependent Propagation of Positive Streamers in a long Point-Plane Gap in Transformer Oil," in *IEEE International Conference on Dielectric Liquids*, Roma, Italy, pp. 1-3, 2019.

[60] J. Jadidian, M. Zahn, N. Lavesson, O. Widlund, and K. Borg, "Impulse breakdown delay in liquid dielectrics," *Applied Physics Letters,* vol. 100, no. 19, p. 192910, 2012.

[61] J. Jadidian, M. Zahn, N. Lavesson, O. Widlund, and K. Borg, "Effects of impulse voltage polarity, peak amplitude, and rise time on streamers initiated from a needle electrode in transformer oil," *IEEE Transactions on Plasma Science,* vol. 40, no. 3, pp. 909-918, 2012.

[62] O. Lesaint and L. Costeanu, "Positive streamer inception in cyclohexane: Experimental characterization and cavitation mechanisms," *IEEE Transactions on Dielectrics and Electrical Insulation,* vol. 25, no. 5, pp. 1949-1957, 2018.

[63] O. Lesaint and G. Massala, "Positive streamer propagation in large oil gaps: experimental characterization of propagation modes," *IEEE Transactions on Dielectrics and Electrical Insulation,* vol. 5, no. 3, pp. 360-370, 1998.

[64] R. E. Hebner, *Measurements of electrical breakdown in liquids* (The Liquid State and its Electrical Properties). (New York: Plenum) 1988.

[65] D. Linhjell, L. Lundgaard, and G. Berg, "Streamer propagation under impulse voltage in long point-plane oil gaps," *IEEE Transactions on Dielectrics and Electrical Insulation,* vol. 1, no. 3, pp. 447-458, 1994.

[66] Y. V. Torshin, "On the existence of leader discharges in mineral oil," *IEEE Transactions on Dielectrics and Electrical Insulation,* vol. 2, no. 1, pp. 167-179, 1995.

[67] G. Massala and O. Lesaint, "Positive streamer propagation in large oil gaps: electrical properties of streamers," *IEEE Transactions on Dielectrics and Electrical Insulation,* vol. 5, no. 3, pp. 371-381, 1998.

[68] T. V. Top, G. Massala, and O. Lesaint, "Streamer propagation in mineral oil in semi-uniform geometry," *IEEE Transactions on Dielectrics and Electrical Insulation,* vol. 9, no. 1, pp. 76-83, 2002.

[69] Y. Sawada, S. Ohta, M. Yamazaki, and H. Honjo, "Self-similarity and a phase-transition-like behavior of a random growing structure governed by a nonequilibrium parameter," *Physical Review A,* vol. 26, no. 6, pp. 3557-3563, 1982.

[70] B. B. Mandelbrot, *Fractals : form, chance and dimension*. San Francisco: Freeman, 1977.

[71] M. Eden, "A Two-dimensional Growth Process," in *Proceedings of the Fourth Berkeley Symposium on Mathematical Statistics and Probability, Volume 4: Contributions to Biology and Problems of Medicine*, Berkeley, Calif., 1961: University of California Press, pp. 223-239.

[72] D. S. McKenzie, "Polymers and scaling," *Physics Reports,* vol. 27, no. 2, pp. 35-88, 1976.

[73] H. E. Stanley, "Cluster shapes at the percolation threshold: and effective cluster dimensionality and its connection with critical-point exponents," *Journal of Physics A: Mathematical and General,* vol. 10, no. 11, p. L211, 1977.

[74] H. Peters, D. Stauffer, H. Hölters, and K. Loewenich, "Radius, perimeter, and density profile for percolation clusters and lattice animals," *Zeitschrift für Physik B Condensed Matter,* vol. 34, no. 4, pp. 399-408, 1979.

[75] T. Witten Jr and L. M. Sander, "Diffusion-limited aggregation, a kinetic critical phenomenon," *Physical review letters,* vol. 47, no. 19, p. 1400, 1981.

[76] C. Laurent and C. Mayoux, "Analysis of the Propagation of Electrical Treeing Using Optical and Electrical Methods," *IEEE Transactions on Electrical Insulation,* vol. EI-15, no. 1, pp. 33-42, 1980.

[77] N. Hozumi, T. Okamoto, and H. Fukagawa, "Simultaneous measurement of microscopic image and discharge pulses at the moment of electrical tree initiation," in *Conference on Electrical Insulation & Dielectric Phenomena — Annual Report*, pp. 531-535, 1987.

[78] H. J. Wiesmann and H. R. Zeller, "A fractal model of dielectric breakdown and prebreakdown in solid dielectrics," *Journal of Applied Physics,* vol. 60, no. 5, pp. 1770-1773, 1986.

[79] H. Fowler, J. Devaney, and J. G. Hagedorn, "Shaping of filamentary streamers by the ambient field," in *Conference on Electrical Insulation and Dielectric Phenomena-Annual Report*, TX, USA, pp. 132-136, 1999.

[80] F. Issouf and B. Abderrahmane, "Predischarge Models in Dielectric Liquids," *Japanese Journal of Applied Physics,* vol. 37, no. 5R, p. 2540, 1998.

[81] T. Aka-Ngnui and A. Beroual, "Modelling of multi-channel streamers propagation in liquid dielectrics using the computation electrical network," *Journal of Physics D Applied Physics,* vol. 34, no. 5, pp. 794-805, 2001.

[82] O. L. Hestad, T. Grav, L. E. Lundgaard, S. Ingebrigtsen, M. Unge, and O. Hjortstam, "Numerical simulation of positive streamer propagation in

cyclohexane," in *IEEE International Conference on Dielectric Liquids*, Bled, Slovenia, pp. 1-5, 2014.

[83] R. Badent, K. Kist, and A. J. Schwab, "Voltage dependence of prebreakdown phenomena in insulating oil," in *IEEE International Symposium on Electrical Insulation*, Pittsburgh, PA, USA, pp. 414-417, 1994.

[84] J. S. E. Townsend, *The theory of ionization of gases by collision*. London: Constable & Company, 1910.

[85] F. M. Meek and J. D. Craggs, *Electrical Breakdown of Gases*. New York: John Wiley & Sons, 1978.

[86] J. M. Meek and J. D. Craggs, "Electrical breakdown of gases," 1978.

[87] I. Madshaven, P. O. Åstrand, O. L. Hestad, S. Ingebrigtsen, M. Unge, and O. Hjortstam, "Simulation model for the propagation of second mode streamers in dielectric liquids using the Townsend-Meek criterion," *Journal of Physics Communications*, vol. 2, no. 10, p. 105007, 2018.

[88] I. Madshaven, O. L. Hestad, M. Unge, O. Hjortstam, and P. O. Åstrand, "Photoionization model for streamer propagation mode change in simulation model for streamers in dielectric liquids," *Plasma Research Express*, vol. 2, no. 1, p. 015002, 2020.

[89] W. F. Schmidt, *Liquid State Electronics of Insulating Liquids*. CRC Press, 1997.

[90] M. Zahn, "Solid, liquid, and gaseous electrical insulation," *digital Encyclopedia of Applied Physics*, 2003.

[91] I. Madshaven, P. O. Åstrand, O. L. Hestad, M. Unge, and O. Hjortstam, "Modeling the transition to fast mode streamers in dielectric liquids," in *IEEE International Conference on Dielectric Liquids*, Manchester, UK, pp. 1-4, 2017.

[92] A. Pedersen, "On the electrical breakdown of gaseous dielectrics-an engineering approach," *IEEE Transactions on Electrical Insulation*, vol. 24, no. 5, pp. 721-739, 1989.

[93] J. J. Lowke and F. D'Alessandro, "Onset corona fields and electrical breakdown criteria," *Journal of Physics D: Applied Physics*, vol. 36, no. 21, pp. 2673-2682, 2003.

[94] G. V. Naidis, "On streamer inception in hydrocarbon liquids in point-plane gaps," *IEEE Transactions on Dielectrics and Electrical Insulation*, vol. 22, no. 5, pp. 2428-2432, 2015.

[95] T. Aka-Ngnui and A. Beroual, "Determination of the streamers characteristics propagating in liquids using the electrical network computation," *IEEE Transactions on Dielectrics and Electrical Insulation,* vol. 13, no. 3, pp. 572-579, 2006.

[96] H. S. Smalø, O. L. Hestad, S. Ingebrigtsen, and P.-O. Åstrand, "Field dependence on the molecular ionization potential and excitation energies compared to conductivity models for insulation materials at high electric fields," *Journal of Applied Physics,* vol. 109, no. 7, p. 073306, 2011.

[97] I. Madshaven, O. Hestad, M. Unge, O. Hjortstam, and P. Åstrand, "Photoionization model for streamer propagation mode change in simulation model for streamers in dielectric liquids," *arXiv preprint arXiv:1909.12694,* 2019.

[98] T. Aka-Ngnui and A. Beroual, "Modeling of branching streamers propagating within dielectric liquids," *Conference on Electrical Insulation and Dielectric Phenomena,* Kitchener, Ontario, Canada, pp. 448-451, 2001.

[99] L. Pietronero and H. J. Wiesmann, "Stochastic model for dielectric breakdown," *Journal of Statistical Physics,* vol. 36, no. 5, pp. 909-916, 1984.

[100] A. Denat, B. Gosse, and J. P. Gosse, "Ion injections in hydrocarbons," *Journal of Electrostatics,* vol. 7, pp. 205-225, 1979.

[101] A. Denat, B. Gosse, and J. P. Gosse, "Electrical conduction of solutions of an ionic surfactant in hydrocarbons," *Journal of Electrostatics,* vol. 12, pp. 197-205, 1982.

[102] A. Denat, B. Gosse, and J. P. Gosse, "High field DC and AC conductivity of electrolyte solutions in hydrocarbons," *Journal of Electrostatics,* vol. 11, no. 3, pp. 179-194, 1982.

[103] F. Pontiga and A. Castellanos, "The effect of field-enhanced injection and dissociation on the conduction of highly-insulating liquids," *IEEE Transactions on Dielectrics and Electrical Insulation,* vol. 3, no. 6, pp. 792-799, 1996.

[104] F. Pontiga and A. Castellanos, "Electrical conduction of electrolyte solutions in nonpolar liquids," *IEEE Transactions on Industry Applications,* vol. 32, no. 4, pp. 816-824, 1996.

[105] U. Gafvert, A. Jaksts, C. Tornkvist, and L. Walfridsson, "Electrical-Field Distribution in Transformer Oil," *IEEE Transactions on Electrical Insulation,* vol. 27, no. 3, pp. 647-660, 1992.

[106] S. W. Ellingson, *Electromagnetics*. Blacksburg, VA: VT Publishing, 2018, p. 225.

[107] M. Becerra and H. Frid, "On the modeling of the production and drift of carriers in cyclohexane," in *Conference on Electrical Insulation and Dielectric Phenomena*, Shenzhen, China, pp. 905-908, 2013.

[108] M. Becerra, H. Frid, and P. A. Vázquez, "Self-consistent modeling of laminar electrohydrodynamic plumes from ultra-sharp needles in cyclohexane," *Physics of Fluids,* vol. 29, no. 12, p. 123605, 2017.

[109] R. Tobazcon, "Prebreakdown phenomena in dielectric liquids," *IEEE Transactions on Dielectrics and Electrical Insulation,* vol. 1, no. 6, pp. 1132-1147, 1994.

[110] W. Sima, C. L. Jiang, P. Lewin, Q. Yang, and T. Yuan, "Modeling of the Partial Discharge Process in a Liquid Dielectric: Effect of Applied Voltage, Gap Distance, and Electrode Type," *Energies,* vol. 6, no. 2, pp. 934-952, 2013.

[111] *A dictionary of physics*. Oxford University Press, 2009.

[112] M. N. Shneider, M. Pekker, and A. Fridman, "Theoretical study of the initial stage of sub-nanosecond pulsed breakdown in liquid dielectrics," *IEEE Transactions on Dielectrics and Electrical Insulation,* vol. 19, no. 5, pp. 1579-1582, 2012.

[113] M. N. Shneider and M. Pekker, "Dielectric fluid in inhomogeneous pulsed electric field," *Physical Review E,* vol. 87, no. 4, p. 043004, 2013.

[114] P. Mikhail, S. Yohan, N. S. Mikhail, F. Alexander, and D. Danil, "Initiation stage of nanosecond breakdown in liquid," *Journal of Physics D: Applied Physics,* vol. 47, no. 2, p. 025502, 2014.

[115] M. N. Shneider and M. Pekker, "Pre-breakdown processes in a dielectric fluid in inhomogeneous pulsed electric fields," *Journal of Applied Physics,* vol. 117, no. 22, p. 224902, 2015.

[116] P. Mikhail and N. S. Mikhail, "Pre-breakdown cavitation nanopores in the dielectric fluid in the inhomogeneous, pulsed electric fields," *Journal of Physics D: Applied Physics,* vol. 48, no. 42, p. 424009, 2015.

[117] M. Becerra, M. Aljure, and J. Nilsson, "Assessing the Production and Loss of Electrons from Conduction Currents in Mineral Oil," in *IEEE International Conference on Dielectric Liquids,* Roma, Italy, pp. 1-4, 2019.

[118] J. A. Amorim, O. Chiavone-Filho, M. L. Paredes, and K. Rajagopal, "Modeling high-pressure densities at wide temperature range with volume scaling: Cyclohexane+ n-hexadecane mixtures," *Fluid Phase Equilibria,* vol. 259, no. 1, pp. 89-98, 2007.

[119] A. J. Rostocki, D. B. Tefelski, and S. Ptasznik, "Compressibility studies of some vegetable oils up to 1 GPa," *High Pressure Research,* vol. 29, no. 4, pp. 721-725, 2009.

[120] L. D. Landau and E. M. Lifshitz, *Electrodynamics of Continuous Media* (2nd ed). Oxford: Pergamon Press, 1984.

[121] J. D. Jackson, *Classical Electrodynamics* (3rd ed). Wiley, New York, 1999.

[122] I. E. Tamm, *Fundamentals of The Theory of Electricity*. Moscow: Mir Publ, 1979.

[123] T. J. Lewis, "A new model for the primary process of electrical breakdown in liquids," *Dielectrics and Electrical Insulation, IEEE Transactions on,* vol. 5, no. 3, pp. 306-315, 1998.

[124] W. K. H. Panofsky and M. Phillips, *Classical Electricity and Magnetism*. Addison-Wesley Pub. Co. , 1962.

[125] V. Y. Ushakov, V. Klimkin, and S. Korobeynikov, "Breakdown in liquids at impulse voltage," *NTL, Russia, Tomsk,* 2005.

[126] M. N. Shneider and M. Pekker, "Liquid dielectrics in an inhomogeneous pulsed electric field," *Liquid Dielectrics in an Inhomogeneous Pulsed Electric Field, by Shneider, MN; Pekker, M.. ISBN: 978-0-7503-1245-5. IOP ebooks. Bristol, UK: IOP Publishing, 2016.*

[127] I. Marinov, O. Guaitella, A. Rousseau, and S. M. Starikovskaia, "Cavitation in the vicinity of the high-voltage electrode as a key step of nanosecond breakdown in liquids," *Plasma Sources Science and Technology,* vol. 22, no. 4, p. 042001, 2013.

[128] D. Dobrynin, Y. Seepersad, M. Pekker, M. Shneider, G. Friedman, and A. Fridman, "Non-equilibrium nanosecond-pulsed plasma generation in the liquid phase (water, PDMS) without bubbles: fast imaging, spectroscopy and leader-type model," *Journal of Physics D: Applied Physics,* vol. 46, no. 10, p. 105201, 2013.

[129] S. Yohan, P. Mikhail, N. S. Mikhail, F. Alexander, and D. Danil, "Investigation of positive and negative modes of nanosecond pulsed discharge in water and

electrostriction model of initiation," *Journal of Physics D: Applied Physics*, vol. 46, no. 35, p. 355201, 2013.

[130] T. V. Oommen, "Vegetable oils for liquid-filled transformers," *IEEE Electrical Insulation Magazine*, vol. 18, no. 1, pp. 6-11, 2002.

[131] N. AB, "Nynas Transformer oil – Nytro 10XN (IEC 60296/03)," 2008.

[132] ExxonMobil., "Marcol 82: medicinal grade white oil," 2009.

[133] L. Dumitrescu, O. Lesaint, N. Bonifaci, A. Denat, and P. Notingher, "Study of streamer inception in cyclohexane with a sensitive charge measurement technique under impulse voltage," *Journal of Electrostatics*, vol. 53, no. 2, pp. 135-146, 2001.

[134] A. Denat, J. P. Gosse, and B. Gosse, "Electrical conduction of purified cyclohexane in a divergent electric field," *IEEE Transactions on Electrical Insulation*, vol. 23, no. 4, pp. 545-554, 1988.

[135] N. Gee and G. R. Freeman, "Free ion yields, electron thermalization distances, and ion mobilities in liquid cyclic hydrocarbons: Cyclohexane and trans- and cis-decalin," *The Journal of Chemical Physics*, vol. 96, no. 1, pp. 586-592, 1992.

[136] H. Polak and B. Jachym, "Mobility of excess charge carriers in liquid and solid cyclohexane," *Journal of Physics C: Solid State Physics*, vol. 10, no. 19, pp. 3811-3818, 1977.

[137] A. Alj, A. Denat, J. P. Gosse, B. Gosse, and I. Nakamura, "Creation of Charge Carriers in Nonpolar Liquids," *IEEE Transactions on Electrical Insulation*, vol. EI-20, no. 2, pp. 221-231, 1985.

[138] R. Tobazeon, "Prebreakdown phenomena in dielectric liquids," in *IEEE International Conference on Conduction and Breakdown in Dielectric Liquids*, Baden-Dattwil, Switzerland, pp. 172-183, 1993.

[139] Y. Li *et al.*, "Transformer Oil Breakdown Dynamics Stressed by Fast Impulse Voltages: Experimental and Modeling Investigation," *IEEE Transactions on Plasma Science*, vol. 42, no. 10, pp. 3004-3013, 2014.

[140] M. Ghassemi, M. B. Tefferi, Q. Chen, and Y. Cao, "A thermo-electrodynamic electric field dependent molecular ionization model to realize positive streamer propagation in a wet-mate DC connector," *IEEE Transactions on Dielectrics and Electrical Insulation*, vol. 24, no. 2, pp. 901-914, 2017.

[141] M. Ghassemi, Q. Chen, and Y. Cao, "The influence of magnitude and rise time of applied voltage and the type of oil on streamer growth in a wet-mate DC

connector," *IEEE Transactions on Dielectrics and Electrical Insulation*, vol. 24, no. 3, pp. 1646-1656, 2017.

[142] G. V. Naidis, "Modeling of Subnanosecond Discharge in Hydrocarbon Liquid," *Ieee Transactions on Plasma Science*, vol. 43, no. 9, pp. 3138-3141, 2015.

[143] W. F. Schmidt, "Electronic Conduction Processes in Dielectric Liquids," *IEEE Transactions on Electrical Insulation*, vol. EI-19, no. 5, pp. 389-418, 1984.

[144] J.-P. Dodelet and G. R. Freeman, "Mobilities and Ranges of Electrons in Liquids: Effect of Molecular Structure in C5–C12 Alkanes," *Canadian Journal of Chemistry*, vol. 50, no. 16, pp. 2667-2679, 1972.

[145] W. F. Schmidt and A. O. Allen, "Mobility of Electrons in Dielectric Liquids," *The Journal of Chemical Physics*, vol. 52, no. 9, pp. 4788-4794, 1970.

[146] A. O. Allen, *Drift mobilities and conduction band energies of excess electrons in dielectric liquids*. U.S. Dept. of Commerce, National Bureau of Standards :--For sale by the Supt. of Docs., U.S. Govt. Print. Off., 1976.

[147] W. F. Schmidt, "Electron mobility in nonpolar liquids: the effect of molecular structure, temperature, and electric field," *Canadian Journal of Chemistry*, vol. 55, no. 11, pp. 2197-2210, 1977.

[148] G. Giuliani and G. Vignale, *Quantum Theory of the Electron Liquid*. Cambridge: Cambridge University Press, 2005.

[149] P. Y. Yu, *Fundamentals of Semiconductors Physics and Materials Properties*, 4th ed. ed. (Graduate Texts in Physics). Berlin, Heidelberg: Springer Berlin Heidelberg, 2010.

[150] W. Shockley, "The Theory of p-n Junctions in Semiconductors and p-n Junction Transistors," *Bell System Technical Journal*, vol. 28, no. 3, pp. 435-489, 1949.

[151] M. Costato and L. Reggiani, "On the saturated drift velocity of electrons in Si from 77° K to 500° K," *Lettere al Nuovo Cimento (1969-1970)*, vol. 3, no. 23, pp. 728-735, 1970.

[152] M. Costato and L. Reggiani, "Electron drift velocity and related phenomena in Si," *physica status solidi (b)*, vol. 42, no. 2, pp. 591-602, 1970.

[153] S. Komirenko, K. Kim, V. Kochelap, and M. Stroscio, "Coherent LO phonons generated by high-velocity electrons in two-dimensional channels and their impact on carrier transport," in *IEEE Conference on Nanotechnology*, Washington DC, USA, pp. 1-4, 2002.

[154] J. M. Lehr, F. J. Agee, R. Copeland, and W. D. Prather, "Measurement of the electric breakdown strength of transformer oil in the sub-nanosecond regime," *IEEE Transactions on Dielectrics and Electrical Insulation,* vol. 5, no. 6, pp. 857-861, 1998.

[155] J. Jadidian, M. Zahn, N. Lavesson, O. Widlund, and K. Borg, "Stochastic and deterministic causes of streamer branching in liquid dielectrics," *Journal of Applied Physics,* vol. 114, no. 6, p. 063301, 2013.

[156] M. Haidara and A. Denat, "Electron Multiplication in Liquid Cyclohexane and Propane - an Estimation of the Ionization Coefficient," *IEEE Transactions on Electrical Insulation,* vol. 26, no. 4, pp. 592-597, 1991.

[157] M. Haidara and A. Denat, "Electron multiplication in liquid cyclohexane and propane," *IEEE Transactions on Electrical Insulation,* vol. 26, no. 4, pp. 592-597, 1991.

[158] A. E. D. Heylen, "The relationship between electron—molecule collision cross-sections, experimental Townsend primary and secondary ionization coefficients and constants, electric strength and molecular structure of gaseous hydrocarbons," *Proceedings of the Royal Society of London. Series A: Mathematical, Physical and Engineering Sciences,* vol. 456, no. 2004, pp. 3005-3040, 2000.

[159] J. Qian *et al.*, "Microbubble-based model analysis of liquid breakdown initiation by a submicrosecond pulse," *Journal of Applied Physics,* vol. 97, no. 11, p. 113304, 2005.

[160] Zener, "A theory of the electrical breakdown of solid dielectrics," *Proceedings of the Royal Society of London. Series A,* 10.1098/rspa.1934.0116 vol. 145, no. 855, p. 523, 1934.

[161] K. C. Kao and J. P. C. Mcmath, "Time-Dependent Pressure Effect in Liquid Dielectrics," *IEEE Transactions on Electrical Insulation,* vol. EI-5, no. 3, pp. 64-68, 1970.

[162] F. O. Sullivan *et al.*, "A Model for the Initiation and Propagation of Positive Streamers in Transformer Oil," in *Conference of IEEE International Symposium on Electrical Insulation,* Vancouver, BC, Canada, pp. 210-214, 2008.

[163] J. G. Hwang, M. Zahn, and L. A. A. Pettersson, "Mechanisms behind positive streamers and their distinct propagation modes in transformer oil," *IEEE*

Transactions on Dielectrics and Electrical Insulation, vol. 19, no. 1, pp. 162-174, 2012.

[164] Y. Li, H.-B. Deng, G.-J. Zhang, and S.-H. Wang, "Simulational study on streamer discharge in transformer oil under positive nanosecond pulse voltage," (in Chinese), *Acta Physical Sinaca*, vol. 62, no. 12, pp. 124703-1-124703.

[165] P. Biller, "A simple qualitative model for the different types of streamers in dielectric liquids," in *International Conference on Conduction and Breakdown in Dielectric Liquids*, Roma, Italy, pp. 189-192, 1996.

[166] D. Sholl and J. A. Steckel, *Density Functional Theory: A Practical Introduction*. Wiley, 2009.

[167] N. Davari, P. O. Astrand, M. Unge, L. E. Lundgaard, and D. Linhjell, "Field-dependent molecular ionization and excitation energies: Implications for electrically insulating liquids," *Aip Advances*, vol. 4, no. 3, 2014.

[168] J. Casanovas, R. Grob, D. Delacroix, J. P. Guelfucci, and D. Blanc, "Photoconductivity studies in some nonpolar liquids," *The Journal of Chemical Physics*, vol. 75, no. 9, pp. 4661-4668, 1981.

[169] H. S. Smalo, P. Astrand, and S. Ingebrigtsen, "Calculation of ionization potentials and electron affinities for molecules relevant for streamer initiation and propagation," *IEEE Transactions on Dielectrics and Electrical Insulation*, vol. 17, no. 3, pp. 733-741, 2010.

[170] H. S. Smalo, P. O. Astrand, and S. Ingebrigtsen, "Calculation of ionization potentials and electron affinities for molecules relevant for streamer initiation and propagation," in *IEEE International Conference on Dielectric Liquids*, Chasseneuil, France, pp. 1-4, 2008.

[171] R. A. Holroyd, J. M. Preses, E. H. Boettcher, and W. F. Schmidt, "Photoconductivity induced by single-photon excitation of aromatic molecules in liquid hydrocarbons," *The Journal of Physical Chemistry*, vol. 88, no. 4, pp. 744-749, 1984.

[172] D. R. Lide, *Handbook of chemistry and physics*, 84th edition ed. Boca Raton: CRC Press, 2004.

[173] M. Harada, Y. Ohga, I. Watanabe, and H. Watarai, "Ionization energies for solvated polycyclic aromatic hydrocarbons," *Chemical Physics Letters*, vol. 303, no. 5, pp. 489-492, 1999.

[174] E. Clar and W. Schmidt, "Correlations between photoelectron and phosphorescence spectra of polycyclic hydrocarbons," *Tetrahedron,* vol. 32, no. 21, pp. 2563-2566, 1976.

[175] J. Jadidian, J. G. Hwang, M. Zahn, N. Lavesson, O. Widlund, and K. Borg, "Streamer dynamics in transformer oil: Influence of applied voltage rise time," in *IEEE International Conference on Plasma Science*, Chicago, IL, USA, pp. 1-1, 2011.

[176] J. Jadidian, J. G. Hwang, M. Zahn, N. Lavesson, O. Widlund, and K. Borg, "Streamer initiation and propagation in transformer oil under positive and negative impulse voltages," in *IEEE Pulsed Power Conference*, Chicago, IL, USA, pp. 251-256, 2011.

[177] J. G. Hwang, M. Zahn, L. A. A. Pettersson, O. Hjortstam, and R. Liu, "Modeling streamers in transformer oil: The transitional fast 3rd mode streamer," in *2009 IEEE International Conference on the Properties and Applications of Dielectric Materials*, Harbin, China, pp. 573-578, 2009.

[178] W. G. Chadband, "On Variations in the Propagation of Positive Discharges between Transformer Oil and Silicone Fluids," *Journal of Physics D: Applied Physics,* vol. 13, no. 7, pp. 1299-&, 1980.

[179] D. R. Lide, *Physical Constants of Organic Compounds*, , pages 519-537,89th ed. CRC Press/Taylor and Francis, Boca Raton, 2009.

[180] M. Zahn, *Electromagnetic Field Theory: A Problem Solving Approach*. Robert E. Krieger, Inc., 2003.

[181] I. Madshaven, "Modeling the propagation of streamer in liquids," Master Thesis, Physics and Mathematics, Norwegian University of Science and Technology, 2015.

[182] S. Ingebrigtsen, N. Bonifaci, A. Denat, and O. Lesaint, "Spectral analysis of light emitted from streamers in chlorinated alkane & alkene liquids," in *IEEE International Conference on Dielectric Liquids*, Chasseneuil, France, pp. 1-4, 2008.

[183] G. W. Penney and G. T. Hummert, "Photoionization Measurements in Air, Oxygen, and Nitrogen," *Journal of Applied Physics,* vol. 41, no. 2, pp. 572-577, 1970.

[184] Z. M. B, M. A. K, and S. S. V, "Photoionization of nitrogen and oxygen mixtures by radiation from a gas discharge," *Teplofizika Vysokikh Temperatur,* vol. 20, pp. 423-428, 1982.

[185] A. Hallac, G. E. Georghiou, and A. C. Metaxas, "Secondary emission effects on streamer branching in transient non-uniform short-gap discharges," *Journal of Physics D: Applied Physics,* vol. 36, no. 20, p. 2498, 2003.

[186] S. K. Dhali and A. K. Pal, "Numerical simulation of streamers in SF6," *Journal of Applied Physics,* vol. 63, no. 5, pp. 1355-1362, 1988.

[187] P. A. Vitello, B. M. Penetrante, and J. N. Bardsley, "Simulation of negative-streamer dynamics in nitrogen," *Physics Review E* vol. 49, no. 6, pp. 5574-5598, 1994.

[188] L. Onsager, "Deviations from Ohm's Law in Weak Electrolytes," *The Journal of Chemical Physics,* vol. 2, no. 9, pp. 599-615, 1934.

[189] F. O. Sullivan *et al.*, "Modeling the Effect of Ionic Dissociation on Charge Transport in Transformer Oil," in *IEEE Conference on Electrical Insulation and Dielectric Phenomena*, Kansas City, MO, USA, pp. 756-759, 2006.

[190] M. Abramowitz and I. A. Stegun, *Handbook of Mathematical Functions*. Washington DC:National Bureau of Standards, 1965.

[191] R. Gomer, *Field emission and field ionization*. NY: American Institute of Physics, Havard University Press, 1993.

[192] N. A. A. Rahim, R. Ranom, and H. Zainuddin, "Mechanism of the free charge carrier generation in the dielectric breakdown," *Journal of Physics: Conference Series,* vol. 949, no. 1, p. 012010, 2017.

[193] B. Halpern and R. Gomer, "Field Emission in Liquids," *The Journal of Chemical Physics,* vol. 43, no. 3, pp. 1069-1070, 1965.

[194] B. Halpern and R. Gomer, "Field Emission in Liquids," *The Journal of Chemical Physics,* vol. 51, no. 3, pp. 1031-1047, 1969.

[195] R. H. Fowler and L. Nordheim, "Electron emission in intense electric fields," *Proceedings of the Royal Society of London. Series A, Containing Papers of a Mathematical and Physical Character,* vol. 119, no. 781, pp. 173-181, 1928.

[196] J. J. O'Dwyer, *The theory of electrical conduction and breakdown in solid dielectrics*. Clarendon Press, 1973.

[197] L. W. Nordhiem and H. Fowler Ralph, "The effect of the image force on the emission and reflexion of electrons by metals," *Proceedings of the Royal Society*

of London. Series A, Containing Papers of a Mathematical and Physical Character, vol. 121, no. 788, pp. 626-639, 1928.

[198] C. A. Spindt, I. Brodie, L. Humphrey, and E. R. Westerberg, "Physical properties of thin-film field emission cathodes with molybdenum cones," *Journal of Applied Physics,* vol. 47, no. 12, pp. 5248-5263, 1976.

[199] G. Forbes Richard and H. B. Deane Jonathan, "Reformulation of the standard theory of Fowler–Nordheim tunnelling and cold field electron emission," *Proceedings of the Royal Society A: Mathematical, Physical and Engineering Sciences,* vol. 463, no. 2087, pp. 2907-2927, 2007.

[200] R. G. Forbes, "Simple good approximations for the special elliptic functions in standard Fowler-Nordheim tunneling theory for a Schottky-Nordheim barrier," *Applied Physics Letters,* vol. 89, no. 11, p. 113122, 2006/09/11 2006.

[201] Y. Nakamura, K. Shinsaka, and Y. Hatano, "Electron mobilities and electron–ion recombination rate constants in solid, liquid, and gaseous methane," *The Journal of Chemical Physics,* vol. 78, no. 9, pp. 5820-5824, 1983.

[202] M. Tachiya, "Breakdown of the Debye theory of bulk ion recombination," *The Journal of Chemical Physics,* vol. 87, no. 7, pp. 4108-4113, 1987.

[203] M. Wojcik and M. Tachiya, "Effect of an external electric field on diffusion-controlled bulk electron-ion recombination in high-mobility systems," *The Journal of Chemical Physics,* vol. 109, no. 10, pp. 3999-4008, 1998.

[204] J. H. Baxendale, J. P. Keene, and E. J. Rasburn, "Conductimetric study of the kinetics of electrons in pulse irradiated n-hexane and cyclohexane at room temperature," *Journal of the Chemical Society, Faraday Transactions 1: Physical Chemistry in Condensed Phases,* vol. 70, pp. 718-728, 1974.

[205] T. Briels, J. Kos, G. Winands, E. Van Veldhuizen, and U. Ebert, "Positive and negative streamers in ambient air: measuring diameter, velocity and dissipated energy," *Journal of Physics D: Applied Physics,* vol. 41, no. 23, p. 234004, 2008.

[206] W. F. Schmidt, "Hot Electron Mobility and Electron Attachment in Non-Polar Liquids," in *The Liquid State and Its Electrical Properties*: Springer, 1988, pp. 273-282.

[207] M. Haidara and A. Denat, "Electron multiplication in liquid cyclohexane and propane: an estimation of the ionization coefficient," in *International*

Conference on Conduction and Breakdown in Dielectric Liquids, Grenoble, France, pp. 397-401, 1990.

[208] Y. Sakai, W. F. Schmidt, and A. G. Khrapak, "Self-trapping of electrons in liquid nitrogen," *IEEE Transactions on Dielectrics and Electrical Insulation*, vol. 1, no. 4, pp. 724-727, 1994.

[209] J. P. Hernandez, "Electron self-trapping in liquids and dense gases," *Reviews of Modern Physics*, vol. 63, no. 3, pp. 675-697, 1991.

[210] K. Dotoku, H. Yamada, S. Sakamoto, S. Noda, and H. Yoshida, "Field emission into nonpolar organic liquids," *The Journal of Chemical Physics*, vol. 69, no. 3, pp. 1121-1125, 1978.

[211] "IEC 60897 "Methods for the determination of the lightning impulse breakdown voltage of insulating liquids"," ed, 1987.

[212] B. Meulenbroek, "Streamer branching: conformal mapping and regularization," Ph.D. Thesis, TEchnische Universiteit Eindhoven Wageningen, Netherlands, 2006.

[213] N. Y. Babaeva and M. J. Kushner, "Streamer branching: The role of inhomogeneities and bubbles," *IEEE Transactions on Plasma Science*, vol. 36, no. 4, pp. 892-893, 2008.

[214] A. Luque and U. Ebert, "Electron density fluctuations accelerate the branching of positive streamer discharges in air," *Physical Review E* vol. 84, no. 4 Pt 2, p. 046411, 2011.

[215] L. Papageorgiou, A. C. Metaxas, and G. E. Georghiou, "Three-dimensional numerical modelling of gas discharges at atmospheric pressure incorporating photoionization phenomena," *Journal of Physics D: Applied Physics*, vol. 44, no. 4, 2011.

[216] N. Y. Babaeva, A. N. Bhoj, and M. J. Kushner, "Streamer dynamics in gases containing dust particles," *Plasma Sources Science & Technology*, vol. 15, no. 4, pp. 591-602, 2006.

[217] N. Y. Babaeva and M. J. Kushner, "Structure of positive streamers inside gaseous bubbles immersed in liquids," *Journal of Physics D: Applied Physics*, vol. 42, no. 13, 2009.

[218] N. Y. Babaeva, D. V. Tereshonok, G. V. Naidis, and B. M. Smirnov, "Streamer branching on clusters of solid particles in air and air bubbles in liquids," *Journal of Physics: Conference Series*, vol. 774, no. 1, p. 012151, 2016.

[219] O. Lesaint and M. Jung, "On the relationship between streamer branching and propagation in liquids: influence of pyrene in cyclohexane," *Journal of Physics D: Applied Physics,* vol. 33, no. 11, pp. 1360-1368, 2000.

[220] S. Singh, Y. V. Serdyuk, and R. Summer, "Streamer branching in air: Physical model and simulations in fully 3D spatial domain," in *IEEE International Conference on the Properties and Applications of Dielectric Materials*, 2015, pp. 220-223.

[221] O. Lesaint, "Pre-breakdown phenomena in liquids and their relationship with breakdown properties in high voltage applications," *Cigre A2-D1 colloquium, Bruges, Belgium, paper PS1-01,* 2007.

[222] C. Hodgman, R. Weast, R. Shankland, and S. Selby, "Handbook of Chemistry and Physics, 2611, The Chemical Rubber Publ," *Co. Cleveland, Ohio,* 1962.

[223] R. C. Reid, J. M. Prausnitz, and T. K. Sherwood, *The properties of gases and liquids*. McGraw-HIll, 1977.

[224] *Data sheet of cyclohexane* [Online]. Available: https://cameochemicals.noaa.gov/chris/CHX.pdf.

[225] V. Majer, V. Svoboda, and H. V. Kehiaian, *Enthalpies of vaporization of organic compounds: a critical review and data compilation*. Blackwell Scientific Oxford, 1985.

[226] J.-Q. Dong, R.-S. Lin, and W.-H. Yen, "Heats of vaporization and gaseous molar heat capacities of ethanol and the binary mixture of ethanol and benzene," *Canadian journal of chemistry,* vol. 66, no. 4, pp. 783-790, 1988.

[227] *Handbook of Chemistry and Physics*. The Chemical Rubber Publication Co, 1962.

[228] J. M. Warman, "Concerning electron-ion recombination and electron thermalization in liquid and solid methane," *The Journal of Physical Chemistry,* vol. 87, no. 22, pp. 4353-4355, 1983.

[229] N. Y. Babaeva and G. V. Naidis, "On streamer dynamics in dense media," *Journal of Electrostatics,* vol. 53, no. 2, pp. 123-133, 2001.

[230] D. M. Anderson, G. B. McFadden, and A. A. Wheeler, "DIFFUSE-INTERFACE METHODS IN FLUID MECHANICS," *Annual Review of Fluid Mechanics,* vol. 30, no. 1, pp. 139-165, 1998.

[231] R. Morrow, "Theory of negative corona in oxygen," *Physical Review A,* vol. 32, no. 3, pp. 1799-1809, 1985.

[232] N. L. Aleksandrov and E. M. Bazelyan, "Simulation of long-streamer propagation in air at atmospheric pressure," *Journal of Physics D: Applied Physics,* vol. 29, no. 3, pp. 740-752, 1996.

[233] R. Morrow and J. J. Lowke, "Streamer propagation in air," *Journal of Physics D: Applied Physics,* vol. 30, no. 4, pp. 614-627, 1997.

[234] G. V. Naidis, "Simulation of interaction between two counter-propagating streamers," *Plasma Sources Science and Technology,* vol. 21, no. 3, p. 034003, 2012.

[235] T. M. P. Briels, E. M. van Veldhuizen, and U. Ebert, "Positive streamers in air and nitrogen of varying density: experiments on similarity laws," *Journal of Physics D: Applied Physics,* vol. 41, no. 23, p. 234008, 2008.

[236] J. Jadidian, M. Zahn, N. Lavesson, O. Widlund, and K. Borg, "Abrupt changes in streamer propagation velocity driven by electron velocity saturation and microscopic inhomogeneities," *IEEE Transactions on Plasma Science,* vol. 42, no. 5, pp. 1216-1223, 2014.

[237] R. A. Holroyd and W. F. Schmidt, "Transport of electrons in nonpolar fluids," *Annual Review of Physical Chemistry,* vol. 40, no. 1, pp. 439-468, 1989.

[238] C. Canali, G. Majni, R. Minder, and G. Ottaviani, "Electron and hole drift velocity measurements in silicon and their empirical relation to electric field and temperature," *IEEE Transactions on Electron Devices,* vol. 22, no. 11, pp. 1045-1047, 1975.

[239] I. Iddrissu, "Study of Electrical Strength and Lifetimes of Polymetric Insulation for DC Application," Ph.D. Thesis, School of Electrical and Electronic Engineering, University of Manchester, UK, 2016.

[240] R. Bozzo, F. Guastavino, and G. C. Montanari, "Evaluation of insulating materials on the basis of electrical treeing and breakdown tests," in *International Conference on Conduction and Breakdown in Solid Dielectrics*, Sestri Levante, Italy, pp. 539-544, 1992.

[241] U. Khayam *et al.*, "Partial Discharge Pattern of Various Defects Measured by Spiral Antenna as UHF External Sensor on 66 kV GIS Model," presented at the International Journal on Electrical Engineering and Informatics, 2014.

[242] D. Liu, Q. Liu, and Z. Wang, "Electric Field Simulation of Needle Tips with Different Shape Formations Using FEM Method," in *The International Symposium on High Voltage Engineering*, Budapest, Hungary, pp. 61-73, 2019.

[243] *COMSOL Multiphysics Reference Manual*.

[244] S. Shen, Q. Liu, and Z. Wang, "Shockwave Characteristics of Streamer Propagation in Insulating Liquids under Positive Lightning Impulse," *IEEE Transactions on Dielectrics and Electrical Insulation,* vol. 28, no. 2, pp. 493-501, 2021.

[245] S. Yohan, P. Mikhail, N. S. Mikhail, D. Danil, and F. Alexander, "On the electrostrictive mechanism of nanosecond-pulsed breakdown in liquid phase," *Journal of Physics D: Applied Physics,* vol. 46, no. 16, p. 162001, 2013.

[246] M. N. Shneider and M. Pekker, *Liquid Dielectrics in an Inhomogeneous Pulsed Electric Field*: IOP Publishing, 2016. [Online]. Available: http://dx.doi.org/10.1088/978-0-7503-1245-5.

[247] V. P. Skripov, R. Kondor, and D. Slutzkin, *Metastable liquids*. Wiley New York, 1974.

[248] V. E. Vinogradov, "Depression of the cavitation centers in water under pulsed tension conditions," *Technical Physics Letters,* vol. 35, no. 1, pp. 54-56, 2009.

[249] Y. Viisanen, R. Strey, and H. Reiss, "Homogeneous nucleation rates for water," *The Journal of Chemical Physics,* vol. 99, no. 6, pp. 4680-4692, 1993.

[250] A. Villares, B. Giner, H. Artigas, C. Lafuente, and F. Royo, "Study of the surface tensions of cyclohexane or methylcyclohexane with some cyclic ethers," *Journal of solution chemistry,* vol. 34, no. 2, pp. 185-198, 2005.

[251] G. Vazquez, E. Alvarez, and J. M. Navaza, "Surface tension of alcohol water+ water from 20 to 50. degree. C," *Journal of chemical and engineering data,* vol. 40, no. 3, pp. 611-614, 1995.

[252] L. Lewand, "Laboratory evaluation of several synthetic and agricultural-based dielectric liquids," in *Doble International Client Conference E*, vol. 5, p. 2001.

[253] S. Tenbohlen and M. Koch, "Aging performance and moisture solubility of vegetable oils for power transformers," *IEEE transactions on power delivery,* vol. 25, no. 2, pp. 825-830, 2010.

[254] J. F. Kolb, R. P. Joshi, S. Xiao, and K. H. Schoenbach, "Streamers in water and other dielectric liquids," *Journal of Physics D: Applied Physics,* vol. 41, no. 23, p. 234007, 2008.

[255] E. A. Melo-Espinosa *et al.*, "Surface Tension Prediction of Vegetable Oils Using Artificial Neural Networks and Multiple Linear Regression," *Energy Procedia,* vol. 57, pp. 886-895, 2014.

Appendix A. List of Publications

Peer Reviewed Journal Papers

[1] **D. Liu**, Q. Liu, and Z.D. Wang, "Modelling of second mode positive streamer in cyclohexane by considering optimized electron saturation velocity," *Journal of Physics D: Applied Physics*, vol. 54, no. 11, p. 115502, 2021.

Conference Publications

[1] **D. Liu**, Q. Liu, and Z.D. Wang, "Electric Field Simulation of Needle Tips with Different Shape Formations Using FEM Method," in *The International Symposium on High Voltage Engineering*, Budapest, Hungary, pp. 61-73, 2019.

[2] **D. Liu**, Q. Liu, B. Liu, and Z.D. Wang, "Modelling the Electrostrictive-force induced Cavitation Formation Process in Dielectric Liquids," in *2020 IEEE International Conference on High Voltage Engineering and Application (ICHVE)*, Beijing, China, pp. 1-4, 2020.

[3] **D. Liu**, Q. Liu, and Z.D. Wang, "Simulation on Electrostrictive-force induced Cavitation Formation Process in Cyclohexane," in *2020 IEEE Conference on Electrical Insulation and Dielectric Phenomena (CEIDP)*, East Rutherford, NJ, USA, pp. 304-307, 2020.

[4] **D. Liu**, Q. Liu, and Z.D. Wang, "Modelling the Effects of Voltage Rise Rates on the Streamer Initiation in Cyclohexane," in *2022 International Conference on Dielectric Liquids (ICDL)* (to be submitted)